Search for new phenomena in events with jets and missing transverse momentum at the high-energy LHC RunII with the ATLAS detector

Andrea Rodríguez Pérez

Ph.D. thesis

Programa de doctorat en Física
Institut de Física d'Altes Energies
Universitat Autònoma de Barcelona
Departament de Física
Facultat de Ciències

Friday 28th September, 2018

Director:
Prof. Mario Martínez Pérez
Institució Catalana de Recerca i Estudis Avançat
Institut de Física d'Altes Energies
Universitat Autònoma de Barcelona

CERN-THESIS-2018-220
04/10/2018

Yo he pensado que a mí también me interesaría ser intelectual, como no tengo nada que perder.

Amanece, que no es poco.

Contents

Introduction

The Large Hadron Collider (LHC) is the world's largest and most powerful particle accelerator. It accelerates and collides protons at a centre-of-mass energy of 13 TeV. The discovery of the Higgs boson in the LHC in 2012 consolidated the Standard Model (SM) of particle physics as a consistent theory, able to predict to a very high level of accuracy all the high-energy particle physics phenomena known to date.

However, some fundamental unanswered issues overshadow the success of the SM. The lack of a dark matter candidate, the inability to predict the matter-antimatter asymmetry observed in the universe, and some theoretical subtleties that make the mass of the higgs boson appear very sensitive to the presence of new physics are some of the reasons why the SM is regarded as an incomplete theory.

Supersymmetry (SUSY) is one of the most popular theories for physics beyond-the-standard-model, because it provides an elegant answer to some of the open issues of the SM. It constitutes an extension of the SM where new particles are introduced, and it has been one of the main focuses of experimental particle physics for a few decades. The experiments at the LHC provide a unique opportunity to search for these particles and prove the existence of SUSY at the high energy frontier.

Of particular interest are the searches for the so-called third generation squarks, stops and sbottoms, which are the main topic of this thesis. The naturalness argument points to masses of the order of the TeV for these particles. If this argument holds, they could in principle be produced in pairs in the high-energy LHC proton-proton collisions. Although the searches during Run-1 set strong limits on their masses, the efforts towards their discovery continue during the higher-energy LHC Run-2 in the ATLAS and CMS experiments.

In this thesis, the search for stop pair production with the ATLAS detector is presented in final states with no leptons, large jet multiplicity and high missing transverse momentum with the data collected by ATLAS in 2015 and 2016 at $\sqrt{s} = 13$ TeV. The analysis of the data relies on a complex definition of control regions allowing to constrain the standard model background predictions to an unprecedented level, and makes use of a profile likelihood fit to determine whether the data agree with the background (SM only) or the signal (presence of SUSY) hypotheses. The results are in good agreement with the SM predictions, and 95% CL limits are set on the masses of the SUSY particles involved in the processes considered.

The thesis is organised as follows: First, a brief summary of the Standard Model is given in chapter 1. Then, the main concepts and the phenomenology of Supersymmetry is presented in chapter 2. The description of the LHC and the ATLAS detector are given in chapter 3. The main points of the statistical analysis used are described in chapter 5. Finally, the analysis strategy is detailed in chapter 6, and the results are shown in chapter 7. Chapter 7.4 is devoted to Conclusions.

The results presented in this thesis led to the following publications of the ATLAS Collaboration:

- *Search for a scalar partner of the top quark in the jets plus missing transverse momentum final state at* $\sqrt{s} = 13$ *TeV with the ATLAS detector* (September 2017, JHEP12 (2017) 085).
- *Search for the Supersymmetric Partner of the Top Quark in the Jets+Emiss Final State at* $\sqrt{s} = 13$ *TeV* (August 2016, ATLAS-CONF-2016-077).

This thesis is complemented with two appendices, describing the activities performed with the ATLAS Tile Calorimeter group. Appendix A refers the studies carried out to develop a correction applied to the jet transverse momentum with the aim to correct for the effects of malfunctioning modules of the calorimeter, which was finally approved as an official ATLAS tool. Appendix B collects results from the test beam carried out in preparation for the TileCal upgrade for the HL-LHC.

CHAPTER 1

Standard Model

1.1 Introduction

The Standard Model (SM) of particle physics [1, 2, 3] is a renormalisable quantum field theory that describes the elementary particles and three of the four fundamental interactions among them, namely the electromagnetic, the weak, and the strong interactions; while gravity is described by Einstein's General Relativity [4]. It is the theory that, to date, describes nature at the sub-nuclear level. It has been thoroughly tested since its development in the 1960s, and all the particles that it predicts have been found experimentally, the last one being the Higgs boson, which was discovered at CERN in 2012 [5, 6].

According to the SM, each of the interactions between the elementary particles arises from a local (*gauge*) symmetry of the theory, and is mediated by a particle of integer spin (a *boson*). The electromagnetic interaction, the first to be discovered and described in a quantum manner, is mediated by a spin-one particle, the photon, and arises from a $U_{\text{em}}(1)$ gauge symmetry. The weak interaction, which is responsible for the nuclear beta-decay, has three spin-one mediators, the $W^{\pm}$ and Z bosons, and has an associated symmetry described by the group $SU_L(2) \otimes U_Y(1)$ (which includes the unification with the electromagnetic interaction), where the "L" refers to left-handed particles (the ones participating in the interaction), and the "Y" refers to the weak hypercharge. The strong interaction is the force that bonds protons and neutrons together in the nucleus, due to the interactions between the quarks that compose them, and appears due to a $SU_C(3)$ symmetry group, where the "C" means color. The mediators of the strong force are gluons, spin-one massless particles. Table 1.1 summarises the characteristics of the interactions and the bosons that mediate them.

Interaction	**Mediator**	**Spin**	**Electric charge**
Electromagnetic	Photon (γ)	1	0
	W^+	1	+1
Weak	W^-	1	-1
	Z	1	0
Strong	Gluon (g)	1	0

TABLE 1.1: Summary of the interactions in the Standard Model and their mediators

In addition to the bosons responsible for the elementary interactions, the scalar Higgs boson is responsible for the masses of the rest of the SM particles, and it will be described in detail in section 1.4.

The fermions, which are particles with half-integer spin, are the components of matter. They are subdivided into six leptons and six quarks (and their antiparticles), which are in turn organised in three generations. The generations only differ from each other by mass. A summary of the SM fermions is given in table 1.2.

SM fermions						
	Leptons			**Quarks**		
	ℓ	Charge	Mass (MeV/c^2)	q	Charge	Mass (MeV/c^2)
First generation	e	-1	0.511	d	-1/3	4.7
	ν_e	0	$< 2 \cdot 10^{-6}$	u	2/3	2.2
Second generation	μ	-1	106	s	-1/3	96
	ν_μ	0	< 0.19	c	2/3	1270
Third generation	τ	-1	1777	b	-1/3	4180
	ν_τ	0	< 18.2	t	2/3	173210

TABLE 1.2: Summary of the fermions of the Standard Model, their masses and electric charges. The u d and s quark masses cited here are the so-called current masses calculated in the $\overline{\text{MS}}$ scheme [7], the c and b masses are the running masses in the $\overline{\text{MS}}$ scheme, and the top mass comes from direct measurements [8].

The lepton generations are composed of a neutrino, which has no charge, and a negatively charged lepton. They interact through weak and electromagnetic forces. The neutrinos are considered massless in the Standard Model, although the observation of neutrino oscillation [9] proves differently. Leptons are assigned a lepton number (L) of 1, while antileptons have $L = -1$. The lepton number is conserved in electroweak interactions.

Quarks interact through electromagnetic, weak and strong forces. They are confined in composite particles called hadrons, and can not be observed as independent particles, as it will be explained in the following. Hadrons are formed by either three quarks (baryons) or a quark and an antiquark pair (mesons). A baryon number is defined, with $B(q) = 1/3$ and $B(\bar{q}) = -1/3$, and therefore the baryon number is 1 for baryons and 0 for mesons. The baryon number is conserved and its conservation is responsible for the stability of the proton.

In the following sections, the different theories that conform the Standard Model are described.

1.2 Quantum Electrodynamics

Quantum Electrodynamics (QED) was developed by Feynman, Schwinger and Tomonaga [10, 11, 12], and describes the interactions between photons and electrically charged particles in a relativistic, quantum manner. It is based on the symmetry (invariance) under phase transformations:

$$\psi \to \psi' = e^{iQ\theta}\psi. \tag{1.1}$$

Here ψ represents a fermionic spinor. This fermion satisfies the Dirac equation of free motion

$$\mathcal{L}_{\text{free}} = \bar{\psi}(i\gamma_\mu \partial^\mu - m)\psi, \tag{1.2}$$

where γ_μ are the Dirac matrices and $\bar{\psi}$ denotes the conjugate of ψ.

This lagrangian is invariant under a global transformation like the one in equation 1.1, but if the parameter of the transformation θ depends on x, and therefore a local gauge transformation is applied, the lagrangian must be changed to remain invariant. This can be done by substituting the partial derivative ∂_μ by a *covariant derivative* of the form:

$$\partial_\mu \to D_\mu = \partial_\mu - ieA_\mu, \tag{1.3}$$

where the new field A_μ behaves under gauge transformations:

$$A_\mu \to A'_\mu = A_\mu + \frac{1}{e}\partial_\mu \theta(x). \tag{1.4}$$

A kinetic term for this new field has to be added to the lagrangian, which is of the form $-\frac{1}{4}F_{\mu\nu}F^{\mu\nu}$, with $F^{\mu\nu} = \partial^\mu A^\nu - \partial^\nu A^\mu$. The QED lagrangian is then

$$\mathcal{L}_{\text{QED}} = \bar{\psi}(i\gamma^\mu D_\mu - m)\psi - \frac{1}{4}F^{\mu\nu}F_{\mu\nu} = \bar{\psi}(i\gamma^\mu \partial_\mu - m)\psi - eQ\bar{\psi}\gamma^\mu A_\mu \psi - \frac{1}{4}F^{\mu\nu}F_{\mu\nu}. \tag{1.5}$$

Due to the introduction of the covariant derivative, an interaction term between the fermion and the field A_μ appears. The quantity e is interpreted as a coupling constant of the interaction between the fermion and the A_μ field, which is identified with the photon. A mass term for the photon would be of the form $m^2 A_\mu A^\mu$, but it can not be included, since it is not gauge invariant. Therefore, the photon has to be a massless vector boson.

QED is then a gauge theory with a U(1) symmetry, where the conserved quantity is the electric charge Q, according to Noether's theorem [13]. The coupling e is a running parameter and is obtained experimentally, and often expressed in terms of the so-called fine structure constant, which asymptotically at low q^2 is

$$\alpha = \frac{e^2}{4\pi\hbar c} \approx \frac{1}{137} \tag{1.6}$$

When one tries to include calculations at higher order in perturbation theory, infinite predictions appear. These are solved using the renormalisation method [14], in such a way that the infinities are absorbed into the coupling parameter of the theory, which after renormalisation depends on the momentum exchange of the interaction q^2. Details on regularisation and renormalisation go beyond the scope of this theory introduction.

$$\alpha(q^2) = \frac{\alpha(0)}{1 - (\alpha(0)/3\pi)\log(q^2/m^2)}. \tag{1.7}$$

The coupling is stronger for increasing momentum transfer q^2, i.e. with decreasing distance.

1.3 Electroweak theory

The theory of weak interactions was first proposed by Fermi in 1933 [15] to explain the β decay of nuclei. In this theory, a neutron decayed to a proton, an electron and a neutrino, with a coupling constant G_F known as Fermi's constant. The predictions of the theory agreed with experiments, but this theory is non-renormalisable.

The solution to this problem was proposed by Glashow and Weinberg [1, 2], who unified it with QED in the 1960s. In this unified Electroweak (EW) theory, the symmetry group is $\text{SU}(2)_L \otimes \text{U}(1)_Y$. The $\text{SU}(2)_L$ part is a three-dimensional group, and therefore has three generators and three gauge bosons, where the L stands for

left-handed, as introduced before. Left- and right-handed chiralities are defined by

$$\psi_{L/R} = \frac{1 \mp \gamma^5}{2}\psi, \tag{1.8}$$

where $\gamma^5 = i\gamma^0\gamma^1\gamma^2\gamma^3$. The three generators are $\hat{T}_i = \sigma_i/2$ $(i = 1, 2, 3)$, where σ_i are the Pauli matrices, and the new conserved quantum number is the weak isospin, which behaves in a spin-like manner. Left- and right-handed fermions transform differently under the operators of the symmetry group. Left-handed particles and right-handed antiparticles transform as doublets, whereas right-handed particles and left-handed antiparticles transform as singlets:

$$f_L^i = \begin{pmatrix} \nu_L^i \\ \ell_L \end{pmatrix}, \begin{pmatrix} u_L^i \\ d_L^i \end{pmatrix}$$

$$f_R^i = \ell_R^i, u_R^i, d_R^i, \tag{1.9}$$

where $i = 1, 2, 3$ is the index of the generation.

The part $\mathrm{U}(1)_Y$ of the symmetry is one-dimensional, and it has one hypercharge Y generator only. The hypercharge quantum number is related to the third component of the weak isospin and the electric charge as

$$Y = 2(Q - T_3). \tag{1.10}$$

The lagrangian is obtained by introducing a covariant derivative to force the invariance under the gauge group:

$$D_\mu = \partial_\mu - igT^i W_\mu^i - ig\frac{Y}{2}g' B_\mu, \tag{1.11}$$

where g and g' are the coupling constants of the $\mathrm{SU}(2)_L$ and $\mathrm{U}(1)_Y$ groups, respectively. The bosons W_μ^i are the mediators of the $\mathrm{SU}(2)_L$ part of the interactions, while B_μ is the vector boson mediator of the $\mathrm{U}(1)_Y$ interaction. The lagrangian will then have a part that describes the fermionic interactions, and two extra terms to include the kinetic terms of the bosons of the two interactions, which are of the form $\frac{1}{4}B_{\mu\nu}B^{\mu\nu}$ and $\frac{1}{4}W_{\mu\nu}^i W^{i\mu\nu}$, with

$$B_{\mu\nu} = \partial_\mu B_\nu - \partial_\nu B_\mu.$$

$$W_{\mu\nu}^i = \partial_\mu W_\nu^i - \partial_\nu W_\mu^i + g\epsilon^{ijk}W_\mu^j W_\nu^k. \tag{1.12}$$

The lagrangian is then of the form

$$\mathcal{L}_W = \sum_{f=\ell,q} \bar{f} i\gamma^\mu D_\mu f - \frac{1}{4}W_{\mu\nu}^i W^{i\mu\nu} - \frac{1}{4}B_{\mu\nu}^i B^{i\mu\nu}, \tag{1.13}$$

where the sum is performed over all generations of quarks and leptons.

But the bosons that are observed are in reality two charged bosons, $(W^\pm)$ and one neutral (Z^0). The W bosons are obtained from a linear combination of W^1 and W^2 such that it makes the electric charge ± 1

$$W_\mu^\pm = \frac{1}{\sqrt{2}}(W_\mu^1 \mp W_\mu^2) \tag{1.14}$$

Similarly, the Z and γ bosons can be obtained as a linear combination of the two remaining fields, which have $T^3 = 0$, B_μ and W^3_μ

$$\begin{pmatrix} Z_\mu \\ A_\mu \end{pmatrix} = \begin{pmatrix} \cos\theta_W & -\sin\theta_W \\ \sin\theta_W & \cos\theta_W \end{pmatrix} \begin{pmatrix} W^3_\mu \\ B_\mu \end{pmatrix}, \tag{1.15}$$

where a new mixing parameter has been added, θ_W, the Weinberg angle, which has to be measured experimentally, and whose most recent value is $\sin^2\theta_W = 0.23129 \pm 2 \cdot 10^{-4}$ [8].

The fermionic mass term of equation 1.2 is not gauge-invariant anymore, since the left- and right-handed fermions transform differently under $\mathrm{SU}(2)_L$. The same happens with the boson masses: The four new bosons have to be massless to respect gauge-invariance, but experimental data suggest otherwise. A mechanism to include these masses has to be introduced, and is described in the following section.

1.4 The Higgs Mechanism

The solution to the problem of the inclusion of the mass terms in the lagrangian was found almost simultaneously by F. Englert [16] and P. Higgs [17] in 1964, using a Spontaneous Symmetry Breaking (SSB) mechanism. In order to do this, a scalar complex field, which is a $\mathrm{SU}(2)_L \otimes \mathrm{U}(1)_Y$ doublet is introduced:

$$\phi \equiv \begin{pmatrix} \phi^+ \\ \phi^0 \end{pmatrix}. \tag{1.16}$$

The lagrangian of this scalar can be written as

$$\mathcal{L}_\phi = D_\mu \phi^\dagger D^\mu \phi - (\lambda(\phi^\dagger\phi)^2 + \mu^2 \phi^\dagger \phi) \tag{1.17}$$

where the second term represents a potential for the field, $V(\phi)$, with two parameters, μ and λ; and the covariant derivative is the electroweak derivative defined in equation 1.11. This lagrangian is invariant under U(1) transformations of the type

$$\phi \to \phi e^{i\alpha}. \tag{1.18}$$

If $\mu^2 > 0$, the first term of the potential is a mass term. However, if μ^2 is negative, the potential gives the vacuum a non-zero expectation value of

$$\phi^\dagger\phi = -\frac{\mu^2}{2\lambda} \equiv \frac{v^2}{2}. \tag{1.19}$$

This minimum of the potential occurs all along a circumference of radius $\mu^2/2\lambda$, and it constitutes therefore a continuous of points which share the original symmetry of the lagrangian. In order to quantize the field one has to choose a specific vacuum value. As was found by Goldstone [18, 19], the acquisition of a non-zero expectation value by a field implies the appearance of a massless boson (usually referred to as Goldstone boson). For the photon to stay massless, the neutral component of the scalar field is the one chosen to have a non-zero expectation value

$$\phi_0 = \begin{pmatrix} 0 \\ v/\sqrt{2} \end{pmatrix}. \tag{1.20}$$

Once the field is perturbatively expanded around the vacuum

$$\phi = e^{iT^i\xi^i(x)/v}\begin{pmatrix}0\\ v/\sqrt{2}+H(x)\end{pmatrix}, \tag{1.21}$$

it can be introduced in the Lagrangian. Four new fields have appeared. The three $\xi^i(x)$ are massless Goldstone bosons that will disappear from the lagrangian in a redefinition of the $SU(2)_L \otimes U(1)_Y$ bosons, which will acquire mass and therefore an extra polarization. The field H(x) is referred to as the Higgs field. The leading-order masses of the gauge bosons are identified as

$$m_W = \frac{vg}{2} \tag{1.22}$$

$$m_Z = v\frac{\sqrt{g^2+g'^2}}{2}, \tag{1.23}$$

and, for the Higgs

$$m_H = \sqrt{2\lambda}v. \tag{1.24}$$

In order to obtain the masses for the fermions, a coupling between them and the scalar field has to be introduced in the lagrangian with a Yukawa term:

$$\mathcal{L}_Y = \sum_{f=q,\ell} \lambda_f[\bar{f}_L\phi f_R + \bar{f}_R\bar{\phi}f_L], \tag{1.25}$$

where the matrices λ_f contain the coupling constants of the Higgs to the fermions. After substituting equation 1.21 in the Yukawa lagrangian, the fermion masses are of the form

$$m_f = \lambda_f\frac{v}{2}. \tag{1.26}$$

1.5 Quantum Chromodynamics

Quantum Chromodynamics (QCD) is the quantum field theory describing strong interactions. As already mentioned, it is responsible for keeping the protons and neutrons together in the nuclei of the atoms, and for the confinement of quarks in hadrons. It is constructed from a *color* SU(3) symmetry. The development of the theory was made by Gell-Mann and Fritzsch in the 1970s [20], although the idea of quarks and color was already introduced by Greenberg [21] following the observations of a heavy baryon that violated Pauli's exclusion principle. The color is defined as a quantum number that can take three different values (green, red and blue) and which only exists in quarks and not in leptons.

As was done for QED, the symmetry is introduced in the theory by adding a covariant derivative to the free lagrangian. In this case:

$$D_\mu = \partial_\mu + g_s\frac{\lambda_a}{2}A^a_\mu, \tag{1.27}$$

where g_s is the coupling of the strong interaction, λ_a are the Gell-Mann matrices, generators of the SU(3) group, with $a = 1, 2, ..., 8$. The eight vector fields A^a_μ are thus the gluons. In an analogous way as was done for QED, a kinematic term for the gluon must also be included, of the form $\frac{1}{4}F^a_{\mu\nu}F^{\mu\nu a}$, where

$$F^a_{\mu\nu} = \partial_\mu A^a_\nu - \partial_\nu A^a_\mu - g_s f_{abc}A^b_\mu A^c_\nu. \tag{1.28}$$

Here f_{abc} are the structure constants of the SU(3) group. The third term of this equation represents the self-interaction of the gluon, which contains vertices with three and four gluons. This means that gluons carry color. This term does not appear in the QED lagrangian because it is an abelian theory, while QCD is not. The QCD lagrangian is thus

$$\mathcal{L}_{\text{QCD}} = \bar{q}_i(iD^\mu\gamma_\mu - m)_{ij}q_j - \frac{1}{4}F^a_{\mu\nu}F^{a\mu\nu}. \tag{1.29}$$

Here the indices i, j account for the color of the quarks and go from 1 to 3.

The strong coupling constant is often expressed in terms of α_s

$$g_s^2 = 4\pi\alpha_s, \tag{1.30}$$

analogously to the fine structure constant of QED. The variable α_s depends on the energy scale of the interaction. This dependency appears when the theory is renormalised [22, 14], as happens with the coupling of the electromagnetic and weak interactions. The main difference is that, in strong interactions, the coupling constant decreases with increasing momentum exchange (or equivalently, with decreasing distance) as can be seen in figure 1.1. At leading order, α_s can be expressed as a function of the momentum transfer as

$$\alpha_s(q^2) = \frac{12\pi}{(11n - 2f)\ln(q^2/\Lambda^2_{\text{QCD}})} \tag{1.31}$$

where n is the number of colours (3 in the SM) and f is the number of quark flavors (6 in the SM). The parameter Λ_{QCD} is a constant of the theory, at which α_s diverges, and it can be therefore interpreted as a limit for the perturbative approximation. As a consequence, quarks and gluons are asymptotically free at very small distances

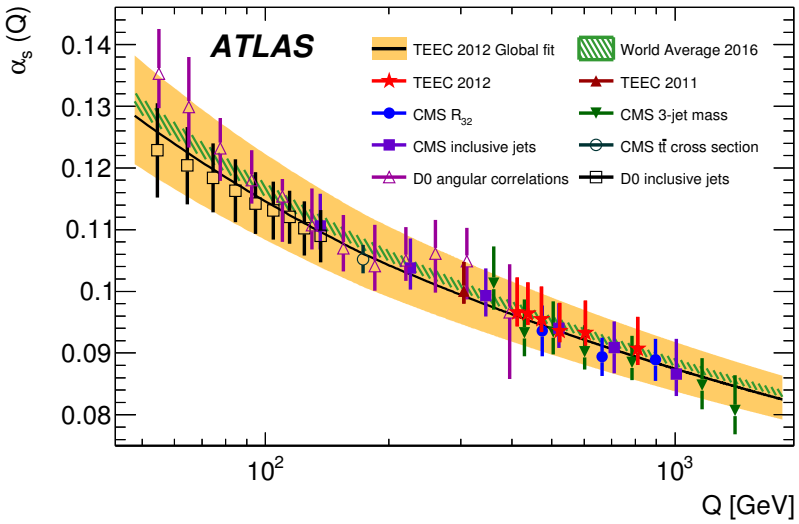

FIGURE 1.1: Measurement of the strong coupling constant with the ATLAS experiment compared to previous experiments [23].

($q^2 << \Lambda^2_{\text{QCD}}$). This property is known as *asymptotic freedom*, and implies that the perturbative approach of QCD can be used to describe strong interactions between quarks in very hard regimes, where quarks and gluons behave almost as free particles. The other main consequence of the behaviour of the strong coupling is the so-called

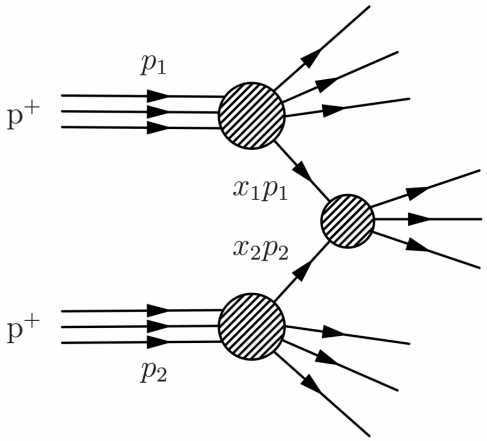

FIGURE 1.2: Diagram of a generic hard scattering proton-proton process. The hard interaction between the partons is separated from the non-perturbative interactions inside the protons and from the later hadronisation.

color confinement. It implies that, due to the very high coupling at low energy scales, color-charged particles are never observed isolated, but are always in colourless bound states. A pair of isolated quarks that are pulled apart will increase their potential energy, in such a way that it will be energetically favourable to radiate quarks and gluons until they bond in a final colourless state. This process is called *hadronisation*, and is responsible for the formation of jets of hadrons that will be described in the following sections.

1.6 Proton structure

Being able to make predictions about the interactions at hadron colliders is fundamental for the research carried out in experimental particle physics. High-energy proton-proton collisions such as the ones happening at the Large Hadron Collider (LHC) are complex processes due to the compositeness of the protons mentioned before, and to the special properties of QCD interactions. Most of the interactions that take place in the collisions are *soft*, the momentum exchange is very small. However, the interesting processes in the search for new physics are the *hard* interactions, where the momentum exchange is larger. In order to study these collisions, the initial-state protons can be described as a combination of quarks and gluons, referred to usually as *partons*, which carry a fraction of the proton momentum x described by a function $f(x)$, normally called parton distribution functions or PDFs:

$$\int_0^1 x \sum_i f_i(x) dx = 1, \tag{1.32}$$

where the sum includes all parton types (quarks and gluons). In fact, these functions also depend on q^2, the momentum transfer of the process under study.

The interactions in proton-proton collisions can be factorised into a hard interaction between two of the partons inside the protons, which can be described by perturbative QCD, and a soft interaction that includes all non-perturbative contributions, separated by a factorisation scale μ_F, according to the factorisation theorem [24]. A scheme of such hard interaction can be seen in figure 1.2. The total cross

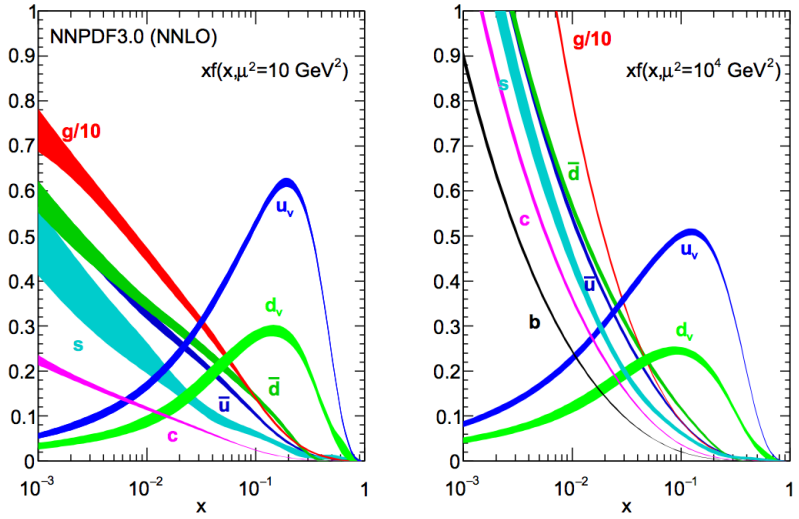

FIGURE 1.3: Proton parton distribution functions for two values of $q^2 = 10$ GeV^2 on the left, and $q^2 = 10000$ GeV^2 on the right with the NNLO NNPDF3.0 global analysis [26] with their uncertainties.

section for a process $pp \to X$ is

$$\sigma_{pp\to X} = \sum_{a,b} \int dx_a dx_b f_a(x_a, \mu_F^2) f_b(x_b, \mu_F^2) \hat{\sigma}_{ab\to X}(x_a p_1, x_b p_2, \mu_F^2, \mu_R^2, q^2), \quad (1.33)$$

where p_1 and p_2 are the momenta of the incoming protons. The parton cross section $\hat{\sigma}_{ab\to X}$ can be calculated at a fixed order in perturbation theory, since it is the hard part of the interaction, and therefore depends on the renormalisation scale μ_R. This calculation is often referred to as matrix element (ME) calculation, and can only be used for inclusive processes.

The parton distribution functions have to be measured experimentally, mostly in deep inelastic scattering experiments combined with fixed-target events and hadron-collider data. The measurements of the PDFs are performed at a certain q_0^2, and then the evolution of $f(x, q^2)$ with the momentum transfer relies on the DGLAP (Dokshitzer-Gribov-Lipatov-Altarelli-Parisi) equation [25]

$$\frac{df_i(x, q^2)}{dq^2} = \sum_j \frac{\alpha_s(q^2)}{2\pi} \int_x^1 \frac{dz}{z} P_{j\to i}(z) f(x/z, q^2), \quad (1.34)$$

where $P_{j\to i}(z)$ is the probability that the parton i emits a gluon and becomes a parton j carrying a fraction z of its original momentum. Figure 1.3 shows the proton PDFs for two values of q^2. It can be seen that the valence quarks [1] u and d carry about 0.5 of the proton momentum, while the rest corresponds to virtual gluons and a sea of quarks.

1.7 Event generation

The properties of the proton collisions and the hadron structure described above are used for the simulation of proton-proton events that aim at accurately describing the

[1] The valence quarks are the ones giving rise to the quantum numbers of the hadron. The rest of the quarks carrying part of the hadron momentum are said to form a *quark sea*.

outcome of the real collisions happening at the LHC. The event generation starts from the hard process that is described in equation 1.33. The calculation of the cross section is performed to a fixed order in perturbative QCD. A process is said to be calculated at leading order (LO) when only tree-level diagrams are included in the computation, while next-to-leading order (NLO) computations include one-loop diagrams.

1.7.1 Parton Shower

The second step in event generation is the parton shower (PS). It consists on the successive emission of soft collinear initial or final-state partons, and it origins the jets that are observed experimentally in the final state. It is used as an approximation to the higher order processes that are not properly included in the fixed-order QCD calculation. The simulation uses the processes $q \to qg$, $g \to gg$ and $g \to q\bar{q}$, which are described by the DGLAP equations 1.34 and applied iteratively until the parton energies reach the Λ_{QCD} scale, below which the perturbative regime is not valid. As a consequence, the outgoing parton of the hard process gives rise to a collimated shower of partons around the initial one, called jet. Figure 1.4 illustrates the splitting of a final-state parton to form a parton shower.

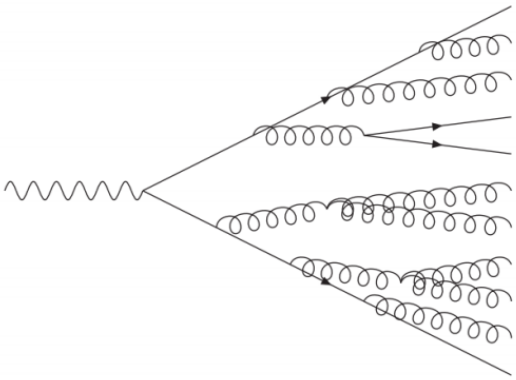

FIGURE 1.4: Example of final-state radiation parton shower.

The implementation of parton showers in the simulation uses the Sudakov factors [27], which give the probability of a parton to evolve without splitting. Parton showering can be applied to the initial or final partons, referred to as initial state radiation (ISR) or final state radiation (FSR), respectively. The simulation is equivalent in both cases, but applied backwards in time for the ISR case; i.e. the momentum of the initial parton is increased iteratively until it matches the initial PDF value. Parton showering provides an approximation, rather than an accurate calculation of the parton radiation, since the parton emissions are considered as completely independent, and any interference between ISR and FSR is ignored.

The combination of the parton shower with the matrix element calculation is not straightforward in general. The phase space regions of the two processes can overlap if the matrix element calculation includes the emission of one or more extra partons. In order to remove this overlap two matching procedures are mainly used: The Catani-Krauss-Kuhn-Webber (CKKW) [28] and the Michelangelo L. Mangano (MLM) [29] algorithms.

In the CKKW method, the separation between the PS and ME is based on the jet resolution as defined in the k_T clustering algorithm [30] [2]. The definition of the

[2] Jet clustering algorithms are discussed later on in section 4.4

jet resolution is based on a distance parameter that depends on the energy of the two objects, in such a way that the two objects are clustered together if they are not resolved, i.e. if the calculated distance is not larger than a certain value. In the CKKW algorithm, if the resolution is larger than a certain value y_{ini}, the cross sections and distributions are given by ME, weighted with the Sudakov factors. If, on the contrary, the resolution is lower than y_{ini}, they are given by parton showers, where the hard emissions are vetoed if they have enough energy to produce a separate jet.

In the MLM method, the events are classified depending on the number of partons in the final state, and then the parton shower is performed. A cone jet-clustering algorithm is applied to the final state partons, and the event is accepted if the number of reconstructed jets matches the number of partons from matrix element, and rejected otherwise.

1.7.2 Hadronisation

Once the parton shower process has reached the Λ_{QCD} scale, the process of hadronisation starts. The partons are combined into colourless hadrons in a non-perturbative phase dominated by the confining effects of QCD. Two main phenomenological models are used to described this phase: The string model [31, 32] and the cluster model [33, 34].

In the string model, the confinement potential between a quark-antiquark pair is represented by a string, in such a way that if the distance between them is so long that the energy of the string exceeds the mass of a quark-antiquark pair, a color singlet pair is produced and the string is split into two smaller strings. This process is repeated until all the energy is converted into quark pairs with short strings.

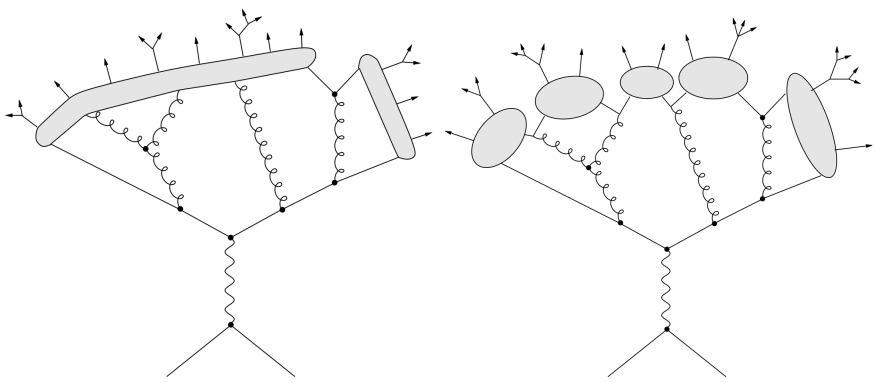

FIGURE 1.5: Sketch of the hadronic process according to the string method (left) and the cluster method (right)

In the cluster model, first the gluons from parton shower split in $q\bar{q}$ pairs. Then, color singlet $q\bar{q}$ are clustered with neighbouring quarks and antiquarks. The clusters can then decay into pairs of hadrons depending on the energy available. A sketch of the hadronisation process according to both methods is shown in figure 1.5.

The hadrons in the final state are combined to form jets (see section 4.4), which approximately reproduce the kinematics of the original hard parton.

1.7.3 Underlying event and pile-up

The underlying event (UE) refers to the soft interactions between the remaining partons of the incoming protons in the collision. These are non-perturbative, and are therefore simulated with phenomenological models that are tuned using data [35].

A non-negligible contribution from relatively hard interactions is usually present, referred to as multiple parton interactions (MPI), generated using low-p_{T} minimum-bias interactions. These are generally described by a combination of perturbative calculations and tuned with experimental data.

Proton-proton collisions are produced in the LHC by crossing *bunches* of many protons in opposite directions. Although in general the only interesting collision in each crossing is the most energetic one, the extra collisions that can take place have to be taken into account. In addition, the interactions arising from a previous or later bunch-crossing can be present in the event, due to the limited time resolution of the readout of the detector. They both consist mostly of low-energy QCD interactions, and are simulated in the same manner as the UE.

1.7.4 Monte Carlo generators

Here an executive list of the most relevant MC generators is presented. Details on how the MC samples are used are offered in chapter 6.

Pythia is a multipurpose generator used to compute the ME at LO of 2-to-n ($n \leq 3$) parton processes and PS. The string model is used for hadronisation and it includes UE simulation. Two versions of the generator are available: Pythia6 [36] in `Fortran` and Pythia8 [37] in `C++`.

Sherpa [38] is a multipurpose MC generator that simulates multi-leg processes at LO. It contains its own parton shower algorithm, and the matching between ME and PS is done with the CKKW method. The hadronisation is simulated using the cluster model and it includes the UE simulation.

Powheg [39] is an event generator that can compute the matrix element at NLO in perturbative QCD. It is normally interfaced with Pythia for the modelling of PS, hadronisation and UE.

MadGraph [40] can compute multi-leg amplitudes at tree level and one-loop for 2-to-n ($n \leq 6$) processes. It is interfaced with Pythia for the parton shower, and the ME-PS matching uses the MLM algorithm.

Herwig [41] is a multipurpose MC generator that can compute leading order ME for 2-to-2 processes and includes the PS calculation. Hadronisation is performed through the cluster model.

CHAPTER 2

Supersymmetry

This chapter introduces the theory of Supersymmetry (SUSY), one of the most popular models of physics beyond the Standard Model (BSM). The reasons to find a theory that extends the SM are first presented. An overview of Supersymmetry is then given, where the main principles are introduced. The Minimal Supersymmetric Standard Model is introduced, which is the simplest supersymmetric extension of the Standard Model, and the model used for the searches presented in this thesis. The mechanism of supersymmetry breaking is introduced, and finally the specific phenomenology related to the production of third generation squarks in hadron colliders is given.

2.1 Motivation

The Standard Model of Particle Physics described in chapter 1 provides a remarkable description of all the particle physics phenomena known. Besides the existence of neutrino masses, which point to physics beyond the SM, no evidence of new physics has been found to date. However, there are some open issues that, even if they do not question the model itself, would affect the physics at higher energies than the electroweak scale. These issues could be the hint that the SM is only an effective theory at low energies of a more general theory that could explain all of them. Supersymmetry is one of the most popular extensions of the Standard Model, and it provides a solution to some of these issues.

On the first place, the Standard Model does not describe gravitation. One would expect to observe non-negligible gravitational quantum effects at the Plank scale $M_P \sim (8\pi G)^{-1/2} = 2.4 \cdot 10^{18}$ GeV. At these scales, a new theory that embeds the SM together with a description of the quantum-gravitational effects would be needed.

But between the Electroweak scale ($M_W \sim 10^2$ GeV) and the Plank scale, there are many orders of magnitude where new physics could appear. This is the so-called *hierarchy problem*, which does not make the SM itself inconsistent, but it represents an uncomfortable sensitivity of the Higgs mass to loop corrections of any kind. Unlike the rest of the masses of the particles of the Standard Model, which are protected by chiral or gauge symmetries, the contributions from loop diagrams to the Higgs mass do not cancel, thus leading to arbitrarily big radiative corrections from any particle that it couples to. The mass of the Higgs boson would then be:

$$m_H^2 = (m_H)_0^2 + \Delta m_H^2, \tag{2.1}$$

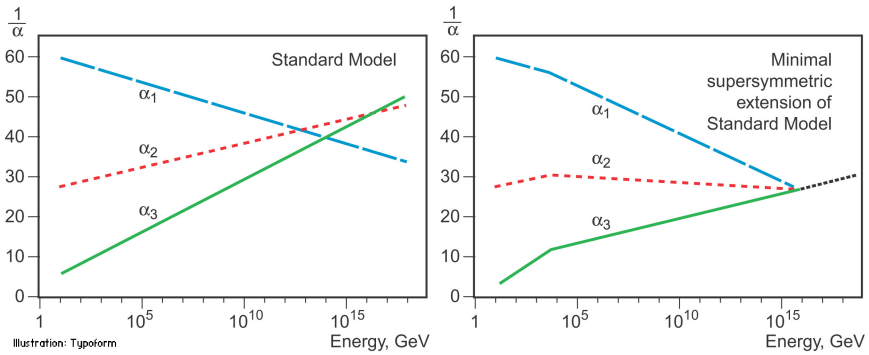

FIGURE 2.1: Evolution of the running couplings in the SM (left) and in the supersymmetric extension of the Minimal Supersymmetric Standard Model (right). The unification of the couplings is achieved at high energy scale in the latter [42].

where Δm_H^2 is the Higgs mass correction to the bare mass $(m_H)_0$. For a fermion loop like the one in figure 2.2, this correction would have the form:

$$\Delta m_H^2 = -\frac{|\lambda_f|^2}{8\pi^2}\Lambda^2 + ... \tag{2.2}$$

where λ_f is the Yukawa coupling of the fermion with the Higgs field, and Λ is a cutoff scale of the SM used to regulate the integral, which represents the energy scale at which new physics appears and the Standard Model no longer holds. Similar contributions appear from the gauge bosons. This scale, in principle, can be as large as the Plank scale, which implies that the corrections to the Higgs mass can be many orders of magnitude bigger than it. The solution of the SM would be to fine tune the bare parameter $(m_H)_0$ so that it cancels the big corrections. This is not forbidden, but this is considered *unnatural*, unless the cancellations occur due to a feature of the theory. Supersymmetry provides a satisfactory solution to this problem by introducing a new

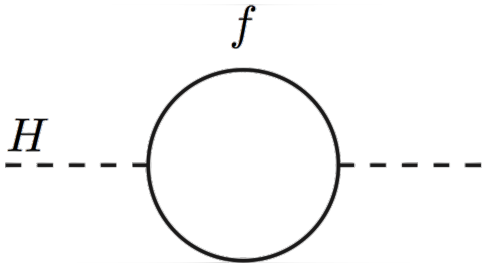

FIGURE 2.2: Fermion loop correction to the higgs mass.

symmetry such that all these contributions cancel naturally, as described in section 2.3.2. Some Supersymmetry models also include the unification with gravitation. In addition, the couplings of the three fundamental forces can be unified at a high scale as it is shown in figure 2.1. This is due to the new particle content introduced with SUSY, which modifies the behaviour of the couplings with energy.

Another of the issues of the Standard Model is the absence of an explanation of what Dark Matter could be made of. Astrophysical observations have evidenced that the amount of observable matter in several galaxies and other systems does not account for the gravitational effects that govern their movement [43]. These results indicate that an extra kind of matter, named Dark Matter [44], must contribute to the gravitational effects interacting only very weakly with ordinary matter. Further

evidence from cosmic microwave background observation confirms the existence of dark matter [45]. The particle spectrum of the SM does not provide any candidate with such characteristics. One of the main hypotheses states that dark matter is formed of weakly interacting massive particles (WIMPs) [46], for which Supersymmetry provides a candidate.

Some other problems of the SM can not find a solution with Supersymmetry only. These include the amount of free parameters it contains, 19, including masses, couplings and mixings which are not predicted by the theory but have to be measured by experiment. The large differences between these parameters is also regarded as an argument against the theory. The fermion masses, for example, range from ~ 0.5 MeV to ~ 200 GeV. This is not by itself a problem of the model, but it is not understood. Supersymmetric extensions of the SM, such as the Minimal Supersymmetric Standard Model, extend the number of free parameters instead of reducing it.

Finally, the asymmetry between matter and antimatter observed in the universe can not be explained with the SM. Although CP violation exists, the size of this violation within the SM framework is not enough to explain such asymmetry. Some Supersymmetric models include new sources of CP-violation, but in the models assumed in this thesis it is not the case.

For all these reasons, theoretical developments towards a theory that could solve the various issues were carried out since the 1960s. Although it does not solve all of them, Supersymmetry conforms one of the most accepted theories for BSM physics among both experimental and theoretical particle physicists. It solves elegantly the hierarchy problem, and provides a candidate for dark matter. A summarised description of the theory is given in the following sections.

2.2 Introduction to Supersymmetry

Supersymmetry [47] extends the Standard Model by including a new space-time symmetry, which introduces a correspondence between fermions and bosons. The generator of SUSY transformations $\hat{Q}$ transforms fermions into bosons and bosons into fermions. It is an anticommuting spinor with spin 1/2.

$$\hat{Q}|\text{fermion}\rangle \propto |\text{boson}\rangle \text{ and } \hat{Q}|\text{boson}\rangle \propto |\text{fermion}\rangle \tag{2.3}$$

Its hermitian conjugate, $\hat{Q}^\dagger$, is also a symmetry generator, and they satisfy the following commutation and anticommutation equations

$$\{\hat{Q}, \hat{Q}^\dagger\} = P^\mu,$$

$$\{\hat{Q}, \hat{Q}\} = \{\hat{Q}^\dagger, \hat{Q}^\dagger\} = 0,$$

$$[P^\mu, \hat{Q}] = [P^\mu, \hat{Q}^\dagger] = 0. \tag{2.4}$$

Furthermore, the supersymmetry generator commutes with the generators of the SM symmetries, which means that the so-called superpartners of the known particles have the same quantum numbers for the $SU_L(2) \otimes U_Y(1) \otimes SU_C(3)$ group. Moreover, from equation 2.4 it can be seen that they also commute with the operator P^2, which means that superpartners must also have the same mass. Supersymmetry predicts at least one new particle for each known SM one, which are found by applying $\hat{Q}$ to the fermions and bosons of the SM.

The SM particles and their superpartners can be organised in supermultiplets, which contain the same number of fermionic and bosonic degrees of freedom. These fermions and bosons forming the multiplets can be transformed into one another with the $\hat{Q}$ and $\hat{Q}^\dagger$ operators. These multiplets can be classified depending on their composition into:

- **Chiral supermultiplets**, which contain a massless Weyl fermion[1] with two helicity states, and two scalars that form a complex scalar field.
- **Gauge supermultiplets** are formed by a Weyl massless fermion with two helicity states that transform in the same way under gauge transformations and a massless vector boson with two chirality states.
- **Gravitational supermultiplet** includes the spin-2 graviton and a spin-3/2 partner, the gravitino. The graviton and gravitino are only included in some supersymmetry models.

All of the SM particles belong to one of these supermultiplets. The fermions, for example, are part of chiral supermultiplets, since their left and right components transform differently under gauge transformations and they are massless before the spontaneous symmetry breaking. Their superpartners are thus scalar bosons and are named by adding a s- prefix. Each fermion has two superpartners, one for each chirality state, and they are denoted by adding a tilde. For example, the superpartner of the left component of the top quark is called left stop and written $\tilde{t}_L$. The spin-1/2 superpartners of the gauge bosons are called with their SM name with the suffix -ino, and denoted also with a tilde.

2.3 Minimal Supersymmetric Standard Model

The Minimal Supersymmetric Standard Model (MSSM) is the simplest supersymmetric extension of the SM. The number of extra particles that it introduces is the minimum necessary, and there are no extra gauge interactions. It preserves the $SU_L(2) \otimes U_Y(1) \otimes SU_C(3)$ gauge symmetry of the SM, and the quantum numbers of the superpartners are thus the same as those of the known particles. The chiral and gauge supermultiplets of the theory are summarised in tables 2.1 and 2.2.

	Supermultiplet	**Spin 0**	**Spin 1/2**
Squarks	Q_i	$(\tilde{u}_L, \tilde{d}_L,)_i$	$(u_L, d_L,)_i$
	$\bar{u}_i$	$(\tilde{u}^*_R)_i$	$(u^\dagger_R)_i$
	$\bar{d}_i$	$(\tilde{d}^*_R)_i$	$(d^\dagger_R)_i$
Sleptons	L_i	$(\tilde{\nu}_L, \tilde{e}_L,)_i$	$(\nu_L, e_L,)_i$
	$\bar{e}_i$	$(\tilde{e}^*_R)_i$	$(e^\dagger_R)_i$
Higgsinos	H_u	(H^+_u, H^0_u)	$(\tilde{H}^+_u, \tilde{H}^0_u)$
	H_d	(H^+_d, H^-_d)	$(\tilde{H}^0_d, \tilde{H}^-_d)$

TABLE 2.1: Chiral supermultiplets of the MSSM.

As it can be seen in table 2.1, the MSSM contains two complex scalar higgs fields (and therefore two supermultiplets), H_u and H_d with $Y = 1/2$ and $Y = -1/2$, respectively. This is necessary for any supersymmetric extension of the SM, in order to avoid

[1] Weyl fermions are massless fermions that are solutions to the Weyl equation, a two-dimensional version of Dirac's equation for massless fields.

triangle gauge anomalies [48]. These anomalies are not present in the Standard Model because all the fermion contributions cancel due to a very fortunate combination of their quantum numbers. However, the fermionic superpartner of the SM Higgs boson creates a contribution that remains uncancelled, unless a second scalar Higgs doublet is added.

The higgs potential is analogous to that of the SM, but it is more complicated now since two complex scalars intervene:

$$\begin{aligned} V =&(|\mu|^2 + m_{H_u}^2)(|H_u^0|^2 + |H_u^+|^2) + (|\mu|^2 + m_{H_d}^2)(|H_d^0|^2 + |H_d^-|^2)+ \\ &[b(H_u^+ H_d^- - H_u^0 H_d^0) + c.c] + \frac{1}{8}(g^2 + g'^2)(|H_u^0|^2 + |H_u^+|^2 - |H_d^0|^2 - |H_d^-|^2)^2+ \\ &\frac{1}{2}g^2|H_u^+ H_d^{0*} - H_u^0 H_d^{-*}|^2, \end{aligned} \tag{2.5}$$

where μ, b, m_{H_u} and m_{H_d} are parameters of the potential. If the vacuum expectation values of H_u and H_d are denoted by v_u and v_d, the SM higgs v is related to them by

$$v = v_u^2 + v_d^2, \tag{2.6}$$

and they are more commonly expressed in terms of

$$\tan\beta = v_u/v_d. \tag{2.7}$$

The higgs doublets have then eight degrees of freedom. Three of them are absorbed during the electroweak symmetry breaking that gives the masses to particles, and five potentially observable higgs states remain:

- $H^{\pm}$: Two charged higgs states.
- A^0: A CP-odd neutral higgs.
- H^0 and h^0: Two CP-even neutral higgs fields, one of which must be the SM higgs boson.

Supermultiplet	**Spin 1/2**	**Spin 1**
Gluon and gluino	$\tilde{g}$	g
Winos and W-bosons	$\tilde{W}^{\pm}, \tilde{W}^0$	$W^{\pm}, W^0$
Bino and B-boson	$\tilde{B}^0$	B^0

TABLE 2.2: Gauge supermultiplets of the MSSM.

The masses of the physical higgs states can be expressed as

$$\begin{aligned} m_{A_0}^2 &= \frac{2b}{\sin 2\beta}, \\ m_{h^0,H^0}^2 &= \frac{1}{2}\left(m_{A_0}^2 + m_Z^2 \mp \sqrt{(m_{A_0}^2 - m_Z^2)^2 + 4m_Z^2 m_{A_0}^2 \sin^2 2\beta}\right), \\ m_{H^{\pm}}^2 &= m_{A_0}^2 + m_W^2. \end{aligned} \tag{2.8}$$

The MSSM Lagrangian is constructed including all possible interaction terms that satisfy the SM symmetries $SU_L(2)\otimes U_Y(1)\otimes SU_C(3)$. In principle, some of these terms can break baryon and lepton number conservation, which is forbidden in the Standard

Model. This is undesirable, since experimental evidences, like the proton decay, prove their conservation. In order to preserve these symmetries, a new quantum number can be introduced

$$R = (-1)^{3(B-L)+2S}, \tag{2.9}$$

where B, L and S are the baryon, lepton and spin quantum numbers of the particle. By requiring the conservation of R (normally referred to as R-partity conservation), the baryon- and lepton-number conservation are automatically achieved. Equation 2.9 immediately implies that $R = 1$ for SM particles, and $R = -1$ for their superpartners. The conservation of R-parity has some important phenomenological consequences. The lightest supersymmetric particle (LSP) can not decay, and if it is neutrally charged, it provides a candidate for dark matter. In the MSSM, the LSP is often identified with the lightest neutralino ($\tilde{\chi}_1^0$). Another important implication is that the SUSY particles that arise in any SM experiment must be produced in pairs.

The conservation of $R-$parity is not required in all SUSY models, and it classifies them in $R-$parity conserving (RPC) and $R-$parity violating (RPV) models. From now on, R-parity conservation is assumed.

2.3.1 Supersymmetry breaking

As it was mentioned before, the existence of supersymmetry implies the introduction of one new SUSY particle for each SM particle with the same quantum numbers (except for R) and the same mass. However, if such particles existed with the same mass as the SM ones, they would have been observed in particle physics experiments already. Since this is not the case, then one concludes that the symmetry, if it exits, must be broken.

A spontaneous breaking like the one presented for the electroweak symmetry in section 1.4 would require the introduction of an extra field, and in the framework of the MSSM the approach is to instead introduce an extra term in the lagrangian that breaks the symmetry explicitly, while keeping the number of fields to the minimum. This extra term that breaks the symmetry does not specify how the symmetry is broken, but describes roughly the consequences of it.

$$\mathcal{L} = \mathcal{L}_{\text{SUSY}} + \mathcal{L}_{\text{soft}}, \tag{2.10}$$

where the index *soft* indicates that the breaking of the symmetry is regarded as a perturbation of the lagrangian that does not introduce quadratic divergences. This term introduces the vast majority of the 105 free parameters of the MSSM, on which the masses of the SUSY particles depend. The mass eigenstates of the SUSY particles are not necessarily the same as the gauge eigenstates, but they are allowed to mix. Below, a summary of the mass eigenstates of the MSSM is given, and it is shown in table 2.3.

- **Sfermions:** The mass eigenstates of the sfermions is a mixing of the superpartners of the left- and right-handed SM fermions. A matrix that mixes the $\tilde{f}_L$ and $\tilde{f}_R$ scalars (which have in general different masses) into the mass eigenstates (denoted by $\tilde{f}_1$ and $\tilde{f}_2$, where $\tilde{f}_1$ is the lightest) is defined. For the quarks, for example:

$$\mathcal{M}_{\tilde{q}}^2 = \begin{pmatrix} m_{\tilde{q}_L} & a_q m_q \\ a_q m_q & m_{\tilde{q}_R} \end{pmatrix}, \tag{2.11}$$

with

$$\begin{aligned} m^2_{\tilde{q}_L} &= M^2_{\tilde{Q}} + m^2_Z \cos 2\beta (T^q_{3L} - e_q \sin^2\theta_W) + m^2_q \\ m^2_{\tilde{q}_R} &= M_{\{\tilde{u},\tilde{d}\}} + e_q m^2_Z \cos 2\beta \sin^2\theta_W + m^2_q \\ a_q &= A_q - \mu\{\cot\beta, \tan\beta\}, \end{aligned} \tag{2.12}$$

where T_3 is the third component of the weak isospin, and e_q and m_q are the the charge and the mass of the corresponding quark. The $M_{\tilde{Q}}$, $M_{\tilde{u}}$ and $M_{\tilde{d}}$ matrices contain the SUSY-breaking masses squarks, and the parameters β and μ are the ones appearing in the higgs potential of the MSSM in equation 2.5. The matrix A_q contains the trilinear couplings of the squarks with the higgs bosons. An analogous equation holds also for slepton masses.

As it can be seen in equation 2.11, the off-diagonal terms are proportional to the quark mass, and therefore they are only relevant for the heavy quarks (and the τ lepton). In this way, squarks and sleptons from the first two generations are generally considered to be degenerate in mass, with $m_{\tilde{q}_1} = m_{\tilde{q}_2}$.

- **Gluinos:** Gluons and gluinos carry colour charge, and therefore they can not mix their gauge eigenstate with any other particle. The mass eigenstates are the same as the gauge ones.

- **Neutralinos and charginos:** Higgsinos and electroweak gauginos mix to form mass eigenstates, called neutralinos and charginos, in the case of neutral and charged particles, respectively. Neutral higgsinos ($\tilde{H}^0_u$ and $\tilde{H}^0_d$) mix with neutral gauginos ($\tilde{W}^0$ and $\tilde{B}^0$), forming four neutralino mass eigenstates, normally indicated by $\tilde{\chi}^0_i$, $i = 1, 2, 3, 4$, being $\tilde{\chi}^0_1$ the lightest. The charged higgsinos ($\tilde{H}^+_u$ and $\tilde{H}^-_d$) mix with the charged winos ($\tilde{W}^\pm$) resulting in four charginos (two positively and two negatively charged) denoted by $\tilde{\chi}^\pm_i$, $i = 1, 2$. The masses of the neutralinos and charginos can be expressed in terms of the MSSM parameters as

$$\begin{aligned} m_{\tilde{\chi}^0_1} &= M_1 - \frac{m^2_Z s^2_W (M_1 + \mu \sin 2\beta)}{\mu^2 - M^2_1}, \\ m_{\tilde{\chi}^0_2} &= M_2 - \frac{m^2_Z (M_2 + \mu \sin 2\beta)}{\mu^2 - M^2_2}, \\ m_{\tilde{\chi}^0_3, \tilde{\chi}^0_4} &= |\mu| + \frac{m^2_W (I - \sin 2\beta(\mu + M_1 c^2_W + M_2 s^2_W))}{3(\mu \pm M_1)(\mu \pm M_2)} \\ m_{\tilde{\chi}^\pm_1, \tilde{\chi}^\pm_2} &= \frac{1}{2}\left(|M_2|^2 + |\mu|^2 \mp \sqrt{(|M^2_2 + |\mu| + 2m^2_W)^2 - 4|(\mu M_2 - m^2_W \sin 2\beta)|^2} \right), \end{aligned} \tag{2.13}$$

with $s_W = \sin\theta_W$ and $c_W = \cos\theta_W$. Here I is the sign of the parameter μ, and M_1 and M_2 are the mass parameters of the soft lagrangian of binos and winos, respectively.

The 105 parameters of the MSSM can be constrained in several ways. A possibility is to assume an unification of the masses at a high energy scale, where the masses of the sparticles are m_0 for the sfermions, $m_{1/2}$ for gauginos. This is motivated by the fact that the gauge couplings are unified in the MSSM at an energy scale of the order of 10^{16} GeV, as shown in figure 2.1.

Furthermore, the number of free parameters can be constrained by specifying the mechanism of the SUSY-breaking. This is done for a number of models, that in general

Name	Spin	R	Gauge eigenstates	Mass eigenstates
Higgs Bosons	0	1	$H_u^0, H_d^0, H_u^+ H_d^-$	h^0, H^0, A^0, H^+, H^-
Squarks	0	-1	$\tilde{d}_L, \tilde{d}_R, \tilde{u}_L, \tilde{u}_R$	(same)
			$\tilde{s}_L, \tilde{s}_R, \tilde{c}_L, \tilde{c}_R$	(same)
			$\tilde{b}_L, \tilde{b}_R, \tilde{t}_L, \tilde{t}_R$	$\tilde{b}_1, \tilde{b}_2, \tilde{t}_1, \tilde{t}_2$
Sleptons	0	-1	$\tilde{e}_L, \tilde{e}_R, \tilde{\nu}_e$	(same)
			$\tilde{\mu}_L, \tilde{\mu}_R, \tilde{\nu}_\mu$	(same)
			$\tilde{\tau}_L, \tilde{\tau}_R, \tilde{\nu}_\tau$	$\tilde{\tau}_1, \tilde{\tau}_2, \tilde{\nu}_\tau$
Neutralinos	1/2	-1	$\tilde{B}^0, \tilde{W}^0, \tilde{H}_u^0, \tilde{H}_d^0$	$\tilde{\chi}_1^0, \tilde{\chi}_2^0, \tilde{\chi}_3^0, \tilde{\chi}_4^0$
Charginos	1/2	-1	$\tilde{W}^\pm, \tilde{H}_u^+, \tilde{H}_d^0$	$\tilde{\chi}_1^\pm, \tilde{\chi}_2^\pm$
Gluino	1/2	-1	$\tilde{g}$	(same)

TABLE 2.3: Summary of the mass and gauge eigenstates of the MSSM, including the higgs sector. The mixing of the first two sfermion generations is assumed to be negligible

assume that the breaking happens in a hidden sector and its effects are transmitted to the visible particles by some kind of messenger. This is the case for mSUGRA (minimal supergravity) [49], where the mechanism of SUSY breaking happens in a hidden sector which is neutral to the SM gauge group, and the effects of the breaking are transmitted to the visible particles through gravity. This assumption reduces the number of free parameters to only 5.

Another technique used to reduce the number of parameters without specifying the SUSY-breaking consists on making some further assumptions

- The only source of CP violation is the CKM matrix [50].
- As in the SM, no flavor-changing neutral currents are allowed at tree level.
- First and second generation universality applies.

By making these three assumptions while leaving the mechanism of supersymmetry breaking unspecified, the number of free parameters is reduced to 19: $\tan\beta$, μ, M_A (mass of the pseudoscalar Higgs boson), $M_{1,2,3}$, (bino, wino and gluino mass parameters); $m_{\tilde{q}_L}$, $m_{\tilde{q}_R}$, $m_{\tilde{\ell}_L}$, $m_{\tilde{\ell}_R}$ (the mass parameters of squarks and sleptons), and A_t, A_b and A_τ, (third generation trilinear couplings). This simplification of the MSSM is referred to as phenomenological MSSM, or pMSSM.

In this way, supersymmetric extensions of the SM can solve some of the issues mentioned in section 2.1. R-parity conserving models offer a candidate for a dark matter particle: The lightest neutralino is a stable, neutral particle that would interact weakly with the SM sector.

The hierarchy problem is solved elegantly with the introduction of the superpartners, which cancel the loop corrections of the SM particles exactly. The contribution from a scalar partner of a fermion to equation 2.2 would be

$$\Delta m_H^2 = \frac{|\lambda_{sf}|^2}{16\pi^2}\Lambda^2, \tag{2.14}$$

where λ_{sf} is the higgs coupling to the sfermions. In SUSY, $\lambda_{sf} = \lambda_f$, and the contribution from the fermions cancel at one-loop level when their two scalar superpartners are taken into account.

As it was briefly mentioned, some SUSY models propose a unification that includes gravity. The simplest one is mSUGRA, but extensions of it in more dimensions

exist. However, Supersymmetry does not solve all of the issues mentioned for the SM. The number of free parameters and the large range covered by particle masses and couplings is actually extended after the introduction of SUSY in the SM. The matter-antimatter asymmetry in the universe can be accommodated in some models of SUSY where more CP-violating terms are included in the lagrangian (but this is not the case in the pMSSM).

2.3.2 Third Generation Squarks

Superpartners of standard particles can be produced in pairs at the LHC, as it was mentioned before, if R-parity conservation is assumed. Searches for third generation squarks are of special interest in experimental tests of supersymmetry, as will be discussed in this section, since their contribution to the radiative corrections of the higgs mass is key to the understanding of the theory.

As it was introduced in section 2.1, one of the main motivations for the search for a theory beyond the Standard Model is the hierarchy problem. This problem arises from the sensitivity of the higgs boson mass to radiative loop corrections of any particle. The introduction of Supersymmetry results in new terms that contribute to equation 2.2 from the superpartners of the standard particles that cancel those of the SM, as shown in equation 2.14. Although the one-loop corrections cancel in a Supersymmetry framework, the corrections to the higgs mass at 2-loop level from third generation squarks are the most dominant ones:

$$\Delta m^2_{H,X} = \pm \frac{\lambda_X}{16\pi^2} m^2_X \log\left(\frac{\Lambda}{m^2_X}\right), \tag{2.15}$$

where X can be a fermion or a boson. The contributions of this form do not cancel for the superpartners since their mass is not the same. It is common to argue, invoking the *naturalness* principle [51], that these corrections should be small, and therefore the masses of the third generation squarks should not differ too much from those of their SM partners, depending on how much fine-tuning one is willing to accept in order to keep the higgs mass at its known value. In general, it is assumed that the mass of the lightest stop should be in the TeV scale (and similar arguments can be applied to the sbottom mass).

Third generation SUSY searches represent a direct test of Natural SUSY, for the reasons stated above. They can be produced in pairs in hadron colliders such as the LHC through gluon fusion or quark-pair annihilation. The searches for stop particles presented in chapters 6 and 7 use simplified pMSSM models where only one or two decay steps are allowed and all the SUSY particles not intervening in the process under study are considered to be very heavy and not to interact. These models do not explore the full parameter space of the pMSSM, but only the relevant quantities for high-energy physics experiments. In this way, experimental tests of the models can set limits on certain parameters of the theory (generally the masses of the particles) that apply to more general models with the same topology.

The direct stop pair production cross section in proton-proton collisions can be calculated and it is mostly independent of the choice of SUSY parameters [53, 54]. Figure 2.3 shows the stop-pair production cross section as a function of the stop mass at $\sqrt{s} = 13$ TeV. The experimental signature of the models varies depending on the decay mode considered, whose branching ratio depends on the mixing of the superpartners of the left- and right-handed top quarks, and the mixing parameters of the higgsinos and gauginos.

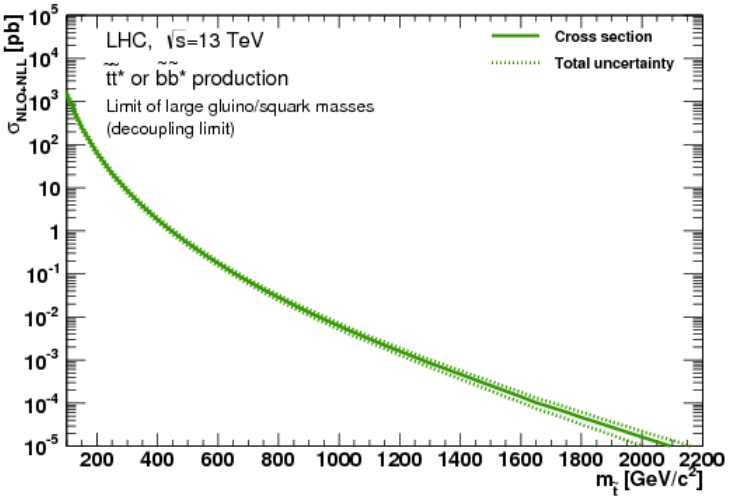

FIGURE 2.3: Cross section at NLO+NLL for stop-pair production at $\sqrt{s} = 13$ TeV at the LHC as a function of the stop mass. The calculation assumes gluinos and squarks to be very massive and decoupled [52].

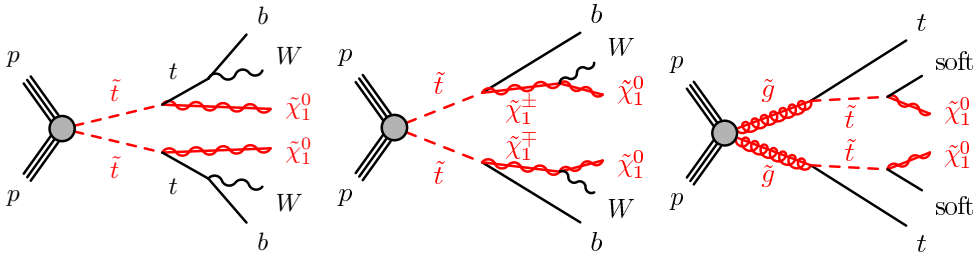

FIGURE 2.4: Feynman diagrams for the main processes considered in the analysis.

In the analysis presented in this thesis, stop pairs are searched for in final states with no leptons. The main processes targeted are shown in figure 2.4. In the first of the processes considered, the stops are produced directly and decay through a top and a neutralino, which is considered to be the LSP and the candidate for dark matter. Maximal mixing between the left and right components of the stop is considered, and the nature of the neutralino is assumed to be pure bino. All the rest of the masses of the SUSY particles are set very high and do not contribute to the process. The second process allows for stop decays to top and neutralino or bottom and chargino, where the chargino mass is very similar to that of the neutralino ($\Delta m(\tilde{\chi}_1^{\pm}, \tilde{\chi}_1^0) = 1$ GeV), with different branching ratios. Finally, also the process where the stops arise from gluino decay is considered. As it can be seen in figure 2.4, a pair of gluinos is produced, which decay into a stop and a top. The mass of the stop for this model is taken to be very close to the neutralino mass ($\Delta m(\tilde{t}_1^0, \tilde{\chi}_1^0) = 5$ GeV), so that the decay products of the stop are the neutralino and soft jets that are not reconstructed in the detector. Again, all the rest of the SUSY particles are assumed to be very massive and not to contribute to the process.

In addition, models where the second neutralino is light enough that the stop can decay through it are used for the interpretation of the results, with different hypotheses on the masses and branching ratios. The several models and their assumptions are described in detail in section 7.3.

CHAPTER 3

The LHC and the ATLAS detector

The results presented in this thesis were obtained using proton-proton collision data produced at the Large Hadron Collider and collected at the ATLAS detector. This chapter will introduce the main aspects of the accelerator and the ATLAS detector.

3.1 The LHC

The Large Hadron Collider (LHC) [55] is a 27-kilometer circular particle accelerator located about 100 meters underground in the border between France and Switzerland, as a part of the CERN accelerator complex. It is located in the same tunnel that once hosted the Large Electron-Positron (LEP) collider. Along the ring, four interaction points are surrounded by four different detectors that study the physics of the particle collisions, namely ALICE [56], ATLAS [57], CMS [58] and LHCb [59]. ATLAS and CMS are multipurpose detectors, while ALICE is focused on heavy-ion collisions and LHCb in b-hadron detection.

The LHC was designed to collide protons at a center-of-mass energy of 14 TeV. During the first years of operations, 2010-2012, the proton-proton collisions were produced at $\sqrt{s} = 7$ and 8 TeV, while since 2015 the collider has been working at 13 TeV. The protons arrive to this energy after going through various steps of the accelerator chain. As it can be seen in Figure 3.1, they start at a linear accelerator (LINAC 2), where they reach an energy of 50 MeV, continue to the Booster circular accelerator, exiting with 1.4 GeV, from where they pass to the Proton Synchrotron (PS), which accelerates them up to 25 GeV and to the Super Proton Synchrotron (SPS) to finally enter the LHC where they pass from 450 GeV to the final 6.5 TeV.

The protons at the LHC are accelerated using radiofrequency cavities, and are then kept in the circular trajectory thanks to the magnetic fields created by the superconducting dipole magnets. The proton beams contain up to 2808 proton bunches and about 1.1×10^{11} protons per bunch, separated from each other by 25 ns. This corresponds to a luminosity of the order of 10^{34} cm$^{-2}s^{-2}$. At the four interaction points of the LHC, two bunches are crossed with a small interaction angle of the order of 150-200 μrad to make them collide at the center of the detectors.

In addition to the proton-proton collisions, the LHC dedicates some of its operating time every year to lead-proton and lead-lead collisions, where the lead ions are accelerated to an energy of 2.76 TeV per nucleon.

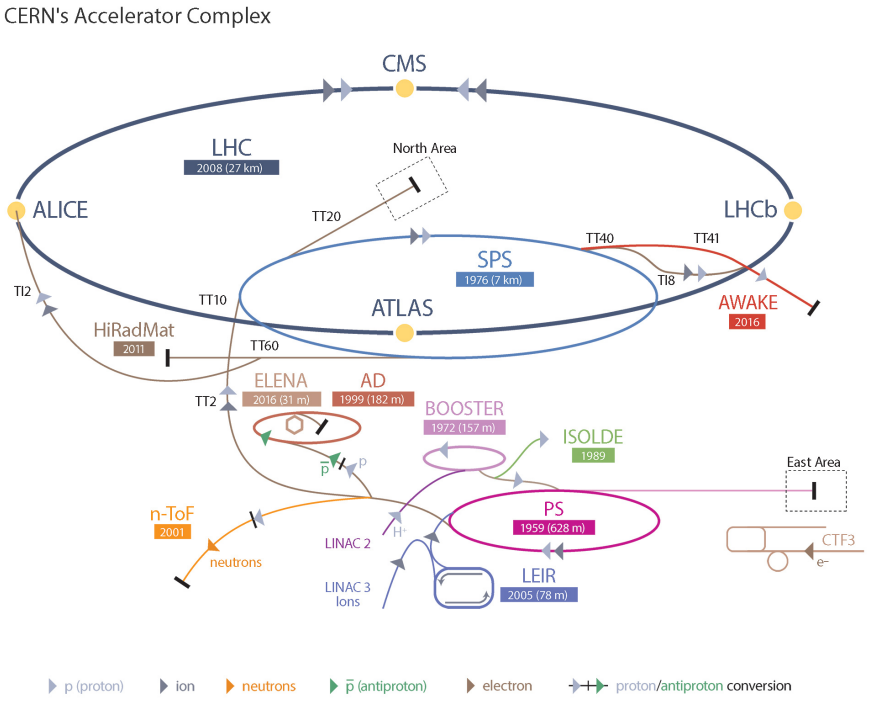

FIGURE 3.1: Schematic representation of the CERN accelerator complex [60]

3.2 The ATLAS detector

ATLAS (A Toroidal LHC ApparatuS) is a multipurpose particle detector located at the CERN LHC. It is designed to cover the widest range of physics at the LHC. It is the biggest particle detector of the complex, measuring 46 meters long and 25 meters diameter, and weighting 7000 tons. It consists of several concentric subdetectors around the beam which have different functions in the particle detection and identification. A scheme of the ATLAS detector can be seen in Figure 3.2 and a full description of it can be found in [57].

The closest layer to the beam pipe is the Inner Detector (ID), which measures the tracks of the charged particles that are bended by a solenoid magnet. Right outside there is the calorimeter system, composed of an electromagnetic and a hadronic part, where the particle showers (jets) are measured and contained. Finally, the outermost layer is the muon spectrometer (MS), dedicated to the measurement of muon properties, immersed in a toroidal magnetic field.

The ATLAS coordinate system is defined as having the origin in the interaction point, and the z-axis in the beam direction. The x-axis is defined as pointing to the center of the LHC ring and the y-axis is pointing upwards. The A-side of the detector is the one in the positive z-axis. As usual, the azimuthal angle ϕ is measured around the z-axis, while the polar angle θ is measured from the z-axis. The pseudorapidity is defined as

$$\eta = -ln\left(tan\frac{\theta}{2}\right) \tag{3.1}$$

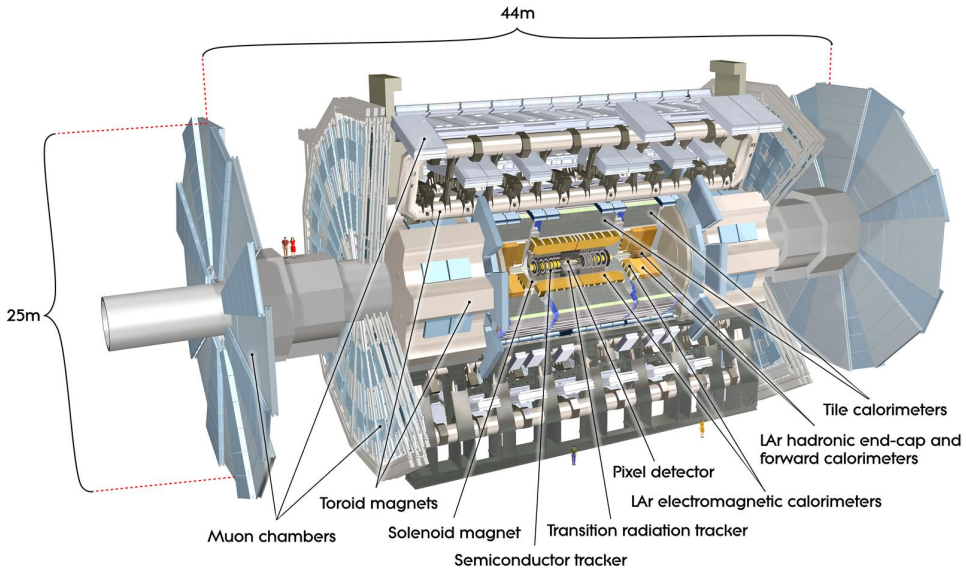

FIGURE 3.2: Scheme of the ATLAS detector

The transverse momentum p_{T}, transverse energy E_{T} and missing transverse energy $E_{\mathrm{T}}^{\mathrm{miss}}$ are defined in the x-y plane. The distance ΔR is defined in the $\eta - \phi$ plane as

$$\Delta R = \sqrt{(\Delta\eta)^2 + (\Delta\phi)^2} \tag{3.2}$$

A more thorough description of the different components of ATLAS can be found in the following sections.

3.2.1 Inner detector

The Inner Detector (ID) is the most internal subdetector in ATLAS, and it is used to reconstruct the tracks of the charged particles and the interaction vertices in the range $|\eta| < 2.5$. It is embedded in a solenoid magnetic field of 2 T which bends the trajectories of the charged particles. The solenoid extends for 5.3 m in length and it has a diameter of 2.5 m. The inner detector is composed of several complementary subdetectors itself, the Pixel detector, closest to the interaction point, the semi-conductor tracker (SCT), and the transition radiation tracker (TRT), in the outermost part of the ID. A scheme of its structure can be viewed in Figure 3.3.

3.2.1.1 The Pixel Detector

The Pixel detector constitutes the innermost layer of the ATLAS experiment, and uses radiation-hard silicon sensors (pixels). With 80.4 million readout channels, it has the highest granularity in the whole ATLAS detector, which is crucial to reconstruct the primary vertex with enough precision. It is composed of four concentric cylindrical layers in the barrel region and three disks in the endcaps. The smallest pixel size is 50 x 400 μm^2 and the resolution is 10 μm in the R$-\phi$ plane and 115 μm in z. The closest layer to the beam pipe, called Insertable B-Layer, or IBL [61], was installed during the first Long Shutdown before Run 2 started (2012-2015). At only 50 mm away from the beam pipe, its goal is to improve the vertex reconstruction resolution. This allows for a more precise secondary-vertex finding, which can help the long-lived particle identification.

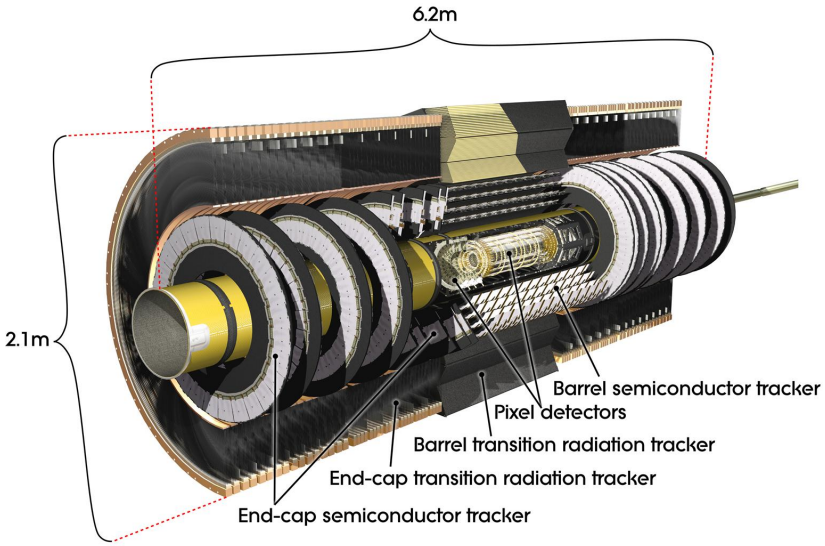

FIGURE 3.3: Layout of the components of the inner detector

3.2.1.2 The Semi-Conductor Tracker

The SCT is the middle part of the ID and it is a silicon microstrip detector. It consists of four layers of stereo strips in the barrel, and nine disks in the endcaps. An SCT module consists of two strips glued back to back with an angle of 40 mrad, which allows for a more accurate position measurement. The resolution of the SCT is 17 μm in the R$-\phi$ plane and 580 μm in z (R) in the barrel (endcap).

3.2.1.3 The Transition Radiation Tracker

The TRT is the outermost subsection of the ID. It is made of 4-mm-diameter straw tubes filled with xenon gas. In the barrel region, the straws are parallel to the beam direction and 144 cm long, while in the endcap, 37-cm tubes are radially arranged. The space between the tubes is filled with plastic material (polyethylene), which produces the transition radiation. The readout is provided by gold-plated tungsten wires located at the center of the straws, which collect the electrons emitted by the ionization of the gas when a particle passes though it. The TRT has a resolution of 130 μm only in R-ϕ. A summary of the layers of the ID in the barrel is shown in Figure 3.4.

The combined p_{T} resolution of the inner detector is

$$\frac{\sigma_{p_{\mathrm{T}}}}{p_{\mathrm{T}}} = 0.05\% \cdot p_{\mathrm{T}} \oplus 1\%, \tag{3.3}$$

where the units are in GeV. The resolution for a low-p_{T} track of, eg. 1 GeV, is then of about 1%, while for a high-energy track of 500 GeV the resolution would be of the order of 25%.

3.2.2 Calorimeters

The ATLAS calorimeters are located outside the ID, and they cover the region $|\eta| <$ 4.9. Figure 3.5 shows an overview of the calorimeter system. The calorimeters are designed to contain showers and measure their energy and position. The electromagnetic calorimeter is located outside of the ID, and is responsible for the measurements

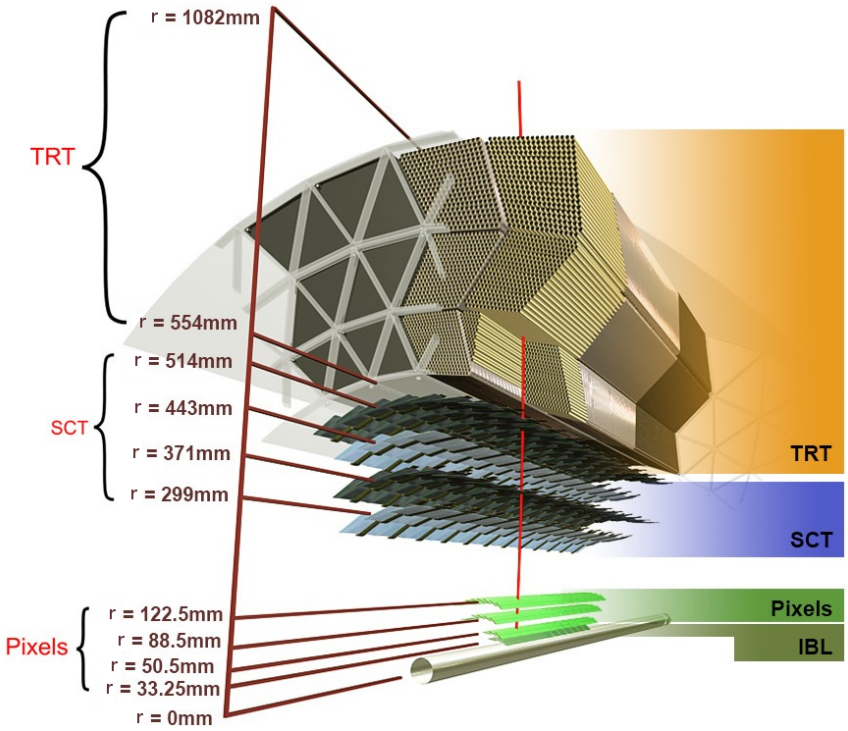

FIGURE 3.4: Scheme of the different layers of the ID in the barrel [62]

of electrons and photons. It has a fine granularity, ranging from 0.025×0.025 in $\eta \times \phi$ to 0.1×0.1 as summarised in table 3.1, depending on the layer. The hadronic calorimeter, while still allowing for accurate measurements of jet energy, has a coarser granularity of 0.1×0.1 in the barrel and 0.2×0.2 in the endcap.

The thickness of the electromagnetic calorimeter is larger than 22 radiation lengths[1] (X_0) in the barrel and larger than $24X_0$ in the endcap. The combined calorimeter system has approximately 9.7 interaction lengths[2] (λ) in the barrel and around 10λ in the endcaps, enough to contain the highest p_{T} jets produced in the collisions.

3.2.2.1 Electromagnetic Calorimeter

The electromagnetic calorimeter (ECAL, also referred to as Liquid Argon calorimeter, LAr) [63] is devoted to the measurement and reconstruction of the electromagnetic-interacting particles, especially electrons and photons, which will deposit all of their energy in it. It uses lead as an absorption material and liquid argon as active medium, kept at 88K thanks to a cryogenic system. The electrons released in the ionization of the argon are absorbed by electrodes located in the lead surfaces. The Barrel covers the region up to $|\eta| = 1.475$, and the endcaps extend to the $1.375 < |\eta| < 3.2$ area. The barrel is structured in three layers, which are organised following an accordion geometry that avoids gaps in the ϕ coverage, and the endcap consists on two wheels on either side of the barrel. At the most central part, a presampler layer is installed closer to the interaction point to correct for the energy lost in the dead parts of the detector between the ID and the ECal. A sketch of a LAr module can be seen in Figure 3.6 (A). The granularity and η coverage of each of the layers is summarised in

[1] Length that an electron has to travel on average in the material to reduce its energy by a factor $1/e$ due to radiation.

[2] Length that a beam of charged particles has to travel through a material to reduce the number of surviving particles by a factor $1/e$.

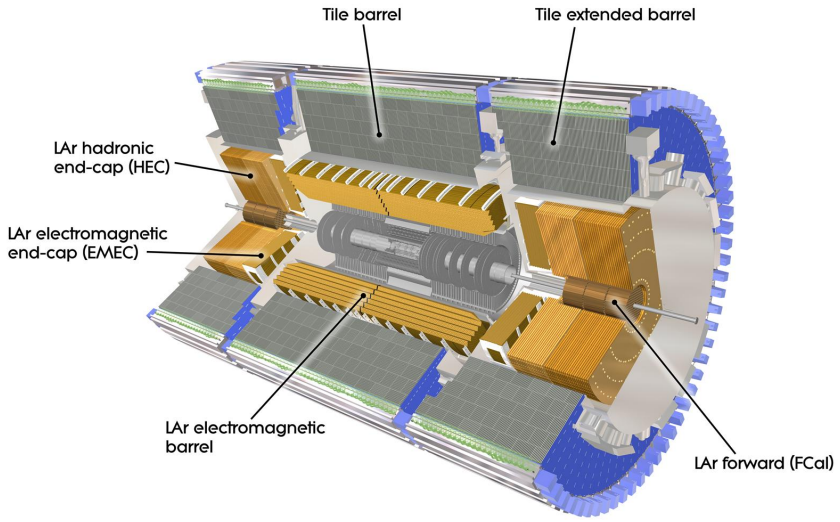

FIGURE 3.5: Scheme view of the ATLAS calorimeters

Table 3.1, and ranges from 0.025×0.025 in $\eta \times \phi$ to 0.1×0.1. The energy resolution of the ECal is

$$\frac{\sigma_E}{E} = \frac{10\%}{\sqrt{E}} \oplus 0.7\%, \tag{3.4}$$

i.e., the resolution for a 1 GeV shower would be of $\sim 10\%$ while for 100 GeV it would be around $\sim 1.7\%$.

	EM calorimeter			
	Barrel		**End-cap**	
	$\Delta\eta \times \Delta\phi$	$\lvert\eta\rvert$	$\Delta\eta \times \Delta\phi$	$\lvert\eta\rvert$
Presampler	0.025×0.1	< 1.52	0.025×0.1	1.5-1.8
First Layer	$0.025/8 \times 0.1$	< 1.4	0.050×0.1	1.375-1.425
	0.025×0.025	1.40-1.475	0.025×0.1	1.425-1.5
			$0.025/8 \times 0.1$	1.5-1.8
			$0.025/6 \times 0.1$	1.8-2.0
			$0.025/4 \times 0.1$	2.0-2.4
			0.025×0.1	2.4-2.5
			0.1×0.1	2.5-3.2
Second Layer	0.025×0.025	< 1.40	0.050×0.025	1.375-1.425
	0.075×0.025	1.40-1.475	0.025×0.025	1.425-2.5
			0.1×0.1	2.5-3.2
Third Layer	0.050×0.025	< 1.35	0.050×0.025	1.5-2.5

TABLE 3.1: Summary of granularity and coverage in $|\eta|$ of the different layers of the electromagnetic LAr calorimeter.

3.2.2.2 Hadronic Calorimeter

The ATLAS hadronic calorimeter is composed of three independent sections, each of them using different technologies and materials. The Tile Calorimeter (TileCal) covers the region $|\eta| < 1.8$, the Hadronic End-cap Calorimeters extend in $1.5 < |\eta| < 3.2$, and the Forward Calorimeter corresponds to the area $3.1 < |\eta| < 4.9$. The energy

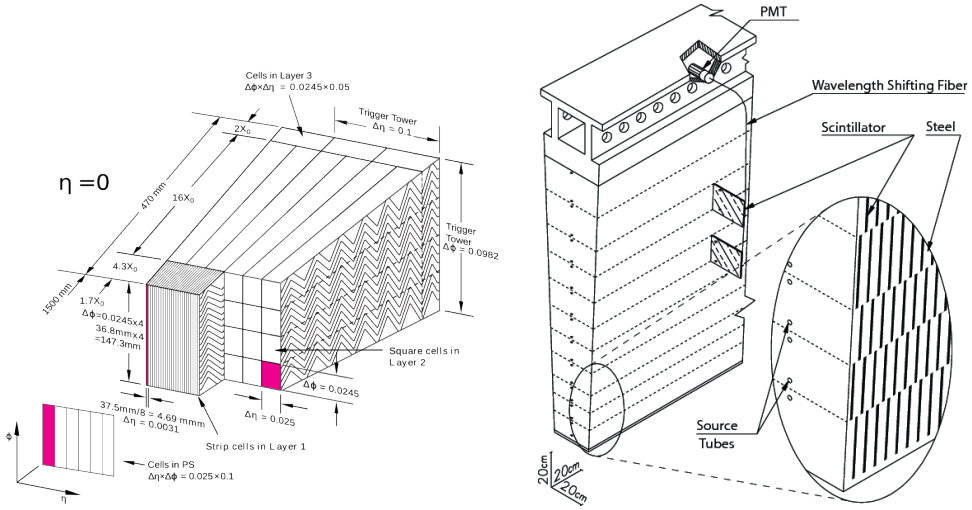

(A) (B)

FIGURE 3.6: A sketch view of a ECAL module (left) and a TileCal module (right)

resolution of the hadronic calorimeter is given by

$$\frac{\sigma_E}{E} = \frac{50\%}{\sqrt{E}} \oplus 3\% \text{ in the barrel and endcap} \tag{3.5}$$

$$\frac{\sigma_E}{E} = \frac{100\%}{\sqrt{E}} \oplus 10\% \text{ in the forward calorimeter.} \tag{3.6}$$

A summary of the coverage and granularity of the hadronic calorimeters can be found in Table 3.2.

	Hadronic calorimeter			
	Scintillator tile		**LAr hadronic**	
	Barrel	Extended barrel	End-cap	
$\|\eta\|$ coverage	< 1.0	0.8-1.7	1.5-2.5	2.5-3.2
Number of layers	3	3	4	
Granularity ($\Delta\eta \times \Delta\phi$)	0.1×0.1	0.1×0.1	0.1×0.1	0.2×0.2
(last layer)	0.2×0.1	0.2×0.1		

TABLE 3.2: Summary of granularity and coverage of the different part of the hadronic calorimeter

The ATLAS **Tile Calorimeter** [64], named after the scintillating tiles that conform it, is located right outside the ECAL, and covers the region $|\eta| < 1.8$. It is subdivided into two central, also called long (LB, $|\eta| < 1$) and two extended (EB, $0.8 < |\eta| < 1.7$) barrels, and is made of low-carbon steel and plastic scintillating material. Each of the central and extended barrels are formed by 64 modules in the azimuthal direction and three layers radially, ranging from an inner radius of 2.28 m and 4.25. A schematic view of one of these modules is shown in Figure 3.6 (B). Although as mentioned before, the resolution of the hadronic calorimeter is lower than that of the electromagnetic one, it is enough to provide accurate measurements of jets, taus, isolated hadrons and missing transverse momentum. The modules are segmented into cells, having 10 (5) cells in the first layer, 9 (5) in the second layer,

and 4 (2) in the third layer in the long (extended) barrel. An image of the structure and naming of the cells can be seen in Figure 3.7. In addition to the LB and EB cells, the Intermediate Tile Calorimeter (ITC), corresponding at the cells labelled D4 and C10 in Figure 3.7, covers the region $0.8 < |\eta| < 1.0$. Each of the cells of the calorimeter contains dozens of scintillating tiles and iron plates. Fibers attached to both sides of the tiles as shown in Figure 3.6 (B) collect the light and are read in two different photomultipliers (PMTs).

The Minimum Bias Trigger Scintillators (MBTS) are located in the front of the liquid argon endcap (E3 and E4 scintillators of Figure 3.7). These special scintillators are used mainly for triggering and cover the region $2.08 < |\eta| < 3.85$ in Run 2. The MBTS system consists of 16 scintillators in each side of the calorimeter.

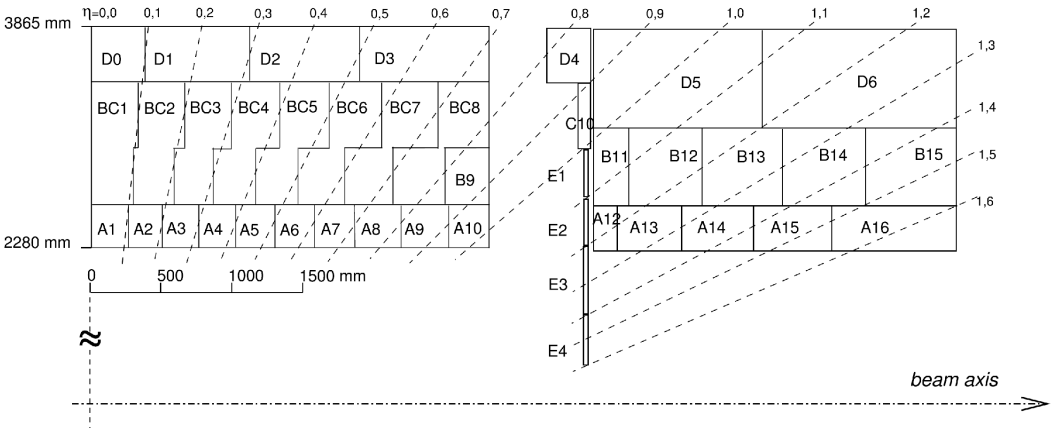

FIGURE 3.7: Segmentation in cells of a long barrel (left) and extended barrel (right) modules

The **Hadronic End-cap Calorimeter** (HEC) is made of liquid argon and copper plates. It consists of two wheels per end-cap, located right next to the electromagnetic end-cap, which are formed by 32 modules. The segmentation in depth consists on two layers per wheel, thus 4 per side. The copper plates have a width of 25 mm for the closer wheels to the interaction point, and 50 mm for the further ones, and are interleaved with liquid argon gaps of 8.5 mm that provide the active material.

The **Forward Calorimeter** (FCal) is located 1.2 m from the ECAL front face, and covers the region $3.1 < |\eta| < 4.9$. It is formed of 3 modules per end-cap. The first one is made of copper and it is optimised for electromagnetic measurements and the other two are made of tungsten and focus on the hadronic particles. All of the modules use liquid argon as active material

3.2.3 Muon spectrometer

The muon spectrometer (MS) is the farthest subdetector from the interaction point, and is designed to measure and identify high-p_{T} muons. It is immersed in a toroidal magnetic field that bends the muon trajectories, as it can be seen in the overview of the muon spectrometer and the toroidal magnetic system in Figure 3.8.

The magnetic system for the muon chambers is different in the barrel and the end-caps. In the range $|\eta| < 1.4$ the barrel toroid provides the magnetic bending of the muons. A smaller end-cap toroid system covers the region $1.6 < |\eta| < 2.7$ in both

sides of the barrel, while in the transition region ($1.4 < |\eta| < 1.6$) a combination of both barrel and end-cap toroids acts on the muons. In this way, the magnetic field (in the azimuthal direction) is mostly perpendicular to the muon trajectory, and bends it over the θ angle. Each of the three toroids (one in the barrel and two end-caps) consists of 8 air-core coils arranged radially symmetrically around the beam axis.

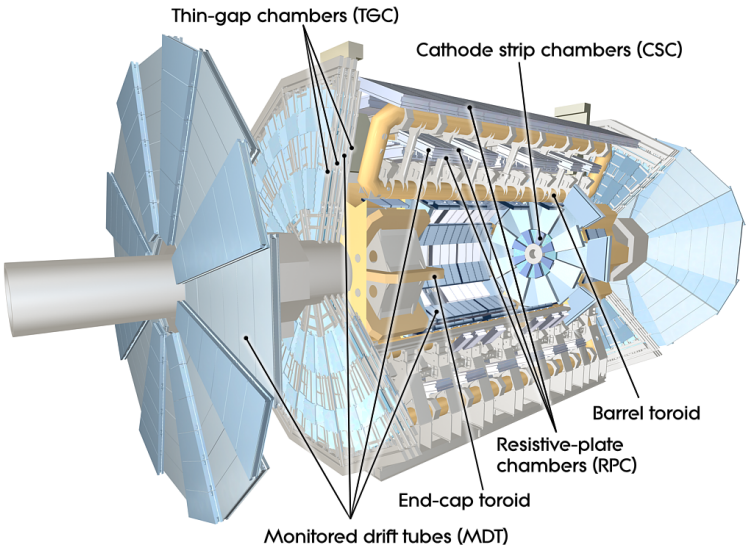

FIGURE 3.8: View of the muon system and the toroidal magnets of ATLAS

The muon chambers are organised in three cylindrical layers in the barrel region, and vertically, also in three layers, in the end-caps. There are different types depending on their position and function: The Monitored Drift Tubes (MDT), the Cathode Strip Chambers (CSC), the Resistive Plate Chambers (RPC) and the Thin Gap Chambers (TGC). A summary of the characteristics of the different chambers is shown in Table 3.3. The combined energy resolution of the muon system ranges from $\sim 4\%$ at 10 GeV to $\sim 10\%$ at 1 TeV.

	Muon Spectrometer			
	MDT	**CSC**	**RPC**	**TGC**
$\|\eta\|$ coverage	< 2.7 (innermost layer < 2.0)	2.0-2.7	< 1.05	1.05-2.7
Function	Precision tracking	Precision tracking	Trigger	Trigger
Resolution (z/R)	35μm (z)	40 μm (R)	10 mm (z)	2-6 mm (R)
Resolution (ϕ)	-	5 mm	10 mm	3-7 mm
Resolution (time)	-	7 ns	1.5 ns	4 ns

TABLE 3.3: Summary of the coverage and resolution of the different muon chambers of the MS

The **Monitored Drift Tubes** provide precision measurement of muon tracks in the bending direction in the central region ($|\eta| < 2.7$). They consist of six to eight tubes filled with a mixture of argon and carbon dioxide that have a high-voltage tungsten-rhenium wire in the center, which collects the electrons released by the passing muon that ionises the gas. It provides a resolution of 80 μm for a single tube, 40 μm for a chamber, and 30 μm for the three layers present in the spectrometer.

The **Cathode Strip Chambers** measure muon momentum at large pseudorapidity ($2.0 < |\eta| < 2.7$) with higher granularity. Located in the layer closest to the

interaction point in the end-cap region, they are multi-wire proportional chambers with two segmented cathodes on both sides of a gas gap and several anode wires oriented in the radial direction in the middle of the gap. They use the same gas mixture as the MDTs and have a higher rate for the more demanding conditions close to the interaction point. Their maximum drift time for signal collection is 40 ns, compared to the 700 ns of the MDTs. Their spatial resolution is of 40 μm in the bending direction and 5 mm in the non-bending one.

The **Thin Gap Chambers** and **Resistive Plate Chambers** are trigger chambers that together cover a pseudorapidity range up to $|\eta| = 2.4$. The RPCs are used in the barrel, and the TGCs in the end-caps. They provide a fast response that allows for triggering and a precise position measurement of the muon track. RPCs are formed of Bakelite plates with a gas mixture in the middle. They cover $|\eta| < 1.05$ and provide the measurement of the ϕ coordinate of the muon tracks. TGPs cover the region $1.05 < |\eta| < 2.7$ and, similarly to the CSCs, are multiwire chambers, where the distance between the wire and cathode is smaller to achieve better drift times.

3.2.4 Trigger system

With around 1.5×10^{11} protons per bunch and 2808 bunches per beam, the LHC can produce up to one billion collisions per second in ATLAS, which corresponds to a data volume of more than 60 megabytes per second. The storage of this amount of data is not manageable and needs to be reduced. The purpose of the trigger system [65] is to select and store only the events relevant for later study and therefore reduce the data volume that needs to be recorded. The event will pass the trigger if it satisfies any of the many conditions that would consider the event as potentially useful for physics. The trigger system in Run II is organised in two stages: the first level trigger (L1), and the high-level trigger (HLT). A scheme of the trigger and data acquisition (TDAQ) systems can be seen in Figure 3.9.

The **Level-1 trigger** is hardware based and, using a limited amount of detector information, will reduce the event rate from 30 MHz to 100 kHz, within a decision time of 2.5 μs. The input data come from the muon chambers (L1Muon), the calorimeters (L1Calo) and topological triggers (L1Topo), where the L1 trigger identifies regions of interest (RoI) that serve as an input to the HLT. The raw data are then sent to the read-out system to the next trigger level.

The **High-Level trigger** is software-based and uses the RoIs as inputs for the trigger algorithms. It reduces the event rate from 100 kHz to approximately 1 kHz, in an average processing time of 200 ms. It uses fully reconstructed data, with similar algorithms to the ones utilised for the offline reconstruction. The events passing the trigger selection are then stored to be used for analysis.

The type of trigger will define the specific requirements on the L1-trigger and HLT, which are based on combinations that are identified at an early stage to possible reconstructed physics objects, such as electrons, muons, jets, or photons, among others. A detailed description of the ATLAS TDAQ system in Run 2 can be found in [65].

3.2.5 Luminosity calculation

As it was mentioned in 3.1, an average proton bunch in the LHC contains about 10^{11} protons. These bunches are focused with a system of quadrupole magnets when they are close to one of the interaction points, in order to increase the probability of proton-proton collisions when two such bunches cross. The measurement of the detected collisions per second over the cross section is the instantaneous luminosity

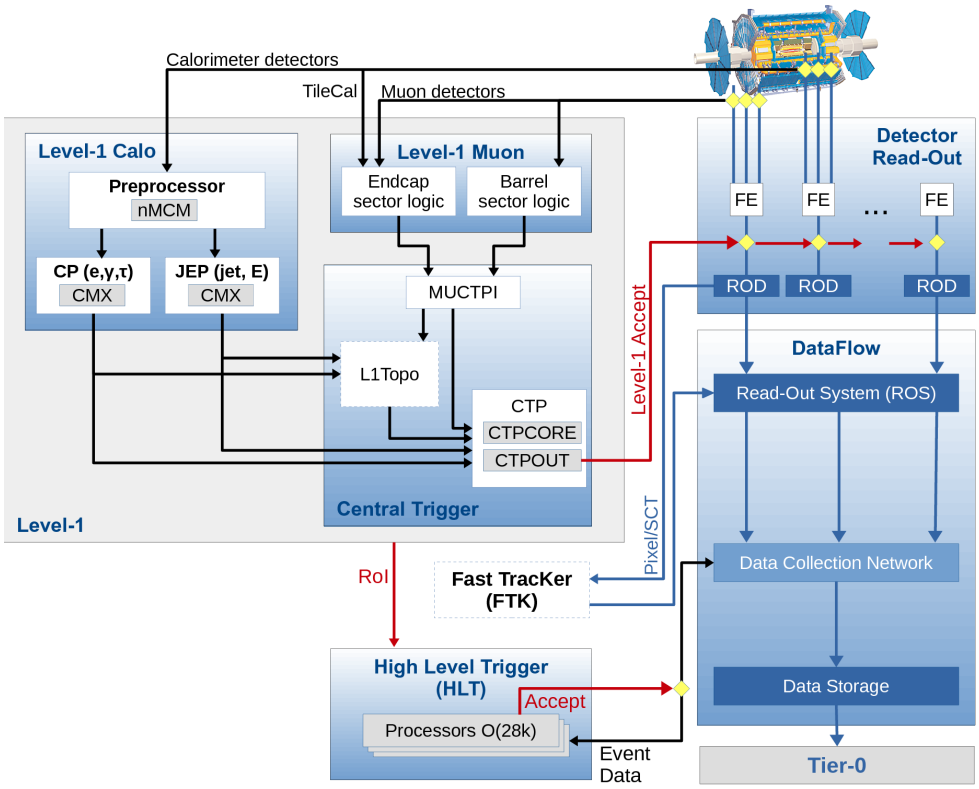

FIGURE 3.9: Scheme of the ATLAS TDAQ system in Run 2 [65]

which can be calculated from the parameters that describe the characteristics of the beam as

$$\mathcal{L} = \frac{n_b f_r n_1 n_2}{2\pi \Sigma_x \Sigma_y}, \tag{3.7}$$

where n_1 and n_2 are the number of protons in bunches 1 and 2, respectively; n_b is the number of bunches in the beam; f_r is the frequency of collisions in the LHC and Σ_x and Σ_y represent the horizontal and vertical convoluted widths of the bunches. The quantities Σ_x and Σ_y are determined by performing a Van der Meer (VdM) scan of the beam, which is done during special LHC runs where the intensity is lower and the bunch-to-bunch distance varies in order to determine the beam profiles. Then, the luminosity can be calculated with equation 3.7. This equation can be rewritten as

$$\mathcal{L} = \frac{R_{inel}}{\sigma_{inel}} = \frac{\langle \mu \rangle n_b f_r}{\sigma_{inel}} = \frac{\langle \mu \rangle_{vis} n_b f_r}{\sigma_{vis}}, \tag{3.8}$$

where R_{inel} is the rate of inelastic collisions, σ_{inel} is the proton-proton inelastic cross section, and $\langle \mu \rangle$ is the average number of interactions per bunch crossing, or pile-up parameter. If ϵ is the efficiency of the detector, then $\langle \mu \rangle_{vis} = \epsilon \langle \mu \rangle$ and $\sigma_{vis} = \epsilon \sigma_{inel}$. The measurement of the visible number of interactions per bunch crossing is the way in which luminosity is monitored in ATLAS, using several independent detectors described in [66]. The two main luminometers are the beam conditions monitor (BCM) and LUCID (LUminosity measurementusing a Cherenkov Integrating Detector), whose results are compared also with a track-counting method and with TileCal minimum bias (MB) integrators. The tracking method uses the multiplicity of charged particles in the tracking system, while the MB system uses the response of TileCal to

soft interactions, which depends linearly on the instantaneous luminosity. These luminosity detectors use as well several algorithms, characterised by different response to pile-up and different sensitivities, reducing significantly the systematic uncertainties in the luminosity measurement. The final error in the 2015+2016 luminosity is 2.1%

In physics analyses, the quantity of interest is the integrated luminosity over a certain period:

$$\mathcal{L}_{int} = \int \mathcal{L} dt. \tag{3.9}$$

During the first two years of Run-2, the peak instantaneous luminosity reached a 13.8×10^{33} cm^{-2}s^{-2} in 2016, and the maximum in 2015 was 5.0×10^{33} cm^{-2}s^{-2}. The integrated luminosity recorded by ATLAS is shown in figure 3.10 for 2015 and 2016, resulting on a total of 36.1 fb^{-1} of good data.

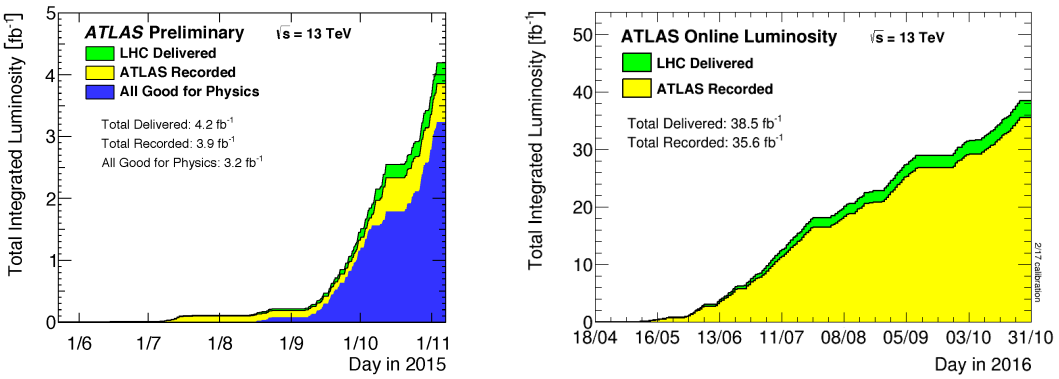

(A) (B)

FIGURE 3.10: Luminosity recorded by the ATLAS detector as a function of time during 2015 (left) and 2016(right)

The final integrated luminosity of a given year is calculated only taking into account the 'good data', i.e. data that was recorded with all the parts of the accelerator and detector working properly, including the subdetectors and the TDAQ system. The status of the detector and all of its components is continuously monitored and recorded. Online and offline applications and detector experts provide feedback on the quality of the data that are being recorded [67, 68, 69]. These checks result in a good-run list (GRL), containing the data runs with good quality that are recommended for physics analysis use.

CHAPTER 4

Physic objects reconstruction

This chapter describes the reconstruction of the main physics objects in the ATLAS detector. This includes a detailed description of the reconstruction of tracks and the identification of the primary vertex, as well as the identification and calibration of electrons, muons, jets, b-jets, and missing transverse momentum.

4.1 Tracks and primary vertex

4.1.1 Track reconstruction

When a charged particle travels through the ID, its path is bended by the solenoidal magnetic field in which it is immersed. By reconstructing their trajectory, or track, the momentum and charge of the particle can be extracted. Tracks serve as input for the reconstruction of most objects and of the primary vertex, and therefore their correct reconstruction is of crucial importance. The reconstruction of the tracks from ID hits is done following a set of algorithms [62].

First, the hits in the SCT and Pixel detector are clustered into a collection of three-dimensional *space-points*, which will be the input for the track reconstruction algorithm. The seeds are formed from sets of three space-points, and a preliminary trajectory is estimated from them, starting from the inner silicon layers and finding compatible hits towards the outer border of the ID. This algorithm is referred to as the *inside-out sequence* [70]. After the inside-out algorithm, the *outside-in* track finding algorithm is run on the TRT hits that were not associated to any track during the first phase, and extrapolates towards the interaction points, adding hits from the SCT and Pixel that were not assigned to any track during the previous step.

This results in a list of track candidates that can often share space-points among them or be incorrectly reconstructed tracks. The tracks are then ordered according to a *track score*, which takes into account the number of hits and holes of the track, its energy, and the number of shared clusters. After discarding the lowest scores, further requirements are applied to the list of tracks in order to remove overlap and keep only the best quality tracks, reducing the number of fakes. A detailed description of the full track-reconstruction chain is given in [62, 70].

4.1.2 Primary Vertex

Primary vertices are points where a proton-proton interaction has occurred. Often there are several per bunch-crossing, due to pile-up events. The number of reconstructed primary vertices gives a measure of the pile-up and is necessary for the correct reconstruction of the physics objects and their kinematics.

The primary vertex reconstruction is done by using an iterative fit that runs on the list of reconstructed tracks. First, a seed for the first vertex is chosen using the z-coordinates of the tracks and centred at the beam spot. Then, the tracks and the seed are used as input parameters for an iterative fitting algorithm to find the best vertex position. Once this is finished, the compatibility of the tracks with the output vertex position is calculated, removing the incompatible ones and using them to find a second vertex. This process is repeated until there are no left tracks. A complete description of the method can be read in [71].

The vertex with highest $\sum p_{\mathrm{T}}^2$ is defined as the main vertex and it corresponds to the hardest interaction, while the rest are considered to be pile-up vertices. Vertices outside of the beam region are considered secondary vertices, which can be useful to identify b- and c- hadron decays.

4.2 Electrons

Electron Reconstruction: A combination of ECal energy deposits and ID tracks is used for electron reconstruction [72]. The seeds are formed of clusters in the ECal, and if possible, they are associated to a track in the ID.

First, a sliding window algorithm [73] is used to identify suitable cluster candidates. The window size is 3×5 towers where $\Delta\eta^{tower} \times \Delta\phi^{tower} = 0.025 \times 0.025$. An overlap-removal algorithm is applied to nearby clusters. The seed clusters are required to have a total energy deposit of at least 2.5 GeV, summing over all the ECal layers in depth.

Then, reconstructed tracks are extrapolated from the ID to the middle layer of the EM calorimeter. This is because the electron will not deposit much energy in the first layer, and low energy electrons will not have much energy left for the outer layers. The coordinates of the tracks are then compared and matched to those of the existing cluster seeds. If two or more tracks are associated with the same cluster, the closest track to the cluster seed is chosen for reconstruction, i. e. the one with smallest ΔR, although the other tracks are saved for further analysis. The tracks associated with cluster seeds are also required to be compatible with the primary vertex.

All seed clusters matched to a track are considered as electron candidates. At this point, the EM clusters are rebuilt using a wider window of 3×7 towers in $\eta \times \phi$ in the barrel and 5×5 in the endcaps. The energy of the electron candidate is calculated taking into account possible leakages in the longitudinal direction into the HCal, and towards the sides due to limited cluster size, as well as correcting for the energy lost between the ID and the ECal. These corrections are derived from MC events produced with the whole ATLAS simulation chain; and from data $Z \to ee$ events. The reconstructed four-momentum of the electron takes into account information from both the cluster and the associated track. The energy is given by the cluster, while the η and ϕ coordinates are taken from the track.

For electron candidates in the forward region ($|\eta| > 2.47$) the procedure is different. Since there is no tracking for this area, all the coordinates of the electron four-momentum are given by the EM cluster.

Electron identification: The reconstructed electron candidates are not all electrons coming from the primary proton-proton interaction. The main background objects are hadronic jets, electrons from photon conversion, or decays from heavy hadrons. Electron identification algorithms [74] are then applied to the electron candidates to select the signal electrons. These algorithms use a likelihood (LH) function composed with the signal and background probability density functions to discriminate. The likelihood function is built using discriminating variables that are based on

track quality, like the number of hits in the different layers or the impact parameter; cluster quality, like the fraction of energy deposited at the centre of the cluster or the shower width; or the hadronic leakage of the shower.

The variables are used as input in a multivariate analysis, and several identification criteria are defined, depending on the background rejection and signal efficiency. These criteria, normally referred to as *working points*, are provided for the use of physics analyses: Tight, Medium, Loose, Loose+B-Layer and VeryLoose, in increasing order of signal efficiency. The Loose and VeryLoose working points are optimised for discrimination against light-flavour jets and photon conversions, while additional variables are included in the Tight and Medium selections for a better discrimination power against heavy-flavour jets.

Electron isolation: Even after the identification requirements are applied, some hadronic jets are still misidentified as electrons. In order to further purify the electron sample, isolation criteria are applied, based on two main variables.

- Calorimeter-based isolation: The variable $E_T^{cone\Delta R}$ is defined as the sum of the energy deposited in a ΔR cone in the calorimeter around the electron, excluding the very central contribution within $\Delta\eta \times \Delta\phi = 0.125 \times 0.175$ from the cluster barycentre.

- Track-based isolation: A similar variable $p_T^{cone\Delta R}$ is defined as the scalar sum of the p_{T} of the tracks within a cone of ΔR having $p_{\mathrm{T}} > 0.4$ GeV around the electron

A set of recommended working points is also provided for analyses, combining selections on the calorimeter and track-based isolation variables.

Electron efficiency is calculated in bins of E_T and η using a tag-and-probe method. MC samples of $Z \to ee$ and $J/\Psi \to ee$ events are used, which provide good statistics. The events are required to have a reconstructed electron following very strict criteria, which will be referred to as the 'tag' electron. A second reconstructed electron is used as the 'probe' electron. Then, this sample is contaminated with background to be compared with data. To separate signal and background the invariant dielectron mass is required to be close to the Z or J/Ψ-mass, selecting the resonance peak as shown in 4.1.The efficiency is then calculated as the fraction of probe electrons that pass the tested criteria. The electron identification efficiency as a function of E_T and η is shown in Figure 4.2. Since the efficiency is not perfectly simulated in the MC, a calibration scale factor is extracted from the observed difference between data and simulation events, which compensates for this difference.

4.3 Muons

Muons are reconstructed and identified mostly from the tracks they leave in the ID and in the MS, although in some cases they also leave a signal in the calorimeters [75]. The muon tracks in the inner detector are built as described in section 4.1.1. The tracks in the muon spectrometer are reconstructed in several steps. First, hits aligned in a trajectory in the bending direction are searched for. They are fit to a straight line in each layer, creating segments. The segments in the CSC are reconstructed by fitting both in the η and ϕ planes. Then, the muon tracks are built by fitting segments from different layers.

Muon reconstruction: The reconstructed muons are classified into four different types depending on the way they are reconstructed

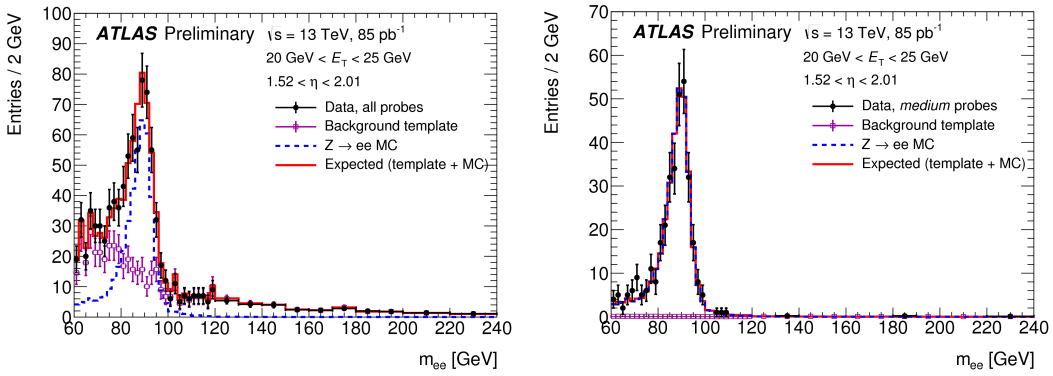

(A) (B)

FIGURE 4.1: Illustration of the background estimation using the mass-based method in the 20 GeV $< E_T <$ 25 GeV, 1.52$< \eta <$2.01 bin, at reconstruction level (left) and for probes passing the likelihood medium identification (right). Efficiencies are determined by taking the ratio of background subtracted probes passing the likelihood identification over background subtracted probes at reconstruction level. The simulated $Z \to ee$ sample is shown for illustration and is scaled to match the background subtracted data in the Z-mass window. Since at reconstruction level the background sample is a subsample of the selected events, fluctuations can be fully correlated [74].

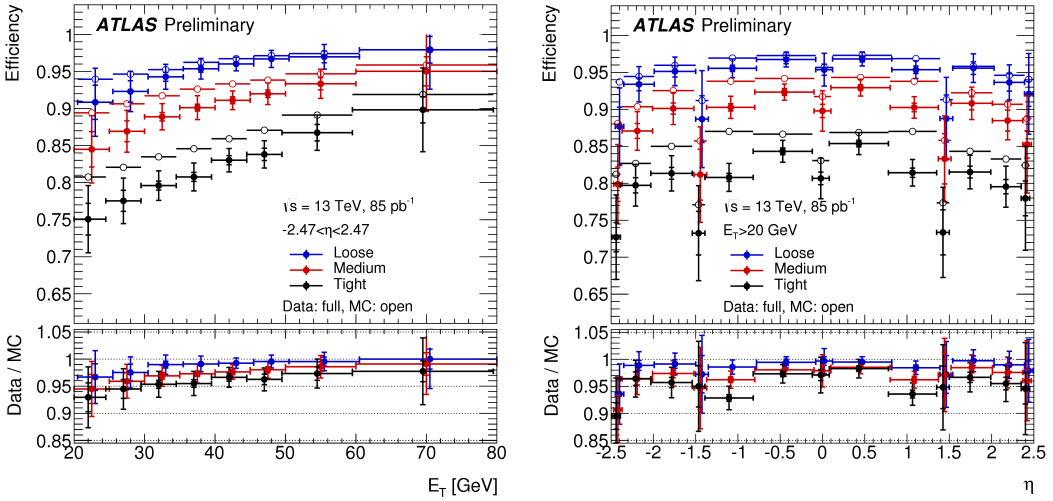

(A) (B)

FIGURE 4.2: Electron identification efficiency in $Z \to ee$ events as a function of transverse energy E_T (left, integrated over η) and pseudo-rapidity η (right, integrated over E_T). Two sets of total uncertainties are shown: For the larger error bars, both statistical and systematic uncertainties are assumed to be fully correlated in the different η/E_T bins, and therefore reflect the limited statistic for each 2D bin. The smaller error bars are obtained with pseudo-experiments, treating the statistical uncertainties as uncorrelated [74].

- Combined muons (CB): Both the ID and MS tracks are used in the reconstruction. The track reconstruction is performed independently in the ID and MS

and a fit is performed to match them and create a combined track. Normally the MS tracks are extrapolated backwards to the ID and matched to an ID track, similarly to the outside-in algorithm described in 4.1.1. An inside-out algorithm is applied complementarily to unmatched tracks.

- Segment-tagged muons (ST): The track in the ID is extrapolated to the MS and matched to at least one segment in the chambers. They are useful for muons which only cross one of the layers of chambers of the MS, because of their low-p_{T} or if they are in a region with reduced acceptance.

- Calorimeter-tagged muons (CT): An extrapolated ID track can be matched to an energy deposit in the calorimeter compatible with a minimum-ionising particle. It is mostly useful in regions where the MS is poorly instrumented.

- Extrapolated muons (ME): The trajectory is reconstructed using only MS information and requiring that it originates from the main primary vertex of the interaction. It is required to leave a trace at least in two of the layers of the MS, or three layers in the forward region. They are mainly used to increase the acceptance in $2.5 < |\eta| < 2.7$, which is not covered by the ID.

Overlaps between the different types of muons are resolved by giving priority to CB, then ST, then CT muons, and finally ME.

Muon identification: The main backgrounds appearing in muon reconstruction come from pion and kaon decays. In order to discriminate between signal and background muons MC $t\bar{t}$ events are used. Muons coming from W decay are considered as signal, while the background is constituted of muons from light-hadron decays. Normally, the tracks of the background muons in the ID and the MS will be less compatible, and will have different momenta. Variables related to the number of hits in the tracks, and the differences between the MS and ID reconstructed tracks are used for discrimination. As with electrons, four muon identification working points are provided for use of the physics analyses, Loose, Medium, Tight and HighPt [75]. Loose, Medium and Tight working points have decreasing signal efficiency, ad HighPT is designed for muons with p_{T} higher than 100-200 GeV, when the resolution is dominated by the MS, and additional requirements are applied.

Muon reconstruction efficiency: It is measured using a tag-and-probe method similar to the one described in 4.2 in the region $|\eta| < 2.5$, corresponding to the ID acceptance [75, 76, 77]. Simulated samples of $Z \to \mu\mu$ and $J/\Psi \to \mu\mu$ are used for the calculation, and compared to the results in data. The resulting efficiencies for medium and loose selections are above 98%, and between 90 and 98% for tight muons. The efficiencies as a function of η are shown in Figure 4.3. For muons outside of the ID acceptance, the efficiency is calculated as described in [78], comparing the number of muon candidates in the high-$|\eta|$ region ($2.5 < |\eta| < 2.7$) with the region $2.2 < |\eta| < 2.5$, in data and simulation. A scale factor is extracted from the differences between data and MC and applied to the simulation.

Muon isolation: As in the case of electrons, muon isolation is required to further discriminate background from signal. The isolation criteria are typically applied to two variables: a calorimeter-based and a track-based variables. They are defined in a similar manner as those for electrons. The track-based isolation ($p_T^{varcone30}$) is defined as the scalar sum of the p_T of the tracks around the muon, while the track-isolation ($E_T^{topocone20}$) is the sum of the E_T of the clusters in a cone around the muon in a radius of 0.2. Isolation criteria (working points) combining selections in both variables are provided for physics analyses, requiring different levels of signal efficiency.

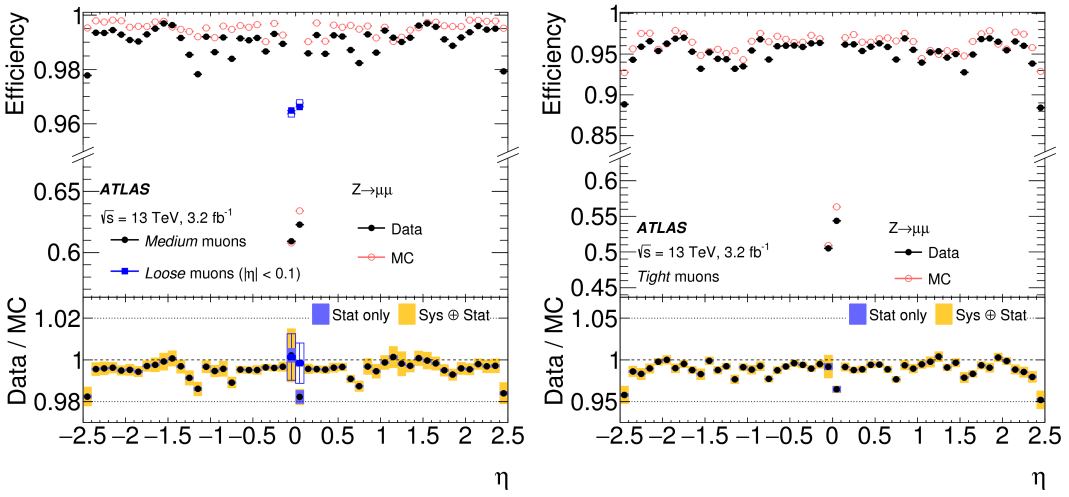

(A) (B)

FIGURE 4.3: Muon reconstruction efficiency as a function η measured in $Z \to \mu\mu$ events for muons with $p_T > 10$ GeV shown for Medium (left) and Tight (right) muon selections. In addition, the left plot also shows the efficiency of the Loose selection (squares) in the region $|\eta| < 0.1$ where the Loose and Medium selections differ significantly. The error bars on the efficiencies indicate the statistical uncertainty. Panels at the bottom show the ratio of the measured to predicted efficiencies, with statistical and systematic uncertainties.

4.4 Jets

Jets are collimated showers of particles that are produced from the hadronisation of quarks and gluons.

In this thesis, jets are reconstructed using the anti-k_T jet algorithm [79], which is used as the default jet algorithm in many particle physics experiments.

4.4.1 Topoclusters

Jets are built from energy clusters in the calorimeter called topoclusters. Each of these reconstructed topoclusters is interpreted as a single particle produced in the shower, which will then be used to reconstruct the jets. Topoclusters are also used as a measurement of the energy flow of softer particles that contribute to the reconstruction of other objects such as missing transverse energy.

The topocluster construction [80] begins with a cell with highly significant signal over noise ($|E/\sigma_{noise}| \geq 4$), which is required not to be in the presampler layers, to avoid seeds that come from pile-up and do not penetrate the calorimeter. The expected noise takes into account electronic noise from the detector as well as pile-up noise, calculated from simulations. Once the seed cell is identified, an iterative algorithm is applied, adding topologically connected cells that have a signal-over-noise ratio of at least 2; and then the direct neighbours are collected in the topocluster. If two seed cells are topologically connected, the two clusters are merged.

The result is a collection of three-dimensional clusters whose kinematic properties are built from those of the cells that form them. The direction of the cluster is calculated weighting the cells by their absolute energy, while its energy the sum of the cell energies. The topoclusters are interpreted as massless pseudo-particles in the

electromagnetic scale in reconstruction of physics objects, since the definition of a cluster *mass* would require a hypothesis on the origin of the signal and the charge of the particle.

4.4.2 Jet finding algorithm

The anti-k_T algorithm [79] is a sequential clustering algorithm which is widely used in the experiments in the LHC. It uses particles as inputs, which can be the already described topoclusters (resulting in *calorimeter jets*), reconstructed tracks (*track jets*), or MC events at the particle level (*truth jets*).

In order to decide how to cluster the signals to form a jet, the anti-k_T method introduces a distance parameter, defined as

$$d_{ij} = min(k_{ti}^{-2}, k_{tj}^{-2}) \cdot \frac{\Delta_{ij}^2}{R^2}, \tag{4.1}$$

$$d_{iB} = k_{ti}^{-2}, \tag{4.2}$$

where k_{ti} is the transverse momentum of particle i, Δ_{ij} is the distance in the $y - \phi$ plane between particles i and j; and R is is a parameter that gives a measure of the approximate size of the jet.

The jet clustering finds first the minimum distance between every possible particle pair using equation 4.1 and between each particle and the beam with equation 4.2 (including the beam). If this minimum is the distance between two particles, it combines them, while if it is between a certain particle i and the beam, it calls i a jet and removes it from the list of particles. Then the distances are recalculated and the procedure starts again, until there are no particles left in the list.

In figure 4.4, the shapes of the jets reconstructed with the anti-k_T jet algorithm and their constituents are shown for a parton level event with randomly distributed soft particles. The shape of most jets is circular, and it is only modified when another hard constituent is found nearby.

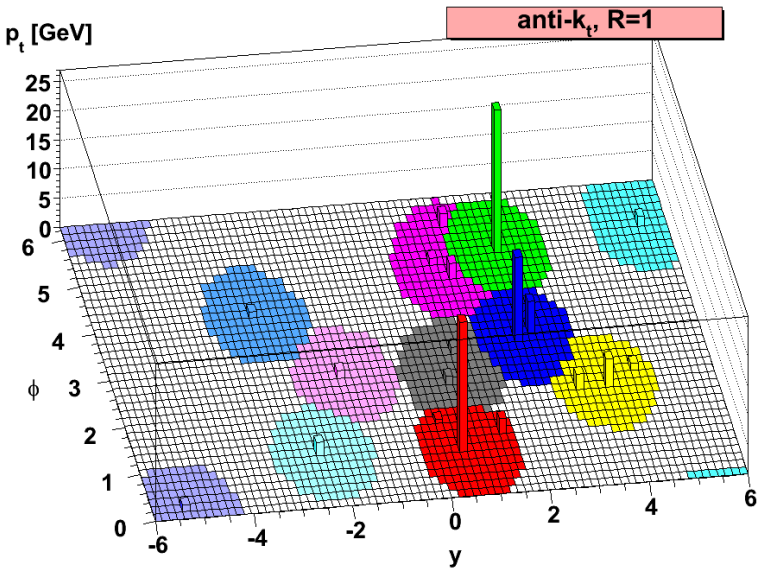

FIGURE 4.4: Illustration of the anti-k_T jet algorithm performance on a parton-level event with soft random particles [79].

This algorithm is chosen because it is infrared and collinear safe, i.e. the addition of a soft particle emitted by the parton does not change the shape of the jet, which facilitates theoretical calculations; and because it results in rather circular shaped jets, as can be seen in figure 4.4.

4.4.3 Jet reconstruction and calibration

Tracks reconstructed in the ID and muon track segments are used in jet reconstruction [81]. They are assigned to the calorimeter jets using their coordinates in the $\eta - \phi$ plane. Jets are reconstructed if they pass a p_T threshold of 7 GeV. The jets used in this analysis have a radius parameter of $R = 0.4$, as will be described in chapter 6.

Jets are calibrated using a series of simulation-based and *in-situ* techniques. *In-situ* calibrations are derived from the balance between a jet and some reference object recoiling against it, like a photon, a Z boson, or a multijet system [81]. An overview of the jet calibration process can be seen in Figure 4.5.

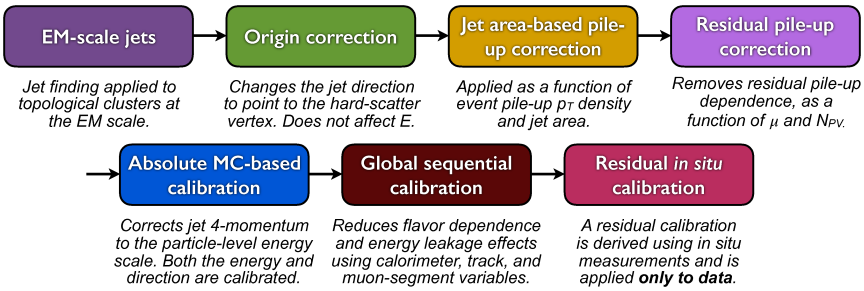

FIGURE 4.5: Calibration steps for EM-scale jets. Apart from the origin correction, each calibration is applied to the jet four-momentum [81]

.

First, a correction to the jets is applied to have them pointing to the primary vertex and not the centre of the detector. This correction leaves the jet energy untouched, and only modifies its η and ϕ coordinates, improving the spatial resolution. This procedure is described in detail in [82]. The subsequent steps of the jet calibration are briefly described in the following sections.

4.4.3.1 Pile-up corrections

The energy of the reconstructed jets is affected by pile-up. There are two types of pile-up that can affect the energy of the jets, in-time and out-of-time pile-up. The in-time pile-up is due to the extra interactions produced in the same bunch-crossing as the hard interaction of the event. The out-of-time pile-up instead is produced by the interactions produced in surrounding bunch-crossings. The average number of interactions per bunch-crossing $\langle\mu\rangle$, from equation 3.8 can be written as

$$\langle\mu\rangle = \frac{\mathcal{L} \cdot \sigma_{inel}}{n_b \cdot f_r}. \tag{4.3}$$

Pile-up can have different effects on the data collected, and thus several corrections are used in steps to compensate for them.

First, a method based on jet-areas [83] subtracts the pile-up contribution to the energy jet-by-jet. It defines a jet area by adding soft particles to the sample randomly and identifying the region in which they are associated to a given jet. This jet area (A) gives a measure of the susceptibility of the jet to pile-up. In this way, if the

average energy density added to the event by the pile-up is ρ, the effect of pile-up on the jet p_T can be calculated by

$$\Delta p_T = A\rho \pm \sigma\sqrt{A} + \text{lower orders.} \tag{4.4}$$

The lower-order terms of equation 4.4 account for non-uniformities of the pile-up contributions, as well as effects in the jet reconstruction at previous stages (results of jet-finding algorithms can be dependent on pile-up). Here σ is the standard deviation of the noise introduced. The calculation of ρ is based on the p_T density of jets in the $\eta - \phi$ plane. The jets used for this calculation are reconstructed with the k_T [84] algorithm with $R = 0.4$, since it tends to reconstruct soft pile-up jets uniformly. The measure of ρ used is the median of the distribution of p_T/A:

$$\rho = median(\frac{p_T}{A}). \tag{4.5}$$

In this way, the correction calculated from equation 4.4 is applied as a global scale to the jet energy, not affecting the η and ϕ coordinates, and neglecting the lower order effects.

However, this correction is derived from central jets $|\eta| < 2$, and it is not enough to describe the pile-up conditions in the forward regions, and a residual dependence on pile-up is observed. Therefore, another correction is derived. The p_T of the jets resulting from the area-based method are dependent on the number of primary vertices (N_{PV}) and μ. These dependencies are shown in figure 4.6 as a function of η. The correction is derived from the differences observed between reconstructed and MC particle level (*truth*) The dependence on N_{PV} (α) and μ (β) are found to be independent from each other and linear, and the values of the α and β parameters are calculated from linear fits in simulations. The corrected p_T of the jets at this stage is given by

$$p_T^{corr} = p_T^{reco} - \rho \cdot A - \alpha(N_{PV} - 1) - \beta \cdot \mu. \tag{4.6}$$

The dependence of the jet pt on pile-up can be seen in figure 4.6 before and after applying the described corrections for in-time pile-up and out-of-time pile-up.

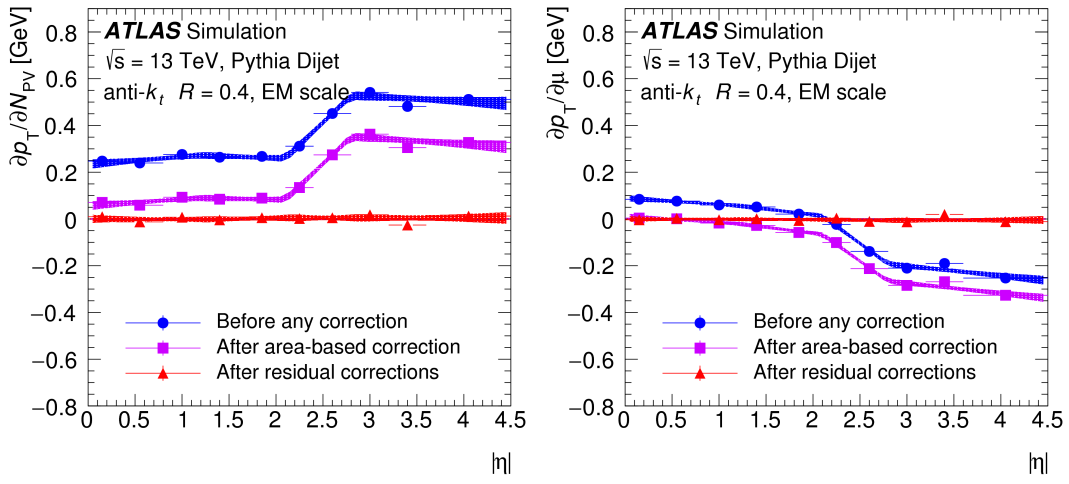

(A) (B)

FIGURE 4.6: Dependence of EM-scale anti-k_T jet p_T on in-time pile-up (left) and out-of-time pile-up

4.4.3.2 Jet energy scale and η calibration

The jet energy scale calibration corrects the reconstructed jet energy to the scale of particle-level jets (truth jets) in MC, and restores the mismeasurements in the jet η due to transitions between calorimeter technologies. It is derived by matching reco jets to truth jets, using only isolated ones. The average energy response is calculated as the mean of a gaussian fit to the E^{reco}/E^{truth} distribution, binned in E^{truth} and η. The actual correction is derived by using a numerical inversion [82] technique, parameterised in terms of E^{reco} and η. This is done in two steps:

- Calculate the response function as a function of the truth E of the jets $\mathcal{R}(E^{truth}) = E^{reco}/E^{truth}$.
- Estimate $\mathcal{R}(E^{reco})$ using $E^{reco} = \mathcal{R}(E^{truth}) \cdot E^{truth}$.

This technique is very widely used for the derivation of similar corrections [85].

A further correction is applied to the jet η, since a bias is observed in the transition regions between calorimeters. They are due to a change in the geometry or technology of the detector, and they alter the jet four momentum. The correction is derived as the difference between the reconstructed and the truth η and binned in E_T^{truth}. Again, a numerical inversion is used to parameterise it in terms of E_T^{reco}. This calibration affects the jet p_T and η and not its full four-momentum.

4.4.3.3 Global sequential calibration

After the previous calibration procedures are applied, it is observed that the jet response has a remnant dependency on detector-related variables, especially for low p_{T} jets. If this dependency can be overcome, the result would be a better resolution for the jet energy. The variables selected for the calculation of the Global Sequential Calibration [86, 81] correction are related to the relative energy deposited in hadronic and electromagnetic calorimeters, the number and width of the tracks associated to the jets, and the number of muon segments associated to the jet:

- f_{Tile0} is the fractional energy in the first layer of the Tile calorimeter.
- f_{LAr3} is the fractional energy in the third layer of the LAr calorimeter.
- n_{trk} is the number of tracks associated to the jet.
- $\mathcal{W}_{trk}$ is the p_T weighted track width.
- $n_{segments}$ is the number of muon segments.

The dependency on this variables appears due to different jet topologies. For example, a jet with a large deposit in the hadronic calorimeter would have a lower response due to non-compensation of the ATLAS calorimeter. The substructure of the jets originating this differences is a sign of the different composition of the showers, which highly depends on the particle that originated the jet. The gluon-initiated jets, for instance, have a less-penetrating shower than the quark-initiated ones, being wider and containing in general more soft particles, since the gluons emit more particles with lower energies.

For each of the described variables, an independent four-momentum correction is derived in a similar way as described in 4.4.3.2. The jets are matched to truth jets in MC, and the response function is inverted to get a correction factor binned in p_T^{truth} and η. Then, a numerical inversion is used to have the correction in terms of p_T^{reco}. The corrections for each observable are applied in the order given above.

4.4.3.4 *In situ* calibrations

The last stage of jet calibration is applied to data, and differences in the jet response between data and MC simulation are accounted for. These differences are due to the imperfect simulation of detector responses, hard scatter interaction, pile-up, jet formation, and interactions with the detector. They are measured by balancing the p_{T} of a jet against another object (called the reference, *ref* object), such as another jet, a photon, a Z boson, or a multijet system. The corrections applied at this stage are derived by using a double ratio:

$$\mathcal{R} = \frac{\langle p_T^{jet}/p_T^{ref}\rangle_{data}}{\langle p_T^{jet}/p_T^{ref}\rangle_{MC}} \tag{4.7}$$

The *in situ* calibrations are derived and applied sequentially in the following order:

- $\eta-$intercalibration in dijet events.
- Z-jet balance.
- γ-jet balance.
- Multijet balance (MJB)

The η-intercalibration corrects the jet response of forward jets ($0.8 < |\eta| < 4.5$) to well-measured central jets ($|\eta| < 0.8$) in dijet events, while the other three calibrate central jets in different p_{T} regions. The Z- and γ-jet balance are used in the calibration of jets with $p_{\mathrm{T}} < 950$ GeV, while MJB focuses in high p_{T} jets ($300 < p_{\mathrm{T}} < 2000$ GeV). The correction is derived again using numerical inversion and correcting the four momentum of the jets. Although the corrections are derived from central jets, they can be applied to forward jets once they have been corrected using the $\eta-$intercalibration method.

4.5 B-tagging algorithm

The identification of jets originated from b-hadrons (b-jets) is important to many analyses in the ATLAS experiment in different areas, and specifically, it is key to the analysis presented in this thesis. The characteristic long lifetime of b-hadrons can be used for b-jet identification (usually called *b-tagging*) in different manners [87, 88]. Typically, a b-hadron can travel for ~ 450 μm in the inner detector before decaying. As illustrated in figure 4.7, besides the primary vertex, a secondary, displaced vertex appears where the b-hadrons decay. This feature is exploited by the several b-tagging algorithms in ATLAS that discriminate b-jets. These algorithms use properties of the tracks associated to a given jet and the reconstructed vertices in the ID to identify the displaced vertex:

- IP2D and IP3D are algorithms based on impact parameters of the tracks. They make use of the variables d_0 and z_0, which measure the distance of the track to the primary vertex. d_0 is defined as the smallest distance in the $r-\phi$ plane between the track and the primary vertex, as can be seen in figure 4.7. The variable $z_0 sin\theta$ is the shortest distance in the z direction between the point of closest approach in the $r-\phi$ projection and the primary vertex. The sign of d_0 and z_0 is positive if the closest point to the PV is between the PV and the jet, and negative otherwise. In jets containing b-quarks, these parameters tend to

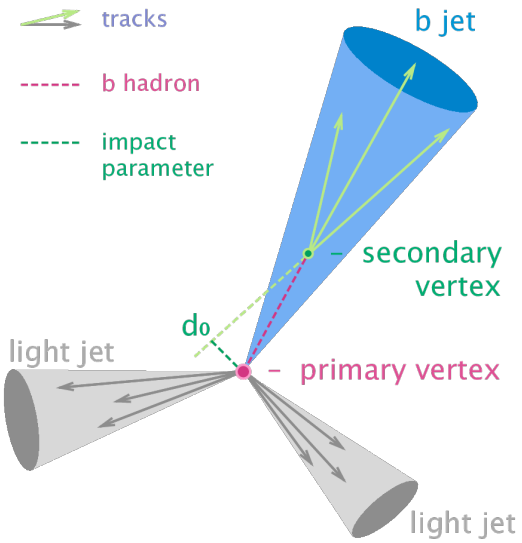

FIGURE 4.7: Sketch of a b-jet, the primary and secondary vertices, and the impact parameter d_0

be large. IP algorithms use these parameters as discriminants to build a Log-Likelihood Ratio (LLR) that classifies them as signal (b-jets) or background (c- and light quark jets).

- SV is an algorithm based on the explicit reconstruction of the secondary displaced vertex. All possible vertices with at least two tracks are built, and the vertices compatible with long-lived particles are rejected, based on the invariant mass of the vertex and its position with respect to the primary vertex. The main discriminant of the algorithm is the flight length, the distance between the reconstructed displaced vertex and the primary vertex.

- The JetFitter algorithm aims at the reconstruction of the full decay chain of the b-hadron.

In order to maximise the efficiency and reduce the fake-rate, all of the outputs of the above mentioned algorithms are combined in a multivariate analysis (MVA) using a boosted decision tree (BDT), giving rise to the final algorithm used for b-tagging in this thesis called MV2c10. The training is performed on $t\bar{t}$ events with b- c- and light jets, and then tested in an independent sample. Figure 4.8 shows the BDT output of the MV2c10 algorithm for b-, c- and light-flavor jets.

4.6 Missing transverse energy

The only Standard Model particles that escape measurement in the detector are neutrinos. Whenever they are produced in the collision, they create an imbalance in the measured momentum of the physics objects. Furthermore, many beyond the standard model theories predict particles that do not interact with the detector, and would thus produce a similar imbalance. For these reasons, the measure of such imbalance is very important for physics analyses. This imbalance is measured in the transverse plane and called missing transverse momentum (p_T^{miss}). The magnitude of this vector is also sometimes used, and referred to as missing transverse energy (E_T^{miss}). Apart from the mentioned neutrinos and non-interacting new particles, mismeasurements of the rest of the physics objects can contribute to the missing transverse energy.

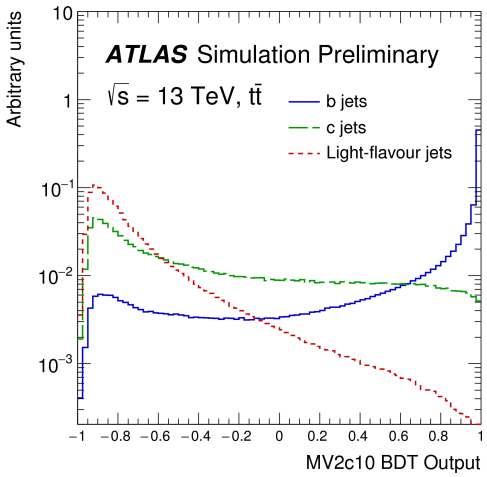

FIGURE 4.8: MV2c10 BDT output for b-, c- and light-flavour jets evaluated with $t\bar{t}$ events.

The $E_{\mathrm{T}}^{\mathrm{miss}}$ is calculated as the sum of several components, one for each physics object [89, 90, 91]

$$E_{\mathrm{T}}^{\mathrm{miss}} = E_{\mathrm{T}}^{\mathrm{miss}}(e) + E_{\mathrm{T}}^{\mathrm{miss}}(\gamma) + E_{\mathrm{T}}^{\mathrm{miss}}(\tau) + E_{\mathrm{T}}^{\mathrm{miss}}(jets) + E_{\mathrm{T}}^{\mathrm{miss}}(\mu) + E_{\mathrm{T}}^{\mathrm{miss}}(soft). \quad (4.8)$$

Each of the terms in equation 4.8 is calculated as the negative sum of the transverse momentum of all the calibrated objects of that type in the event. The calorimeter energy deposits are associated to physics objects in the following order: electrons, photons, taus, jets and muons. The soft term is reconstructed from detector signals not associated to any object, and it can be calculated from either calorimeter or ID signals. For the work presented here, only the track soft term is taken into account, which is reconstructed as the negative sum of the reconstructed tracks that are not associated to any object. The calorimeter soft term is instead calculated as the negative sum of the calorimeter deposits not used in the reconstruction of any object.

The resolution of the $E_{\mathrm{T}}^{\mathrm{miss}}$ is measured in data and compared to simulation in $Z \to \mu\mu$ and $W \to e\nu$ events. $Z \to \mu\mu$ events are not expected to have much genuine $E_{\mathrm{T}}^{\mathrm{miss}}$, and it is thus a good method for measuring the resolution. To remove background, two opposite charged muons are selected, with $p_{\mathrm{T}} > 25$ GeV, and compatible with the Z mass in a 25 GeV window. The $E_{\mathrm{T}}^{\mathrm{miss}}$ and the soft term distributions are shown for data and MC in figure 4.9

A sample of $W \to e\nu$ events is used to evaluate the $E_{\mathrm{T}}^{\mathrm{miss}}$ reconstruction performance in events where genuine $E_{\mathrm{T}}^{\mathrm{miss}}$ is expected due to the neutrino. The selection requires exactly one electron with $p_{\mathrm{T}} > 17$ GeV, $E_{\mathrm{T}}^{\mathrm{miss}} > 25$ GeV and the transverse mass as calculated from the electron and the $E_{\mathrm{T}}^{\mathrm{miss}}$ is required to be $m_T > 50$ GeV. The transverse mass is defined as

$$m_T(W) = \sqrt{2p_{\mathrm{T}}^{e}E_{\mathrm{T}}^{\mathrm{miss}}(1 - \cos\Delta\phi)}, \quad (4.9)$$

where p_{T}^{e} is the transverse momentum of the electron and $\Delta\phi$ is the distance in ϕ between the electron and the direction of the missing transverse momentum. The data and MC distributions of $E_{\mathrm{T}}^{\mathrm{miss}}$ and $E_{\mathrm{T}}^{\mathrm{miss}}$ soft term are shown in 4.10.

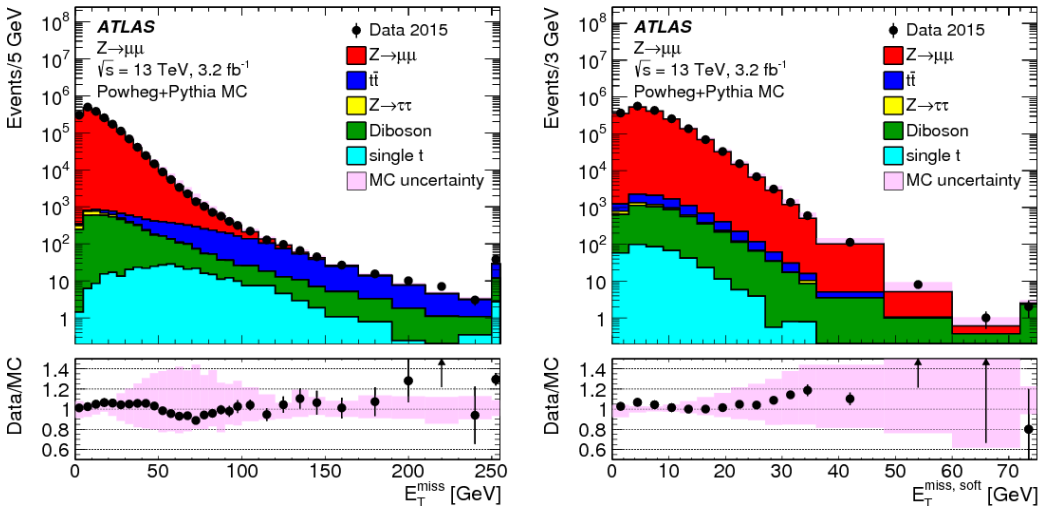

(A) (B)

FIGURE 4.9: Distributions of total $E_{\mathrm{T}}^{\mathrm{miss}}$ and $E_{\mathrm{T}}^{\mathrm{miss}}$ soft term in $Z \to \mu\mu$ events. The expectation from MC simulation is superimposed and normalised to data, after each MC sample is weighted with its corresponding cross-section [89].

The measurement of the $E_{\mathrm{T}}^{\mathrm{miss}}$ resolution is done in bins of $\sum E_T$, the scalar sum of the p_{T} of all the hard object and the soft term in an event:

$$\sum E_T = \sum p_{\mathrm{T}}^{e} + \sum p_{\mathrm{T}}^{\gamma} + \sum p_{\mathrm{T}}^{\tau} + \sum p_{\mathrm{T}}^{jets} + \sum p_{\mathrm{T}}^{\mu} + \sum p_{\mathrm{T}}^{soft}. \tag{4.10}$$

For the calculation of the resolution, the calorimeter soft term is used instead of the track-based term. Each bin is calculated as the root mean squared (RMS) of the combined x and y components of the $E_{\mathrm{T}}^{\mathrm{miss}}$ in $Z \to \mu\mu$ events. The resolution as a function of $\sum E_T$ is shown in figure 4.11 (A).

The calculation of the $E_{\mathrm{T}}^{\mathrm{miss}}$ scale is another measure of the reconstruction performance. It is defined in Z+jets events as the average of the projection of the $E_{\mathrm{T}}^{\mathrm{miss}}$ in the direction of the Z boson p_{T}, $\langle \overrightarrow{A}_Z \cdot \overrightarrow{E_{\mathrm{T}}^{\mathrm{miss}}} \rangle$, where $\overrightarrow{A}_Z$ is the unit vector in the direction of the Z:

$$\overrightarrow{A}_Z = \frac{\overrightarrow{p_{\mathrm{T}}}^{\mu+} + \overrightarrow{p_{\mathrm{T}}}^{\mu-}}{|\overrightarrow{p_{\mathrm{T}}}^{\mu+} + \overrightarrow{p_{\mathrm{T}}}^{\mu-}|} \tag{4.11}$$

This direction is sensitive to the balance between the hadronic recoil and the hard objects of the interaction. In a case of perfect balance, this projection would be 0. The $E_{\mathrm{T}}^{\mathrm{miss}}$ scale as a function of the p_{T} of the Z is shown in figure 4.11 (B).

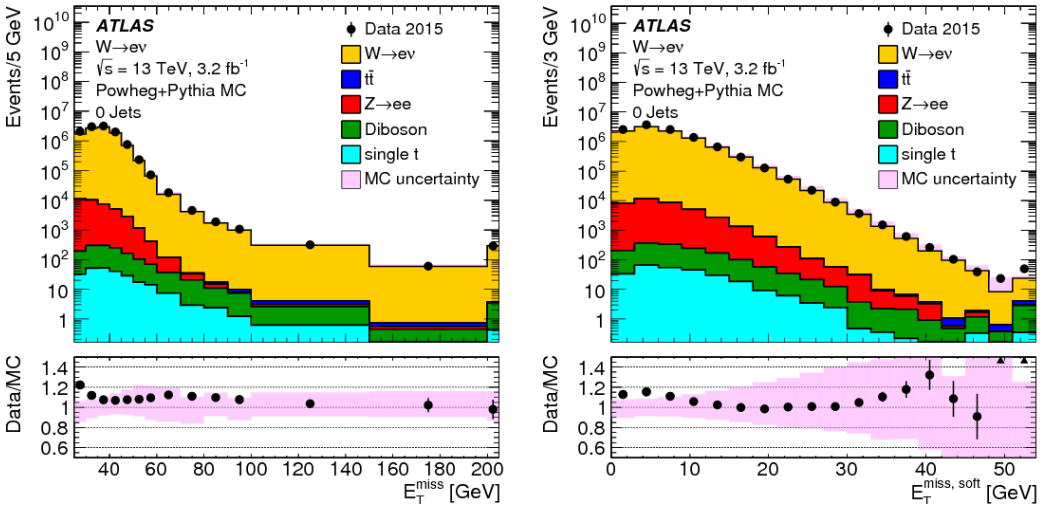

(A) (B)

FIGURE 4.10: Distributions of total $E_{\mathrm{T}}^{\mathrm{miss}}$ and $E_{\mathrm{T}}^{\mathrm{miss}}$ soft term in $W \to e\nu$ events. The expectation from MC simulation is superimposed and normalised to data, after each MC sample is weighted with its corresponding cross-section [89].

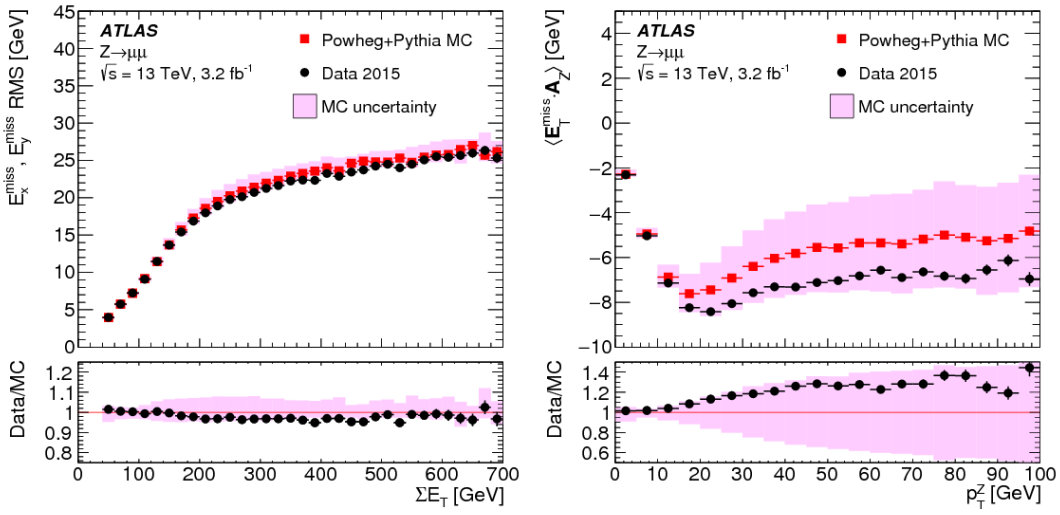

(A) (B)

FIGURE 4.11: Distribution of $E_{\mathrm{T}}^{\mathrm{miss}}$ resolution as a function of $\sum E_T$ and $E_{\mathrm{T}}^{\mathrm{miss}}$ scale as a function of p_{T}^{Z}. The data (black circles) and MC simulation (red squares) are overlaid [89].

CHAPTER 5

Statistical Model

This chapter is devoted to introduce the principles of the statistical treatment of the data used for the analysis. A brief description of the hypothesis test techniques is given, and the Likelihood and profile likelihood ratio functions are defined, which are used widely in particle physics. The concept of p-values and the CL_s method are introduced. Finally, a brief description of the types of fits used in the analysis is given. Details of the use of it and the definition of the likelihood are included in chapters 6 and 7.

5.1 Hypothesis testing

In searches for new phenomena in particle physics, the decision on whether a data sample can be described solely by a known theory like the Standard Model (which will be denoted as *background*) or if there is a contribution from new physics (*signal plus background*) is done by using what in statistics theory is called a *Hypothesis test* [92]. In order to do this, two hypotheses are defined.

- The "null" hypothesis H_0, which represents the possibility of the data being described by the Standard Model (background-only hypothesis).
- The "alternative" hypothesis, H_1, which corresponds to the signal-plus-background hypothesis.

These two hypotheses can be represented in the most simple way by introducing a signal strength parameter μ that multiplies the predicted signal cross-section, where $\mu = 0$ indicates H_0 and the data correspond to a background-only scenario, and $\mu = 1$ corresponds to the signal+background hypothesis H_1 with the predicted cross-section.

The probability density functions (PDF) of the measured variables are different under these two hypotheses, and the objective of the hypothesis test is to decide which of them is more compatible with the data. In order to do this, a variable called *test statistic* is defined, which summarises the data and whose PDF also depends on the hypothesis chosen.

From the test statistic the p-value p_μ can be computed. It gives the probability of the data to have been originated by a certain model with signal strength μ. In the case stated above, for when the background-only hypothesis is the null, the p_0 value is computed. The background-only hypothesis is considered excluded, and thus a *discovery* is claimed when $p_0 \leq 2.9 \cdot 10^{-7}$, which corresponds to a gaussian significance (number of standard deviations corresponding to the p-value) of $Z = 5$. *Evidence for new physics* is announced if $Z \geq 3$, so $p_0 \leq 1.3 \cdot 10^{-3}$.

When the number of events does not exceed the background expectation, the p-value is calculated by taking the signal-plus-background hypothesis as the null hypothesis, and thus it represents the probability of a signal underfluctuation. The p_μ value can be used to decide whether to exclude a signal. However, its use may lead to unphysical exclusions in experiments where the signal and background distributions are not very well separated (low sensitivity to the signal) or in regions of phase space with few events, for which the number of observed events could be a downward fluctuation of the background.

5.2 The CL_s method

The CL_s method [93] is introduced to avoid the exclusion of signals the experiment is not sensitive to. It is defined as a ratio of two probabilities, which are illustrated in figure 5.1:

$$CL_s = \frac{p_\mu}{1 - p_b}, \tag{5.1}$$

Here p_μ represents the compatibility of the data with the signal-plus-background hypothesis, while p_b is the compatibility with the background one. A downward fluctuation will give large values of p_0, increasing the CL_s and preventing the exclusion of the signal. Similarly, if the signal-plus-background $(s + b)$ and background (b) distributions are not very well separated, like in figure 5.1 (B), the value of p_0 will also be large and the signal will not be excluded. If, on the other hand, the experiment is more sensitive (figure 5.1 (A)), the p_0 value will be small and the CL_s will be very similar to p_μ. Since the denominator of equation 5.1 is ≤ 1, the CL_s is always larger and thus more conservative than the p_μ value. The convention is to exclude a signal when $CL_s < 0.05$, i.e. at the 95% confidence level.

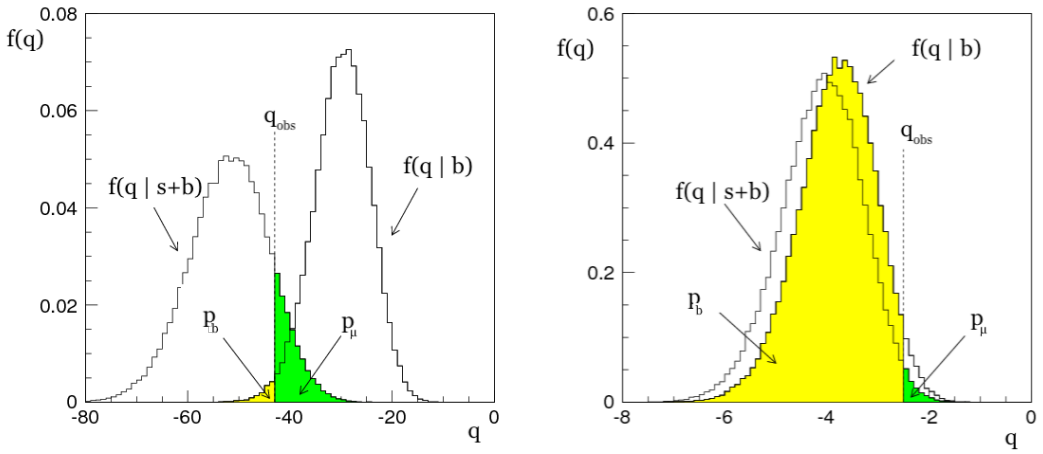

(A) (B)

FIGURE 5.1: Example of p_b and p_μ in two different examples. On the left, the distributions for the two hypotheses are well separated, and the probability of the data to be compatible with the background is very small if the signal+background hypothesis is true. The CL_s value will then be very similar to the p_μ. On the right, however, the sensitivity of the experiment is low to the signal, since the distributions of the test statistic are very similar in the $s + b$ and b hypotheses. The CL_s value will be $CL_s < p_\mu$ [94].

5.3 Likelihood and Profile Likelihood Ratio

The test statistic used in ATLAS searches is a function of a likelihood, which depends on the number of events that satisfy certain criteria. According to the definition of the signal strength μ given above, the number of expected events can be written as

$$n = \mu \cdot s + b, \tag{5.2}$$

where s and b are the number of expected signal and background events, respectively. In general, $s(\theta)$ and $b(\theta)$ can depend on several parameters, called *nuisance parameters*, which define the shape of the PDFs and account for systematic and statistical uncertainties of the measurements. The signal strength parameter is considered the parameter of interest (POI) of the test.

The likelihood function gives the probability that an observation has been originated from a certain model. In general, if a random variable X is described by a PDF $f(\boldsymbol{\theta}|x)$, where $\boldsymbol{\theta}$ is the set of parameters; and N measurements of the variable X have been taken, giving as a result $x_1, x_2, ..., x_N$, the likelihood function

$$L(\theta|x_1, x_2, ..., x_N) = \prod_{i=1}^{N} f(\boldsymbol{\theta}|x_i), \tag{5.3}$$

represents the probability function of the parameters $\boldsymbol{\theta}$ given the measurements of the variable x.

In order to define the profile likelihood ratio and to illustrate its use [95], one can consider an experiment where certain variables are measured and the results are represented in some histograms with N bins: $\boldsymbol{n} = (n_1, n_2, ..., n_N)$. The number of background and signal events expected in each bin is given by

$$E[n_i] = \mu s_i + b_i, \tag{5.4}$$

and the mean value of signal and background events s_i and b_i are calculated from the signal and background PDFs. Assuming that the data follow a Poisson distribution, the likelihood function is the product of the likelihoods in each bin:

$$L(\mu, \boldsymbol{\theta}) = \prod_{i=1}^{m} \frac{(\mu s_i + b_i)^{n_i}}{n_i!} e^{-(\mu s_i + b_i)}. \tag{5.5}$$

Often some extra measurements are performed in order to constrain the NPs. The number of background predicted events, for example, can be measured in a channel where no signal is expected. A similar histogram to equation 5.4 can be constructed $\boldsymbol{N} = (N_1, ..., N_M)$, where the expected values of the bins are

$$E[N_i] = u_i(\boldsymbol{\theta}). \tag{5.6}$$

This kind of measurement provides constraints to the background normalisation as well as the parameters that affect the shape of both signal and background. These constraints are included in the likelihood of equation 5.5 as extra factors

$$L(\mu, \boldsymbol{\theta}) = \prod_{i=1}^{m} \frac{(\mu s_i + b_i)^{n_i}}{n_i!} e^{-(\mu s_i + b_i)} \prod_{j=1}^{M} \frac{u_j^{m_j}}{m_j!} e^{-u_j}. \tag{5.7}$$

This likelihood function is maximised with respect to μ and $\boldsymbol{\theta}$ to construct the profile likelihood ratio, which is used to test a hypothesised value of μ:

$$\lambda(\mu) = \frac{L(\boldsymbol{x}|\mu, \hat{\hat{\boldsymbol{\theta}}}(\mu))}{L(\boldsymbol{x}|\hat{\mu}, \hat{\boldsymbol{\theta}}(\hat{\mu}))}. \tag{5.8}$$

Here $\hat{\theta}$ and $\hat{\mu}$ are the values of the parameters that maximise the likelihood, while $\hat{\hat{\boldsymbol{\theta}}}$ are the values of the nuisance parameters that maximise it for a given test value of μ. If the value of λ is close to 0, the data do not agree very well with the proposed value of μ, while values of λ close to one are a sign that the data agree well with the hypothesis being tested.

The test statistic used in the analysis presented in this thesis is the logarithm of this ratio:

$$t_\mu = -2ln\lambda(\mu) \tag{5.9}$$

where now, the higher the value of t_μ, the bigger the discrepancy between the data and the prediction of the model.

Since the signal is only supposed to increase the number of observed events, the possibility of $\mu < 0$ is not considered in the statistical interpretation of the data as an argument against the background-only hypothesis. To take this into account, a modified version of the profile likelihood ratio is defined for testing the background-only hypothesis

$$q_0 = \begin{cases} -2\ln\lambda(0) & \hat{\mu} \geq 0 \\ 0 & \hat{\mu} < 0 \end{cases} \tag{5.10}$$

In terms of q_0, the p_0 value can be calculated as

$$p_0 = \int_{q_{0,obs}}^{\infty} f(q_0|0) dq_0, \tag{5.11}$$

where $q_{0,obs}$ is the value of the test statistic observed in the data and $f(q_0|0)$ is the PDF of the test statistic under the null hypothesis ($\mu = 0$). It represents thus the probability of the test statistic to have a value higher than the one found in data, i.e. the probability to find a result more incompatible with the background-only hypothesis. In general, the way to determine the shape of f is by generating a large number of random pseudo-experiments under the $\mu = 0$ hypothesis, but in some cases an asymptotic approximation can be used [95], in such a way that one single dataset can substitute the ensemble of simulated datasets.

In the case in which no excess over the background expectation is found, the signal-plus-background hypothesis is used as the new null hypothesis to set upper limits on the signal strength (on the cross section) or exclude the signal. The test statistic in that case is constructed as

$$q_\mu = \begin{cases} -2\ln\lambda(\mu) & \hat{\mu} \leq \mu \\ 0 & \hat{\mu} > \mu \end{cases} \tag{5.12}$$

where now the test statistic is 0 when $\hat{\mu} > \mu$, because an upward fluctuation is not considered as an argument against the signal-plus-background hypothesis. Here again $\hat{\mu}$ represents the value of μ that maximises the likelihood. The p-value in this case is calculated as

$$p_\mu = \int_{q_{\mu,obs}}^{\infty} f(q_\mu|\mu) dq_\mu, \tag{5.13}$$

where $q_{\mu,obs}$ is again the value of the test statistic observed in the data and $f(t_\mu|\mu)$ is the pdf of the test statistic under the assumed value of μ.

The calculation of p_μ introduced in equation 5.13 is used to calculate the CL_s value in equation 5.1, and p_b is defined as

$$p_b = 1 - \int_{q_{\mu,obs}}^{\infty} f(q_\mu|0)dq_\mu. \tag{5.14}$$

5.4 Fit configurations

In practice, a series of requirements are applied to the kinematic variables of the events in the data in order to obtain a sample where a contribution from the signal under study is expected. These requirements result in what is called a *signal region* (SR). Additionally, a set of extra measurements in other *regions* are defined to constrain the expected number of background events and the nuisance parameters. These are control regions (CR), which consist of a set of requirements similar to those in the SR, but ensuring that the expected contribution from the signal is negligible. The number of events in each region is then measured and used to construct the likelihood and the test statistic. Uncertainties in the measurements are taken into account and enter the fit as nuisance parameters that can be modelled in order to find the maximum of the likelihood. Three types of fits are then performed with different purposes, using the HistFitter framework [96], which incorporates the principles introduced above.

- Background-only fit: Only the control regions are used to constrain the nuisance parameters and the background contributions from different processes. Any contribution from the signal is neglected, and normalisation factors for the backgrounds are extracted with their uncertainties. In this way an estimate of the background contribution to the SRs is obtained. The inclusion of the systematic uncertainties in all the regions allows for the correlations between regions to be taken into account. If the number of observed events in the signal regions is compatible with the expectation, signal fits are carried out.

- Model-independent signal fit: The fit is performed without assuming any particular model. Signal and control regions are used to set 95% confidence level upper limits to the visible cross section of a potential signal. Any signal contribution to the CRs is neglected. The observed upper-limit is calculated taking into account the total background prediction after the fit in the signal region with its uncertainty, and the number of observed events. The expected upper limit is in turn calculated only taking into account expected background events in the signal regions.

- Model-dependent signal fit: The signal and control regions are used in the fit. The signal prediction for a given model is also taken into account and compared to the observed events in all regions. The signal is considered excluded when the CL_s value is below the threshold of 0.05. Expected and observed limits are calculated in a similar way as for the model-independent limits. The fit is performed over a number of models with different parameters, which translates into exclusion limits on those parameters, presented in 2-D figures in chapter 7.

CHAPTER 6

Search for the stop squark at $\sqrt{s} = 13$ TeV

Searches for supersymmetry, and in particular third generation squarks (stop and sbottom) in ATLAS are main ingredients of the LHC physics program. In this chapter, the search for the stop squark pair production in all hadronic final states is presented. The results were published in

- *Search for a scalar partner of the top quark in the jets plus missing transverse momentum final state at* $\sqrt{s} = 13$ *TeV with the ATLAS detector* (September 2017, JHEP12 (2017) 085).
- *Search for the Supersymmetric Partner of the Top Quark in the Jets+*$E_{\mathrm{T}}^{\mathrm{miss}}$ *Final State at* $\sqrt{(s)} = 13$ *TeV* (August 2016, ATLAS-CONF-2016-077).

Similar searches at $\sqrt{s} = 8$ and $\sqrt{s} = 13$ TeV have been performed in ATLAS [97, 98, 99, 100, 101] and CMS [102, 103, 104, 105, 106].

The Feynman diagrams of the main processes targeted are shown in figure 6.1, for which a simplified model approach [107] is adopted. In figure 6.1 (A), a pair of stop squarks ($\tilde{t}_1$) is directly produced and decays into a top (t) and a neutralino ($\tilde{\chi}_1^0$), and the top decays hadronically. The decay of the stops into a b quark and a chargino ($\tilde{\chi}_1^{\pm}$) is also studied, as shown in figure 6.1 (B). Finally, figure 6.1 (C) shows the process where the squark pair is produced through gluino ($\tilde{g}$) decay. All these processes have similar final states, characterised by two b-tagged jets, large jet multiplicity and large missing transverse momentum originated by the neutralinos, which are not detected in ATLAS [53, 54, 108, 109].

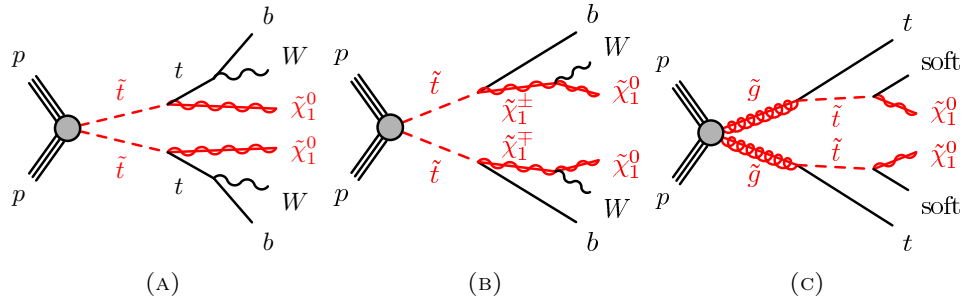

FIGURE 6.1: Feynman diagram for the stop pair production decaying into top and neutralino, where the top decays hadronically (A), stop to b and chargino (B) and gluino mediated stop production (C).

As introduced briefly in chapter 5, the analysis strategy consists on the definition of a signal region, i.e. a set of requirements that are designed to maximise the presence of

signal events and reduce the background from Standard Model processes. In order to set constraints on the estimation of the number of background events that are expected in the signal region, an extra set of regions are defined, control regions, normally one for each of the main background processes. These consist of some selection criteria on the events designed to enhance one of the backgrounds and reduce the signal, while being similar to the signal region. When the control region selections are not close to the signal regions, validation regions are defined, designed to be an intermediate step in the extrapolation and check the agreement of the data with the MC. The background estimation techniques are described in section 6.5.

A profile likelihood function is built as a product of Poisson distribution functions that describe the number of events in the signal and control regions, as presented in chapter 5. The theoretical and experimental systematic uncertainties are included as nuisance parameters. A background-only fit is first performed to constrain the prediction of the background events in the signal regions, and its results are discussed in section 6.7. The results of the background-only fit in the signal regions and the signal fits are presented in chapter 7.

Since the topology and kinematics of the events highly depend on the masses of the supersymmetric particles, a grid of signal samples with different masses are generated, as is described in section 6.1. Different signal regions are designed and optimised for the processes in figure 6.1, and for different masses of the stop and the neutralino particles. The description of the selection applied in these regions is described in section 6.4.

6.1 Data and Monte Carlo samples

The data used for this analysis was collected with the ATLAS detector during 2015 and 2016 in LHC Run 2 at centre-of-mass energy of $\sqrt{s} = 13$ TeV. The total integrated luminosity accumulated after applying quality requirements is 36.1 fb^{-1}.

The main SM background processes and the SUSY signals are estimated using simulated MC samples. The samples were simulated with different generators depending on the background process, as described in the following sections. The propagation of the particles in the ATLAS detector and their interaction with it are simulated using either GEANT4 [110] or a fast simulation. For the latter, the showers in the calorimeters are simulated using a parameterisation and the rest is simulated with GEANT4. The fast simulation is applied to all signal samples, while all background samples use the full GEANT4 set-up. The output format of this simulation is identical as that of the data. The reconstruction is carried out in the same way as done for the data. Pileup is simulated by superimposing simulated minimum bias events to the hard-scattering ones in all the MC samples. The minimum bias events are simulated using Pythia8 and the MSTW 2008 PDF set [111]. The MC events were then reweighted to match the pileup to what is observed in data. A detailed description of the ATLAS simulation chain can be found in [112].

6.1.1 Z+jets and W+jets samples

Background samples for Z+jets and W+jets processes were generated using SHERPA 2.2.1 [38] and the NNPDF3.0NNLO [113] PDF set. They are generated in non-overlapping slices depending on the boson p_{T} and the presence of light, c- and b-quarks, with up to five additional partons in the matrix element (three leading jets at NLO and two additional at LO). The samples are normalised to the NNLO cross section.

6.1.2 Top samples

Top-pair production and single top samples were simulated with POWHEG-BOX 2 [114] and interfaced with PYTHIA6 [36] for parton shower and hadronization using the CT10 PDF set [115], and the PERUGIA2012 [116] set of tuned shower and underlying event parameters. The $t\bar{t}$ samples are normalised to NNLO cross section, while for single top NLO cross sections are used. More information can be found in [117].

6.1.3 Other Background samples

Samples for $t\bar{t}+Z/W/\gamma$ are generated using MG5_AMC@NLO [118] interfaced with PYTHIA8 [37] for hadronization and parton shower. They are generated at NLO with the NNPDF3.0 PDF set and normalised to NLO cross sections.

Diboson samples are generated with SHERPA 2.1 using the CT10 PDF set [119]. The details of the generation depend on the process. Fully leptonic processes are generated with up to 3 additional partons in the final state. The 4ℓ and $2\ell 2\nu$ processes include NLO ME calculations with up to one additional parton, while all the rest of the leptonic processes only include NLO ME calculations for the inclusive process, with all the rest of the parton configurations at LO level. Electroweak diboson processes are generated at LO accuracy with up to one extra parton in the final state. Loop-induced diboson processes of the form $gg \to VV$ are generated using `OpenLoops` with one additional parton in the final state. Finally, semileptonic processes are generated with up to three additional partons in the final state. The ZZ processes include NLO calculations of the ME for up to one additional parton in the final state, while WW and WZ processes have NLO calculations only for the inclusive process, with all the other configurations at LO.

6.1.4 Signal samples

Signal models allow only one or two decay modes. The samples are generated using MG5_AMC@NLO interfaced with PYTHIA8 for the parton shower and hadronization, and with EVTGEN 1.2.0 [120] for the c- and b-hadron decays. The matrix element is calculated at leading order including up to two extra partons emitted. The PDF set used is NNPDF2.3LO, and the parton shower matching is done with the CKKW-L [121] method, and all signal cross sections are calculated at NLO in the strong coupling constant.

For $\tilde{t}_1 \to t\tilde{\chi}_1^0$ models, a branching fraction of 100% is assumed to generate a grid of models with different stop and neutralino masses, where stop masses go from 100 to 1300 GeV and neutralino masses range between 1 and 600 GeV. Models where the top decays to b and chargino ($\tilde{t}_1 \to b\tilde{\chi}_1^{\pm}$) are also generated, assuming that $m(\tilde{\chi}_1^{\pm}) = \cdot m(\tilde{\chi}_1^0) + 1$ GeV. The mass of the stop ranges in this case from 400 GeV to 800, and the neutralino from 50 to 300 GeV. Mixed scenarios are also considered, where one of the stops decays to top and neutralino and the other one to bottom and chargino, with the same assumption for the mass. The range of masses used in this case is 450 GeV $< m(\tilde{t}_1) <$ 1000 GeV and 50 GeV $< m(\tilde{\chi}_1^0) <$ 400 GeV. Three-body-decay models are used for the region where the mass difference between stop and neutralino is not enough to produce a top, and the stop decays directly to a b-quark, a W-boson and a neutralino.

For the gluino-mediated models, the stop mass is assumed to be $m(\tilde{t}_1) = m(\tilde{\chi}_1^0)+5$ GeV, so that the other products of the stop decay are soft and out of acceptance. The gluino mass range generated goes from 1500 GeV to 2000 GeV, while the stop mass goes from 300 to 1400 GeV.

6.2 Object definitions

In this section, the definitions of jets, electrons, muons, $E_{\mathrm{T}}^{\mathrm{miss}}$ and b-jets used in the search are given. The reconstruction of such objects is described in detail in Chapter 4. Jets, b-jets and missing transverse energy are used for the selection of signal events, whereas leptons are used in the control region selection and to veto electroweak processes in the signal regions.

- **Jets:** Jets are reconstructed and calibrated as described in Section 4.4 with the anti-k_T algorithm with a radius parameter of $R = 0.4$. Calibrated jets are required to have at least $p_{\mathrm{T}} > 20$ GeV and $|\eta| < 2.8$. Additional requirements to discriminate the jets originating from pileup are applied to jets with $p_{\mathrm{T}} < 60$ and $|\eta| < 2.4$ using the Jet Vertex Tagger method [122] (JVT). The selection makes use of the ratio between the scalar sum of p_{T} of the tracks associated with a given jet and with the primary vertex, and the scalar sum of p_{T} of all the tracks associated with a jet to identify pileup jets.

- **Electrons:** Electrons are reconstructed as described in Section 4.2. They are required to have $p_{\mathrm{T}} > 7$ GeV and $|\eta| < 2.47$. Electrons can sometimes be misidentified as jets, and a procedure is applied to remove the overlap between the jet and the electron candidates. If the separation between an electron and a jet is below $\Delta R < 0.2$, the object is considered to be an electron and removed from the list of jets. If, on the other hand, the separation satisfies $0.2 < \Delta R < 0.4$, the object is assumed to be a jet and removed from the electron list. The electrons used in the control samples are additionally required to have $p_{\mathrm{T}} > 20$ GeV, and pass the tight identification criteria, as well as isolation requirements such that the isolation efficiency for electrons of $p_{\mathrm{T}} = 25$ GeV is 95% and for $p_{\mathrm{T}} = 60$ the efficiency is 99%.

- **Muons:** Muons are reconstructed as described in section 4.3 and are required to have $p_{\mathrm{T}} > 6$ GeV and $|\eta| < 2.7$. As with electrons, a procedure to remove the overlap between muons and jets is applied. In this case, if the distance between a muon candidate and a jet is $\Delta R < 0.4$, the muon is removed. Events containing muons identified as originated from cosmic rays are removed. Muons used in the control background samples are in addition required to have $p_{\mathrm{T}} > 20$ and to pass medium quality selection and isolation criteria equivalent to that of electrons.

- **Missing transverse energy:** The $\boldsymbol{p_{\mathrm{T}}}^{\mathrm{miss}}$ is reconstructed as described in section 4.6. The missing transverse momentum in the tracking system only ($\boldsymbol{p_{\mathrm{T}}}^{\mathrm{miss,track}}$) is also used. It is calculated as the negative sum of all the reconstructed tracks with $p_{\mathrm{T}} > 400$ MeV associated with the primary vertex.

- **B-jets:** B-tagged jets are identified as described in section 4.5. The algorithm used is MV2c10, with an average efficiency of 77%. A rejection factor of 130 is achieved for jets originated from light quarks and gluons, and 6 for jets from charm quarks.

- **τ-veto:** Most signal regions include a veto to τ leptons. In these cases, every event in which a non b-tagged jet with less than 4 associated tracks and within $|\eta| < 2.5$ has azimuthal distance to the $E_{\mathrm{T}}^{\mathrm{miss}}$ smaller than $\pi/5$ is rejected.

6.3 Trigger strategy

Different trigger selections are applied to the signal regions and the control samples in the analysis. In all the signal regions a calorimeter $E_{\mathrm{T}}^{\mathrm{miss}}$ trigger is used, and a requirement $E_{\mathrm{T}}^{\mathrm{miss}} > 250$ GeV is applied to ensure full efficiency of this trigger. The $t\bar{t}$, single top and W control regions use the same trigger. This guarantees a similar selection in the control and signal regions.

Control regions designed for Z+jets background are characterised by low $E_{\mathrm{T}}^{\mathrm{miss}}$, and therefore the $E_{\mathrm{T}}^{\mathrm{miss}}$ trigger can not be used. Instead, events are required to pass electron or muon triggers. Electron triggers are based on the presence of clusters in the electromagnetic calorimeters that are matched to a track in the inner detector. Muon triggers are based on reconstructed tracks in the MS and the ID. Muons and electrons in the control regions are required to have $p_{\mathrm{T}} > 28$ GeV for the lepton trigger to be fully efficient. The lepton triggers are also used in the control region for $t\bar{t} + \gamma$, where a lepton is required and low $E_{\mathrm{T}}^{\mathrm{miss}}$ is expected.

6.4 Signal Region definitions

Signal regions are a collection of selection criteria chosen to maximise the presence of a potential SUSY signal, and minimise the SM background. The remaining background expected composition is dominated by $t\bar{t}$, Z+jets and $t\bar{t}+Z$ processes. The final state of the signal processes considered is characterised by multiple jets, at least one of which is b-tagged, no leptons, and large missing transverse energy that arises from the LSPs. These and other requirements are included in a common preselection applied to all the signal regions that are summarised in table 6.1 and briefly described in the following:

- At least four jets with $p_{\mathrm{T}} > 80, 80, 40, 40$ GeV, since the jets in the signal events are more energetic than in the backgrounds.
- At least one b-tagged jet.
- No electrons and no muons.
- Missing transverse energy larger than 250 GeV. This requirement helps discriminating against $t\bar{t}$ events and multijet background.
- A minimum azimuthal separation between the two leading jets (the two with highest p_{T}) and the missing transverse momentum of 0.4 is required. This condition helps rejecting events with mismeasured $E_{\mathrm{T}}^{\mathrm{miss}}$ coming from multijet and $t\bar{t}$.
- The $E_{\mathrm{T}}^{\mathrm{miss}}$ calculated from the tracking system only is required to be > 30 GeV and an extra requirement on its azimuthal separation with the $\boldsymbol{p_{\mathrm{T}}}^{\mathrm{miss}}$ as calculated from all the calibrated physics objects is set as $|\Delta\phi(\boldsymbol{p_{\mathrm{T}}}^{\mathrm{miss}}, \boldsymbol{p_{\mathrm{T}}}^{\mathrm{miss,track}})| < \pi/3$. A misalignment between them is likely originated from pileup or jet mismeasurements, and this requirement guarantees coherence between the tracking and calorimeter information in the event.

Several sets of signal regions are defined and described in the following. Signal regions SRA, SRB and SRC are designed to target processes with $\tilde{t}_1 \to t\tilde{\chi}_1^0$, shown in figure 6.1 (A). The final state consists of two top quarks and large $E_{\mathrm{T}}^{\mathrm{miss}}$. The signal regions are optimised independently, since they target different scenarios regarding the masses of the SUSY particles. SRA targets processes with large mass splitting

Preselection
$N_b \geq 1$
$N_{jet} \geq 4$
$N_\ell = 0$
jet $p_{\mathrm{T}} > (80, 80, 40, 40)$ GeV
$E_{\mathrm{T}}^{\mathrm{miss}} > 250$ GeV
$\lvert\Delta\phi(\boldsymbol{p_{\mathrm{T}}}^{\mathrm{miss}}, \mathrm{jet}^{0,1})\rvert > 0.4$
$E_T^{\mathrm{miss,track}} > 300$ GeV
$\lvert\Delta\phi(\boldsymbol{p_{\mathrm{T}}}^{\mathrm{miss,track}}, \boldsymbol{p_{\mathrm{T}}}^{\mathrm{miss}})\rvert < \pi/3$

TABLE 6.1: Summary of the common preselection required in all the signal regions.

between the stop and the neutralino, SRB targets moderate $\Delta m(\tilde{t}_1, \tilde{\chi}_1^0)$ scenarios, and SRC is designed for the cases close to the diagonal in the stop-neutralino mass plane, where $\Delta m(\tilde{t}_1, \tilde{\chi}_1^0) \sim m_t$. SRD is optimised for direct stop pair production where both stops decay through a b quark and a chargino $\tilde{t}_1 \to b\tilde{\chi}_1^{\pm}$, shown in figure 6.1 (B). The final state in this case contains two b-quarks and large missing energy. SRE is designed to target processes where the stops are produced through gluino decays, figure 6.1 (C). The final state contains as well two top quarks and large missing energy, where the tops are very energetic.

The main background process after applying the selection is, in most of the signal regions, Z+jets. In SRC, $t\bar{t}$ is the main background, being also an important contribution to the rest of the regions. In addition, $t\bar{t} + Z$, W+jets and Single Top production constitute a non-negligible fraction of the SM background contribution in most of the regions.

6.4.1 SRA

SRA targets models where directly produced stop pairs decay through a top and a neutralino with a large mass difference between the SUSY particles $\Delta m(\tilde{t}_1, \tilde{\chi}_1^0) \gg m_t$. It is optimised for $m_{\tilde{t}} = 1000$ GeV and $m_{\tilde{\chi}_1^0} = 1$ GeV.

In this scenario, since the mass of the stop squark is much bigger than the top and the neutralino masses, the top quark is boosted. This means that the decay products of the top may produce jets that are not very separate from each other and thus not resolved into separate jets. The technique used to reconstruct the top consists on applying the anti-k_T algorithm [79] described in section 4.4, using as an input the reconstructed anti-k_T jets with $R = 0.4$ and reclustering them into *fat jets* with radius parameters of $R = 0.8$ and $R = 1.2$. The masses of the reclustered jets ($m_{R=1.2}^{0,1}$) are used as discriminating variables.

The signal regions are divided in three categories depending on the number of reconstructed $R = 1.2$ reclustered jets that are compatible with a top decay.

- The *TT category* requires two reconstructed tops, i.e. two $R = 1.2$ reclustered jets with masses above 120 GeV.
- The *TW category* requires one reconstructed top and one reconstructed W boson, i.e., masses above 120 and 60 GeV for the leading and subleading reclustered $R = 1.2$ jets, respectively.

- The *T0 category* only requires one reconstructed top, i.e. the mass of the second fat jet is below 60 GeV.

The events classified in the three categories are used for optimisation individually, since the background composition varies from one another, having thus 3 SRA *subregions*.

The main discriminating variable against $t\bar{t}$ background is the $E_{\mathrm{T}}^{\mathrm{miss}}$. In $t\bar{t}$ events it comes from jet mismeasurements, and leptonically decaying tops where the lepton is misidentified or is a tau that decays hadronically. Tight cuts are thus applied to the $E_{\mathrm{T}}^{\mathrm{miss}}$, requiring it to be larger than 400, 500 and 550 GeV for the TT, TW and T0 categories, respectively. Additional requirements are placed to reject leptonically decaying tops. Events containing a tau lepton are identified and rejected using the definition introduced in section 6.2. The transverse mass calculated from the closest b-jet to the $E_{\mathrm{T}}^{\mathrm{miss}}$ in ϕ and the $\boldsymbol{p_{\mathrm{T}}}^{\mathrm{miss}}$ is required to be larger than 200:

$$m_T^{b,min} = \sqrt{2p_T^b \cdot E_{\mathrm{T}}^{\mathrm{miss}}[1 - cos\Delta\phi(\boldsymbol{p_{\mathrm{T}}}^b, \boldsymbol{p_{\mathrm{T}}}^{\mathrm{miss}})]} > 200\mathrm{GeV}. \tag{6.1}$$

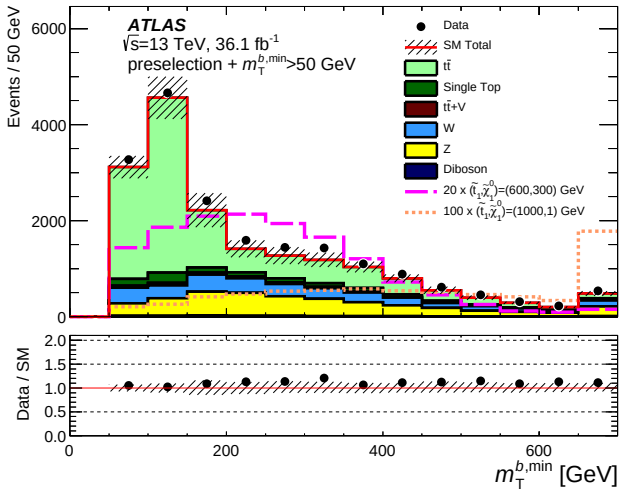

FIGURE 6.2: Distribution of $m_T^{b,min}$ after applying preselection shown in table 6.1. The coloured histograms show the SM backgrounds and the black dots the data. the signal contributions have been multiplied by a factor to make them visible. The Data/SM plot show the agreement of the data with the total SM prediction. The uncertainty band includes systematic and statistical uncertainties.

The distribution of the $m_T^{b,min}$ variable after applying the preselection cuts is shown in figure 6.2. In $t\bar{t}$ events the average value of the $m_T^{b,min}$ is lower than the top mass, and therefore the cut at 200 GeV removes most of the $t\bar{t}$ background.

Further requirements are applied to the variable m_{T2} as defined in [123, 124], which is defined as a variation of the transverse mass calculated from the $\boldsymbol{p_{\mathrm{T}}}^{\mathrm{miss}}$ and two reconstructed tops. The reconstructed tops used for this calculation are built using a sequential χ^2 method [125]. First, pairs of non-b-tagged jets or single jets are used to build a W candidate, minimising the function $(m_{candidate} - m_W)^2/m_W$. Then, they are combined with a b-quark to form a top candidate with a reconstructed mass as close to the true top mass as possible. From these reconstructed tops, the m_{T2} variable is calculated as

$$m_{T2} = \min_{\boldsymbol{p_{\mathrm{T}}}^{\chi 1} + \boldsymbol{p_{\mathrm{T}}}^{\chi 2} = \boldsymbol{p_{\mathrm{T}}}^{\mathrm{miss}}} \{\max[m_T^2(\boldsymbol{p_{\mathrm{T}}}^{t_1}, \boldsymbol{p_{\mathrm{T}}}^{\chi_1}), m_T^2(\boldsymbol{p_{\mathrm{T}}}^{t_2}, \boldsymbol{p_{\mathrm{T}}}^{\chi_2})]\}, \tag{6.2}$$

where the minimisation is done over all possible combinations of the $\boldsymbol{p_T}$ of the two neutralinos such that the sum is the observed $\boldsymbol{p_T}^{\text{miss}}$, and the $\boldsymbol{p_T}^{t_{1,2}}$ are the $\boldsymbol{p_T}$ of the reconstructed top quarks. The value of m_{T2} has as limit the mass of the stop particle, and is always lower than it. This variable is required to be larger than 400 GeV for the TT and TW categories, and larger than 500 GeV for T0.

Finally, the distance between the two b-tagged jets is required to be larger than 1 in the TT category, to reject events where two b-jets may come from a gluon.

SRA			
Variable	**TT**	**TW**	**T0**
N_b		≥ 2	
$m^0_{R=1.2}$		> 120 GeV	
$m^1_{R=1.2}$	> 120 GeV	[60,120] GeV	< 60 GeV
$m_T^{b,min}$		> 200 GeV	
τ-veto		yes	
$\lvert\Delta\phi(\text{jet}^{0,1,2}, \boldsymbol{p_T}^{\text{miss}})\rvert$		>0.4	
$m^0_{R=0.8}$		> 60 GeV	
m_{T2}	> 400 GeV	> 400 GeV	> 500 GeV
$E_{\text{T}}^{\text{miss}}$	> 400 GeV	> 500 GeV	> 550 GeV
$\Delta R(b,b)$	> 1	-	

TABLE 6.2: Selection criteria for SRA in addition to the common preselection described in table 6.1

A summary of the SRA selection by categories is given in table 6.2.

The expected background composition in SRA is summarised in table 6.3. The expected number of signal events is also shown for the benchmark point used for optimisation: $m_{\tilde{t}_1} = 1000$ GeV and $m_{\tilde{\chi}^0_1} = 1$ GeV. The main background contributions in SRA come from Z+jets, with a significant amount of $t\bar{t} + Z/W$ events, especially in SRA-TT. As anticipated, the background composition changes significantly in the different categories.

	SRA-TT	**SRA-TW**	**SRA-T0**	**SRB-TT**	**SRB-TW**	**SRB-T0**
$t\bar{t}$	0.6 ± 0.1	0.45 ± 0.12	1.45 ± 0.31	6.09 ± 0.59	12.80 ± 1.03	47.19 ± 1.79
Z+jets	2.15 ± 0.27	4.20 ± 0.50	8.62 ± 0.65	7.71 ± 0.66	14.36 ± 1.07	1.03 ± 0.56
W+jets	0.65 ± 0.16	0.70 ± 0.20	1.58 ± 0.47	6.12 ± 2.74	3.83 ± 0.62	20.40 ± 3.15
$t\bar{t} + Z/W$	2.46 ± 0.28	1.43 ± 0.21	2.02 ± 0.21	7.25 ± 0.50	8.37 ± 0.51	15.92 ± 0.62
SingleTop	1.03 ± 0.55	0.60 ± 0.15	2.52 ± 1.02	3.59 ± 0.64	5.09 ± 0.46	22.43 ± 1.59
Dibosons	0.00	0.35 ± 0.25	0.00	0.13 ± 0.13	0.60 ± 0.35	1.30 ± 0.56
Total MC	6.88 ± 0.70	7.72 ± 0.65	16.20 ± 1.35	30.89 ± 2.99	45.05 ± 1.78	160.57 ± 4.53
Signal	8.21 ± 0.37	4.61 ± 0.27	6.43 ± 0.33	20.42 ± 1.05	25.96 ± 1.13	43.54 ± 1.39

TABLE 6.3: Expected background events in SRA and SRB. The signal benchmark for SRA is $m_{\tilde{t}_1} = 1000$ GeV and $m_{\tilde{\chi}^0_1} = 1$ GeV, while for SRB $m_{\tilde{t}_1} = 600$ GeV and $m_{\tilde{\chi}^0_1} = 300$ GeV is shown. Only statistical uncertainties are taken into account in the MC prediction.

6.4.2 SRB

SRB is optimised for the process $\tilde{t_1} \rightarrow t\tilde{\chi}_1^0$ with moderate $\Delta m(\tilde{t_1}, \tilde{\chi_1^0})$. It makes use of some of the variables already described for SRA, and it is also optimised separately for the TT, TW and T0 categories. In this case, lower $E_{\mathrm{T}}^{\mathrm{miss}}$ is expected, since the mass difference between the top and stop is not as high as for the SRA target models, and therefore the neutralinos are less boosted. The cuts on $m_T^{b,min}$ and $|\Delta\phi(\mathrm{jet}^{0,1,2}, \boldsymbol{p_{\mathrm{T}}}^{\mathrm{miss}})|$ are the same as in SRA, and the τ-veto is also applied. However, no selection is applied on m_{T2} and the $E_{\mathrm{T}}^{\mathrm{miss}}$ cut is kept at 250 as in the preselection. In addition, the $\Delta R(b,b)$ requirement is applied now to all the categories and raised to $\Delta R(b,b) > 1.2$. An extra variable is considered, $m_T^{b,max}$, defined in the same way as $m_T^{b,min}$ but using the b-jet farthest from the $\boldsymbol{p_{\mathrm{T}}}^{\mathrm{miss}}$ instead of the closest. A common cut to all the categories at 200 GeV is applied. A summary of the SRB selection is shown in table 6.4. The expected background composition and signal events for the benchmark signal point $m_{\tilde{t_1}} = 600$ GeV and $m_{\tilde{\chi_1^0}} = 300$ can be seen in table 6.3. In contrast with SRA, in SRB $t\bar{t}$ contribution becomes more significant, while Z+jets is still an important background.

SRB			
Variable	**TT**	**TW**	**T0**
N_b		≥ 2	
$m^0_{R=1.2}$		> 120 GeV	
$m^1_{R=1.2}$	> 120 GeV	[60,120] GeV	< 60 GeV
$m_T^{b,min}$		> 200 GeV	
τ-veto		yes	
$\lvert\Delta\phi(\mathrm{jet}^{0,1,2}, \boldsymbol{p_{\mathrm{T}}}^{\mathrm{miss}})\rvert$		>0.4	
$m_T^{b,max}$		> 200 GeV	
$\Delta R(b,b)$		> 1.2	

TABLE 6.4: Selection applied in SRB in addition to the preselection in table 6.1

6.4.3 SRC

SRC targets processes where the stop decays via $\tilde{t}_1 \rightarrow t\tilde{\chi}_1^0$ and the mass difference between the stop and the neutralino is of the order of the top mass. This means that the top quarks produced in the processes are not boosted. Additionally, the neutralino is not boosted either, resulting in events with lower $E_{\mathrm{T}}^{\mathrm{miss}}$, and much more difficult to distinguish from the background. In this type of scenario, events with a strong jet (or several jets) from initial state radiation (ISR) are used, so that the stop pair is produced recoiling against it [126, 127, 128] and is therefore boosted. However, the identification of the ISR objects of the event is not straightforward, since a jet coming from the stop decay is not different from an ISR one. The technique used for such identification is the *recursive jigsaw* technique [126], where the objects are clustered together based on their proximity in the phase space by minimising the transverse masses of the two systems: the ISR system and the products of the stop pair decay, or the *sparticle system*. The masses of the invisible particles (neutralinos) are approximated to zero for this process. In this way, the event is divided in two hemispheres in the transverse plane. The ratio of the $E_{\mathrm{T}}^{\mathrm{miss}}$ to the ISR p_{T} in the centre

of mass system is proportional to the ratio of the neutralino and stop masses

$$R_{\mathrm{ISR}} \equiv \frac{E_{\mathrm{T}}^{\mathrm{miss}}}{p_{\mathrm{T}}^{\mathrm{ISR}}} \sim \frac{m_{\tilde{\chi}_1^0}}{m_{\tilde{t}_1}}. \tag{6.3}$$

The kinematic variables of both the sparticle system and the ISR can be defined according to the classification of the objects into the two systems, and are used for the selection applied in SRC.

	SRC				
Variable	**SRC1**	**SRC2**	**SRC3**	**SRC4**	**SRC5**
N_b			≥ 1		
N_b^S			≥ 1		
N_{jet}^S			≥ 5		
$p_{\mathrm{T},b}^{0,S}$			> 40 GeV		
m_S			> 300 GeV		
$\Delta\phi(\mathrm{ISR}, \boldsymbol{p_{\mathrm{T}}}^{\mathrm{miss}})$			> 3.0		
$p_{\mathrm{T}}^{\mathrm{ISR}}$			> 400 GeV		
$p_{\mathrm{T}}^{4,S}$			> 50 GeV		
R_{ISR}	0.3-04	0.4-0.5	0.5-0.6	0.6-0.7	0.7-0.8

TABLE 6.5: SRC selection in addition to the preselection in 6.1. The superindeces S correspond to the variables of the sparticle system, while ISR is for the initial state radiation.

The requirements applied to SRC are summarised in table 6.5. The events are divided in five non-overlapping regions according to the value of R_{ISR}. At least five jets where at least one of them is b-tagged in the sparticle system are required. The p_{T} of the fifth leading jet in the sparticle system has to be larger than 50 GeV, and the leading b-jet p_{T} is required to be higher than 40 GeV. The transverse mass calculated from the sparticle system and the $E_{\mathrm{T}}^{\mathrm{miss}}$, represented by m_S, must be larger than 300 GeV, and the p_{T} f the ISR system must be greater than 400 GeV. The angular ϕ separation between the ISR system and the $\boldsymbol{p_{\mathrm{T}}}^{\mathrm{miss}}$ has to be larger than 3.

The expected number of background events is shown in table 6.6. The signal yields for the point $m_{\tilde{t}_1} = 300$ GeV and $m_{\tilde{\chi}_1^0} = 127$ GeV are also shown. As anticipated, the dominant background is $t\bar{t}$, and the rest of the background contributions are negligible compared to it.

	SRC1	**SRC2**	**SRC3**	**SRC4**	**SRC5**
$t\bar{t}$	18.19 ± 1.57	31.20 ± 1.82	20.62 ± 1.07	6.95 ± 0.46	0.89 ± 0.24
Z+jets	0.46 ± 0.09	0.90 ± 0.13	0.74 ± 0.15	0.45 ± 0.09	0.09 ± 0.03
W+jets	0.64 ± 0.13	1.53 ± 0.31	1.51 ± 0.37	1.53 ± 0.41	0.17 ± 0.09
$t\bar{t} + Z/W$	0.22 ± 0.10	0.46 ± 0.19	0.44 ± 0.11	0.07 ± 0.08	0.05 ± 0.03
SingleTop	1.44 ± 0.51	1.02 ± 0.19	1.04 ± 0.41	0.62 ± 0.17	0.00
Dibosons	0.39 ± 0.28	0.21 ± 0.21	0.28 ± 0.28	0.00	0.00
Total MC	21.34 ± 1.69	35.30 ± 1.88	24.64 ± 1.25	9.61 ± 0.65	1.12 ± 0.36
Signal	30.68 ± 4.17	72.20 ± 7.29	14.80 ± 2.56	0.80 ± 0.57	0.55 ± 0.39

TABLE 6.6: Expected background events in SRC. The yields for the signal point $m_{\tilde{t}_1} = 300$ GeV and $m_{\tilde{\chi}_1^0} = 127$ GeV are shown. Only statistical uncertainties are taken into account in the MC prediction.

6.4.4 SRD

The process $\tilde{t}_1 \rightarrow b\tilde{\chi}_1^{\pm}$ is targeted with SRD. Two non-orthogonal subregions are defined separately, SRD-high and SRD-low, in order to cover a wider phase space. The selection criteria are presented in table 6.7. SRD-high is optimised for $m_{\tilde{t}_1} = 700$ GeV and $m_{\tilde{\chi}_1^0} = 100$ GeV, while SRD-low for $m_{\tilde{t}_1} = 400$ GeV and $m_{\tilde{\chi}_1^0} = 50$ GeV. At least 5 jets are required, two of which must be b-tagged. The p_{T} of the two leading jets is required to be larger than 150 GeV; the third leading jet is required to have $p_{\mathrm{T}} > 100$ GeV for SRD-low and $p_{\mathrm{T}} > 80$ GeV for SRD-high, and the fourth leading p_{T} is required to be greater than 60 GeV. The variables $m_T^{b,min}$ and $m_T^{b,max}$ are also used in the selection, requiring $m_T^{b,min} > 250$ GeV and and $m_T^{b,max} > 300$ GeV in SRD-low and $m_T^{b,min} > 350$ GeV and $m_T^{b,max} > 450$ GeV in SRD-high. The sum of the p_{T} of the two leading b-jets is required to be > 300 and > 400 GeV in SRD-low and SRD-high respectively.

SRD		
Variable	**SRD-low**	**SRD-high**
$\lvert\Delta\phi(\mathrm{jet}^{0,1,2}, \boldsymbol{p_{\mathrm{T}}}^{\mathrm{miss}})\rvert$	> 0.4	
N_b	≥ 2	
$DeltaR(b,b)$	> 0.8	
$p_{\mathrm{T}}^{0,b} + p_{\mathrm{T}}^{1,b}$	> 300GeV	> 400GeV
τ-veto	yes	
p_{T}^1	> 150 GeV	
p_{T}^3	> 100 GeV	> 80 GeV
p_{T}^4	> 60 GeV	
$m_T^{b,\mathrm{min}}$	> 250 GeV	> 350 GeV
$m_T^{b,\mathrm{max}}$	> 300 GeV	> 450 GeV

TABLE 6.7: Selection criteria for SRD in addition to the preselection described in table 6.1.

The expected background composition in SRD-low and SRD-high is shown in table 6.8. The signal shows the expected events from the benchmarks used for optimisation. The biggest background contribution comes from Z+jets, and the composition varies noticeably from SRD-low to SRD-high, especially in the case of the contribution from W+jets background.

6.4.5 SRE

SRE is designed to target models where a pair of gluinos is produced in the collision, which decay to a stop and a top particles. The mass splitting between the stop and the neutralino in the phase space considered is very low, and thus the stop decays into neutralino and a very soft jet that is not reconstructed. The two tops in the final state come directly from the gluino decay, which is massive, and are therefore boosted. For this reason this region is also sensitive to direct stop production models with very high $\Delta m(\tilde{t}_1, \tilde{\chi}_1^0)$.

It is optimised for $m_{\tilde{g}} = 1700$ GeV, $m_{\tilde{t}_1}$=400 GeV and $m_{\tilde{\chi}_1^0} = 395$ GeV. The selection applied is summarised in table 6.9. In this case, the masses of the two leading reclustered jets with $R = 0.8$ are used, since the jets are expected to be more collimated than in previous models. They are required to be higher than 120 and 80 GeV, and $m_T^{b,\mathrm{min}}$ must be larger than 200 GeV. The $E_{\mathrm{T}}^{\mathrm{miss}}$ is expected to be high in

	SRD-low	**SRD-high**
$t\bar{t}$	3.43 ± 0.37	1.04 ± 0.20
Z+jets	6.67 ± 0.44	3.10 ± 0.27
W+jets	4.78 ± 2.68	0.84 ± 0.16
$t\bar{t} + Z/W$	3.06 ± 0.31	1.06 ± 0.15
Single Top	3.30 ± 0.47	1.30 ± 0.22
Dibosons	0.00	0.00
Total MC	21.25 ± 2.80	7.34 ± 0.46
Signal	33.33 ± 6.07	10.49 ± 1.15

TABLE 6.8: Expected background events in SRD. The yields for the signal points $m_{\tilde{t}_1} = 400$ GeV, $m_{\tilde{\chi}_1^\pm} = 100$ GeV, and $m_{\tilde{\chi}_1^0} = 50$ GeV, and $m_{\tilde{t}_1} = 700$ GeV, $m_{\tilde{\chi}_1^\pm} = 200$ GeV, and $m_{\tilde{\chi}_1^0} = 100$ GeV are shown for SRD-low and SRD-high, respectively. Only statistical uncertainties are taken into account in the MC prediction.

this model, and the requirement is set on 550 GeV. The variable H_T is also used for selection, defined as the scalar sum of the p_{T} of all the jets in the event. It is used to calculate the $E_{\mathrm{T}}^{\mathrm{miss}}$ significance, defined as the ratio between the $E_{\mathrm{T}}^{\mathrm{miss}}$ and the square root of H_T. The requirements applied are $H_T > 800$ GeV and $E_{\mathrm{T}}^{\mathrm{miss}}/\sqrt{H_T} > 18\sqrt{GeV}$.

Variable	**SRE**
$\lvert\Delta\phi(\mathrm{jet}^{0,1,2}, \boldsymbol{p_{\mathrm{T}}}^{\mathrm{miss}})\rvert$	> 0.4
N_b	≥ 2
$m^0_{R=0.8}$	> 120 GeV
$m^1_{R=0.8}$	> 80 GeV
$m_T^{b,\mathrm{min}}$	> 200 GeV
$E_{\mathrm{T}}^{\mathrm{miss}}$	> 550 GeV
H_T	> 800 GeV
$E_{\mathrm{T}}^{\mathrm{miss}}/\sqrt{H_T}$	$> 18\ \sqrt{\mathrm{GeV}}$

TABLE 6.9: Selection criteria for SRE in addition to the preselection described in table 6.1.

The expected background composition in SRE is shown in table 6.10. The expected signal events for $m_{\tilde{g}} = 1700$ GeV and $m_{\tilde{t}_1} = 400$, with $m_{\tilde{\chi}_1^0} = 395$ are shown. The most significant background contribution to this signal region is Z+jets.

6.5 Background estimation

As it was introduced before, the main background process in SRA, SRB, SRD and SRE is $Z \to \nu\nu$ production in association with jets. In SRC, the major background is $t\bar{t}$ and the contributions of the rest of the backgrounds are negligible. The $t\bar{t}$ background process also represents a significant contribution to SRA, SRB, SRD and SRE, where one of the W bosons decays leptonically and the lepton is misidentified as a jet. Other important processes are $W \to \ell\nu$+jets and single top production, and the irreducible background of $t\bar{t}$+Z/W, which is dominated by $t\bar{t}$+Z, where the Z decays to neutrinos. The contributions of the mentioned background processes are estimated by comparing the data and the simulation in regions where no signal is expected. Control regions are defined with this aim, as mentioned before.These CRs are used to normalise the

	SRE
$t\bar{t}$	0.21 ± 0.06
Z+jets	1.15 ± 0.18
W+jets	0.42 ± 0.13
$t\bar{t} + Z/W$	0.69 ± 0.13
Single Top	0.56 ± 0.14
Dibosons	0.00
Total MC	3.02 ± 0.30
Signal	9.49 ± 0.15

TABLE 6.10: Expected background events in SRE. The yields for the signal point $m_{\tilde{g}} = 1700$ GeV and $m_{\tilde{t}_1} = 400$ are also shown. Only MC statistical uncertainties are included.

simulation to the data, obtaining a factor for each background contribution, which is then used in the signal regions, extrapolating the normalisation. The control regions are designed with a similar selection as the SR to minimise the systematic uncertainties in the extrapolation. The statistical uncertainties are reduced by ensuring enough data events in the control regions (enough statistics). In this way, the estimated number of events from a certain background process in a signal region can be estimated by a transfer factor:

$$N_{\text{bkg}}^{\text{SR}} = N_{\text{bkg,MC}}^{\text{SR}} \cdot \frac{N_{\text{data}}^{\text{CR}} - N_{\text{bkg(others),MC}}^{\text{CR}}}{N_{\text{bkg,MC}}^{\text{CR}}}, \tag{6.4}$$

where $N_{\text{bkg,MC}}^{\text{SR}}$ is the number of events of the background under study in the SR in MC, $N_{\text{data}}^{\text{CR}}$ is the number of data events in the CR, $N_{\text{bkg(others),MC}}^{\text{CR}}$ is the number of events in MC from all other backgrounds in the CR, and $N_{\text{bkg,MC}}^{\text{CR}}$ is the number of MC events of the background in the CR.

The normalisation factor that is applied to the MC prediction is in reality extracted in a simultaneous fit with all the control regions, so that the contamination from all processes is taken into account in all the regions. This technique requires that all signal and validation regions are orthogonal to the control regions, i.e. that there are no events shared among them. This is ensured in most cases by inverting some of the selection criteria. The simultaneous fit technique will be described in chapter 7.

When the control region topology is farther from that of the signal regions, validation regions are defined. These are not required to have as many events as the control regions, and constitute an intermediate step between the control and the signal region definitions. They are used to validate the background extrapolation towards the signal region, checking that the predicted number of events using the normalisation factor from the control regions agrees with what is found in data.

Detailed descriptions of the control regions for the different backgrounds are given in the following. The control regions for $t\bar{t}$ are separated for each of the signal regions defined in the previous section. Control regions for $Z \to \nu\nu$ background are also defined separately for all SRs, except for SRC, where the Z background is negligible. The single top, W+jets and $t\bar{t} + Z/W$ backgrounds are estimated in control regions that are common for all SRs. Validation regions for the control regions that require it are also described in the corresponding sections in the following.

6.5.1 $t\bar{t}$ background

The main background process in SRC and one of the most important in all the rest of the SRs is $t\bar{t}$ production. Dedicated control regions for $t\bar{t}$ background are defined for each of the signal regions. All of them include in the selection one lepton (electron or muon) and use a $E_{\mathrm{T}}^{\mathrm{miss}}$ trigger as in the SRs. At least four jets are required with $p_{\mathrm{T}} > (80, 80, 40, 40)$ GeV, where the lepton is counted as a jet, to emulate the hadronic τ-decay in the signal regions. At least two b-jets are required, and the transverse mass calculated from the $\boldsymbol{p_{\mathrm{T}}}^{\mathrm{miss}}$ and the lepton and the distance between the b-jet and the lepton are used in the selection, in order to make the events compatible with a semileptonic top decay. The rest of the selection is specific to each signal region to have a close topology. A summary of the top control regions is given in tables 6.11 for top control regions for SRA and SRB (CRTA, CRTB), 6.14 for CRTC, and 6.15 for CRTD and CRTE.

The number of background expected events and data events in the $t\bar{t}$ control regions can be found in tables 6.12 and 6.13. The purity of $t\bar{t}$ events varies between 84% in CRTC and 95% in CRTB-T0. Some distributions in the $t\bar{t}$ control regions are shown in figures 6.3-6.7. The agreement is generally good before the fit.

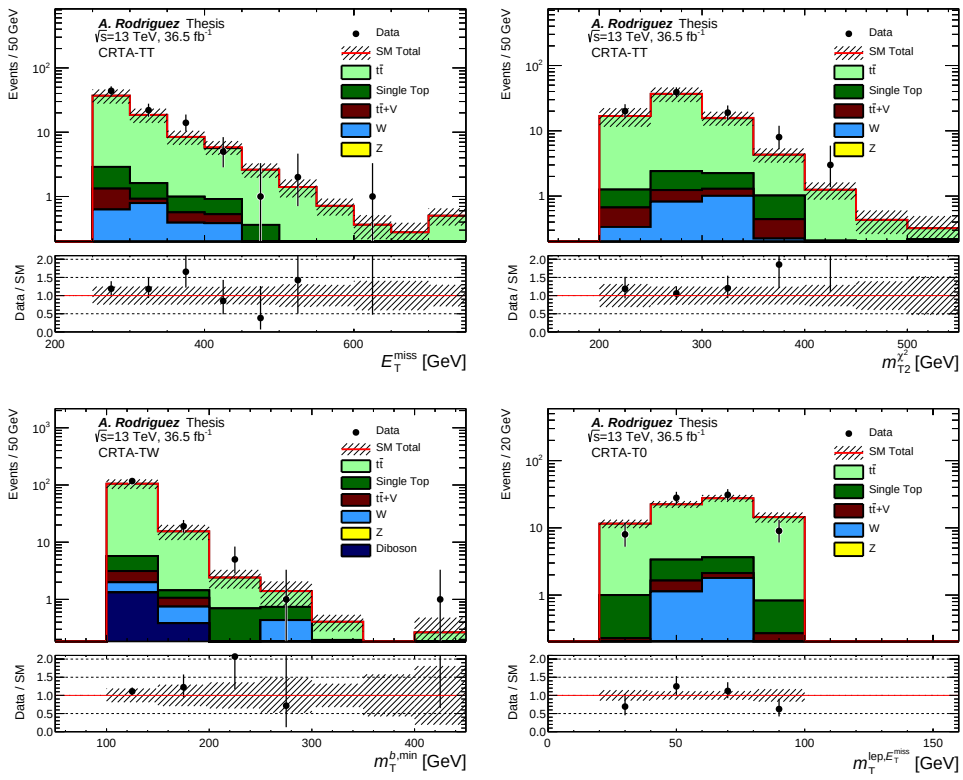

FIGURE 6.3: Distributions of (A) $E_{\mathrm{T}}^{\mathrm{miss}}$ for CRTATT, (B) m_{T2} for CRTATT, (C) $m_T^{b,\mathrm{min}}$ for CRTATW and (D) $m_T(\boldsymbol{p_{\mathrm{T}}}^{\mathrm{miss}}, \ell)$ in CRTAT0. The data and MC events are superimposed, and statistical and systematic uncertainties are shown.

Validation regions are defined to test the extrapolation of some of the variables to the signal regions. For SRA and SRB, a validation region is defined for each category. For SRC, SRD and SRE one $t\bar{t}$ validation region is defined for each case.

Variable	CRTA-TT	CRTA-TW	CRTA-T0	CRTB-TT	CRTB-TW	CRTB-T0
Trigger	$E_{\mathrm{T}}^{\mathrm{miss}}$					
N_ℓ	1					
p_{T}^{ℓ}	> 20 GeV					
N_j	≥ 4 (including lepton)					
jet p_{T}	$> (80, 80, 40, 40)$ GeV					
N_b	≥ 2					
$\lvert\Delta\phi(\mathrm{jet}^{0,1,2}, \boldsymbol{p_{\mathrm{T}}}^{\mathrm{miss}})\rvert$	> 0.4					
$m_T(\ell, E_{\mathrm{T}}^{\mathrm{miss}})$	$[30, 100]$ GeV					
$m_T^{b,\mathrm{min}}$	> 100 GeV					
$\Delta R(b, \ell)$	< 1.5					
$m_{R=1.2}^{0}$	> 120 GeV					
$m_{R=1.2}^{1}$	> 120 GeV	$[60, 120]$ GeV	< 60 GeV	> 120 GeV	$[60, 120]$ GeV	< 60 GeV
$m_{R=0.8}^{0}$	> 60 GeV			-		
$E_{\mathrm{T}}^{\mathrm{miss}}$	> 250 GeV	> 300 GeV	> 350 GeV	> 250 GeV		
$\Delta R(b, b)$	> 1	-		> 1.2		
$m_T^{b,\mathrm{max}}$	-			> 200 GeV		

TABLE 6.11: Selection in the control region for ttbar (CRT) for signal regions A and B. Dedicated regions are defined for each signal regions and divided in categories as in the signal regions.

	CRTA-TT	CRTA-TW	CRTA-T0	CRTB-TT	CRTB-TW	CRTB-T0
$t\bar{t}$	68.09 ± 2.33	116.40 ± 2.20	74.97 ± 1.30	63.09 ± 2.21	262.49 ± 4.60	423.18 ± 5.73
Z+jets	0.02 ± 0.01	0.01 ± 0.01	0.00	0.02 ± 0.01	0.01 ± 0.01	0.18 ± 0.15
W+jets	2.60 ± 0.41	1.57 ± 0.54	2.41 ± 0.87	3.27 ± 0.75	3.59 ± 1.04	4.37 ± 0.97
$t\bar{t} + Z/W$	1.32 ± 0.20	1.50 ± 0.19	2.41 ± 0.87	1.20 ± 0.20	2.78 ± 0.27	3.05 ± 0.28
Single Top	3.54 ± 0.42	4.27 ± 0.87	3.85 ± 0.70	3.83 ± 0.34	9.26 ± 1.19	13.48 ± 1.20
Dibosons	0.00	1.70 ± 1.35	0.00	0.00	1.58 ± 1.34	0.46 ± 0.36
Total MC	75.55 ± 2.41	125.45 ± 2.78	82.14 ± 1.72	71.42 ± 2.37	279.70 ± 5.05	444.72 ± 5.95
Data	89.00 ± 9.43	143.00 ± 11.96	76.00 ± 8.72	86.00 ± 9.27	275.00 ± 16.58	417.00 ± 20.42

TABLE 6.12: Number of expected and observed events in the $t\bar{t}$ control regions for SRA and SRB.

	CRTC	CRTD	CRTE
$t\bar{t}$	652.85 ± 7.66	137.84 ± 3.34	42.44 ± 1.82
Z+jets	1.84 ± 0.26	0.09 ± 0.06	0.02 ± 0.01
W+jets	51.34 ± 2.62	$, 4.05 \pm 0.53$	1.71 ± 0.31
$t\bar{t} + Z/W$	8.78 ± 0.56	2.21 ± 0.22	0.84 ± 0.16
Single Top	54.53 ± 2.49	14.69 ± 2.03	1.98 ± 0.43
Dibosons	7.58 ± 2.06	1.32 ± 1.32	1.46 ± 1.33
Total MC	776.91 ± 8.74	160.20 ± 4.16	48.46 ± 2.32
Data	611.00 ± 24.72	157.00 ± 12.53	50.00 ± 7.07

TABLE 6.13: Number of expected and observed events in the $t\bar{t}$ control regions for SRC, SRD and SRE.

The complete selection applied in the validation regions for $t\bar{t}$ background for SRA and SRB is described in table 6.16, and for SRC, SRD and SRE in 6.17

6.5.2 Z+jets background

The $Z(\rightarrow \nu\nu)$+jets process is the main background contribution in most of the signal regions. Since $Z \rightarrow \nu\nu$ is very similar to the signal, it is also difficult to isolate it. In

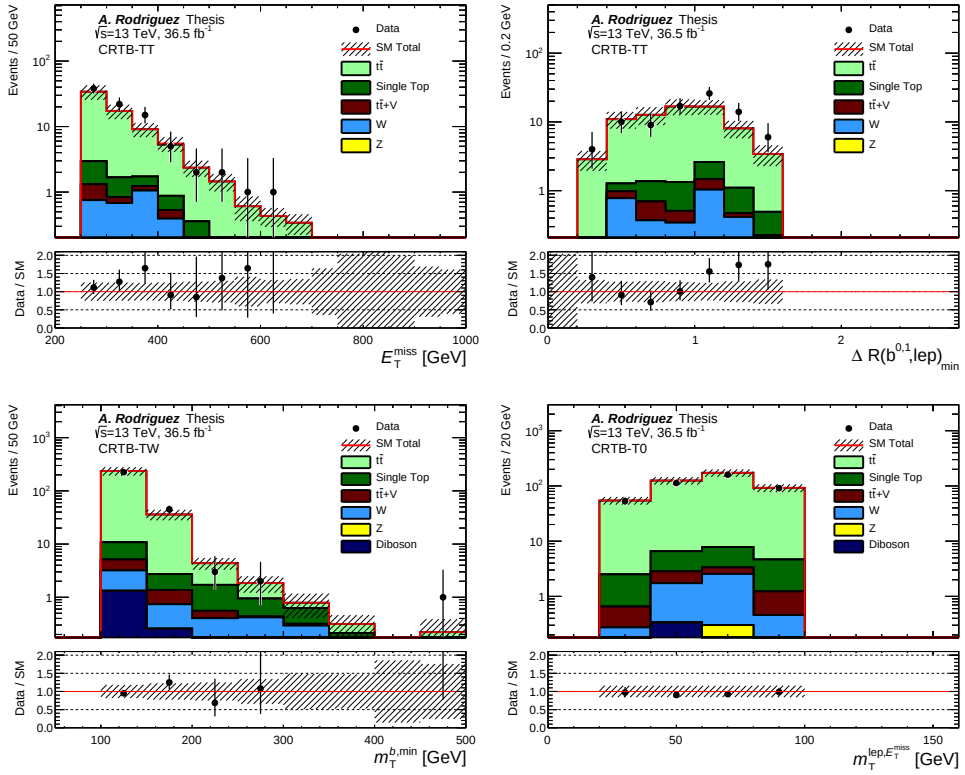

FIGURE 6.4: Distributions of (A) $E_{\mathrm{T}}^{\mathrm{miss}}$ for CRTBTT, (B) $\Delta R(b, \ell)$ for CRTBTT, (C) $m_T^{b,\mathrm{min}}$ for CRTBTW and (D) $m_T(\boldsymbol{p_{\mathrm{T}}}^{\mathrm{miss}}, \ell)$ in CRTBT0. The data and MC events are superimposed, and statistical and systematic uncertainties are shown.

Variable	CRTC selection
Trigger	$E_{\mathrm{T}}^{\mathrm{miss}}$
N_ℓ	1
N_b^S	≥ 1
p_{T}^ℓ	> 20 GeV
N_j^S	≥ 5 (including lepton)
jet p_{T}	$> (80, 80, 40, 40)$ GeV
$\lvert\Delta\phi(\mathrm{jet}^{0,1}, \boldsymbol{p_{\mathrm{T}}}^{\mathrm{miss}})\rvert$	> 0.4
$m_T(\ell, E_{\mathrm{T}}^{\mathrm{miss}})$	< 100 GeV
$\Delta R(b, \ell)$	<2
$E_{\mathrm{T}}^{\mathrm{miss}}$	> 250 GeV
$p_{\mathrm{T}}^{\mathrm{ISR}}$	> 450 GeV
$p_{\mathrm{T}}^{4,S}$	> 40 GeV

TABLE 6.14: Selection criteria for the $t\bar{t}$ control region for SRC (CRTC).

order to estimate its contribution, control regions are designed by enhancing $Z \to \ell\ell$ processes, which have a very similar topology and good statistics, and then the results are extrapolated to the 0-lepton scenario. Validation regions are defined to test the extrapolation. The selection in all Z control regions includes thus two opposite-charge leptons (electrons or muons), which are required to have $p_{\mathrm{T}} > 28$ GeV to be above the lepton trigger full-efficiency threshold. In order to mimic the behaviour of $Z \to \nu\nu$ processes, the leptons are treated as invisible in the $E_{\mathrm{T}}^{\mathrm{miss}}$ calculation, in such a way

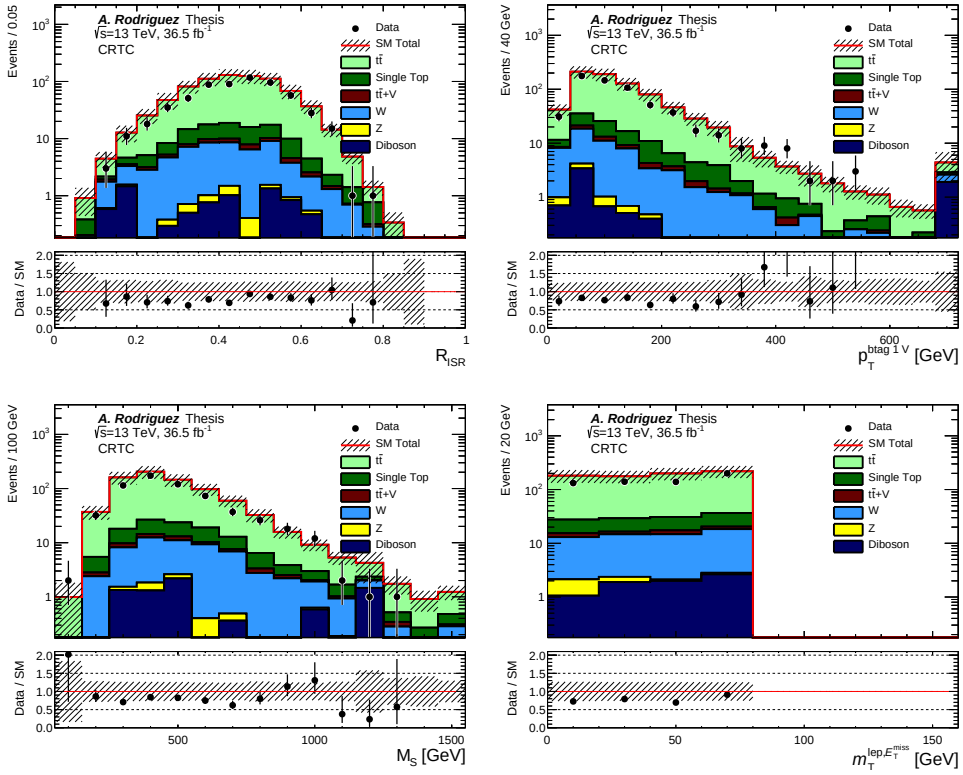

FIGURE 6.5: Distributions of (A) R_{ISR}, (B) p_{T}^{0b}, (C) m_S and (D) $m_T(\boldsymbol{p_{\mathbf{T}}}^{\mathrm{miss}}, \ell)$ in CRTC. The data and MC events are superimposed, and statistical and systematic uncertainties are shown.

Variable	**CRTD**	**CRTE**
Trigger	$E_{\mathrm{T}}^{\mathrm{miss}}$	
N_ℓ	1	
N_b^S	≥ 2	
p_{T}^{ℓ}	>20 GeV	
N_j^S	≥ 4 (including lepton)	
jet p_{T}	$>(80, 80, 40, 40)$ GeV	
$\lvert\Delta\phi(\mathrm{jet}^{0,2}, \boldsymbol{p_{\mathbf{T}}}^{\mathrm{miss}})\rvert$	>0.4	
$m_T(\ell, E_{\mathrm{T}}^{\mathrm{miss}})$	$[30, 100]$ GeV	
$\Delta R(b, \ell)$	<1.5	
$E_{\mathrm{T}}^{\mathrm{miss}}$	>250 GeV	
$m_T^{b,\mathrm{min}}$	>100 GeV	
$m_{R=0.8}^{0}$	-	>120 GeV
$m_{R=0.8}^{1}$	-	>80 GeV
$\Delta R(b, b)$	>0.8	-
$m_T^{b,\mathrm{max}}$	>100 GeV	-
jet p_{T}	$>(150, 15080, 80)$ GeV	-
$p_{\mathrm{T}}^{b,0} + p_{\mathrm{T}}^{b,1}$	>300 GeV	-
H_T	-	>500 GeV

TABLE 6.15: Selection criteria for the $t\bar{t}$ control region for SRD and SRE (CRTD, CRTE).

that the $E_{\mathrm{T}}^{\mathrm{miss}}$ is recalculated by vectorially summing the lepton p_{T} to the $\boldsymbol{p_{\mathbf{T}}}^{\mathrm{miss}}$. All the quantities that depend on the $E_{\mathrm{T}}^{\mathrm{miss}}$ are recalculated with the modified $E_T^{miss'}$.

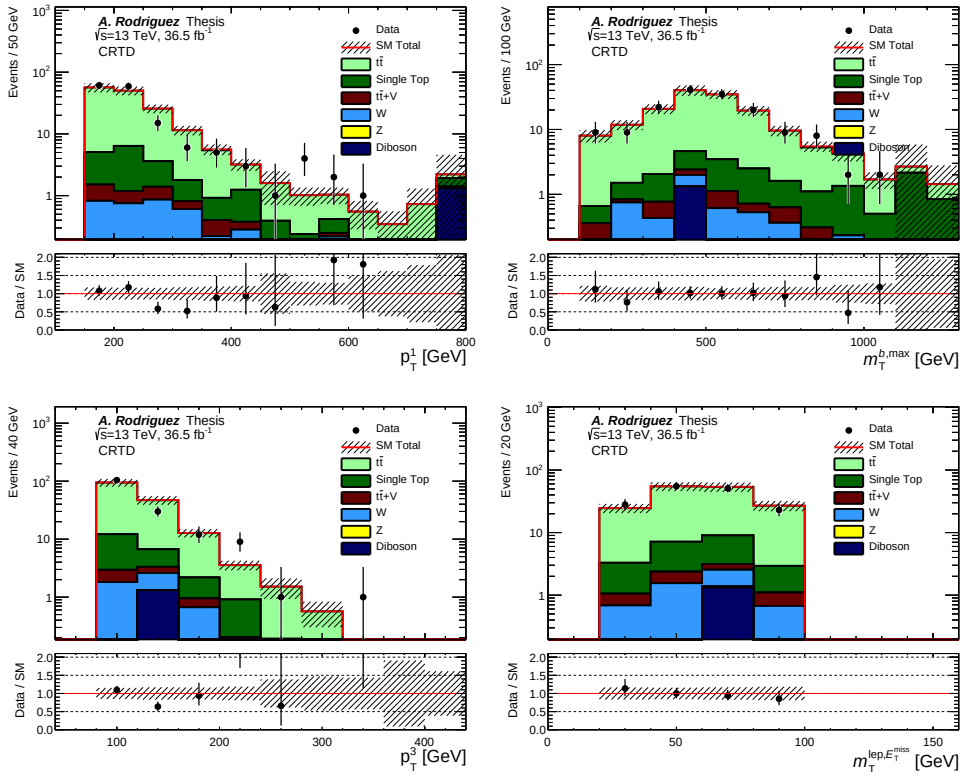

FIGURE 6.6: Distributions of (A) p_{T}^{0}, (B) $m_{T}^{b,\mathrm{max}}$, (C) p_{T}^{1} and (D) $m_{T}(\boldsymbol{p_{\mathrm{T}}}^{\mathrm{miss}}, \ell)$ in CRTD. The data and MC events are superimposed, and statistical and systematic uncertainties are shown.

	Variable	TT	TW	T0
	$m^{0}_{R=1.2}$	>120 GeV		
	$m^{1}_{R=1.2}$	>120 GeV	[60,120] GeV	<60 GeV
	$m_{T}^{b,\mathrm{min}}$	[100,200] GeV	[140,200] GeV	[160,200] GeV
	N_b	≥ 2		
A	$m^{0}_{R=0.8}$	>60 GeV		
	$\Delta R(b,b)$	>1	-	
	$E_{\mathrm{T}}^{\mathrm{miss}}$	>300 GeV	>400 GeV	>450 GeV
B	$\Delta R(b,b)$	>1.2		
	$m_{T}^{b,\mathrm{max}}$	>200 GeV		

TABLE 6.16: Selection applied for the $t\bar{t}$ validation regions for SRA and SRB, classified by categories.

The selection criteria applied in the CRZ regions are summarised in table 6.18. A window of 10 GeV in the invariant mass of the two leptons around the mass of the Z boson is selected to enhance the $Z \to \ell\ell$ process and reduce the presence of other backgrounds. At least four jets are required to have a similar topology as in the signal regions, and specific requirements are applied to each of the regions dedicated to the different SRs. One CRZ is dedicated to SRA-TT, SRA-TW, SRB-TT and SRB-TW, a different one is defined to estimate Z background in SRA-T0 and SRB-T0, and CRZD and CRZE are defined to be used in SRD and SRE, respectively. No control region is used in SRC, since the Z+jets background constitutes a negligible contribution.

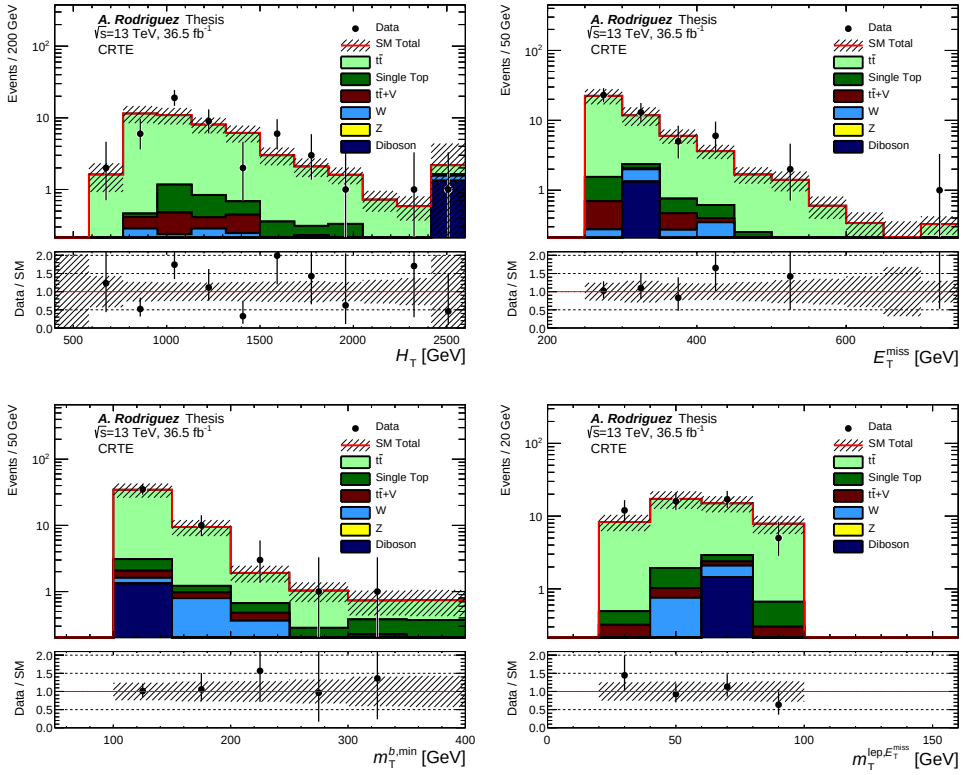

FIGURE 6.7: Distributions of (A) Ht, (B) $E_{\mathrm{T}}^{\mathrm{miss}}$, (C) $m_T^{b,\mathrm{min}}$ and (D) $m_T(\boldsymbol{p_{\mathrm{T}}}^{\mathrm{miss}}, \ell)$ in CRTE. The data and MC events are superimposed, and statistical and systematic uncertainties are shown.

	VRTC	**VRTD**	**VRTE**
$m_T^{b,\mathrm{min}}$	-	[100,200] GeV	
N_j	≥ 4	≥ 5	≥ 4
N_b	≥ 1	≥ 2	
$p_{\mathrm{T}}^{\mathrm{ISR}}$	≥ 400 GeV	-	
jet p_{T}^S	$> (40, 40, 40, 40)$	-	
m_S	> 100 GeV	-	
m_V/m_S	< 0.6	-	
$\Delta\phi(\mathrm{ISR}, \boldsymbol{p_{\mathrm{T}}}^{\mathrm{miss}})$	< 3	-	
$\Delta R(b,b)$	-	> 0.8	-
$m_T^{b,\mathrm{max}}$	-	> 300 GeV	-
jet p_{T}	-	$> (150, 150, 80, 80)$	-
$p_{\mathrm{T}}^{b,0} + p_{\mathrm{T}}^{b,1}$	-	> 300 GeV	-
$\tau-$veto	-	yes	-
$m^0_{R=0.8}$	-		> 120 GeV
$m^0_{R=0.8}$	-		> 80 GeV

TABLE 6.17: Selection criteria applied in the validation regions for $t\bar{t}$ background used in signal regions C, D and E.

The expected background contributions with the Z+jets control region selections are shown in table 6.19. The purity of Z+jets processes varies between 73 and 82%. Some distributions of data and MC before the fit are shown in figures 6.8-6.10. The

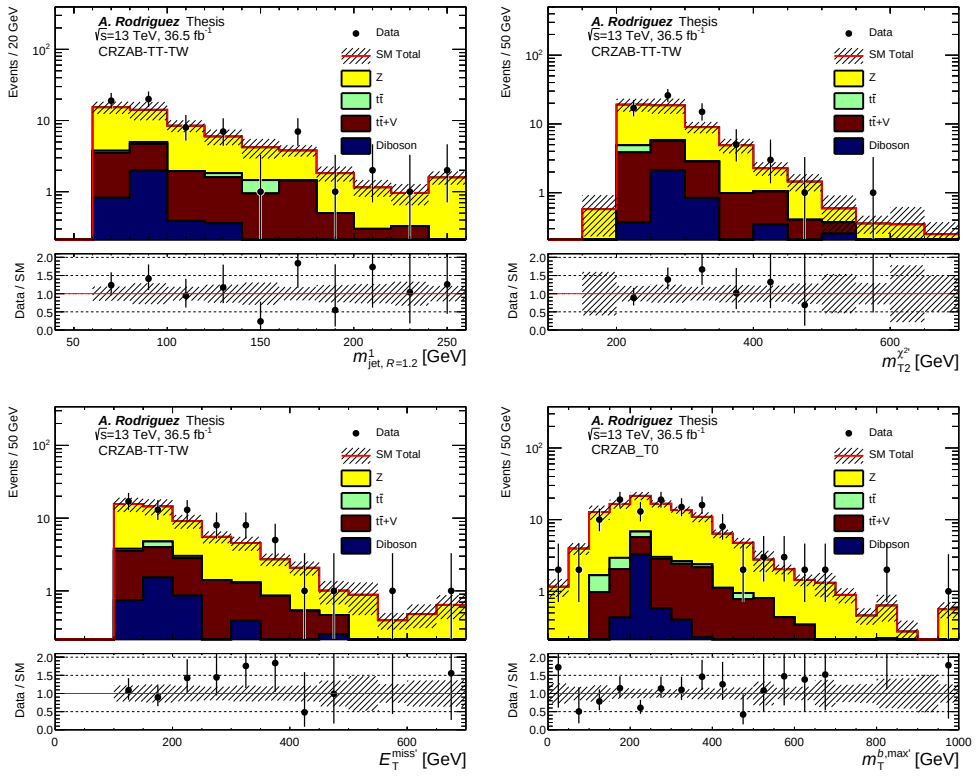

FIGURE 6.8: Distributions of $m^0_{R=1.2}$ (top left), m_{T2} (top right) and $E_T^{\text{miss}'}$ in CRZAB-TT-TW (bottom left) and $m_T^{b,\max'}$ (bottom right) in CRZAB-T0. The MC and data are superimposed, and the ratio of data to MC prediction is shown in the Data/MC. Statistical and systematic uncertainties are shown.

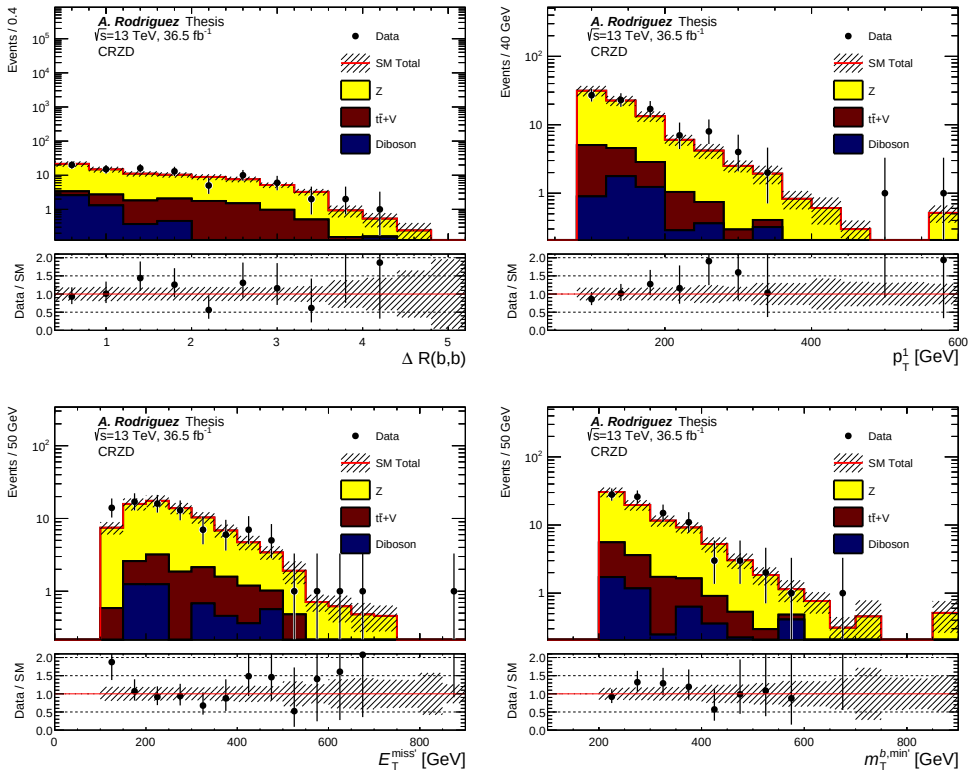

FIGURE 6.9: Distributions of $\Delta R(b,b)$ (top left), subleading jet p_{T} (top right),$E_T^{\mathrm{miss}'}$ (bottom left) and $m_T^{b,\mathrm{min}'}$ (bottom right) in CRZD. The MC and data are superimposed, and the ratio of data to MC prediction is shown in the Data/MC. Statistical and systematic uncertainties are shown.

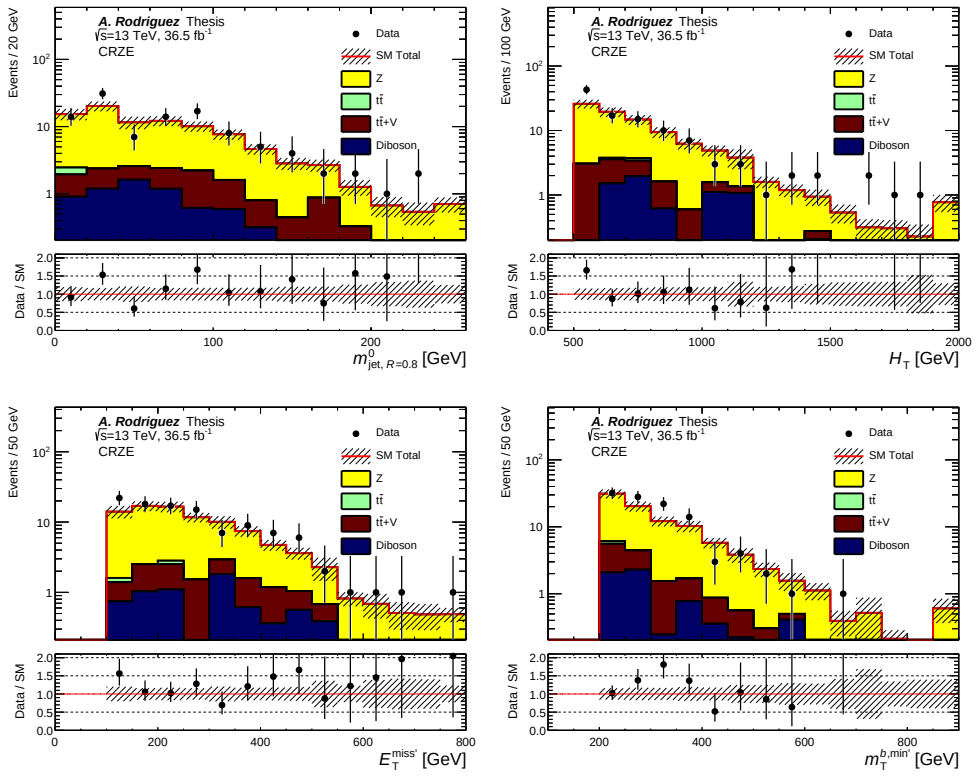

FIGURE 6.10: Distributions of $m^0_{R-0.8}$ (top left), H_T (top right),$E_T^{\mathrm{miss}'}$ (bottom left) and $m_T^{b,\mathrm{min}'}$ (bottom right) in CRZE. The MC and data are superimposed, and the ratio of data to MC prediction is shown in the Data/MC. Statistical and systematic uncertainties are shown.

Variable	CRZAB-TT-TW	CRZAB-T0	CRZD	CRZE
Trigger	electron or muon			
N_ℓ	2 (opposite charge, same flavor)			
p_{T}^{ℓ}	> 28 GeV			
$m_{\ell\ell}$	[86,96] GeV			
N_j	≥ 4			
jet p_{T}	$> (80, 80, 40, 40)$ GeV			
$E_{\mathrm{T}}^{\mathrm{miss}}$	< 50 GeV			
$E_T^{miss'}$	> 100 GeV			
N_b	≥ 2			
$m^0_{R=1.2}$	> 120 GeV		-	
$m^1_{R=1.2}$	> 60 GeV	< 60 GeV	-	
$m_T^{b,\mathrm{min}'}$	-		> 200 GeV	
$m_T^{b,\mathrm{max}'}$	-		> 200 GeV	-
H_T	-			> 500 GeV

TABLE 6.18: Selection criteria for the Z+jets control regions.

	CRZAB-TT-TW	CRZAB-T0	CRZD	CRZE
$t\bar{t}$	1.08 ± 0.56	4.28 ± 1.06	0.00	0.52 ± 0.37
Z+jets	44.03 ± 1.34	90.702.01	69.56 ± 1.69	74.19 ± 1.65
W+jets	0.00	0.00	0.00	0.00
$t\bar{t} + Z/W$	11.76 ± 0.30	11.75 ± 0.29	10.07 ± 0.27	9.20 ± 0.27
Single Top	0.00	0.00	0.00	0.00
Dibosons	3.51 ± 1.06	5.75 ± 1.6	4.99 ± 1.15	6.62 ± 1.60
Total MC	60.38 ± 1.83	112.47 ± 2.83	84.62 ± 2.06	90.53 ± 2.34
Data	74.00 ± 8.60	126.00 ± 11.22	90.00 ± 9.49	107.00 ± 10.34

TABLE 6.19: Expected and observed number of events in the Z+jets control regions. Only statistical uncertainties shown.

agreement between data and prediction is in general good.

Three different validation regions are used for the Z+jets background, one for SRA and SRB, one for SRD, and one for SRE. All of them have a 0-lepton selection, and the preselection for the signal regions in table 6.1 is applied. The selection is listed in table 6.20.

6.5.3 Single Top, W+jets, $t\bar{t} + Z$ and Diboson backgrounds

The Single Top background is estimated using a control region common for all SRs, where one lepton, four jets and two b-jets are required. The ΔR between the two b-jets is used to reject some of the $t\bar{t}$ process. The transverse mass calculated from the $E_{\mathrm{T}}^{\mathrm{miss}}$ and the lepton is used to select events where they come from a W decay. Requirements on the $E_{\mathrm{T}}^{\mathrm{miss}}$, $m_T^{b,\mathrm{min}}$ and $m^0_{R=1.2}$ are also placed to ensure a similar selection to that in the SRs.

Another significant background is W+jets. It is estimated using a common CR for all SRs, where one lepton, at least four jets and exactly one b-jet are required. The transverse mass calculated from the $E_{\mathrm{T}}^{\mathrm{miss}}$ and the lepton is used, and an upper cut is set to the $m^0_{R=1.2}$.

Finally, the $t\bar{t}+Z/W$ process is a very significant background in most of the signal regions. It is dominated by $t\bar{t} + Z(\rightarrow \nu\nu)$, and in order to estimate its contribution, a control region for common use in all SRs is designed. Since it is a very difficult process

Variable	VRZAB	VRZD	VRZE
jet p_{T}	$> (80, 80)$ GeV	$> (150, 80)$ GeV	$> (80, 80)$ GeV
N_j	≥ 4	≥ 5	≥ 4
N_b	≥ 2		
τ-veto	yes		no
$m_T^{b,\mathrm{min}}$	> 200 GeV		
$m^0_{R=1.2}$	< 120 GeV	-	
$\Delta R(b, b)$	< 1	< 0.8	< 1
$m_T^{b,\mathrm{max}}$	-	> 200 GeV	-
H_T	-		> 500 GeV
$E_{\mathrm{T}}^{\mathrm{miss}}/H_T$	-		$> 14\ \sqrt{\mathrm{GeV}}$
$m^0_{R=0.8}$	-		< 120 GeV

TABLE 6.20: Selection criteria for Z+jets validation regions, in addition to the preselection in table 6.1

to isolate, it is estimated from $t\bar{t} + \gamma$, where the photon emulates the Z. The $E_{\mathrm{T}}^{\mathrm{miss}}$ is modified by adding the photon to the $\boldsymbol{p_{\mathrm{T}}}^{\mathrm{miss}}$ in a similar way as it is done with the leptons in the CRZs, and all the quantities depending on the met are recalculated. One lepton is required to remove the contamination from γ+jets processes with $p_{\mathrm{T}} > 28$ GeV to be above the lepton trigger threshold, and the photon is required to have $p_{\mathrm{T}} > 150$ GeV. At least four jets and two b-jets are also required.

The selection criteria for single top, W and $t\bar{t} + \gamma$ control regions is described in table 6.21, and the expected and observed events in CRW, CRST and CRTTGamma are shown in table 6.22. The purity of the W+jets, single top and $t\bar{t}$+γ control regions is of 60, 44 and 87%, respectively. Figures 6.11-6.13 show data-MC comparisons in these regions. The agreement is generally good.

The contribution of the diboson background to all of the signal regions is negligible, and thus no control region is designed for it. The MC samples are used to predict the contribution to the signal regions instead.

Variable	CRW	CRST	CRttγ
Trigger	$E_{\mathrm{T}}^{\mathrm{miss}}$		electron or muon
N_ℓ	1		
p_{T}^{ℓ}	> 20 GeV		> 28 GeV
N_γ	-		1
p_{T}^{γ}	-		> 150 GeV
N_j	≥ 4 (including lepton)		≥ 4
jet p_{T}	$> (80, 80, 40, 40)$ GeV		
N_b	1	≥ 2	
$\lvert\Delta\phi(\mathrm{jet}^{0,2}, \boldsymbol{p_{\mathrm{T}}}^{\mathrm{miss}})\rvert$	> 0.4		-
$m_T(\ell, \boldsymbol{p_{\mathrm{T}}}^{\mathrm{miss}})$	[30,100] GeV		-
$\Delta R(b, \ell)_{\mathrm{min}}$	> 2		-
$E_{\mathrm{T}}^{\mathrm{miss}}$	> 250 GeV		-
$\Delta R(b, b)$	-	> 1.5	-
$m^0_{R=1.2}$	< 60 GeV	> 120 GeV	-
$m_T^{b,\mathrm{min}}$	-	> 200 GeV	-

TABLE 6.21: Selection criteria for W, Single top and $t\bar{t} + \gamma$ control regions.

	CRW	**CRST**	**CRTTGamma**
$t\bar{t}$	122.27 ± 3.68	32.24 ± 1.4	5.14 ± 1.20
Z+jets	1.79 ± 0.35	0.09 ± 0.05	0.66 ± 0.17
W+jets	275.97 ± 8.02	20.82 ± 2.11	0.04 ± 0.02
$t\bar{t} + Z/W$	0.89 ± 0.14	2.44 ± 0.20	2.34 ± 0.25
Single Top	47.00 ± 1.76	45.41 ± 1.35	2.07 ± 0.80
Dibosons	10.31 ± 1.82	1.58 ± 0.57	0.00
$t\bar{t} + \gamma$	-	-	111.76 ± 1.45
Total MC	458.23 ± 9.19	102.58 ± 2.97	128.29 ± 2.17
Data	533.00 ± 23.09	114.00 ± 10.68	161.00 ± 12.69

TABLE 6.22: Expected and observed number of events in the W+jets, Single Top and $+\gamma$ control regions. Only statistical uncertainties are shown.

A validation region is used to test the extrapolation of the W+jets background prediction to the signal regions. The selection applied is similar to that of the control region for W in table 6.21, adding $\Delta R(b, \ell) > 1.8$, and $m_T^{b,\text{min}} > 150$ GeV.

6.5.4 Jet Smearing for Multijet Background

The background from all-hadronic $t\bar{t}$ and QCD multijet is estimated using the jet smearing method [129]. The main assumption of the method is that the largest contribution to the $E_{\text{T}}^{\text{miss}}$ in the multijet background comes from hadronic jet mismeasurements. It can be due to poorly reconstructed hadronic showers, imperfect calorimeter granularity, or leaks of the jet energy in dead material regions or beyond the calorimeter system. These can originate contributions to the $E_{\text{T}}^{\text{miss}}$. The estimation of such contribution is done following a data-driven method in four steps:

1. Seed events are selected with low $E_{\text{T}}^{\text{miss}}$ and well measured jets in the data.
2. The response function is determined from MC dijet events comparing the reconstructed with the particle level jets.
3. Pseudo-data events are generated by convoluting the seed event jets with the response function. They are compared to experimental data, and a new response function is defined as the difference between them. The process is repeated until good agreement is found.
4. A final sample of pseudo-data events is obtained convoluting the seed jets with the last response function obtained from the data.

The pseudo-data events are used to constrain the number of multijet events in the signal and control regions of the analysis, which is found to be negligible. The predicted events are introduced in the signal and validation regions and taken into account in the simultaneous fit.

6.6 Systematic uncertainties

A complete study of the systematic uncertainties was carried out, where both experimental and theoretical uncertainties were considered. Experimental uncertainties arise from detector and reconstruction efficiencies, while theoretical uncertainties are related to the choices of renormalisation and factorisation scales, PDFs and MC shower simulation.

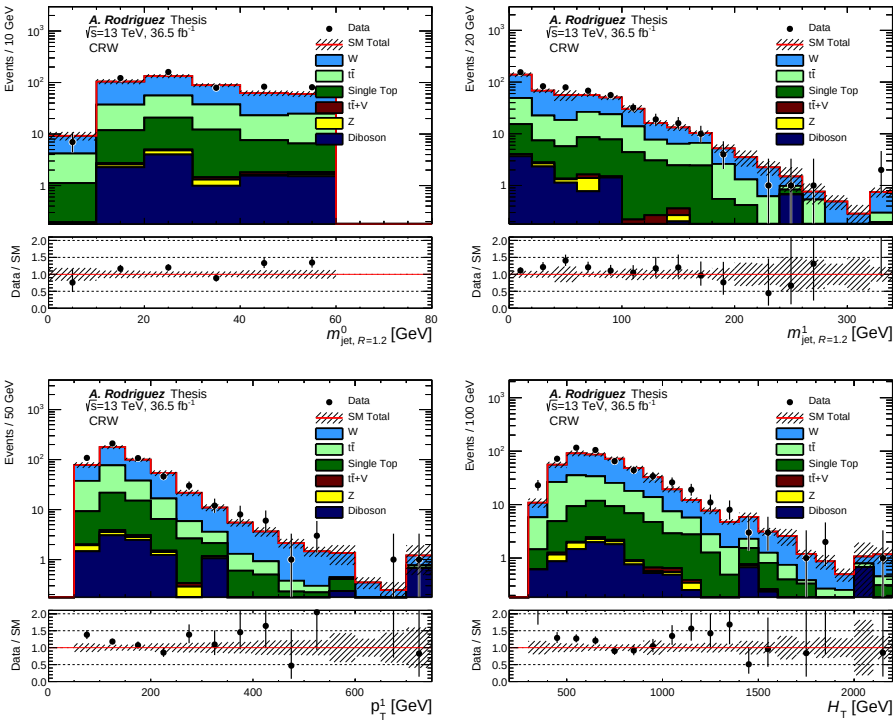

FIGURE 6.11: Distributions of $m^0_{R=1.2}$ (top left), $m^1_{R=1.2}$ (top right), subleading jet p_{T} (bottom left) and H_T (bottom right) in CRW. The MC and data are superimposed, where the MC prediction is shown before the fit, and the ratio of data to MC prediction is shown in the Data/MC. Statistical and systematic uncertainties are shown.

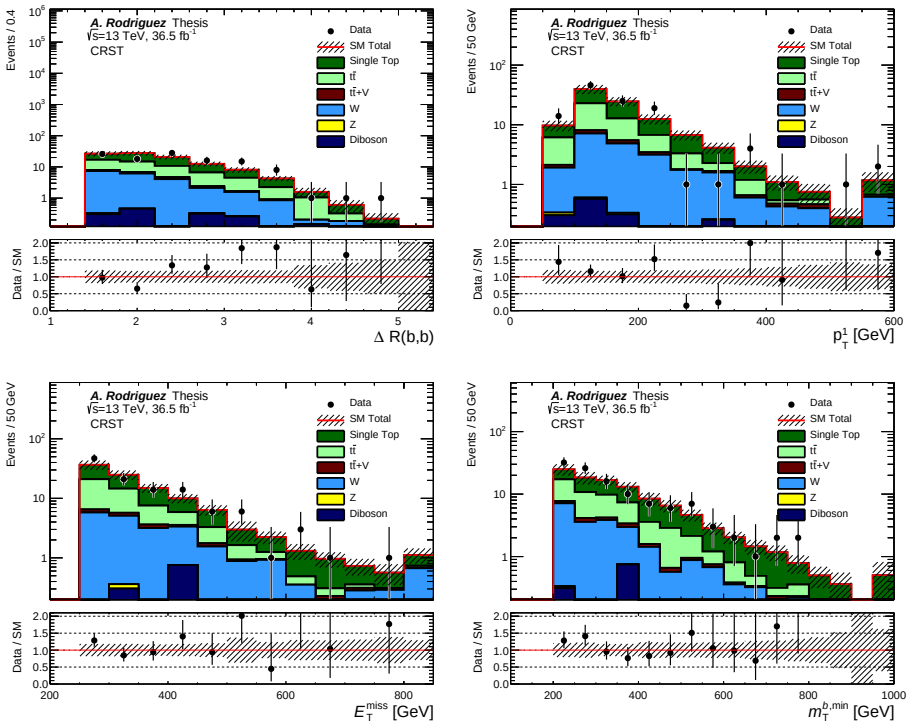

FIGURE 6.12: Distributions of $\Delta R(b,b)$ (top left), subleading jet p_{T} (top right),E_T^{miss} (bottom left) and $m_T^{b,\mathrm{min}}$ (bottom right) in CRST. The MC and data are superimposed, where the MC prediction is shown before the fit, and the ratio of data to MC prediction is shown in the Data/MC. Statistical and systematic uncertainties are shown.

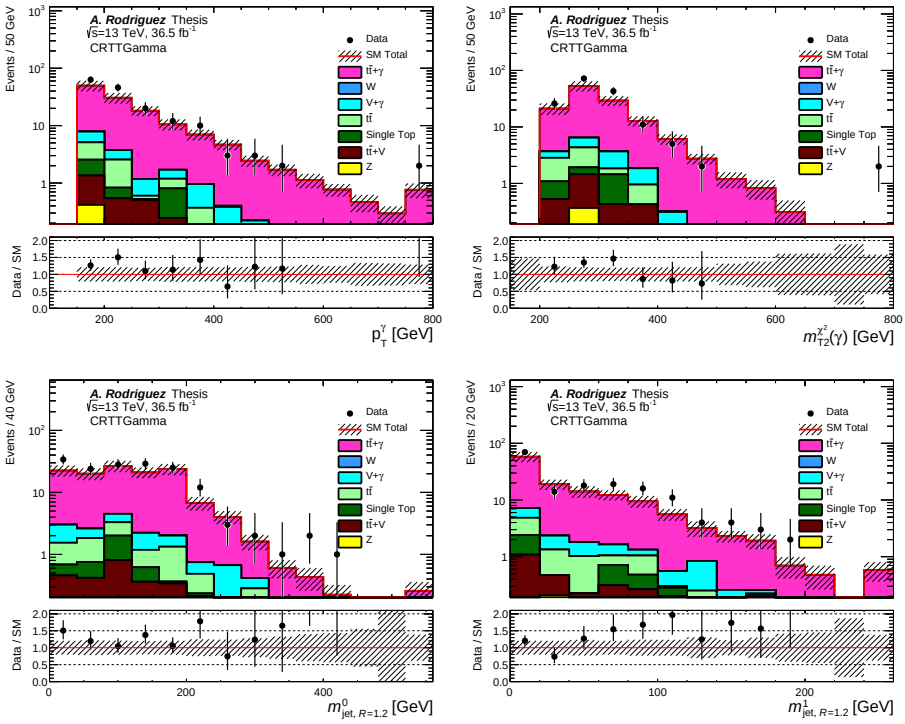

FIGURE 6.13: Distributions of p_{T}^{γ} (top left), m_{T2} calculated including the photon in the $E_{\mathrm{T}}^{\mathrm{miss}}$ (top right),$m^0_{R=1.2}$ (bottom left) and $m^1_{R=1.2}$ (bottom right) in CRTTγ. The MC and data are superimposed, where the MC prediction is shown before the fit, and the ratio of data to MC prediction is shown in the Data/MC. Statistical and systematic uncertainties are shown.

Systematic uncertainties are described in the fit by NPs. They are modelled by Gaussian probability density functions. The fit takes into account the correlation of these uncertainties in the control and signal regions, and finds the value of the NPs that maximises the likelihood.

The sources of experimental and theoretical uncertainties are described in the following.

6.6.1 Experimental uncertainties

Experimental uncertainties arise from the reconstruction efficiency of all physics objects described in chapter 4. The uncertainties with bigger impact in this analysis originate from jet calibration, b-tagging, and $E_{\mathrm{T}}^{\mathrm{miss}}$. These uncertainties are applied to the background as well as to the signal samples used in the analysis, and the numbers cited correspond to the uncertainties before the global fit.

- **Jet uncertainties:** Jet Energy Scale and Resolution (JES and JER) uncertainties [81] are the result of a combination of the uncertainties in the different steps of the jet calibration described in 4.4. The impact of the jet uncertainties in the total background estimation is found to be between 12% and 30% in the different SRs.

- **B-tagging:** B-tagging uncertainties are relevant for the analysis due to the two b-jet requirement in most of the regions. They arise from b-jet identification and calibration described in section 4.5. The total contribution of b-tagging uncertainties in the signal regions before performing the fit is of 15% to 35%.

- $\boldsymbol{E_{\mathrm{T}}^{\mathrm{miss}}}$**:** The uncertainties of the different terms of the $E_{\mathrm{T}}^{\mathrm{miss}}$ are evaluated by propagating the uncertainties of the different objects used to reconstruct them. The soft term, however, can not be treated in that way, since it is calculated from signals that are not associated to any object. Scale and resolution uncertainties on the $E_{\mathrm{T}}^{\mathrm{miss}}$ soft term are calculated [89] and included in the fit. The total contributions of MET uncertainties in the different signal regions are $< 10\%$ before the global fit.

- **Lepton uncertainties:** Electron and muon momentum scale and resolution uncertainties are applied. In addition, uncertainties related to efficiencies in identification, isolation, reconstruction and trigger are included. These uncertainties were found to be negligible in the signal regions, since they only affect through the lepton vetoes, and therefore they are only applied in the control regions.

- **Luminosity:** The uncertainty in the luminosity calculation is computed centrally in ATLAS as described in [66], and included as a systematic uncertainty in the analysis. The total uncertainty on the 2015+2016 luminosity is 3.2%.

6.6.2 Theoretical uncertainties

Theoretical uncertainties arise from the choice of renormalisation and factorisation scales, PDFs and parton shower simulation. For each of the main background processes, uncertainties are evaluated by varying these choices and using the resulting samples to compute the number of events expected in each of the regions. The comparison with what is obtained with the nominal sample is taken as the size of the

uncertainty, calculated as the difference of the transfer factor defined in equation 6.4 in the variation and the nominal case

$$\Delta = \frac{T_f^{\text{up}} - T_f^{\text{down}}}{T_f^{\text{up}} + T_f^{\text{down}}} \tag{6.5}$$

In the cases where the variations are not symmetric (i.e. there is no up and down), the uncertainty is calculated in a similar way to 6.5

$$\Delta = \frac{T_f^{\text{nom}} - T_f^{\text{var}}}{T_f^{\text{nom}}} \tag{6.6}$$

Uncertainties for Z+jets and W+jets backgrounds are obtained by varying scales of renormalisation, factorisation, merging and resummation by a factor two, up and down. In addition, PDF uncertainties are estimated by changing the PDF set used in the sample generation, and found to be negligible. The uncertainties obtained are then added in quadrature, resulting in a total uncertainty of up to 3% for both W and Z backgrounds, depending on the SR.

For the $t\bar{t}$ background, the sources of uncertainties are obtained from variations of the matrix-element calculation, parton-showering model and the number of partons emitted in the final and initial states, which is done by comparing Powheg-Box+Pythia with Herwig++ and Sherpa. The total uncertainty on the $t\bar{t}$ background is up to 90% in SRA-TT, SRC5 and SRD-high, where the statistics are very low, and smaller elsewhere.

Single top theory uncertainties are calculated varying the choice of parton showering model (Pythia and Herwig++) and the number of emitted partons in the initial and final state. An extra 30% uncertainty accounts for the interference between single top and $t\bar{t}$ productions. This is due to the fact that some processes contribute to $t\bar{t}$ at LO and single top at NLO, and the removal of this interference is non-trivial. In total, the uncertainties on single top background reach up to 41%.

The uncertainties on $t\bar{t} + W/Z/\gamma$ are evaluated varying the choice of PDF, the renormalisation and factorisation scales, and comparing MC@NLO with OpenLoops+Sherpa. The highest uncertainties are 95% in SRC1 and 55% in SRE, where $t\bar{t}$+W/Z is a very subdominant background, and lower than 16% elsewhere.

6.6.3 Signal Uncertainties

The theoretical systematic uncertainties considered for the signal samples include variations of the QCD coupling constant α_s and renormalisation and factorisation scales. The CKKW matching scale and the parton-shower tune variations are also taken into account. Finally, the theoretical uncertainty on the cross section for the different models is used to calculate variations of the observed exclusion limits which will be described in section 7.3. Table 6.23 shows the level of uncertainty of the models used.

6.7 Background-only fit

The background-only fit is performed using only the control regions to constrain the background. The signal regions are not taken into account, and any potential signal contamination is neglected. The systematic uncertainties introduced in section 6.6 are included in the fit using nuisance parameters. In total, 32 NPs are used for the modelling of systematics. Normalisation factors for the main backgrounds are

Model	Uncertainty
$\tilde{t}_1 \to t\tilde{\chi}_1^0$	10-25%
Mixed BR=75%	10-25%
Mixed BR=50%	10-25%
Mixed BR=25%	10-25%
Mixed BR=0%	15-30%
Gluino mediated stop	10-25%
Wino NLSP	15-20%
Well tempered ($\tilde{t}_1 \approx \tilde{t}_R$)	10-20%
Well tempered ($\tilde{t}_1 \approx \tilde{t}_L$)	20-35%
Non asymptotic higgsino	10-25%

TABLE 6.23: Level of uncertainty of the signals used for interpretation. The numbers are approximate and they vary depending on the signal region.

obtained and extrapolated to the validation regions, where the number of expected and observed events is compared to test the validity of these factors in the extrapolation towards the signal regions. Once the agreement between data and MC has been tested in the validation regions, and the background composition has been understood, one can look at the signal regions. If no excess of data events is observed over the MC prediction, an exclusion fit will determine whether the signal can be excluded.

The scale factors for the different backgrounds are obtained in the fit in order to match the data and simulation events, and are shown in table 6.24. The calculation takes into account any cross-contamination from the different background processes in the control regions. They are allowed to vary in the fit in order to obtain the best agreement between data and normalised MC. The factors vary with the signal region in some cases since the normalisation is obtained from different control regions designed for each of them, which have different background composition. Most of the normalisation factors shown are compatible with unity within errors, which include statistical and systematic uncertainties.

The understanding of the agreement of the shapes of the main variables in data and MC in the control regions after the fit is essential for the understanding of the backgrounds. Figures 6.3-6.7 show some of the distributions of these variables in the $t\bar{t}$ control regions. Figures 6.8-6.10 show distributions for the Z+jets control regions. In figures 6.11, 6.12 and 6.13, some distributions are shown in W+jets, Single Top and $t\bar{t}+\gamma$ control regions, respectively. The agreement between data and the MC prediction after the fit is good in general. Small deviations are observed in figure 6.5 in CRTC in the p_{T}^{btag1}, although the general agreement in the rest of the distributions is good.

The agreement of the MC prediction after the fit with the data is validated in the VRs before looking at the data events in the signal regions. The tables with the values of expected and observed events after the fit and their uncertainties can be seen in 6.25-6.27 for $t\bar{t}$ validation regions. Table 6.28 shows after-fit yields in Z+jets validation regions, and VRW yields are shown in table 6.29. The agreement between the observed and fitted background events is very good in general, with some small excesses of data events in VRTB-TW VRTD and VRZE.

As already mentioned, the understanding of the SM background processes is validated in the VRs. Distributions of some variables in the validation regions are shown in figures 6.25-6.29 in the $t\bar{t}$ VRs. In figures 6.30-6.32, distributions of several variables

Background process	Scale factor
$t\bar{t}$ (SRA-TT)	1.173 ± 0.146
$t\bar{t}$ (SRA-TW)	1.138 ± 0.112
$t\bar{t}$ (SRA-T0)	0.898 ± 0.121
$t\bar{t}$ (SRB-TT)	1.202 ± 0.156
$t\bar{t}$ (SRB-TW)	0.969 ± 0.068
$t\bar{t}$ (SRB-T0)	0.924 ± 0.053
$t\bar{t}$ (SRC)	0.707 ± 0.050
$t\bar{t}$ (SRD)	0.945 ± 0.103
$t\bar{t}$ (SRE)	1.012 ± 0.180
Z+jets (SRA and SRB-TT and TW)	1.170 ± 0.238
Z+jets (SRA and SRB-T0)	1.131 ± 0.144
Z+jets (SRD)	1.035 ± 0.146
Z+jets (SRE)	1.185 ± 0.152
W+jets	1.267 ± 0.146
Single Top	1.166 ± 0.390
$t\bar{t} + \gamma$	1.290 ± 0.204

TABLE 6.24: Scale factors for the normalisation of the different background processes. Several scale factors are obtained for $t\bar{t}$ and Z+jets where several control regions are used for the normalisation.

are shown in Z+jets validation regions. The validation region for $W + jets$ is shown in figure 6.33. The small excesses mentioned before can be seen in figure 6.26, 6.28 and 6.32. In all the cases, some of the bins of the distribution present a small excess while the general agreement is good within uncertainties.

The pull plot after the fit showing the deviation from the central value of the nuisance parameters is shown in figure 6.34. All the nuisance parameters related to systematic uncertainties are shown, as well as the normalisation factors. A deviation from the central value or an uncertainty significantly different from $\sigma = 1$ of any of the parameters would indicate a mismodelling that has been artificially adjusted by varying this parameter. As it can be seen in figure 6.34, non of the systematic parameters presents such a deviation. The normalisation factors are named with a `mu_` prefix, and as it was mentioned above, they are mostly compatible with unity within uncertainties, except for the $t\bar{t}$ parameter in SRC. A small deviation from one is also observed for the W+jets and $t\bar{t} + V$ scale factors.

The reduced correlation matrix is shown in figure 6.35. It can be seen that the biggest correlations arise from the different normalisation factors, due to the contamination of the different background processes in the control regions. Some correlations with the systematic parameters are also observed, for example with the b-tagging systematics `alpha_bEff, alpha_cEff` or the JER systematic uncertainty `alpha_JER`. Parameters related to statistical uncertainties in the regions have a prefix `gamma_`.

VRTopA yields	VRTopATT	VRTopATW	VRTopAT0
Observed events	80	63	74
Fitted bkg events	79.33 ± 24.94	64.18 ± 10.58	68.58 ± 12.00
Fitted TTbar events	64.57 ± 25.08	54.76 ± 10.80	53.05 ± 12.11
Fitted Wjets events	2.04 ± 0.80	$0.41^{+0.50}_{-0.41}$	2.75 ± 0.75
Fitted Zjets events	3.78 ± 0.91	3.32 ± 0.99	6.15 ± 1.04
Fitted TtbarV events	3.67 ± 0.65	2.55 ± 0.42	2.85 ± 0.49
Fitted SingleTop events	3.63 ± 1.94	2.76 ± 1.30	3.65 ± 1.82
Fitted Diboson events	0.65 ± 0.47	0.26 ± 0.17	0.00 ± 0.00
Fitted Multijets events	0.98 ± 0.65	$0.12^{+0.12}_{-0.12}$	0.14 ± 0.08
MC exp. SM events	67.49 ± 20.17	56.01 ± 8.14	72.15 ± 10.48
MC exp. TTbar events	55.01 ± 20.10	48.12 ± 8.12	59.06 ± 10.46
MC exp. Wjets events	1.62 ± 0.55	$0.33^{+0.39}_{-0.33}$	2.17 ± 0.55
MC exp. Zjets events	3.23 ± 0.35	2.84 ± 0.55	5.43 ± 0.52
MC exp. TtbarV events	2.86 ± 0.49	1.98 ± 0.30	2.22 ± 0.25
MC exp. SingleTop events	3.13 ± 1.44	2.37 ± 0.73	3.14 ± 1.13
MC exp. Diboson events	0.65 ± 0.47	0.26 ± 0.17	0.00 ± 0.00
MC exp. Multijets events	0.98 ± 0.65	$0.12^{+0.12}_{-0.12}$	0.14 ± 0.08

TABLE 6.25: Background-only fit results in $t\bar{t}$ validation regions for SRA. The uncertainties are statistical and systematic.

VRTopB yields	VRTopBTT	VRTopBTW	VRTopBT0
Observed events	143	188	209
Fitted bkg events	140.00 ± 35.15	138.55 ± 31.20	202.36 ± 29.36
Fitted TTbar events	114.04 ± 34.93	112.20 ± 30.99	146.93 ± 27.49
Fitted Wjets events	3.67 ± 1.22	4.59 ± 1.60	8.25 ± 2.11
Fitted Zjets events	5.69 ± 1.71	7.58 ± 1.64	21.90 ± 3.44
Fitted TtbarV events	6.64 ± 1.14	5.79 ± 0.98	8.42 ± 1.13
Fitted SingleTop events	7.28 ± 3.28	7.53 ± 3.43	15.92 ± 7.43
Fitted Diboson events	0.70 ± 0.60	$0.26^{+0.35}_{-0.26}$	$0.28^{+0.39}_{-0.28}$
Fitted Multijets events	2.00 ± 1.65	$0.60^{+0.68}_{-0.60}$	0.66 ± 0.55
MC exp. SM events	116.72 ± 27.08	137.77 ± 31.62	206.09 ± 30.80
MC exp. TTbar events	94.83 ± 26.41	115.82 ± 30.79	159.04 ± 27.79
MC exp. Wjets events	2.91 ± 0.78	3.65 ± 1.10	6.53 ± 1.21
MC exp. Zjets events	4.86 ± 0.88	6.48 ± 0.61	19.36 ± 1.77
MC exp. TtbarV events	5.17 ± 0.92	4.50 ± 0.75	6.55 ± 0.76
MC exp. SingleTop events	6.26 ± 2.25	6.47 ± 2.04	13.68 ± 4.43
MC exp. Diboson events	0.70 ± 0.60	$0.26^{+0.35}_{-0.26}$	$0.28^{+0.40}_{-0.28}$
MC exp. Multijets events	2.00 ± 1.65	$0.60^{+0.68}_{-0.60}$	0.66 ± 0.55

TABLE 6.26: Background-only fit results in $t\bar{t}$ validation regions for SRB. The uncertainties are statistical and systematic.

VRTop yields	VRTopC	VRTopD	VRTopE
Observed events	286	331	105
Fitted bkg events	289.15 ± 20.51	269.81 ± 47.31	83.32 ± 24.34
Fitted TTbar events	162.17 ± 18.47	225.40 ± 47.74	69.65 ± 24.36
Fitted Wjets events	47.34 ± 10.15	5.93 ± 1.46	2.45 ± 0.75
Fitted Zjets events	36.17 ± 9.86	9.00 ± 1.59	4.24 ± 1.05
Fitted TtbarV events	8.87 ± 1.49	6.75 ± 1.04	2.93 ± 0.62
Fitted SingleTop events	28.64 ± 13.51	19.72 ± 9.03	3.90 ± 1.82
Fitted Diboson events	3.00 ± 1.87	0.58 ± 0.56	$0.16^{+0.29}_{-0.16}$
Fitted Multijets events	2.96 ± 2.33	2.43 ± 0.84	0.00 ± 0.00
MC exp. SM events	335.18 ± 20.77	276.62 ± 42.88	80.13 ± 20.86
MC exp. TTbar events	229.37 ± 19.21	238.07 ± 42.41	68.83 ± 20.76
MC exp. Wjets events	37.46 ± 5.90	4.69 ± 0.82	1.94 ± 0.47
MC exp. Zjets events	30.88 ± 4.22	8.68 ± 0.91	3.58 ± 0.74
MC exp. TtbarV events	6.90 ± 1.15	5.25 ± 0.65	2.28 ± 0.41
MC exp. SingleTop events	24.60 ± 7.93	16.93 ± 5.34	3.35 ± 1.16
MC exp. Diboson events	3.01 ± 1.88	0.57 ± 0.56	$0.16^{+0.29}_{-0.16}$
MC exp. Multijets events	2.96 ± 2.33	2.43 ± 0.84	0.00 ± 0.00

TABLE 6.27: Background-only fit results in $t\bar{t}$ validation regions for SRC, SRD and SRE. The uncertainties are statistical and systematic.

VRZ yields	VRZAB	VRZD	VRZE
Observed events	133	79	104
Fitted bkg events	130.77 ± 17.16	66.34 ± 6.61	84.44 ± 7.85
Fitted TTbar events	20.09 ± 5.24	12.74 ± 4.25	11.33 ± 3.31
Fitted Wjets events	36.25 ± 8.15	15.85 ± 2.85	21.30 ± 4.27
Fitted Zjets events	63.75 ± 16.40	30.86 ± 4.96	38.87 ± 5.86
Fitted TtbarV events	2.67 ± 0.52	3.00 ± 0.57	3.49 ± 0.75
Fitted SingleTop events	4.78 ± 2.29	2.14 ± 1.13	7.22 ± 3.27
Fitted Diboson events	2.59 ± 1.50	0.99 ± 0.56	2.22 ± 1.15
Fitted Multijets events	$0.63^{+1.14}_{-0.63}$	0.76 ± 0.57	0.00 ± 0.00
MC exp. SM events	109.64 ± 8.73	61.68 ± 5.08	71.97 ± 4.67
MC exp. TTbar events	17.10 ± 3.98	13.42 ± 4.14	11.18 ± 2.86
MC exp. Wjets events	28.70 ± 4.66	12.54 ± 1.61	16.87 ± 2.48
MC exp. Zjets events	54.43 ± 7.60	29.80 ± 2.62	32.79 ± 2.68
MC exp. TtbarV events	2.07 ± 0.27	2.33 ± 0.38	2.72 ± 0.50
MC exp. SingleTop events	4.10 ± 1.41	1.83 ± 0.78	6.19 ± 2.04
MC exp. Diboson events	2.60 ± 1.50	0.99 ± 0.56	2.22 ± 1.15
MC exp. Multijets events	$0.63^{+1.14}_{-0.63}$	0.76 ± 0.57	0.00 ± 0.00

TABLE 6.28: Background-only fit results for Z+jets validation regions. The uncertainties are statistical and systematic.

VRW yields	VRW
Observed events	136
Fitted bkg events	154.83 ± 22.28
Fitted TTbar events	40.01 ± 7.78
Fitted Wjets events	61.55 ± 9.87
Fitted Zjets events	0.25 ± 0.10
Fitted TtbarV events	0.68 ± 0.21
Fitted SingleTop events	49.29 ± 23.03
Fitted Diboson events	3.05 ± 1.67
Fitted Multijets events	0.00 ± 0.00
MC exp. SM events	128.86 ± 14.48
MC exp. TTbar events	34.05 ± 5.18
MC exp. Wjets events	48.68 ± 3.91
MC exp. Zjets events	0.21 ± 0.08
MC exp. TtbarV events	0.53 ± 0.13
MC exp. SingleTop events	42.33 ± 13.11
MC exp. Diboson events	3.06 ± 1.68
MC exp. Multijets events	0.00 ± 0.00

TABLE 6.29: Background-only fit results for W+jets validation region. The uncertainties are statistical and systematic.

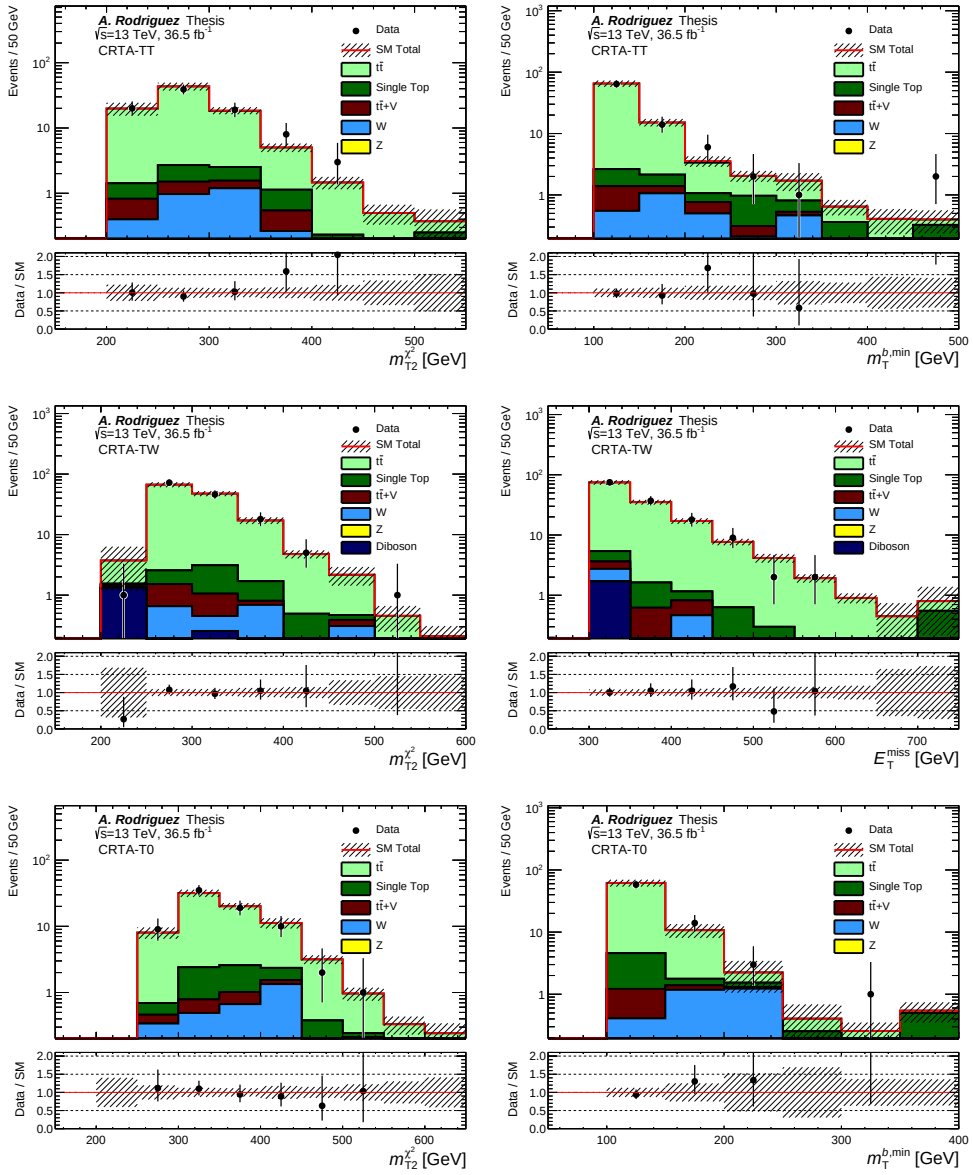

FIGURE 6.14: Distributions of extrapolating variables in the $t\bar{t}$ control regions for SRA. From top to bottom, m_{T2} and $m_T^{b,\min}$ in CRA-TT, m_{T2} and $E_{\mathrm{T}}^{\mathrm{miss}}$ in CRA-TW and m_{T2} and $m_T^{b,\min}$ in CRA-T0. Statistical and systematic uncertainties are shown, and the background MC samples have been scaled with the factors in 6.24.

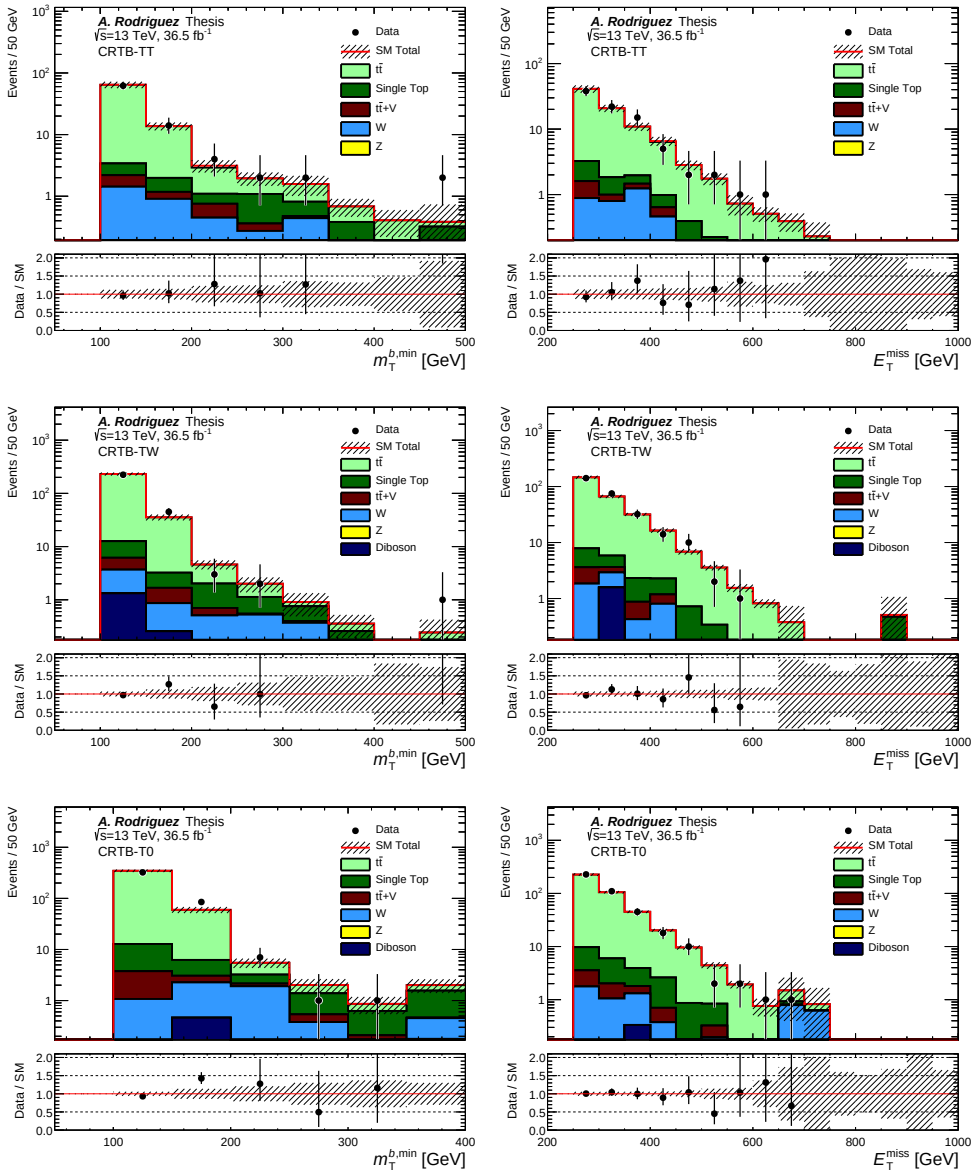

FIGURE 6.15: Distributions of $m_T^{b,\min}$ and $E_{\mathrm{T}}^{\mathrm{miss}}$ in the $t\bar{t}$ control regions for SRB. From top to bottom, CRB-TT, CRB-TW and CRB-T0. Statistical and systematic uncertainties are shown, and the background MC samples have been scaled with the factors in 6.24.

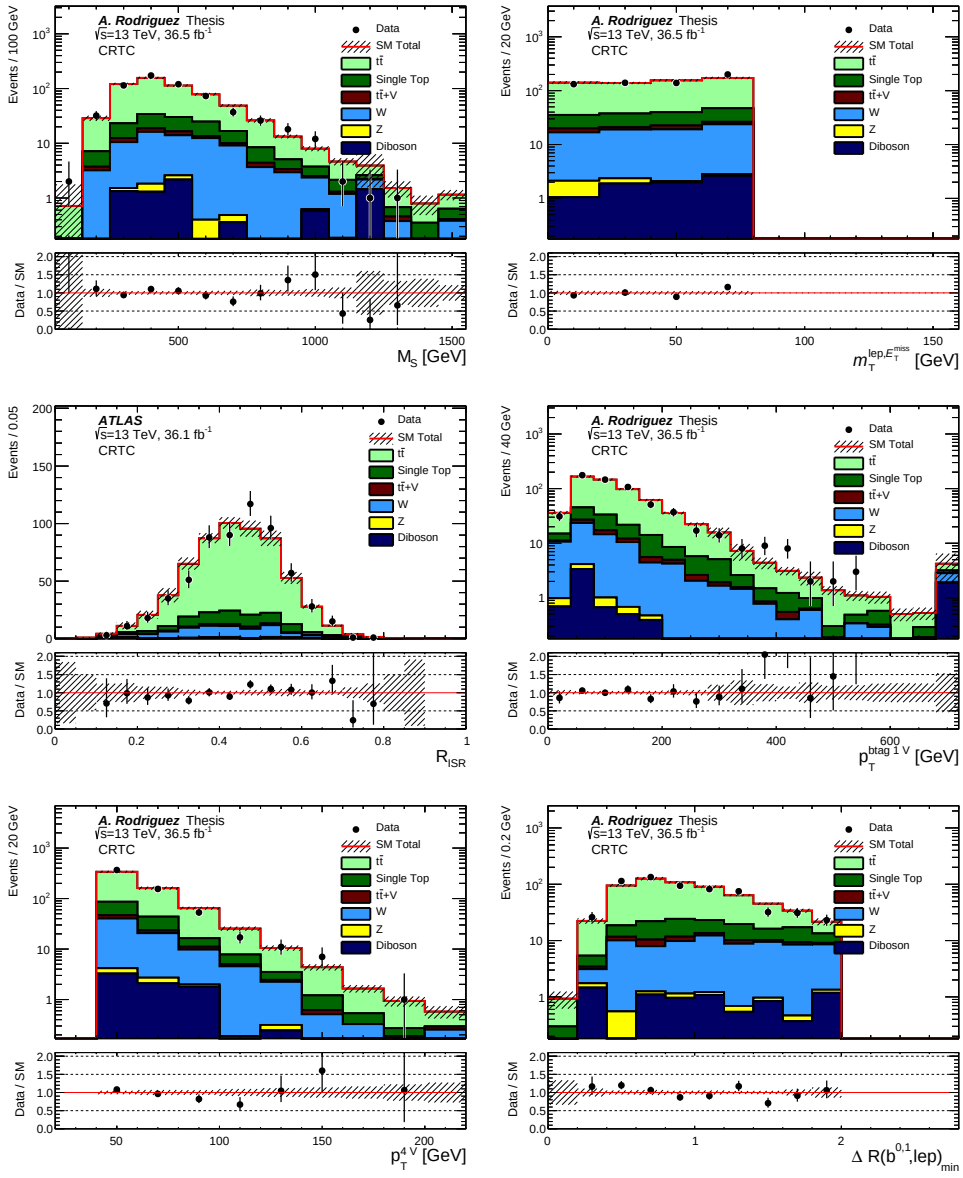

FIGURE 6.16: Distributions of m_S, $m_T(E_{\mathrm{T}}^{\mathrm{miss}}, \ell)$, R^{ISR}, leading b-tagged jet p_{T}, fourth leading jet p_{T} and number of b-tagged jets in the $t\bar{t}$ control region for SRC, CRTC. Statistical and systematic uncertainties are shown, and the background MC samples have been scaled with the factors in 6.24.

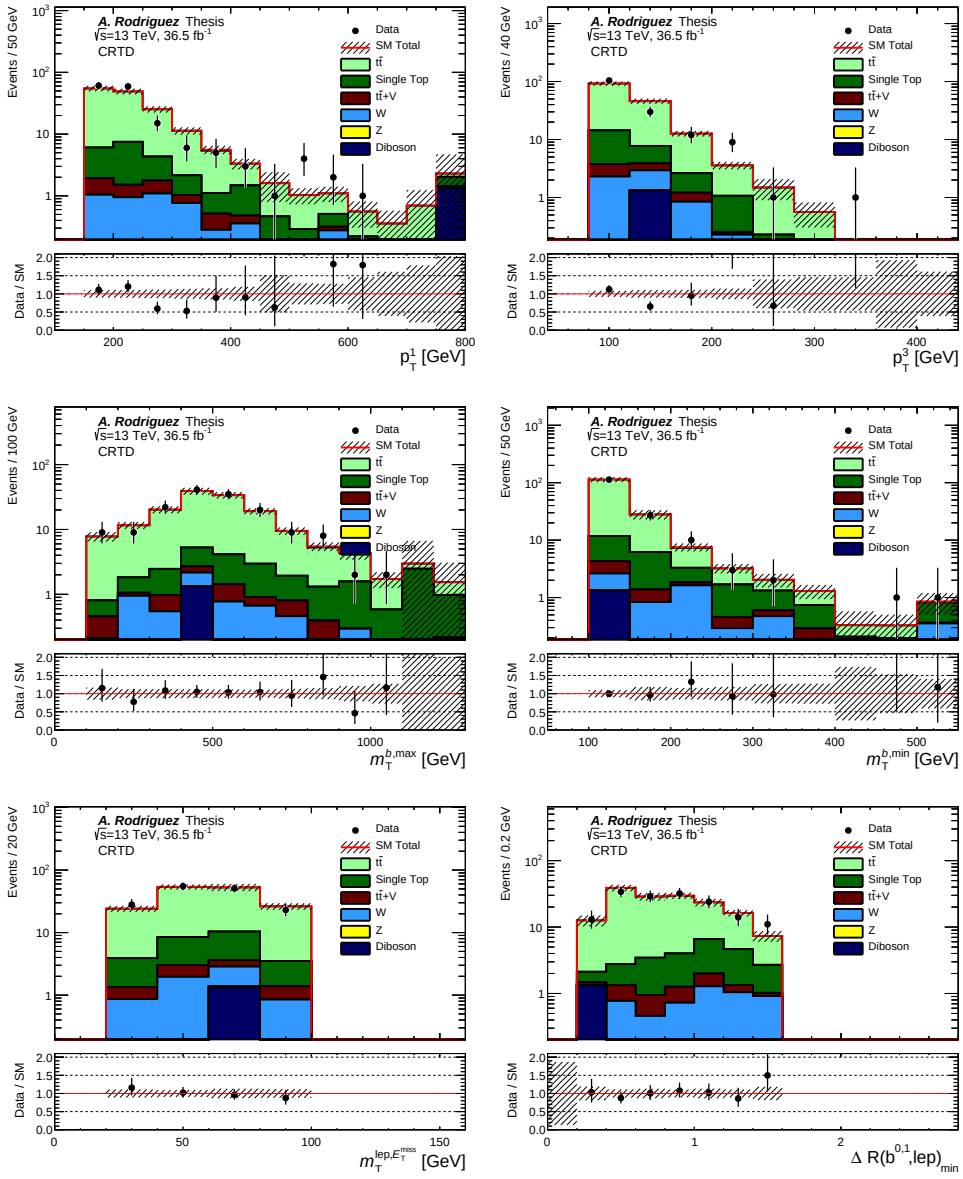

FIGURE 6.17: Distributions of subleading and third leading jet p_{T}, $m_T^{b,\mathrm{min}}$, $m_T^{b,\mathrm{max}}$, $m_T(E_{\mathrm{T}}^{\mathrm{miss}}, \ell)$ and $\Delta R(b, \ell)$ in the $t\bar{t}$ control region for SRD, CRTD. Statistical and systematic uncertainties are shown, and the background MC samples have been scaled with the factors in 6.24.

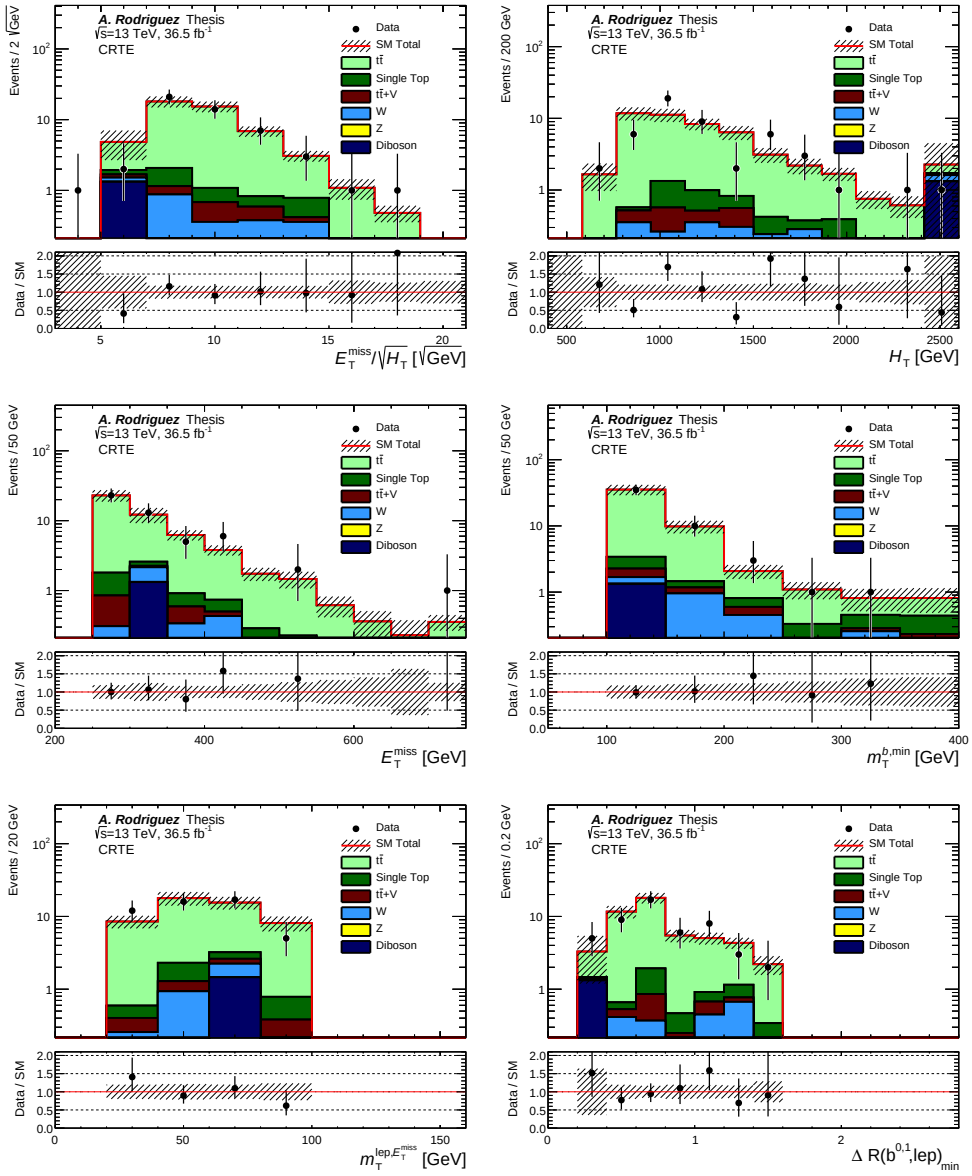

FIGURE 6.18: Distributions of $E_{\mathrm{T}}^{\mathrm{miss}}/\sqrt{H_T}$, H_T, $E_{\mathrm{T}}^{\mathrm{miss}}$, $m_T^{b,\mathrm{min}}$, $m_T(E_{\mathrm{T}}^{\mathrm{miss}}, \ell)$ and $\Delta R(b, \ell)$ in the $t\bar{t}$ control region for SRE, CRTE. Statistical and systematic uncertainties are shown, and the background MC samples have been scaled with the factors in 6.24.

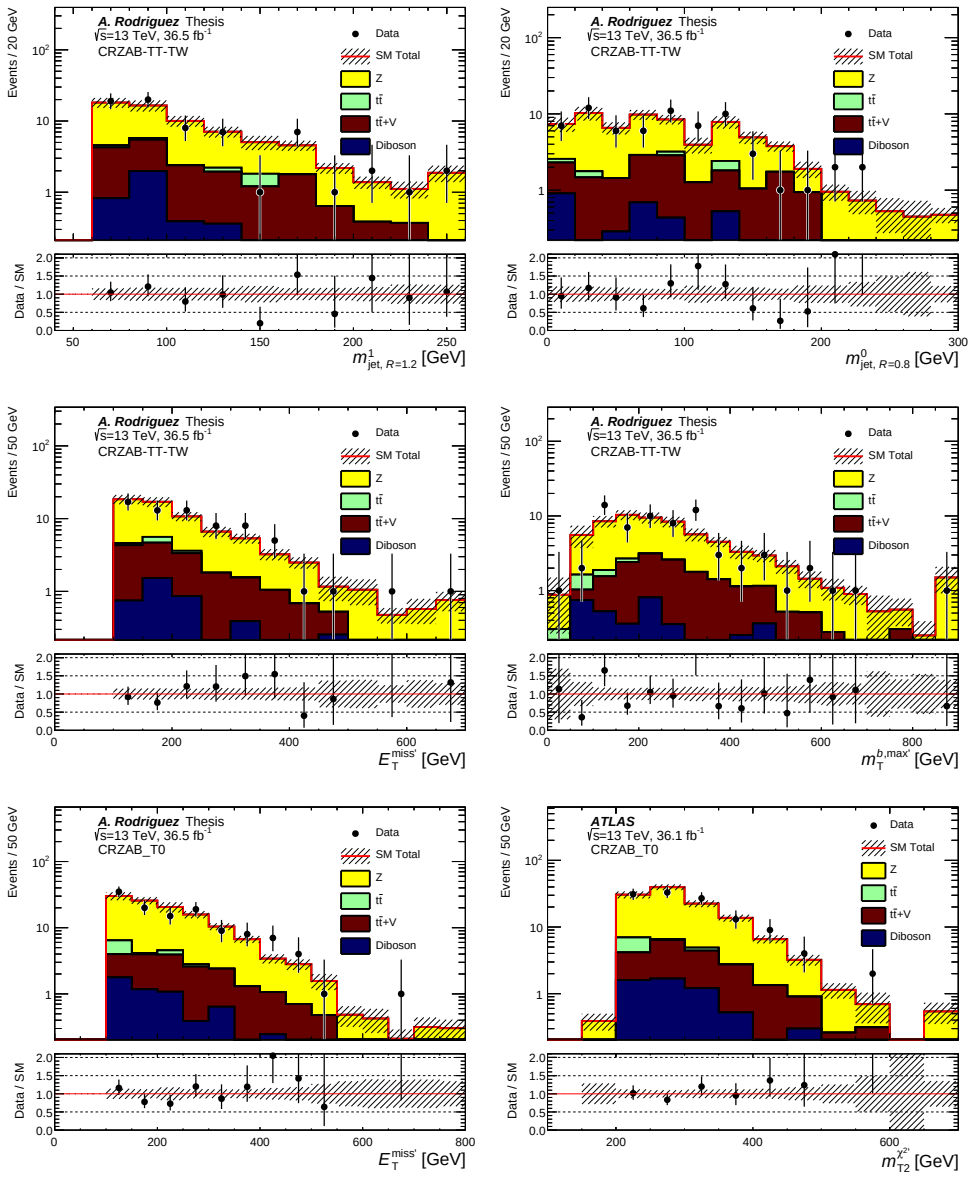

FIGURE 6.19: Distributions of $m^1_{R=1.2}$, $m^0_{R=0.8}$, $E_T^{\mathrm{miss}'}$, $m_T^{b,\mathrm{max}'}$ in CRZAB-TT-TW, and $E_T^{\mathrm{miss}'}$ and m'_{T2} in the Z+jets control region for SRA-T0 and SRB-T0, CRZAB-T0. Statistical and systematic uncertainties are shown, and the background MC samples have been scaled with the factors in 6.24.

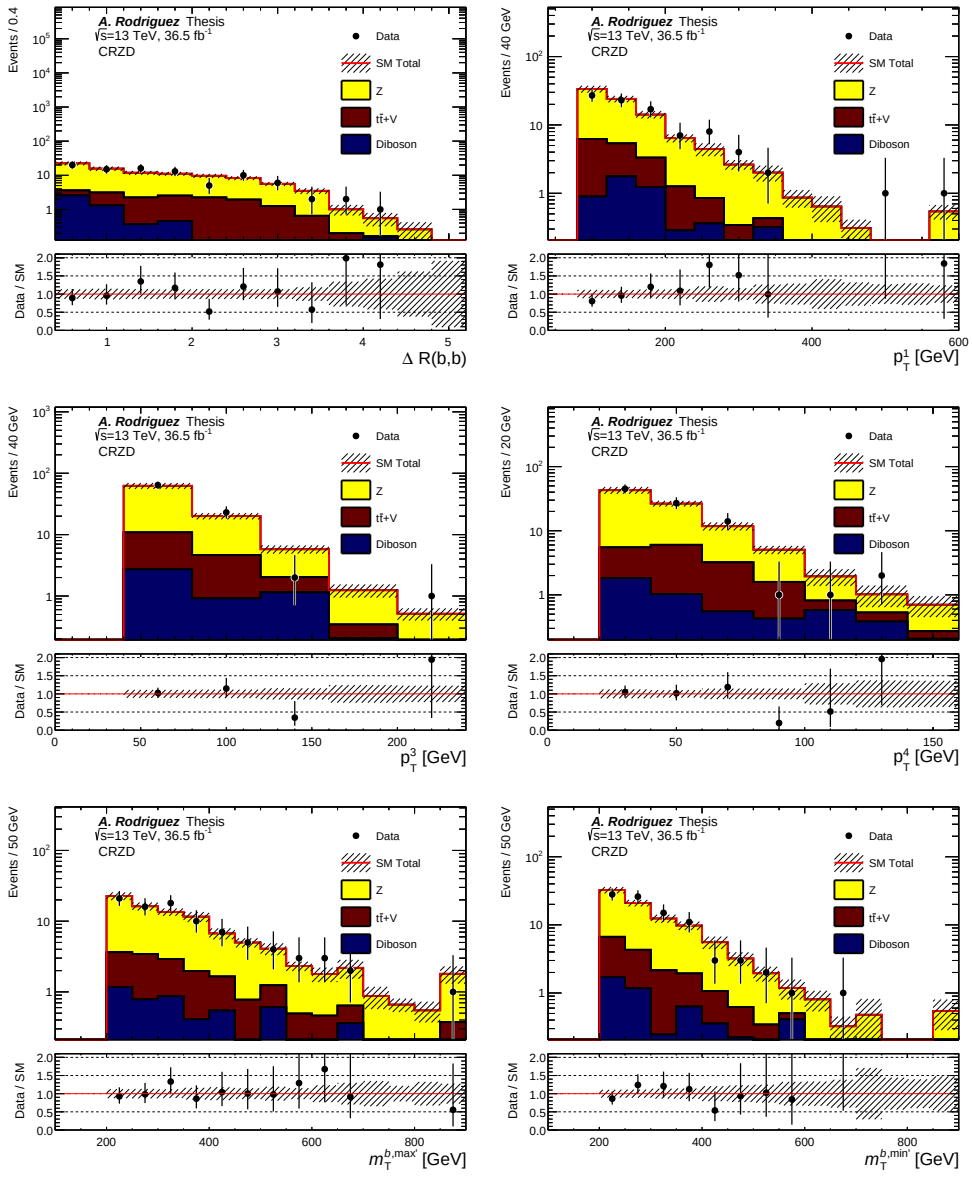

FIGURE 6.20: Distributions of $\Delta R(b,b)$, the second, fourth, and fifth leading jet p_{T}, $m_T^{b,\mathrm{max}'}$ and $m_T^{b,\mathrm{min}'}$ in the Z+jets control region for SRD, CRZD. Statistical and systematic uncertainties are shown, and the background MC samples have been scaled with the factors in 6.24.

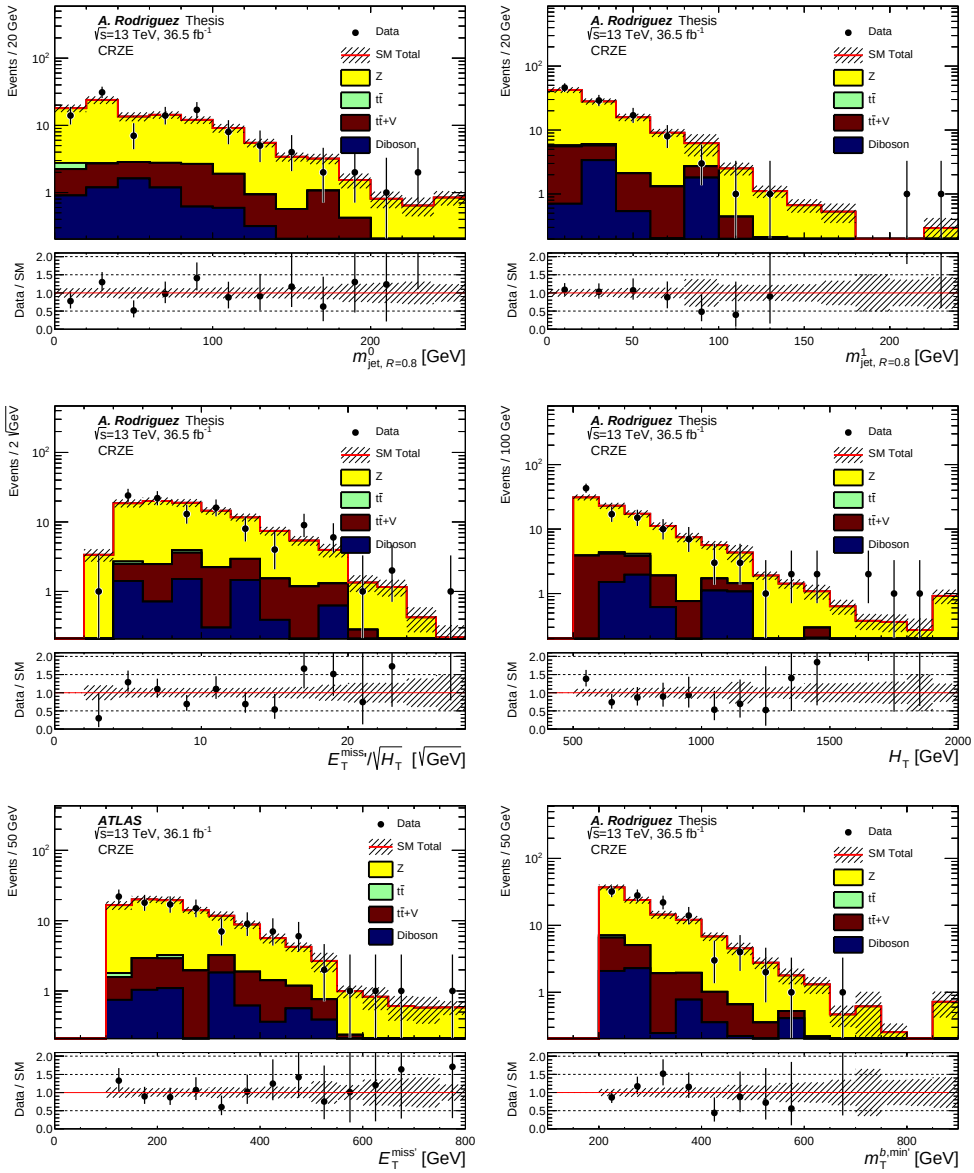

FIGURE 6.21: Distributions of leading and subleading R=1.2 reclustered jet masses, $E_{\mathrm{T}}^{\mathrm{miss}}$ significance, H_T, $E_{\mathrm{T}}^{\mathrm{miss}}$ and $m_T^{b,\mathrm{min}}$ in the Z+jets control region for SRE, CRZE. Statistical and systematic uncertainties are shown, and the background MC samples have been scaled with the factors in 6.24.

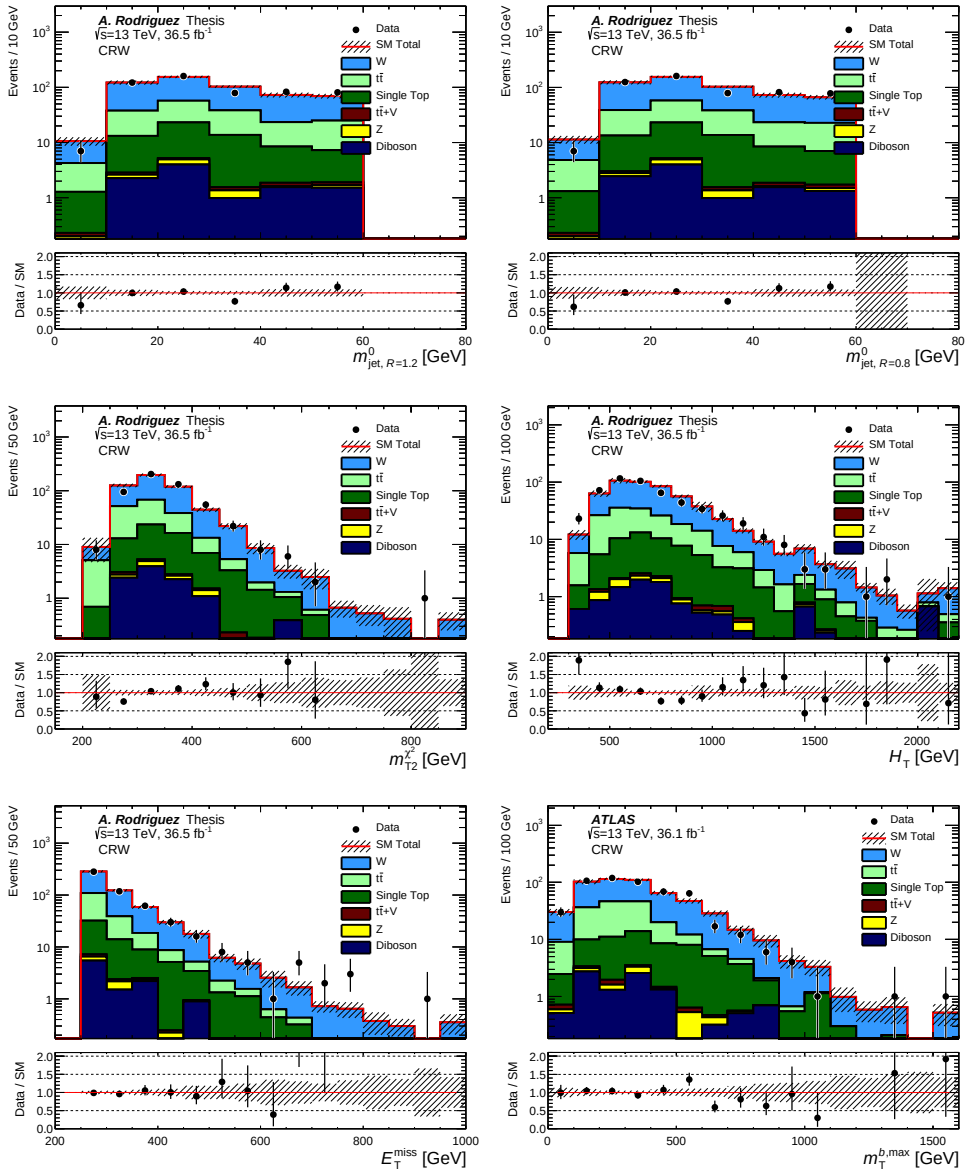

FIGURE 6.22: Distributions of leading R=1.2 and R=0.8 reclustered jet masses, m_{T2}, H_T, $E_{\mathrm{T}}^{\mathrm{miss}}$ and $m_T^{b,\mathrm{max}}$ in the W+jets control region. Statistical and systematic uncertainties are shown, and the background MC samples have been scaled with the factors in 6.24.

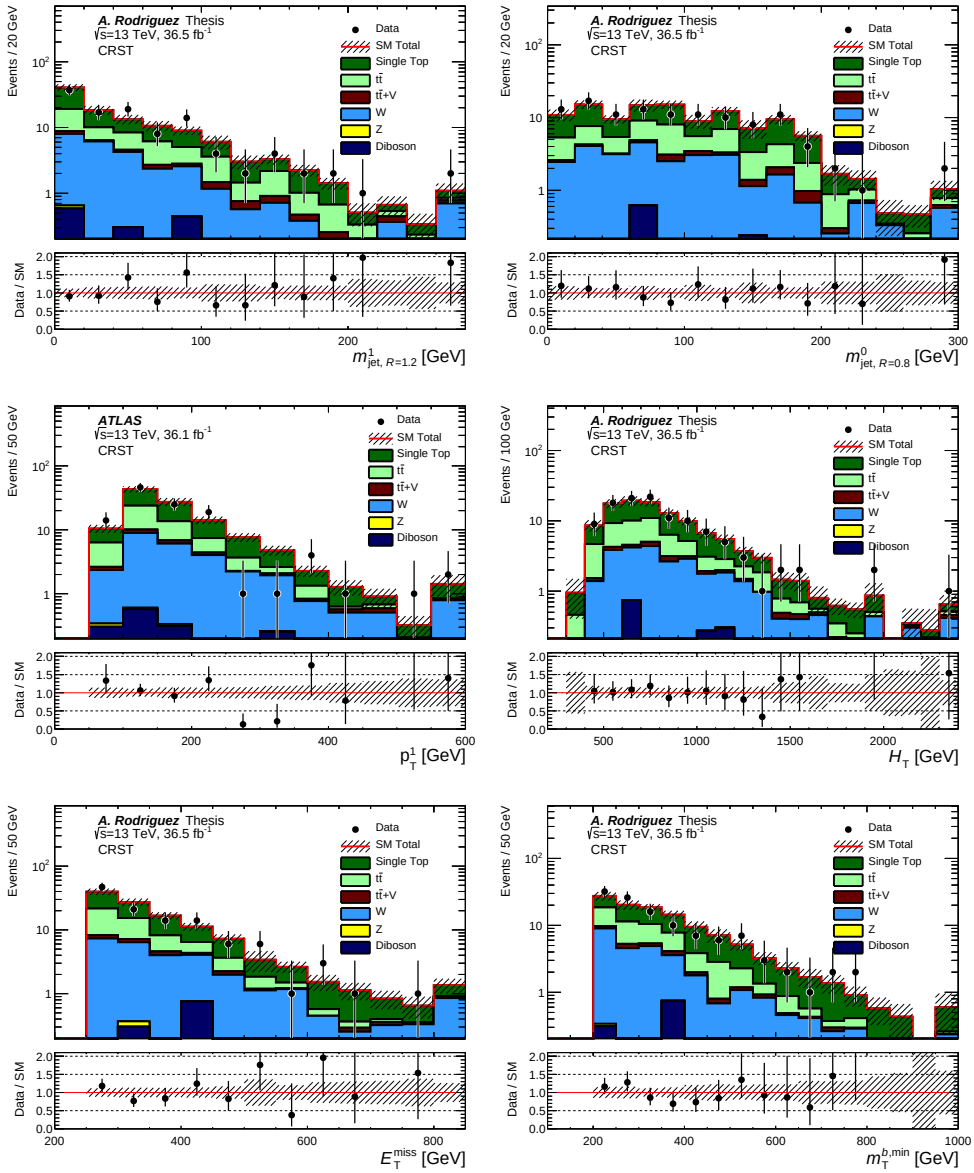

FIGURE 6.23: Distributions of subleading R=1.2 and leading R=0.8 reclustered jet masses, subleading jet p_{T}, H_T, $E_{\mathrm{T}}^{\mathrm{miss}}$ and $m_T^{b,\mathrm{min}}$ in the Single Top control region. Statistical and systematic uncertainties are shown, and the background MC samples have been scaled with the factors in 6.24.

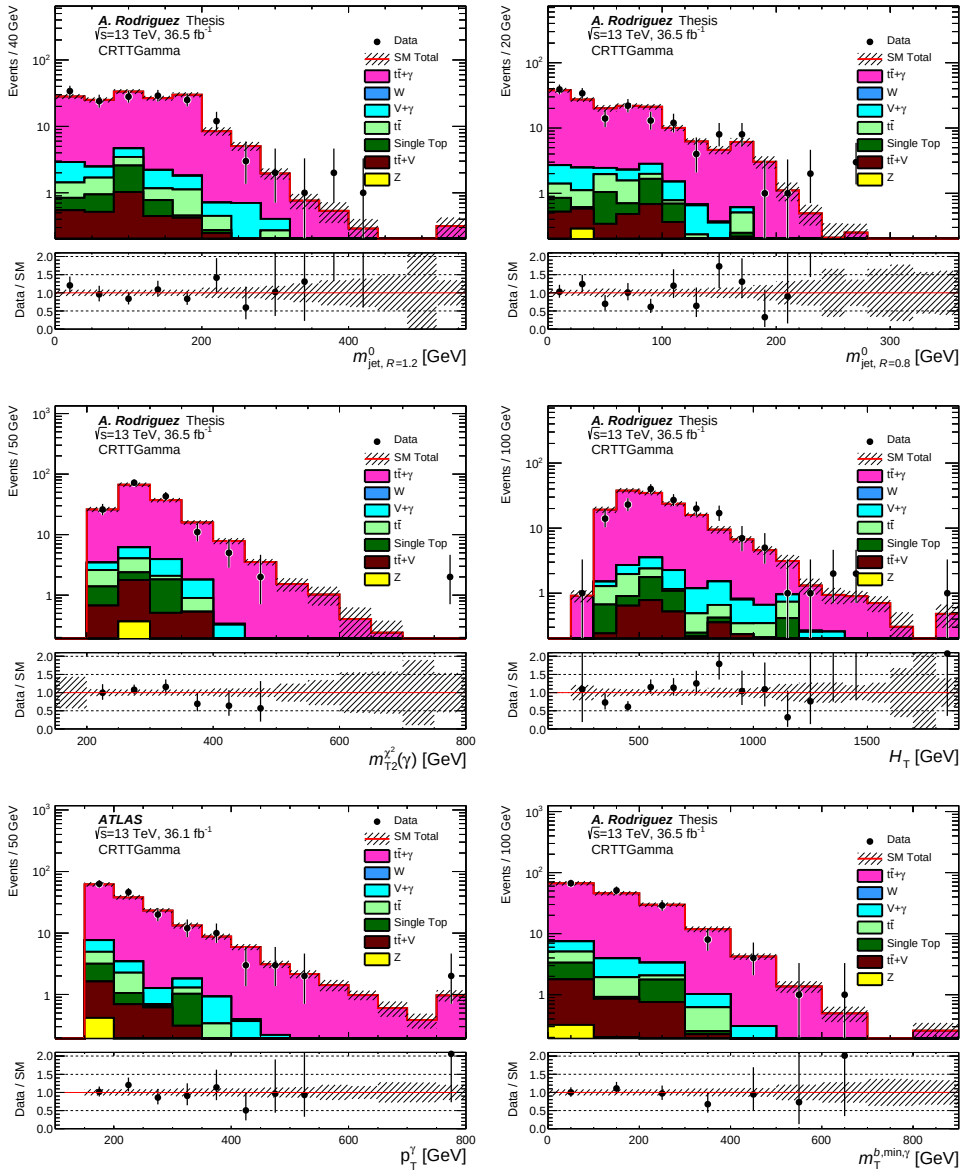

FIGURE 6.24: Distributions of leading R=1.2 and R=0.8 reclustered jet masses, m'_{T2}, H_T, leading photon p_{T} and $m_T^{b,\mathrm{min}'}$ in the $t\bar{t} + \gamma$ control region. Statistical and systematic uncertainties are shown, and the background MC samples have been scaled with the factors in 6.24.

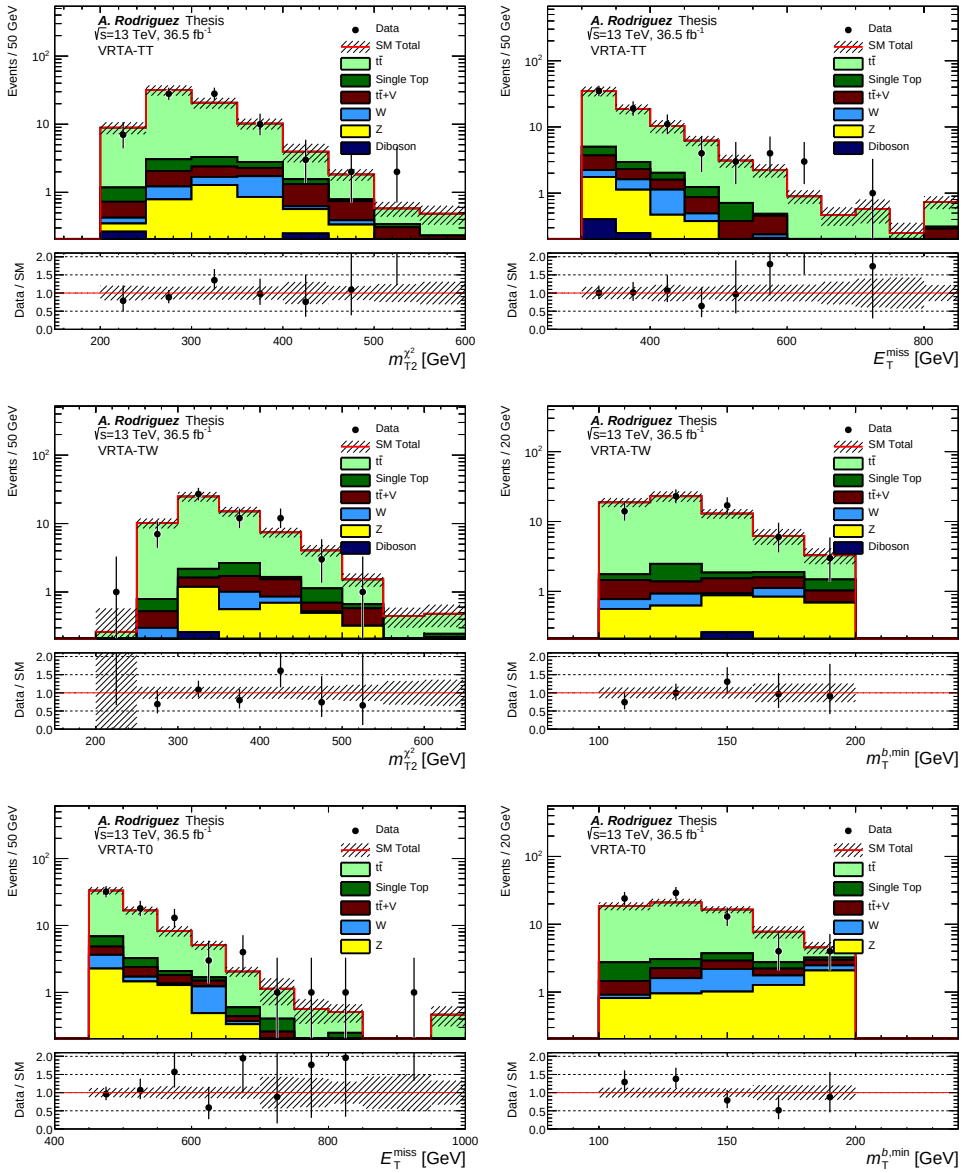

FIGURE 6.25: Distributions of extrapolating variables in the $t\bar{t}$ validation regions for SRA. From top to bottom, m_{T2} and $E_{\mathrm{T}}^{\mathrm{miss}}$ in VRTA-TT, m_{T2} and $m_T^{b,\mathrm{min}}$ in VRTA-TW and $E_{\mathrm{T}}^{\mathrm{miss}}$ and $m_T^{b,\mathrm{min}}$ in VRTA-T0. Statistical and systematic uncertainties are shown, and the background MC samples have been scaled with the factors in 6.24.

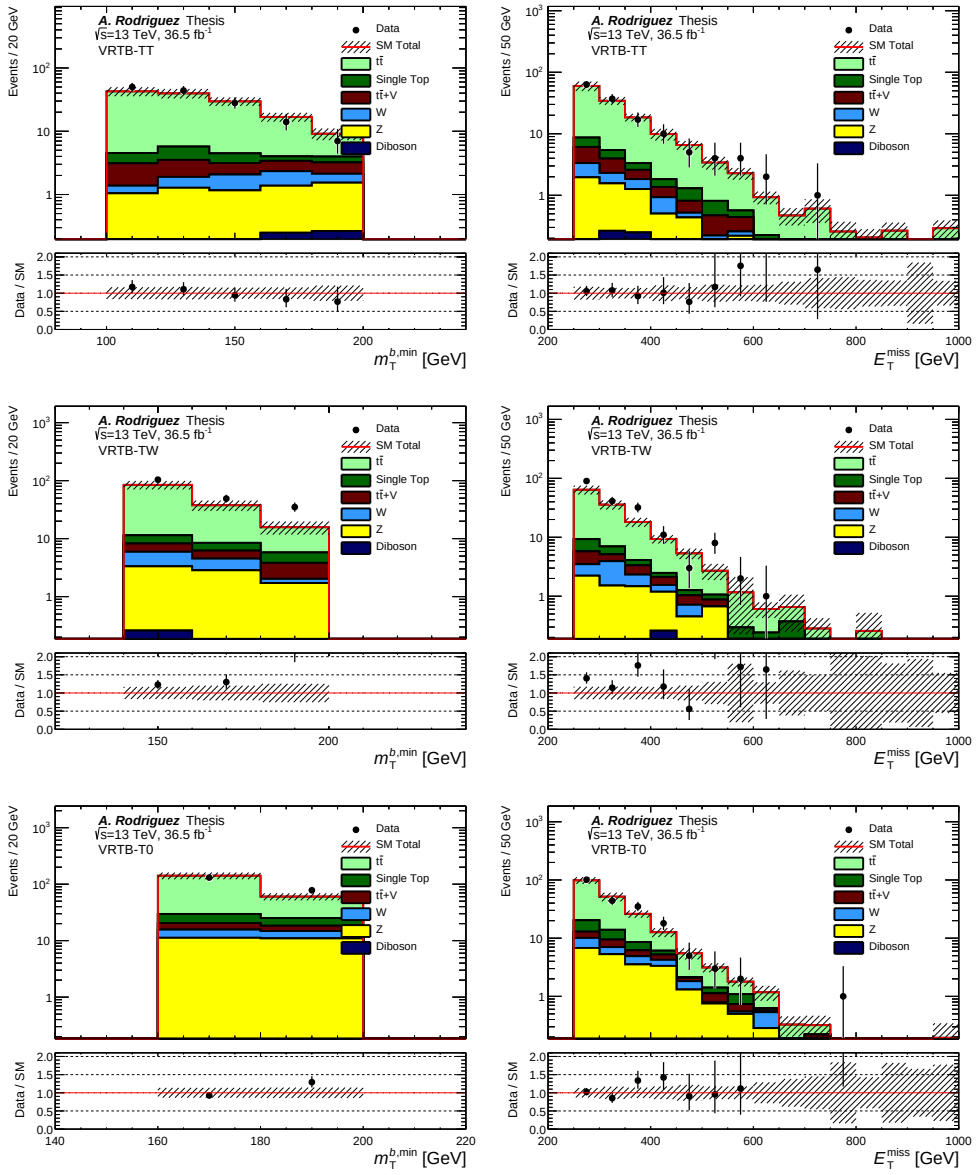

FIGURE 6.26: Distributions of $m_T^{b,\min}$ and $E_{\mathrm{T}}^{\mathrm{miss}}$ in the $t\bar{t}$ validation regions for SRB. From top to bottom, VRTB-TT, VRTB-TW and VRTB-T0. Statistical and systematic uncertainties are shown, and the background MC samples have been scaled with the factors in 6.24.

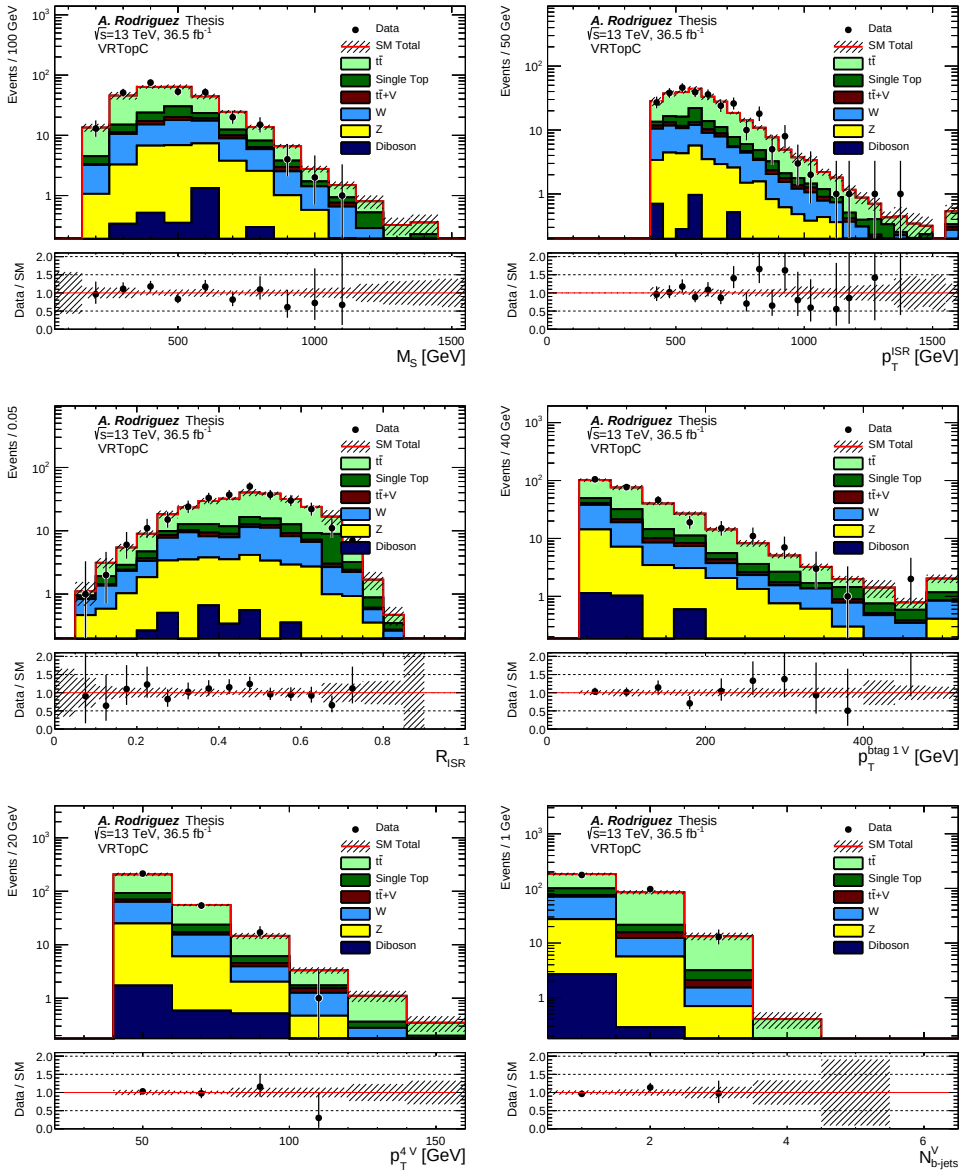

FIGURE 6.27: Distributions of m_S, $p_{\mathrm{T}}^{\mathrm{ISR}}$, R^{ISR}, leading b-tagged jet p_{T}, fourth leading jet p_{T} and number of b-tagged jets in the $t\bar{t}$ validation region for SRC, VRTC. Statistical and systematic uncertainties are shown, and the background MC samples have been scaled with the factors in 6.24.

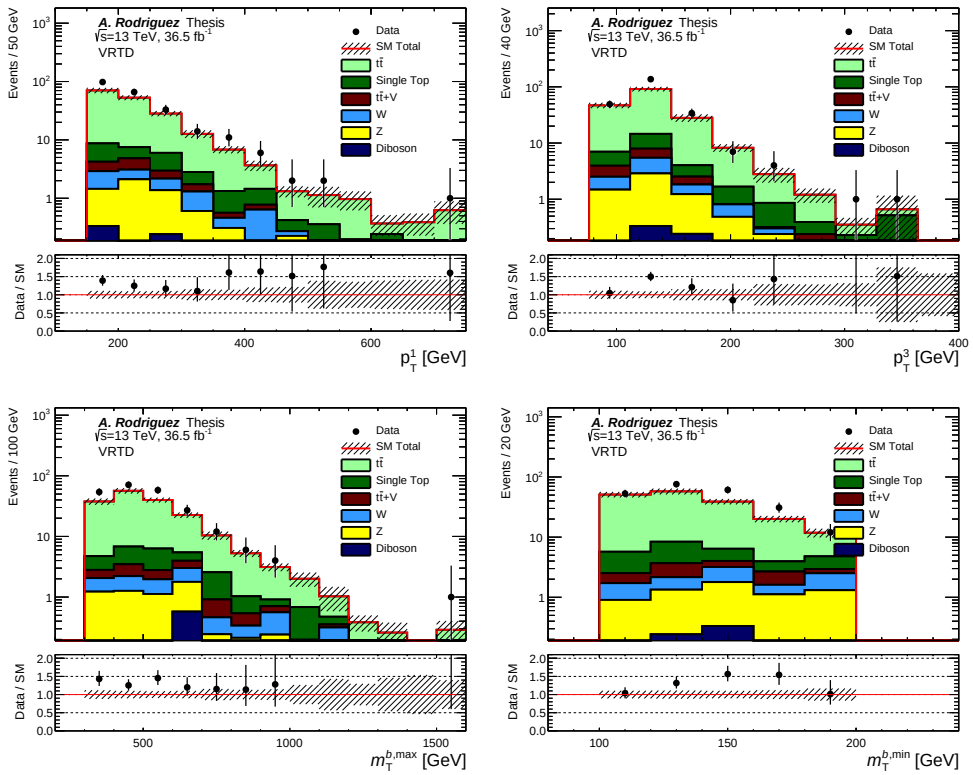

FIGURE 6.28: Distributions of subleading and third leading jet p_{T}, $m_T^{b,\mathrm{min}}$ and $m_T^{b,\mathrm{max}}$ in the $t\bar{t}$ validation region for SRD, VRTD. Statistical and systematic uncertainties are shown, and the background MC samples have been scaled with the factors in 6.24.

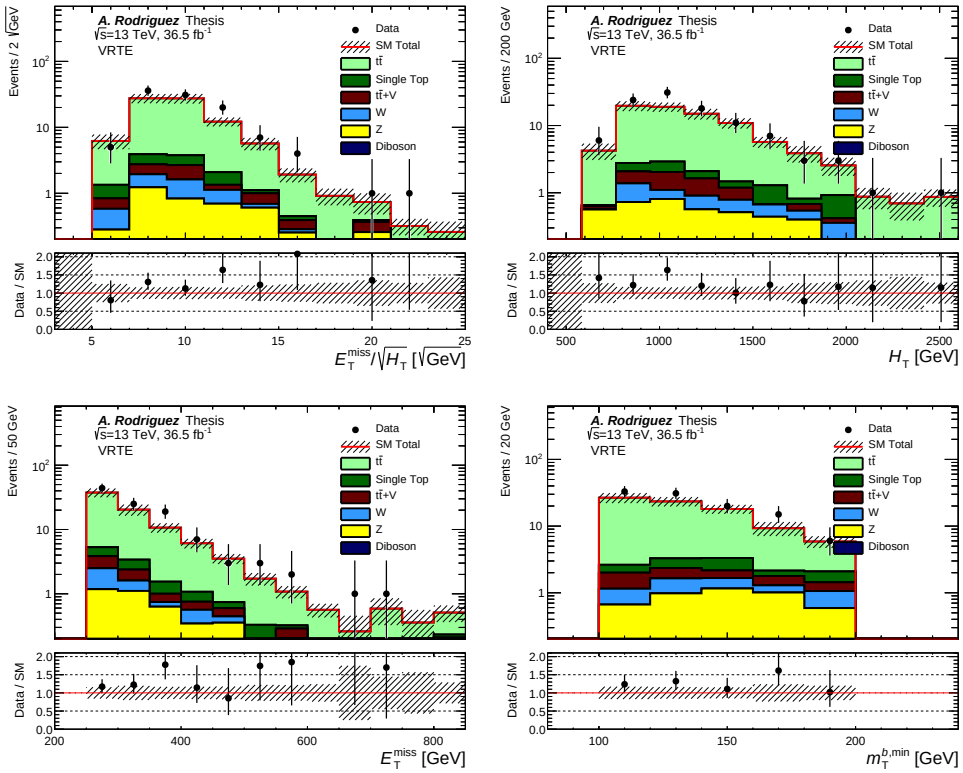

FIGURE 6.29: Distributions of $E_{\mathrm{T}}^{\mathrm{miss}}/\sqrt{H_T}$, H_T, $E_{\mathrm{T}}^{\mathrm{miss}}$ and $m_T^{b,\mathrm{min}}$ in the $t\bar{t}$ validation region for SRE, VRTE. Statistical and systematic uncertainties are shown, and the background MC samples have been scaled with the factors in 6.24.

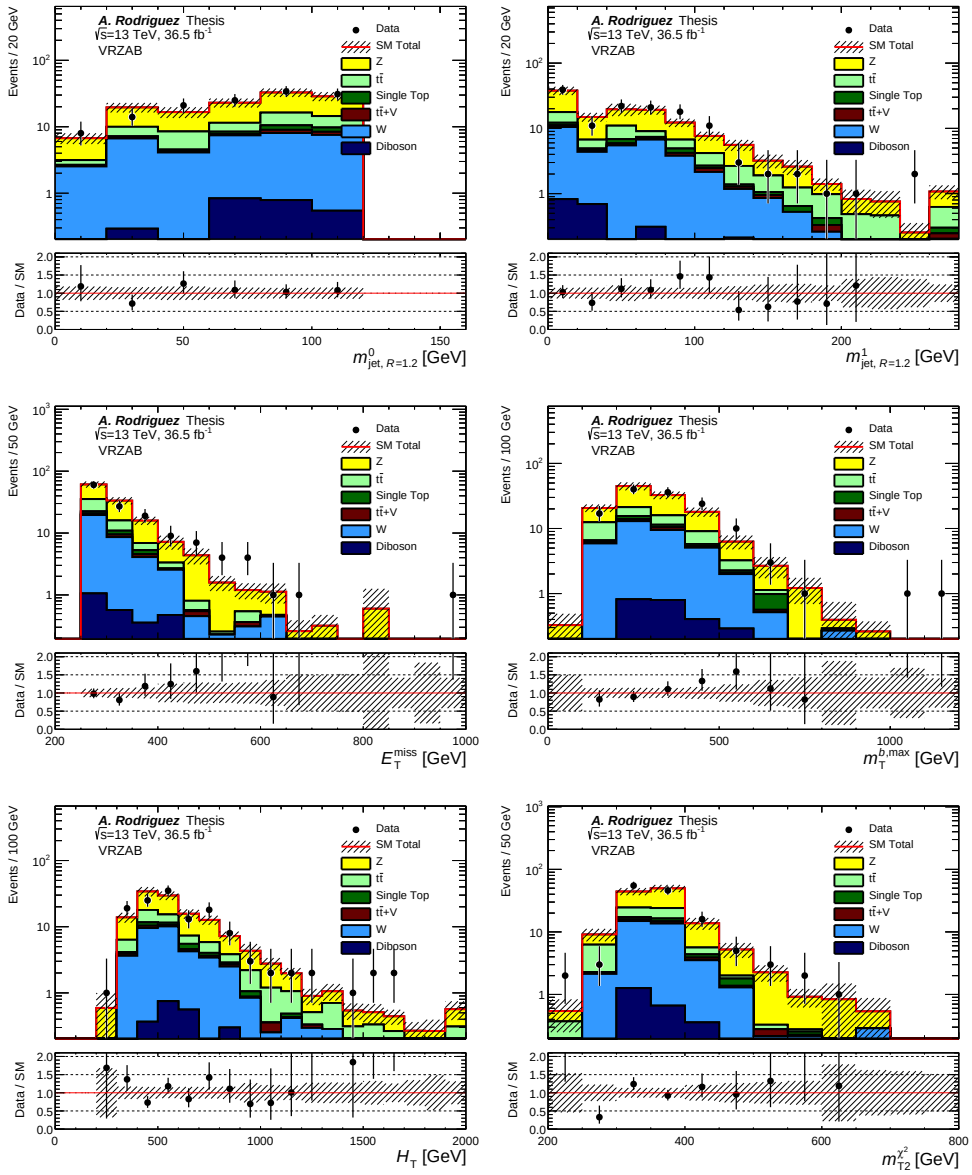

FIGURE 6.30: Distributions of $m^0_{R=1.2}$, $m^1_{R=1.2}$, $E_{\text{T}}^{\text{miss}}$, $m_T^{b,\text{max}}$, H_T and m_{T2} in the Z+jets validation region for SRA and SRB, VRZAB. Statistical and systematic uncertainties are shown, and the background MC samples have been scaled with the factors in 6.24.

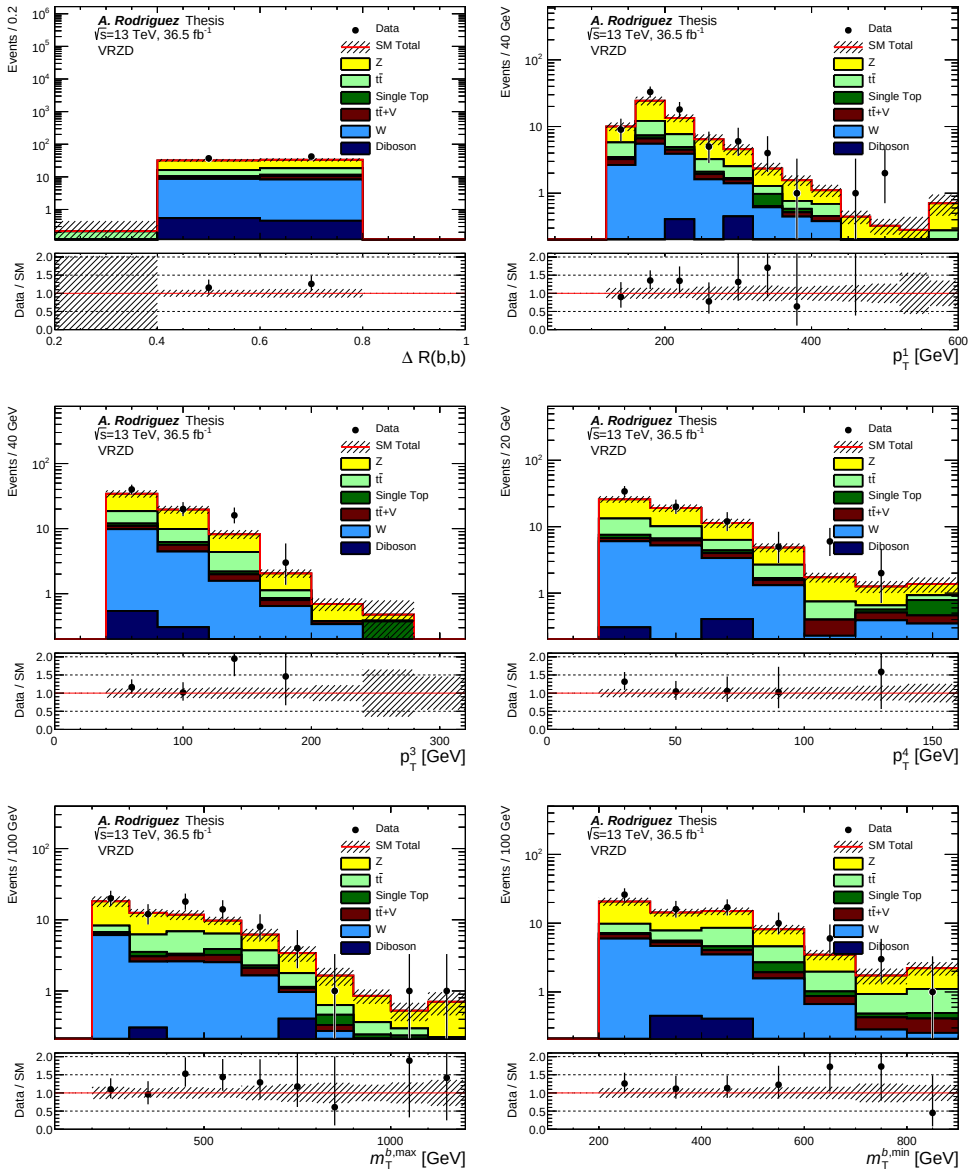

FIGURE 6.31: Distributions of $\Delta R(b,b)$, the second, fourth, and fifth leading jet p_{T}, $m_T^{b,\mathrm{max}}$ and $m_T^{b,\mathrm{min}}$ in the Z+jets validation region for SRD, VRZD. Statistical and systematic uncertainties are shown, and the background MC samples have been scaled with the factors in 6.24.

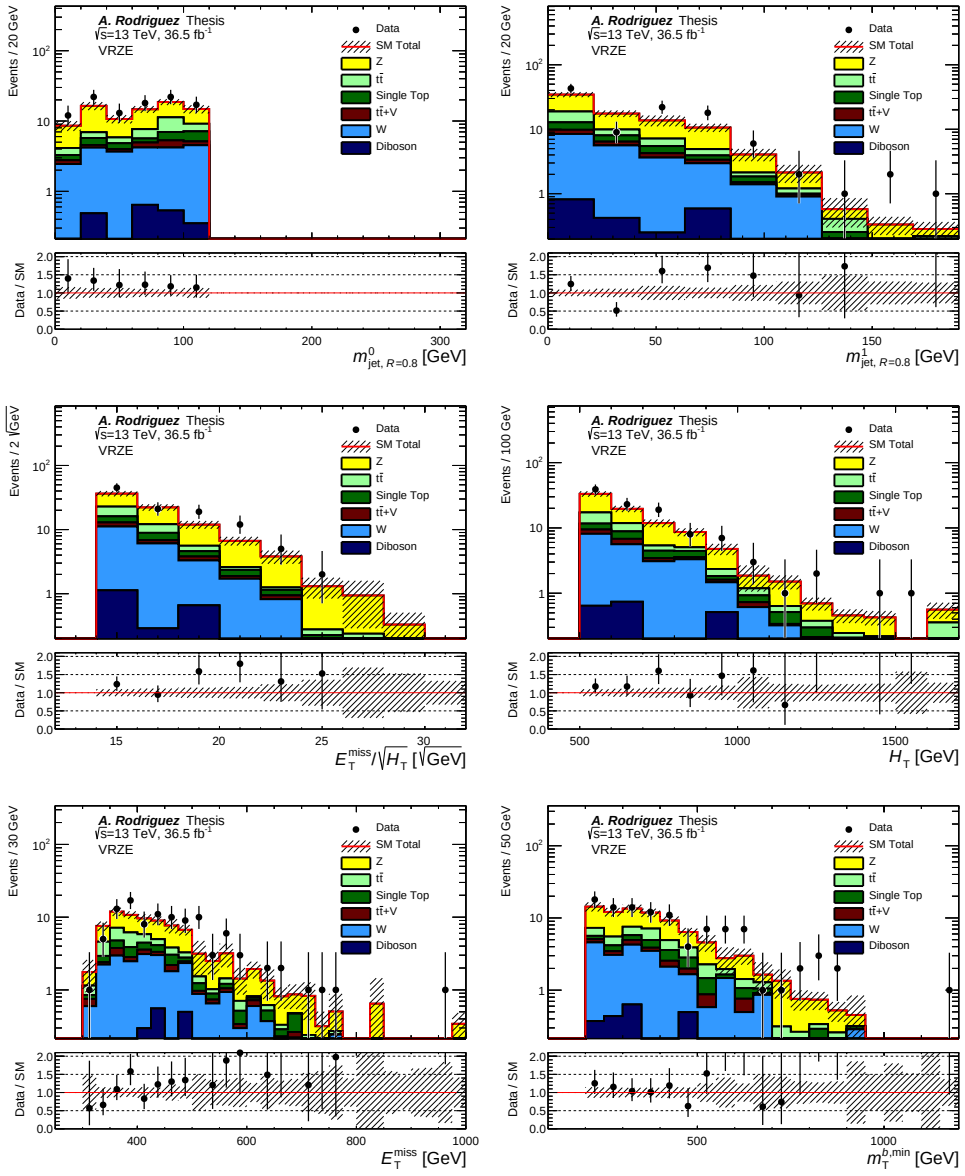

FIGURE 6.32: Distributions of leading and subleading R=1.2 reclustered jet masses, $E_{\mathrm{T}}^{\mathrm{miss}}$ significance, H_T, $E_{\mathrm{T}}^{\mathrm{miss}}$ and $m_T^{b,\mathrm{min}}$ in the Z+jets validation region for SRE, VRZE. Statistical and systematic uncertainties are shown, and the background MC samples have been scaled with the factors in 6.24.

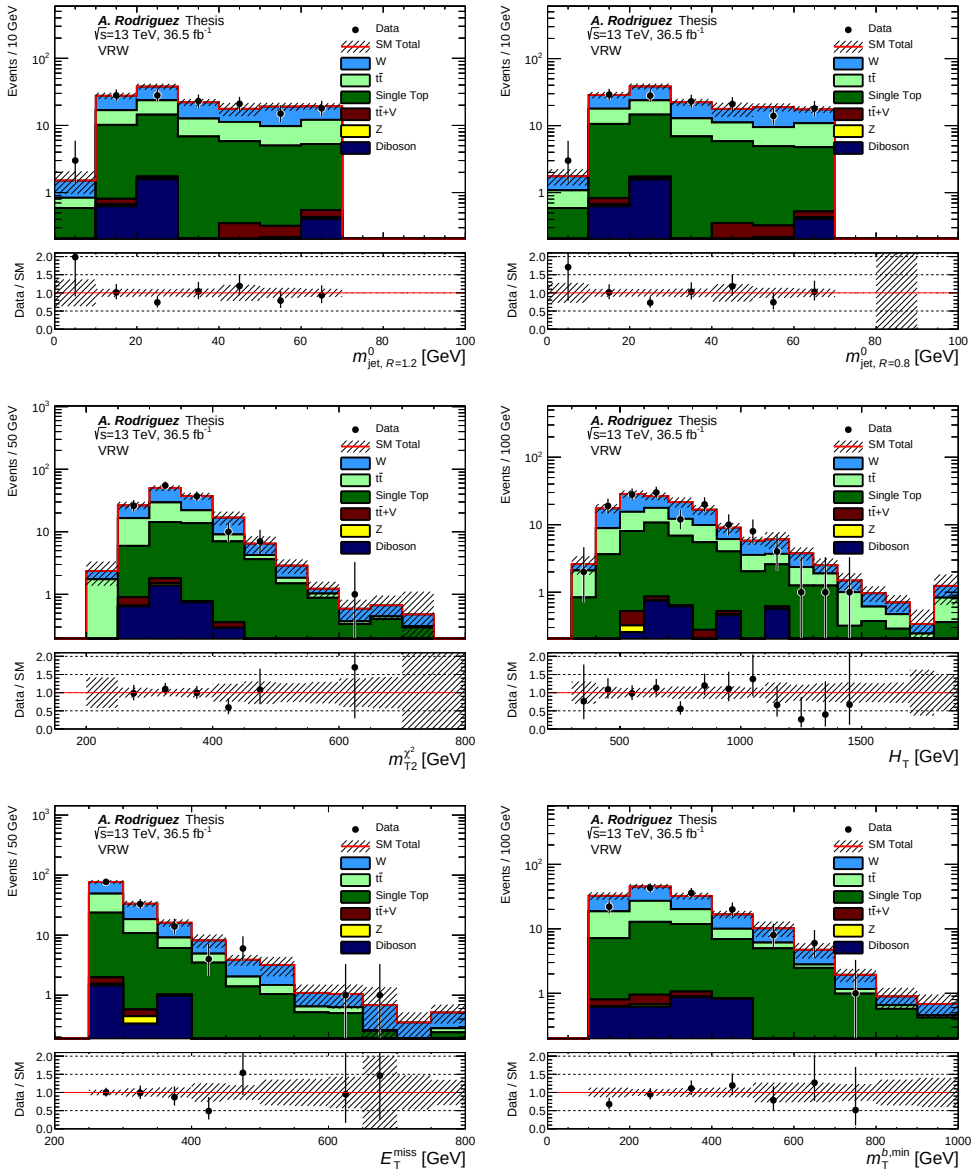

FIGURE 6.33: Distributions of leading R=1.2 and R=0.8 reclustered jet masses, m_{T2}, H_T, $E_{\mathrm{T}}^{\mathrm{miss}}$ and $m_T^{b,\mathrm{min}}$ in the W+jets validation region. Statistical and systematic uncertainties are shown, and the background MC samples have been scaled with the factors in 6.24.

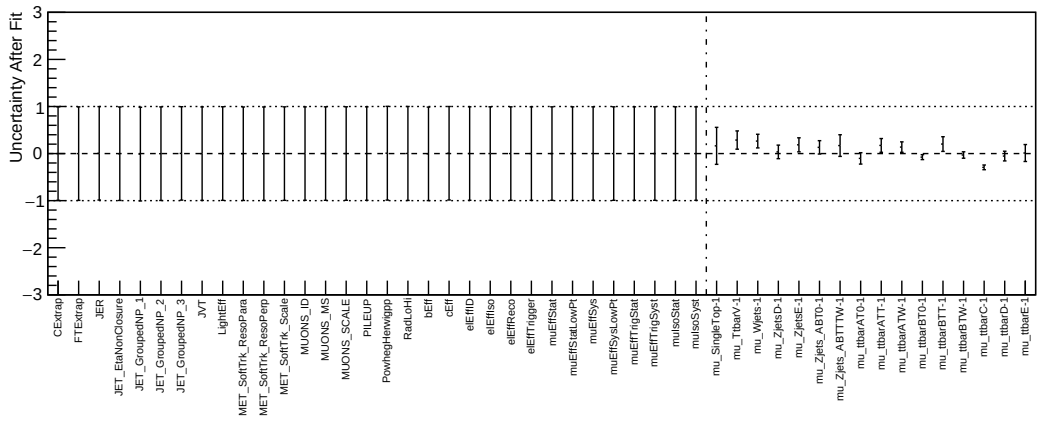

FIGURE 6.34: Pull plot of the nuisance parameters of the fit. The normalisation factors are named *mu_* .

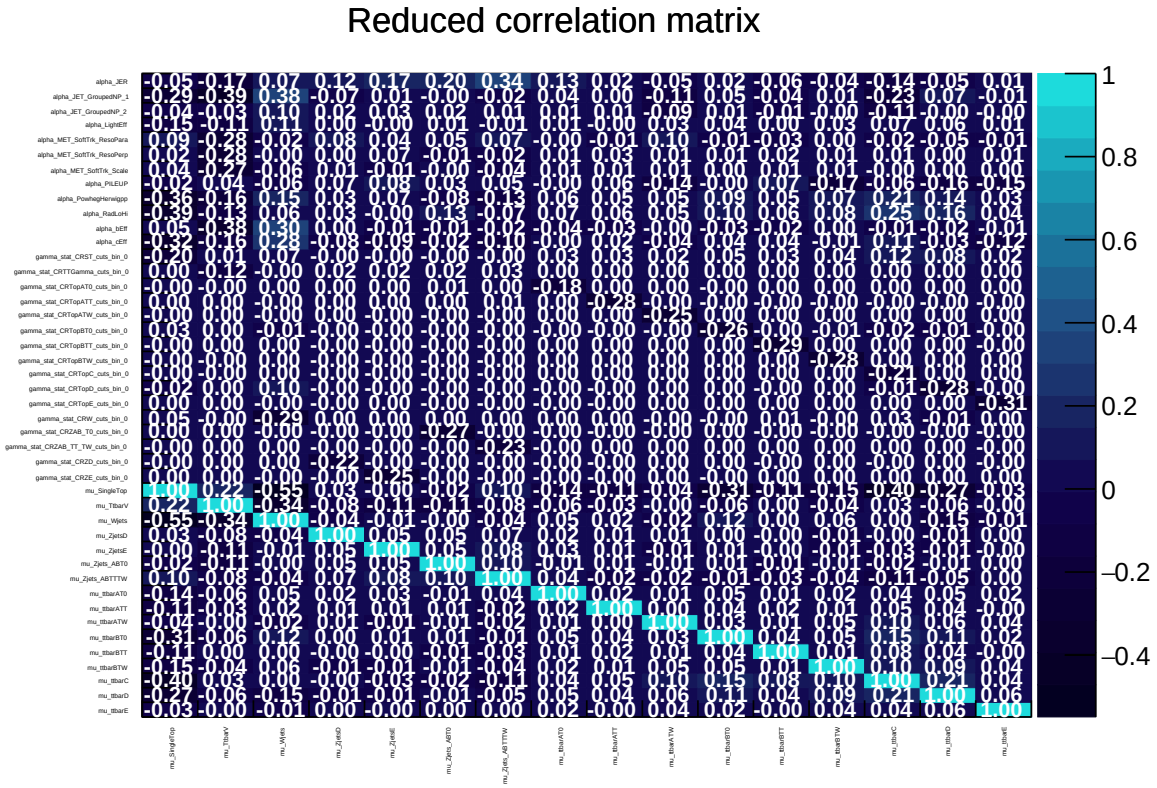

FIGURE 6.35: Correlation Matrix after the background-only fit. A reduced number of nuisance parameters is shown.

CHAPTER 7

Results

This chapter presents the results of the search introduced in chapter 6. As already addressed, the analysis is designed as a number of signal regions optimised for different SUSY models, and a set of control regions dedicated to constrain the main background SM processes in the signal regions. The analysis is carried out blind [1] and the reliability of the SM predictions of the MC samples was first tested in validation regions in section 6.7. The background-only fit results in the signal regions are presented in this chapter. Since good agreement is found with the Standard Model predictions, model-independent limits are calculated on the visible cross section of any new physics model in section 7.2. Limits are then set on the masses of the supersymmetric particles for a number of models in section 7.3.

7.1 Background-only fit in signal regions

The results of the background-only fit on the predicted and observed number of Standard Model events in the signal regions are shown in tables 7.1, 7.2, and 7.3 for signal regions SRA and SRB; SRC, and SRD and SRE, respectively. Systematic uncertainties after the fit are also included. The tables include the total background prediction before and after the fit, with the breakdown of the contributions from the different processes, and the observed number of events. Good agreement is found between data and MC predictions in all regions. Small upper deviations of the data due to fluctuations in SRA-TT, SRB-T0 and SRD-high are, however, observed, with p-values for the background-only hypothesis corresponding to probabilities for background compatibility of 29%, 27% and 27%, respectively. These numbers prove that the deviation from the SM expectation is not large enough to suggest the presence of any signal. Downward fluctuations are also observed, the largest one in SRC4.

Several distributions of the main variables in the signal regions are collected in figure 7.1. The figures are produced after the fit is performed and include normalisation factors and constraints of the systematic uncertainties obtained from the fit (see table 6.24), and the full signal-region selection has been applied. A histogram showing the expected benchmark signal shape is included, as well as the several background processes and the observed data. The shape agreement between data and the MC prediction is in general good within uncertainties.

A summary of the contribution of the different systematics to the total uncertainty in the signal regions can be seen in tables 7.4 and 7.5. Statistical, experimental, and theoretical uncertainties are included, as well as the uncertainties on the normalisation

[1] In a blind analysis, the data events observed in the signal regions is not looked at until the agreement of data and simulation has been thoroughly tested

factors. The correlations of the uncertainties are taken into account by the fit. The largest total uncertainty of 80% is found in SRC5, and in the rest of the regions the total uncertainties oscillate between 14% and 31%. The uncertainties in the Standard Model events predicted in the signal regions are dominated by statistical uncertainties in all the regions except for SRB, where the dominant systematic is the $t\bar{t}$ theory uncertainty. The dominant theoretical systematic uncertainty comes from $t\bar{t}$ modelling in most of the regions, while the largest contribution from detector uncertainties are JER and JES, which constitute up to 17%. The contribution from normalisation factor uncertainties oscillates between 1% and 10 %.

	SRA-TT	SRA-TW	SRA-T0	SRB-TT	SRB-TW	SRB-T0
Observed	11	9	18	38	53	206
Fitted background events						
Total SM	8.6 ± 2.1	9.3 ± 2.2	18.7 ± 2.7	39.3 ± 7.6	52.4 ± 7.4	179 ± 26
$t\bar{t}$	$0.71^{+0.91}_{-0.71}$	$0.51^{+0.55}_{-0.51}$	1.31 ± 0.64	7.3 ± 4.3	12.4 ± 5.9	43 ± 22
W+jets	0.82 ± 0.15	0.89 ± 0.56	2.00 ± 0.83	7.8 ± 2.8	4.8 ± 1.2	25.8 ± 8.8
Z+jets	2.5 ± 1.3	4.9 ± 1.9	9.8 ± 1.6	9.0 ± 2.8	16.8 ± 4.1	60.7 ± 9.6
$t\bar{t}+V$	3.16 ± 0.66	1.84 ± 0.39	2.60 ± 0.53	9.3 ± 1.7	10.8 ± 1.6	20.5 ± 3.2
Single top	1.20 ± 0.81	0.70 ± 0.42	2.9 ± 1.5	4.2 ± 2.2	5.9 ± 2.8	26 ± 13
Dibosons	$--$	0.35 ± 0.26	$--$	0.13 ± 0.07	0.60 ± 0.43	1.04 ± 0.73
Multijets	0.21 ± 0.10	0.14 ± 0.09	0.12 ± 0.07	1.54 ± 0.64	1.01 ± 0.88	1.8 ± 1.5
Expected events before fit						
Total SM	7.1	7.9	16.3	32.4	46.1	162
$t\bar{t}$	0.60	0.45	1.45	6.1	12.8	47
W+jets	0.65	0.70	1.58	6.1	3.83	20.4
Z+jets	2.15	4.2	8.63	7.7	14.4	53.6
$t\bar{t}+V$	2.46	1.43	2.02	7.3	8.4	15.9
Single top	1.03	0.60	2.5	3.6	5.1	22.4
Dibosons	$--$	0.35	$--$	0.13	0.60	1.03
Multijets	0.21	0.14	0.12	1.54	1.01	1.8

TABLE 7.1: Expected and observed number of events before and after the simultaneous background-only fit is SRA and SRB. The errors include systematic and statistical uncertainties

7.2 Model-independent limits

The good agreement between the data and the Standard Model prediction translates into limits on the presence of new physics phenomena. The model-independent limits are calculated in a fit including control and signal regions, where no signal model is assumed, and any signal contamination in the control regions is ignored, as described in section 5.4. The limits are set based on the expected number of SM events and its uncertainty as obtained from MC simulation, and on the observed events in data. In this way, 95% confidence-level model-independent upper limits are set on the visible cross section of any new physics process. The visible cross section is defined as

$$\sigma_{vis} = \sigma \cdot A \cdot \epsilon, \tag{7.1}$$

where σ is the cross section of the process, A is the acceptance of the detector and ϵ is the efficiency of the selection for the signal regions. The values of $A \cdot \epsilon$ obtained

	SRC1	SRC2	SRC3	SRC4	SRC5
Observed	20	22	22	1	0
Fitted background events					
Total SM	20.6 ± 6.5	27.6 ± 4.9	18.9 ± 3.4	7.7 ± 1.2	0.91 ± 0.73
$t\bar{t}$	12.9 ± 5.9	22.1 ± 4.3	14.6 ± 3.2	4.91 ± 0.97	$0.63 \, ^{+0.70}_{-0.63}$
W+jets	0.80 ± 0.37	1.93 ± 0.49	1.91 ± 0.62	1.93 ± 0.46	0.21 ± 0.12
Z+jets	$--$	$--$	$--$	$--$	$--$
$t\bar{t}+V$	0.29 ± 0.16	0.59 ± 0.38	0.56 ± 0.31	0.08 ± 0.08	0.06 ± 0.02
Single top	1.7 ± 1.3	$1.2 \, ^{+1.4}_{-1.2}$	1.22 ± 0.69	0.72 ± 0.37	$--$
Dibosons	0.39 ± 0.33	$0.21 \, ^{+0.23}_{-0.21}$	0.28 ± 0.18	$--$	$--$
Multijets	4.6 ± 2.4	1.58 ± 0.77	0.32 ± 0.17	0.04 ± 0.02	$--$
Expected events before fit					
Total SM	25.4	36.0	24.2	9.2	1.1
$t\bar{t}$	18.2	31.2	20.6	7.0	0.89
W+jets	0.64	1.53	1.51	1.53	0.17
Z+jets	$--$	$--$	$--$	$--$	$--$
$t\bar{t}+V$	0.22	0.46	0.44	0.07	0.05
Single top	1.44	1.0	1.04	0.62	$--$
Dibosons	0.39	0.21	0.28	$--$	$--$
Multijets	4.6	1.58	0.32	0.04	$--$

TABLE 7.2: Expected and observed number of events before and after the simultaneous background-only fit is SRC. The errors include systematic and statistical uncertainties

in the analysis range from 0.05% to 9%. In particular, for SRA and SRE are of 9% and 6% for their respective benchmark signals of $(m_{\tilde{t}_1}, m_{\tilde{\chi}^0_1}) = (1000, 1)$ GeV and $(m_{\tilde{g}}, m_{\tilde{t}_1}) = (1700, 400)$ GeV. In SRB, for $(m_{\tilde{t}_1}, m_{\tilde{\chi}^0_1}) = (600, 300)$ the value of $A \cdot \epsilon$ is 1.4%. SRD-low and SRD-high have $A \cdot \epsilon$ of 0.05% and 0.5%, for their benchmarks $((m_{\tilde{t}_1}, m_{\tilde{\chi}^1_1}, m_{\tilde{\chi}^0_1}) = (400, 100, 50)$ GeV and $((m_{\tilde{t}_1}, m_{\tilde{\chi}^1_1}, m_{\tilde{\chi}^0_1}) = (700, 200, 100)$ GeV. Finally, in SRC, combining all the bins in R_{ISR}, $A \cdot \epsilon = 0.08\%$ for $(m_{\tilde{t}_1}, m_{\tilde{\chi}^0_1}) = (400, 227)$.

The values of the 95% CL model-independent upper limits for the different signal regions are displayed in table 7.6. Upper limits in the range of 0.09 to 2.19 fb are obtained. In addition to the limits on the visible cross section, an upper limit on the number of BSM events in the signal regions is also shown. The CL_B value, defined as the confidence level of the background-only hypothesis, can also be seen in the table, as well as the p-value. The smallest p-value of 0.13 is found in SRB-T0, which indicates good agreement with SM predictions.

Values of visible cross sections above 0.3, 0.27 and 0.31 fb are excluded in SRA for the TT, TW and T0 categories, respectively. In SRB, the values are higher, specially in SRB-T0, due to the excess of observed events commented above. The upper limits for the visible cross sections in SRB are 0.54, 0.60 and 2.19 fb in SRB-TT, SRB-TW an SRB-T0 respectively. In SRC, the upper limits are 0.42, 0.31, 0.42, 0.10 and 0.09 fb for different bins in R_{ISR} of the signal region. In SRD-high and low all cross sections above 0.5 and 0.3 fb, respectively, are excluded, and for SRE the limit is 0.17 fb.

	SRD-low	SRD-high	SRE
Observed	27	11	3
Fitted background events			
Total SM	25.1 ± 6.2	8.5 ± 1.5	3.64 ± 0.79
$t\bar{t}$	3.3 ± 3.3	0.98 ± 0.88	$0.21 \,^{+0.39}_{-0.21}$
W+jets	6.1 ± 2.9	1.06 ± 0.34	0.52 ± 0.27
Z+jets	6.9 ± 1.5	3.21 ± 0.62	1.36 ± 0.25
$t\bar{t}+V$	3.94 ± 0.85	1.37 ± 0.32	0.89 ± 0.19
Single top	3.8 ± 2.1	1.51 ± 0.74	0.66 ± 0.49
Dibosons	$--$	$--$	$--$
Multijets	1.12 ± 0.37	0.40 ± 0.15	$--$
Expected events before fit			
Total SM	22.4	7.7	3.02
$t\bar{t}$	3.4	1.04	0.21
W+jets	4.8	0.84	0.42
Z+jets	6.7	3.10	1.15
$t\bar{t}+V$	3.06	1.07	0.69
Single top	3.3	1.30	0.56
Dibosons	$--$	$--$	$--$
Multijets	1.12	0.40	$--$

TABLE 7.3: Expected and observed number of events before and after the simultaneous background-only fit is SRD and SRE. The errors include systematic and statistical uncertainties

7.3 Interpretation

An exclusion fit is used to set limits on the specific simplified models [107, 130] of new physics using as test statistic the profile likelihood ratio described in chapter 5. The fit is performed separately for each of the signal models used. The signal contamination in the control regions is taken into account, and the signal strength parameter is allowed to float in the fit. In this case, signal systematics are taken into account, both detector-related and theoretical uncertainties. The main sources of detector uncertainties are, as for the background, JER and JES uncertainties, which range from 2% to 6%. Theoretical uncertainties vary across the signal regions between 10 and 25% for all models except the well-tempered neutralino pMSSM, where they can be up to 35%, as presented in table 6.23.

Orthogonal signal subregions are statistically combined multiplying their likelihoods, while overlapping subregions such as SRD-low and SRD-high are combined by choosing the one with the lowest CL_s value (best expected) for each signal model. Then, for each model, the signal region with lowest expected CL_s is chosen. The observed limits are calculated using the observed event yield in data in the signal regions, while for the expected limits the nominal event yield is set to the nominal background expectation as determined by the MC simulation constrained to the data in the control regions. The $\pm 1\sigma$ uncertainty for the observed limits is calculated from the cross section theory uncertainty, while for the expected limits the $\pm 1\sigma$ is calculated from the uncertainties in the background estimations.

Signal models considering several decay modes of the stop to $t+\tilde{\chi}_1^0$, $b+\tilde{\chi}_1^\pm$ and additional massive neutralinos are used in the interpretation of the results and described in the following.

	SRA-TT	SRA-TW	SRA-T0	SRB-TT	SRB-TW	SRB-T0
Total stat. unc.	34	33	23	16	14	7
Total syst. unc.	24	23	15	19	14	15
$t\bar{t}$ theory	10	6	3	10	11	12
$t\bar{t}+Z/W$ theory	2	<1	<1	1	<1	<1
Z theory	1	3	2	<1	1	<1
Single top theory	6	3	5	3	4	5
Diboson theory	<1	2	<1	<1	<1	<1
$\mu_{t\bar{t}}$	<1	<1	<1	2	2	1
$\mu_{t\bar{t}+Z}$	6	3	2	4	3	2
μ_Z	6	10	7	5	6	4
μ_W	1	1	1	2	1	2
$\mu_{\text{single top}}$	5	3	5	4	4	5
JER	10	12	4	3	4	3
JES	4	7	1	7	4	<1
b-tagging	1	3	2	5	4	4
$E_{\text{T}}^{\text{miss}}$ soft term	2	2	<1	1	<1	<1
Multijet estimate	1	<1	<1	2	2	<1
Pileup	10	5	5	8	1	3

TABLE 7.4: Summary of the dominant systematic uncertainties and their contribution to the total uncertainty in the SM prediction in signal regions A and B. The uncertainties indicated with a μ correspond to the normalisation factors of the different backgrounds.

	SRC1	SRC2	SRC3	SRC4	SRC5	SRD-low	SRD-high	SRE
Total stat. unc.	22	19	23	36	100	20	34	52
Total syst. unc.	31	18	18	16	80	25	18	22
$t\bar{t}$ theory	27	11	14	11	71	12	10	11
$t\bar{t}$+V theory	<1	<1	<1	<1	<1	<1	<1	1
Z theory	<1	<1	<1	<1	<1	<1	<1	2
W theory	<1	<1	1	3	2	<1	<1	1
Single top theory	3	2	2	3	<1	5	6	12
$\mu_{t\bar{t}}$	4	6	6	5	5	1	1	<1
μ_{tt+Z}	<1	<1	<1	<1	<1	2	2	4
μ_Z	<1	<1	<1	<1	<1	4	5	5
μ_W	<1	<1	1	3	3	3	1	2
$\mu_{\text{single top}}$	3	2	2	3	<1	5	6	6
JER	4	10	6	5	10	3	6	4
JES	4	5	2	2	17	8	4	5
b-tagging	2	2	<1	2	4	9	7	<1
$E_{\text{T}}^{\text{miss}}$ soft term	1	3	2	3	15	4	3	2
Multijet estimate	12	3	<1	<1	<1	2	2	<1
Pileup	<1	1	<1	2	14	9	<1	2

TABLE 7.5: Summary of the dominant systematic uncertainties and their contribution to the total uncertainty in the SM prediction in signal regions C, D and E. The uncertainties indicated with a μ correspond to the normalisation factors of the different backgrounds.

Signal channel	$\langle \sigma A \epsilon \rangle^{95}_{\text{obs}}$ [fb]	S^{95}_{obs}	S^{95}_{exp}	CL_B	p (z)
SRA-TT	0.30	11.0	$8.7^{+3.0}_{-1.4}$	0.78	0.23 (0.74)
SRA-TW	0.27	9.6	$9.6^{+2.8}_{-2.1}$	0.50	0.50 (0.00)
SRA-T0	0.31	11.2	$11.5^{+3.8}_{-2.0}$	0.46	0.50 (0.00)
SRB-TT	0.54	19.6	$20.0^{+6.5}_{-4.9}$	0.46	0.50 (0.00)
SRB-TW	0.60	21.7	$21.0^{+7.3}_{-4.3}$	0.54	0.50 (0.00)
SRB-T0	2.19	80	58^{+23}_{-17}	0.83	0.13 (1.15)
SRC1	0.42	15.1	$15.8^{+4.8}_{-3.5}$	0.48	0.50 (0.00)
SRC2	0.31	11.2	$13.9^{+5.9}_{-3.6}$	0.24	0.50 (0.00)
SRC3	0.42	15.3	$12.3^{+4.7}_{-3.4}$	0.73	0.27 (0.62)
SRC4	0.10	3.5	$6.7^{+2.8}_{-1.8}$	0.00	0.50 (0.00)
SRC5	0.09	3.2	$3.0^{+1.1}_{-0.1}$	0.23	0.23 (0.74)
SRD-low	0.50	17.9	$16.4^{+6.3}_{-4.0}$	0.62	0.36 (0.35)
SRD-high	0.30	10.9	$8.0^{+3.4}_{-1.3}$	0.79	0.21 (0.79)
SRE	0.17	6.1	$6.4^{+1.4}_{-2.4}$	0.42	0.50 (0.00)

TABLE 7.6: Upper limit table for the different signal regions. From left to right: 95% confidence level limits on the average visible cross section ($\langle \sigma A \epsilon \rangle^{95}_{\text{obs}}$), observed ($S^{95}_{\text{obs}}$) and expected ($S^{95}_{\text{exp}}$) upper limit on the number of signal events, where the expected number is calculated from the expected number of background events; confidence level for the background-only hypothesis (CL_B), and discovery p-value, with its associated significance value (z).

7.3.1 Stop to top and neutralino

In figure 7.2, the scenario in which both stops decay through $\tilde{t}_1 \to t\tilde{\chi}^0_1$ is considered for exclusion. The observed and expected exclusion contours at 95% CL are shown in the stop-neutralino mass plane. For neutralino masses below 200 GeV, stop masses between 400 and 1000 GeV are excluded. The limits improve largely those obtained in Run-1 analyses with $\sqrt{s} = 8$ TeV, from 700 to 100 GeV of stop mass for neutralino masses of around 100 GeV. The previous Run-1 limits are shown in the figure as well. The remarkable extension of the limits in the area close to the diagonal, where $m_{\tilde{t}_1} \sim m_t + m_{\tilde{\chi}^0_1}$ is due to the inclusion of SRC, which is very sensitive to such models thanks to the usage of an ISR system for background discrimination.

7.3.2 Natural SUSY-inspired mixed grid

Two decay modes are simultaneously considered [131], $\tilde{t}_1 \to t\tilde{\chi}^0_1$ and $\tilde{t}_1 \to b\tilde{\chi}^\pm_1$; with branching fractions for the $\tilde{t}_1 \to t\tilde{\chi}^0_1$ process of 0%, 25%, 75% and 100%. The same nature of the LSP is assumed as for the previous case (pure bino), and the mass of the chargino is considered to be $m_{\tilde{\chi}^\pm_1} = m_{\tilde{\chi}^0_1} + 1$ GeV. The exclusion limits at 95% CL in the stop-neutralino mass plane obtained for the different branching fraction assumptions are shown in figure 7.3. For neutralino masses below 150 GeV, stop masses are excluded for the pure $b + \tilde{\chi}^\pm_1$ up to 800 GeV. For higher branching ratios of $t + \tilde{\chi}^0_1$ decays the exclusion contour expands, reaching $m(\tilde{t}_1) \sim 900$ GeV for 25% and 50%, and 950 for BR=75%. The better exclusion for higher branching fractions of the $t\tilde{\chi}^0_1$ decay is expected, since most of the signal regions were optimised for this case.

7.3.3 Non-asymptotic higgsino

A pMSSM-inspired simplified model [132] with a higgsino LSP is considered, where three different decays of the stop are allowed, $\tilde{t}_1 \to t\tilde{\chi}_2^0$, $\tilde{t}_1 \to t\tilde{\chi}_1^0$ and $\tilde{t}_1 \to b\tilde{\chi}_1^\pm$. The masses are assumed to be $m_{\tilde{\chi}_2^0} = m_{\tilde{\chi}_1^0} + 10$ GeV and $m_{\tilde{\chi}_1^\pm} = m_{\tilde{\chi}_1^0} + 5$ GeV. Three sets of branching ratios are considered. First, the branching ratios are set to $B(\tilde{t}_1 \to t\tilde{\chi}_2^0, \tilde{t}_1 \to t\tilde{\chi}_1^0, \tilde{t}_1 \to b\tilde{\chi}_1^\pm)$=33%,33%,33%, which corresponds to a pMSSM model with $\tan\beta = 60$, where the lightest top squark mostly consists of the superpartner of the left-handed top quark. In addition, models with branching ratios $B(\tilde{t}_1 \to t\tilde{\chi}_2^0, \tilde{t}_1 \to t\tilde{\chi}_1^0, \tilde{t}_1 \to b\tilde{\chi}_1^\pm)$=45%,10%,45% are considered, which correspond to scenarios where the third-generation left-handed mass parameter is smaller than the superpartner of the right-handed top quark mass parameter, i.e. $m_{\tilde{q}3L} < m_{\tilde{t}R}$. Finally, branching ratios $B(\tilde{t}_1 \to t\tilde{\chi}_2^0, \tilde{t}_1 \to t\tilde{\chi}_1^0, \tilde{t}_1 \to b\tilde{\chi}_1^\pm)$=25%,50%,25% correspond to $\tan\beta$=20 and they are also included in the interpretations. The obtained exclusion limits in the stop-neutralino mass plane are shown in figure 7.4 at 95% confidence level. For models with BR=(25,50,25)%, stop masses up to $\sim$ 840 GeV are excluded when $m(\tilde{\chi}_1^0) = 200$ GeV, while for BR=(33,33,33)% and (45,10,45)% stop masses up to 860 and 900 are excluded for the same neutralino mass, respectively.

7.3.4 Wino-NLSP pMSSM grid

A pMSSM model with bino-like LSP and wino-like NLSP with masses M_1 and $M_2 = 2 \cdot M_1$ is used. Sbottom and stop pair production are included, with decays

- $\tilde{t}_1 \to t\tilde{\chi}_2^0$
- $\tilde{t}_1 \to b\tilde{\chi}_1^\pm$
- $\tilde{b}_1 \to t\tilde{\chi}_1^\pm$
- $\tilde{b}_1 \to b\tilde{\chi}_2^0$

Where the second neutralino decays through $\tilde{\chi}_2^0 \to h/Z\tilde{\chi}_1^0$, where the dominant decay depends on the sign of the higgsino mass parameter μ. The chargino decays through $\tilde{\chi}_1^\pm \to W\tilde{\chi}_1^0$. The pMSSM parameters are $M_3 = 2.2$ TeV (gluino mass), $M_S = \sqrt{m_{\tilde{t}_1} m_{\tilde{t}_2}} = 1.2$ TeV, $\tan\beta = 20$ and $a_t/M_S = \sqrt{6}$, where a_t is the mixing parameter between the left and right components of the stop. The masses of the rest of the SUSY particles are set to > 3 TeV. The exclusion limits are shown in figure 7.5.

7.3.5 Well-tempered neutralino pMSSM

A model where three light neutralinos and a light chargino with masses within 50 GeV of the LSP are considered is used. Sbottom and stop production is considered, which decay to $t\tilde{\chi}_{1,2,3}^0$ or $b\tilde{\chi}_1^\pm$. The pMSSM parameters for this model are $M_1 = -(\mu + \delta)$, with $\delta = 20 - 50$ GeV, $M_2 = 2$ TeV, $M_3 = 0.8 - 1.2$ TeV, $X_t/M_S \sim \sqrt{6}$ and $\tan\beta$=20. The 95% confidence level exclusion limits are shown in figure 7.6. The contours for $\tilde{t}_L$ and $\tilde{t}_R$ scans are shown. Models with $\tilde{t}_1 \approx \tilde{t}_L$ of stop masses up to 800 GeV are excluded for $m(\tilde{\chi}_1^0) = 200$ GeV. The exclusion contour for $\tilde{t}_1 \approx \tilde{t}_R$ models is smaller, reaching stop masses of 600 GeV only for neutralino masses below 150 GeV.

7.3.6 Gluino mediated stop

The SRE results are used for an exclusion fit with gluino-mediated stop production models. The exclusion limits at 95% confidence level are shown in figure 7.7 in the

gluino-stop mass plane, with $\Delta m(\tilde{t}_1, \tilde{\chi}_1^0) = 5$ GeV. Gluino masses up to 1800 GeV for stop masses up to 800 GeV are excluded as can be seen in the figure. The results extend widely those of previous searches, which were set at 1400 GeV stop mass for a 300 GeV neutralino and are overlaid in the figure.

7.4 Future prospects

The results shown extensively improve limits from previous searches, and set limits on models not explored before. These improvements are due to the increase of luminosity and centre-of-mass energy of the LHC from the previous Run-1, but to the developments in the analyses that optimise background/signal separation, reduce systematic uncertainties and improve the background constraints in the signal regions.

The extensive searches for Supersymmetric particles carried out in the ATLAS and CMS Experiments during Run-1 and Run-2 of the LHC have set stringent limits on the existence of natural SUSY. Searches for a variety of particles and decay modes have shown no evidence of signals compatible with the models studied. Good agreement with the SM expectations was observed now and again, not only in dedicated SUSY analyses, but also on the properties of the Higgs boson and other SM particles.

However, all LHC searches use simplified models, and the limits set on the parameters derived from them are not necessarily representative of the full model. In fact, due to the large amount of free parameters of a complete supersymmetric theory like the MSSM, it is not easy to constrain it with the available information. A full scan on the pMSSM parameters was published after the Run-1 data-taking period, using the results from 22 separate SUSY searches in ATLAS [135], but such a study is not yet available for Run-2 data. Consequently, it is not easy to estimate the implications of the current status of the SUSY searches on the viability of a natural supersymmetric extension of the SM.

The upgrade of the LHC scheduled between 2019 and 2026 will increase the instantaneous luminosity to up to 7 times more than the LHC design luminosity. This will translate in an integrated luminosity after Run-3 of about 300 fb^{-1}, and after the High Luminosity LHC era (HL-LHC) of 3000 fb^{-1}. It will thus provide a unique opportunity to further probe natural SUSY, and discover, or rule out, the existence of superpartners. The results presented in this chapter are dominated by statistics, and therefore an increase in luminosity is expected to provide an improvement in the exclusion or discovery reach. As an example, figure 7.8 shows some prospects on the exclusion of stop and neutralino masses by the end of Run-3 and HL-LHC. The studies are based on the Run-1 analysis, and therefore are pessimistic since they do not include the developments included in the Run-2 analysis presented in this chapter.

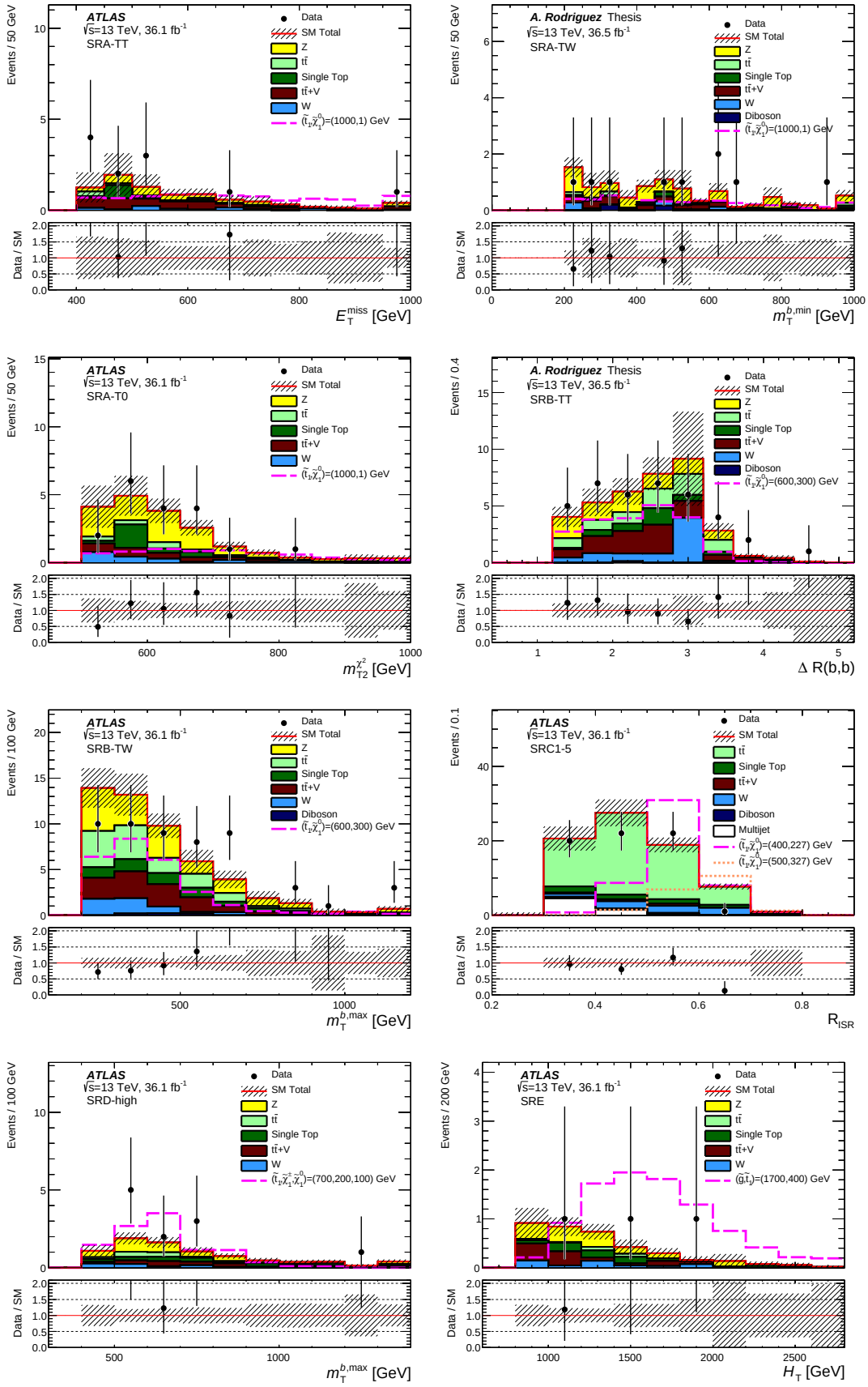

FIGURE 7.1: Distributions of $E_{\mathrm{T}}^{\mathrm{miss}}$ in SRA-TT, m_{T2} in SRA-T0, $m_T^{b,\mathrm{max}}$ in SRB-TW, R_{ISR} in SRC, $m_T^{b,\mathrm{max}}$ in SRD-high and H_T in SRE. The errors include statistical and systematic uncertainties

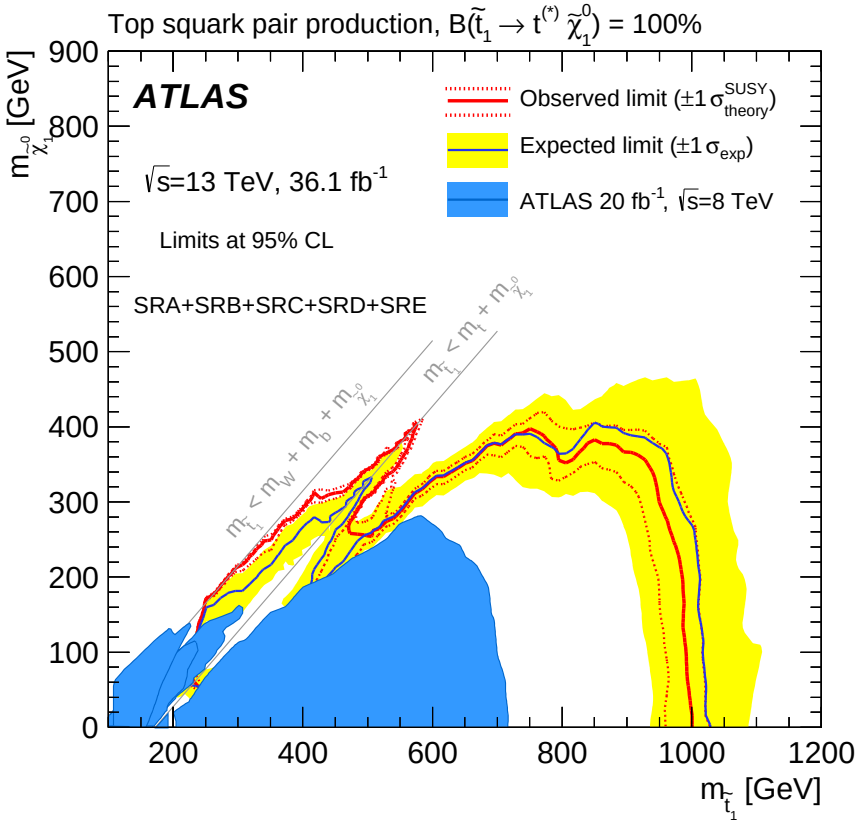

FIGURE 7.2: Observed (red solid line) and expected (blue solid line) exclusion limits at 95% confidence level as a function of $\tilde{t}_1$ and $\tilde{\chi}_1^0$ masses in the scenario where both directly produced stops decay to a top and a neutralino. Models with masses inside the contours are excluded. Uncertainty bands of $\pm 1\sigma$ are also shown. Observed limits from previous analysis in Run-1 searches at $\sqrt{s} = 8$ TeV [97] are overlaid for comparison in blue.

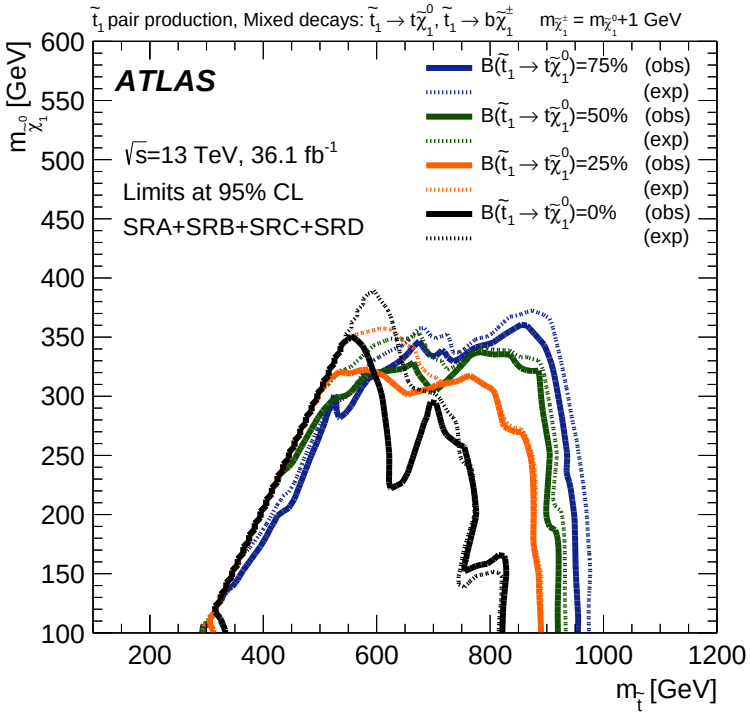

FIGURE 7.3: Observed (solid line) and expected (dashed line) exclusion limits at 95% CL as a function of $m_{\tilde{t}_1}$ and $m_{\tilde{\chi}_1^0}$ for different branching ratios of $\tilde{t}_1 \to t\tilde{\chi}_1^0$ and $\tilde{t}_1 \to b\tilde{\chi}_1^\pm$. The chargino mass is assumed to be $m_{\tilde{\chi}_1^\pm} = m_{\tilde{\chi}_1^0} + 1$ GeV.

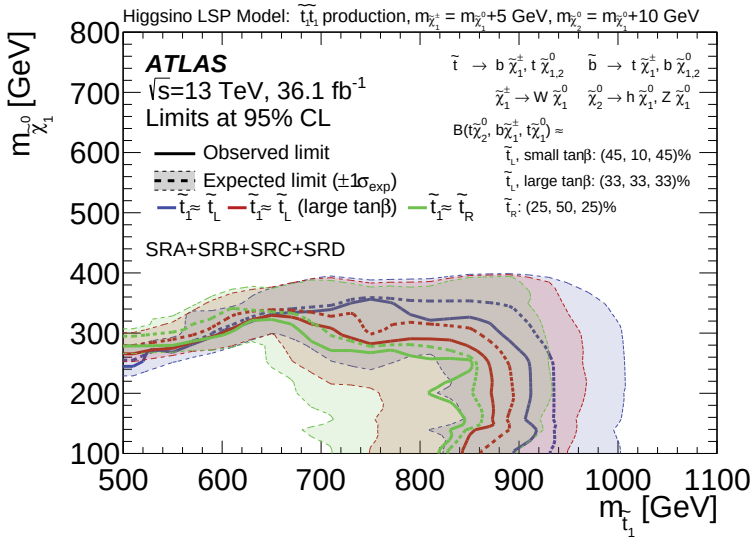

FIGURE 7.4: Observed (solid line) and expected (dashed line) exclusion limits at 95% CL as a function of $m_{\tilde{t}_1}$ and $m_{\tilde{\chi}_1^0}$ for the non-asymptotic higgsino models. Three sets of branching ratios are considered: $B(\tilde{t}_1 \to t\tilde{\chi}_2^0, \tilde{t}_1 \to t\tilde{\chi}_1^0, \tilde{t}_1 \to b\tilde{\chi}_1^\pm)$=(33,33,33)% (red), $B(\tilde{t}_1 \to t\tilde{\chi}_2^0, \tilde{t}_1 \to t\tilde{\chi}_1^0, \tilde{t}_1 \to b\tilde{\chi}_1^\pm)$=(45,10,45)% (blue) and $B(\tilde{t}_1 \to t\tilde{\chi}_2^0, \tilde{t}_1 \to t\tilde{\chi}_1^0, \tilde{t}_1 \to b\tilde{\chi}_1^\pm)$=(25,50,25)% (green). The uncertainty bands show the $\pm 1\sigma$ variation of the expected limit.

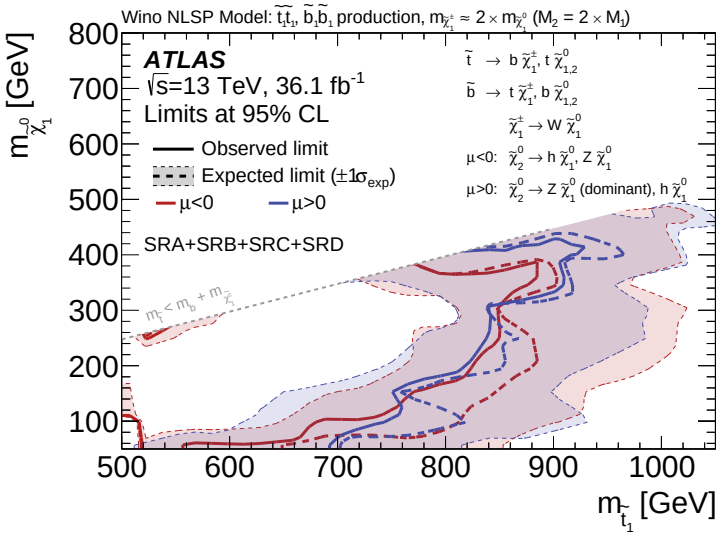

FIGURE 7.5: Observed (solid line) and expected (dashed line) exclusion limits at 95% CL as a function of $m_{\tilde{t}_1}$ and $m_{\tilde{\chi}_1^0}$ for the Wino NLSP pMSSM model for positive (blue) and negative (red) values of μ. The uncertainty bands show the $\pm 1\sigma$ variations of the expected limit.

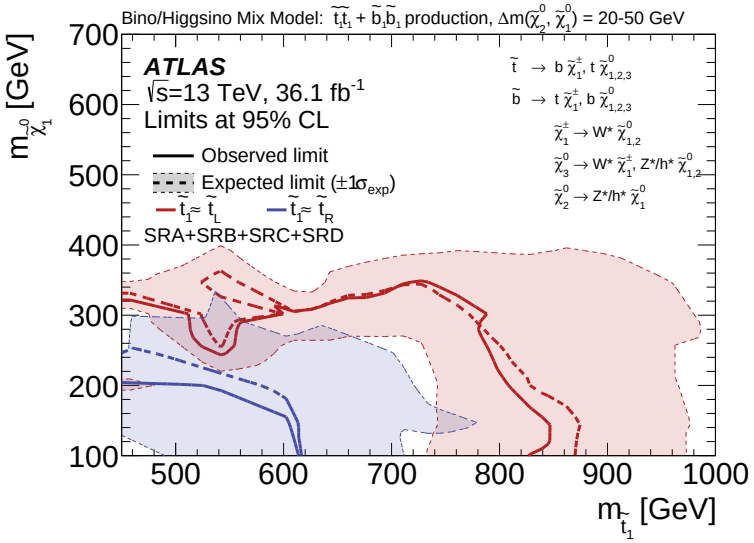

FIGURE 7.6: Observed (solid line) and expected (dashed line) exclusion limits at 95% CL as a function of $m_{\tilde{t}_1}$ and $m_{\tilde{\chi}_1^0}$ for well-tempered pMSSM model, where the $\tilde{t}_L$ (red) and the $\tilde{t}_R$ (blue) scans are shown. The uncertainty bands show the $\pm 1\sigma$ variations of the expected limit.

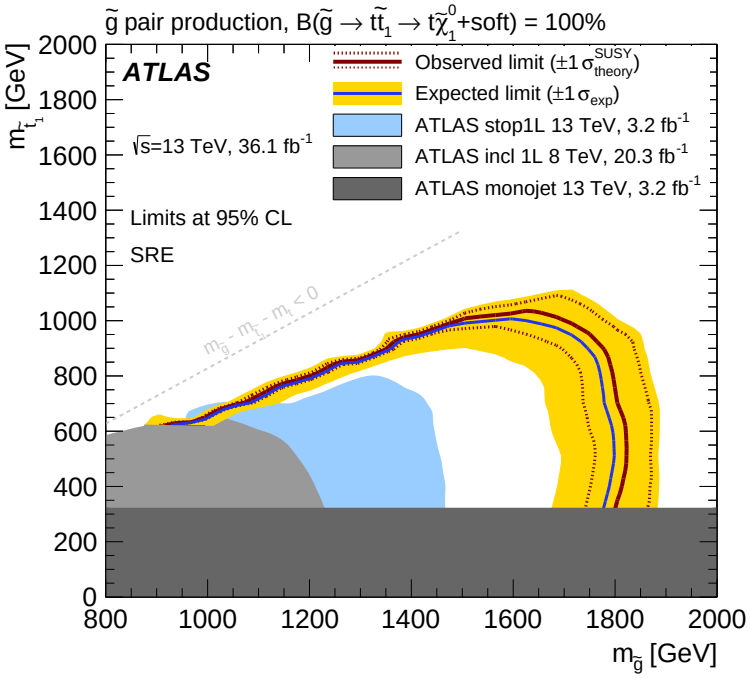

FIGURE 7.7: Observed (solid red line) and expected (solid blue line) exclusion limits at 95% CL as a function of $m_{\tilde{g}}$ and $m_{\tilde{t}_1}$ for the scenario in which a pair of gluinos decay into stop and top and $m_{\tilde{t}_1} = m_{\tilde{\chi}_1^0} + 5$ GeV. The uncertainty bands show the $\pm 1\sigma$ variation of the expected limit (yellow band) and the $\pm 1\sigma$ variation of the signal theoretical cross section (dotted red lines). Observed limits obtained in previous ATLAS searches are also shown [133, 134, 99].

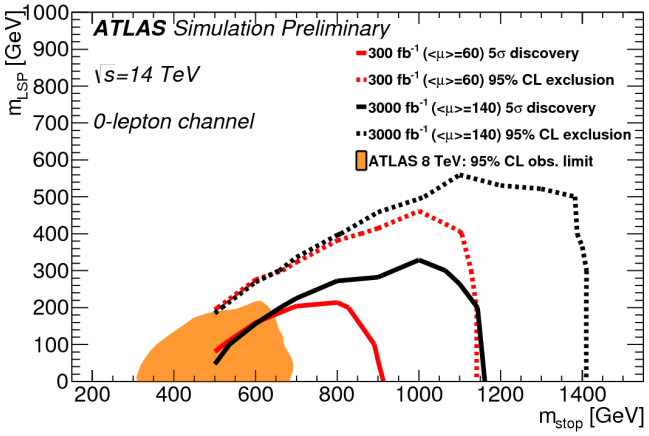

FIGURE 7.8: Exclusion limits at 95% confidence level (dashed) and 5σ discovery reach (solid) for 300 fb^{-1} (red) and 3000 fb^{-1} (black) in the stop-neutralino mass plane assuming the decay $\tilde{t}_1 \to t\tilde{\chi}_1^0$ with 100% branching ratio. Observed limits in the 8-TeV analysis are also shown [136].

Conclusions

The main topic of this thesis is the search for light stops produced in pairs in pp collisions at $\sqrt{s} = 13$ TeV at the LHC. The data analysed were collected with the ATLAS detector during 2015 and 2016, reaching a total integrated luminosity of 36.1 fb^{-1}. The search is performed on final states with no leptons, large jet multiplicity and large missing transverse momentum. The main model targeted consists on a pair of directly produced stops that decay into a top and a neutralino, although additional models are used for the interpretation of the results.

The analysis strategy consists on the definition of several signal regions, which consist on a combination of requirements on the events that are optimised to enhance the signal events and reduce the SM backgrounds. The different signal regions target different models, including several decay modes of the stops and different scenarios regarding the masses of the SUSY particles. The contributions of SM processes are constrained in control regions, defined independently for the main background processes in such a way that the selection resembles that of the signal regions. A profile likelihood fit is used to estimate the signal region composition, including the systematic uncertainties as nuisance parameters.

No deviation from the Standard Model predictions was found, and the results were interpreted in terms of 95% confidence level limits on the visible cross section of any new physics phenomena with the same signature. Exclusion limits were also set at 95% confidence level on the masses of the SUSY particles involved. Stop masses of up to 1 TeV are excluded for neutralino masses of under 300 GeV, and stop masses of 800 GeV are excluded for neutralinos of 400 GeV. These limits extend by about 300 GeV the limits on the stop masses and by 100 GeV those of the neutralino. The limits on models where the difference in mass between the stop and the neutralino is similar to the top quark mass improve largely those in Run-1 thanks to developments on the analysis strategy such as the use of ISR jets in the selection.

Future prospects for similar stop searches in the high-luminosity LHC are also shown. By the end of Run-3, where 300 fb^{-1} of integrated luminosity are expected, SUSY signals of stop masses up to 900 GeV could be discovered with a 5 σ significance, and, in absence of a signal, stop masses of about 1200 GeV are expected to be excluded for neutralino masses below 300 GeV. By the end of the high-luminosity phase, the integrated luminosity is expected to reach 3000 fb^{-1}, and the signals of up to 1200 GeV of stop mass could be discovered with a 5 σ significance, while if no signal is found, the exclusion of stops with masses up to 1400 GeV with neutralino masses below 400 GeV is predicted.

APPENDIX A

TileCal Dead Module Correction

The presence of masked regions in the Tile calorimeter in ATLAS can severely affect the measurements of hadronic energy deposits and compromise the data, especially the jets and the missing transverse energy. This chapter details the studies towards a correction to be applied to the affected jets. These studies are documented in an ATLAS internal note [137].

During the Run-2 data-taking period, these masked regions were present nearly at all times. Previous studies during Run-1 aiming to correct this issue were focused on isolated masked cells in the calorimeter, and failed to correct for jets in a satisfactory manner when a larger area (like a full module) was masked. The studies presented in this chapter aim to find a correction for the jets when a full module of the calorimeter is masked. In section A.1, the simulated samples used to derive the correction are described. Section A.2 gives an overview of the effects of the masked modules in the jet p_{T}, and the correction itself is described in section A.3. The studies performed to validate the correction in MC and data are documented in section A.4, where dijet and γ+jets samples are employed. Finally, a short description of the tool developed to implement the correction is given in A.4.5.

A.1 Monte Carlo samples

The effects on the jet reconstruction and the derived energy correction were studied in dijet events generated using the POWHEG generator [39] interfaced with Pythia8 [37]. The MC samples were simulated with two different configurations in order to study the effects of the masked modules in TileCal:

- *Real detector* configuration: The two masked modules present at the beginning of Run-2 in the ATLAS detector (LBA10 and EBC21) were masked in the simulation.
- *Ideal detector* configuration: No masked TileCal modules were included in the simulation. The cell noise configuration is also slightly different, since it is calculated without bad channels.

This pair of otherwise identical samples allowed for a precise knowledge of the effects of the masked modules in jets and other reconstructed objects. Previous attempts to emulate the effect of the masked regions by hand, modifying the topocluster information of the jets according to the expected fraction lost in the hadronic calorimeter were found to model poorly the real effect.

The two simulation conditions stated above will be referred to as ideal and real samples, and similar naming will be used for the jets coming from either of them.

Simulated samples of γ+jets events with PYTHIA8 were used for the validation of the correction.

The final validation and the calculation of the systematic uncertainties of the correction was done using real data collected with the ATLAS detector during 2015. The full integrated luminosity, after applying good data requirements was 3.32 fb^{-1}.

A.2 Effects of the modules

The technique to study the effect of the masked modules of TileCal consists on comparing the energy jet-by-jet in the two samples. In order to properly do this, it is important to associate correctly the jets, which is done relying on particle-level information. The matching is done as follows

- The same event number is read in the two samples.
- The two leading reconstructed jets are matched to the most energetic truth jet within $\Delta R = 0.2$ in both samples.
- The real and ideal reconstructed jets that are associated to the same truth jet are matched together.

This identification of real and ideal jets can be used to study the effects of the modules on the properties of the jets. This is done as a function of the relative position between the jet and the masked module. Considering that the sizes of the modules are of about 0.9 in η and 0.1 in ϕ, the jets can be classified into three categories depending on this position, measured from the centre of the module to the centre of the jet:

- Core-affected jets: The jet is pointing to a masked module, i.e. $|\Delta\eta| < 0.45$ and $|\Delta\phi| < 0.05$.
- Edge-affected jets: The jet is pointing outside of the module, but close to it, i.e. $0.45 < |\Delta\eta| < 0.85$ and $0.05 < |\Delta\pi| < 0.45$.
- Not affected (or *healthy*) jets: They are far enough from any masked modules and therefore not affected by it.

The position of the two masked modules and the areas of the calorimeter that they affect are shown in figure A.1. Since the influence regions of the modules do not overlap, the effects of these two modules are studied independently.

The jet response was studied as a function of the jet p_{T} and its position relative to the damaged module. Figure A.2 shows the energy losses of jets that overlap in ϕ with the module ($|\Delta\phi|<0.05$) as a function of the distance in η for several p_{T} ranges. The losses are evaluated as the relative difference between the jet from the real and ideal samples. The energy losses increase dramatically when the central part of the jet gets inside the limits of the module ($|\Delta\eta| < 0.45$). This is an expected feature, since the central part of the jets is on average the most energetic. The asymmetry in $\Delta\eta$ can be explained by looking at the geometry of the detector. The Long Barrel modules cover the region $0 < |\Delta\eta| < 0.9$, while the Extended Barrel covers $0.8 < |\Delta\eta| < 1.7$. The existing overlap between the two explains the asymmetry, since part of the energy of a jet falling in the overlap region will be measured by the contiguous, non-masked module. It is also observed that the losses are larger in the LB than the EB, reaching up to 24% for jets between 800 GeV and 1 TeV in the LB, and 20% in the EB for the same energy range.

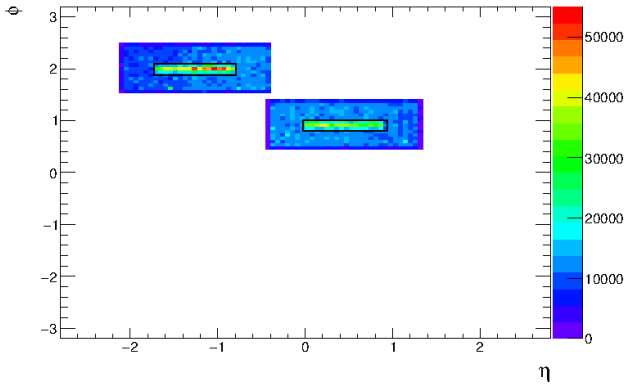

FIGURE A.1: Position of the two masked modules in 2015 and the areas of affected jets around them

A.3 Correction

The features of the energy losses of the jets shown in the previous chapter have been used to develop a correction for the jets. It is calculated independently for the long and extended barrels, and it depends on the jet p_{T} and its position with respect to the module. The approach followed for the computation of the correction is based on the numerical inversion technique [85], which was already described in chapter 4, in such a way that the correction is initially calculated as the ratio $\mathcal{R} = p_{\mathrm{T}}^{D}/p_{\mathrm{T}}^{H}$, in bins of the healthy jet p_{T}, and the result is a function of the damaged p_{T}. The response $\mathcal{R}$ is computed in bins of $\Delta\phi$ and $\Delta\eta$. The binning in ϕ is done in absolute value, as the energy loss is assumed to be symmetric in $\Delta\phi$. The binning is 0.05 for $\Delta\phi \leq 0.1$ and 0.1 for $\Delta\phi > 0.1$. In $\Delta\eta$ the binning is constant at 0.1, and it is no longer symmetric to account for the η dependence of the jet resolution.

In principle the function $\mathcal{R}$, once inverted and written as a function of p_{T}^{D} can already be used as a correction for the jets, but in order to avoid any discontinuities in the p_{T} spectrum of the jets it is fit with a smooth function. Two different functions are used for this purpose, f_1 for jets whose axis is falling inside the module and f_2 for the rest, being

- $f_1 = \exp[p_0 + p_1 x] + p_2$
- $f_2 = p_0 x + p_1$

These functions showed a good modelling of the data. The fits for two configurations are shown in figure A.3, with the confidence intervals at 1σ confidence level, including only statistical uncertainties.

The uncertainties on the fit are not enough to cover for the non-closure observed in the jets pointing to the centre of the modules. For this reason, for the jets in these regions, an extra uncertainty is estimated in a closure test with an analogous configuration to that of figure A.2. This is shown in figure A.4. It can be seen that good closure is achieved in general, and a flat systematic uncertainty of about 3% is added to the jets with $|\Delta\eta| < 0.4$ to cover for the non-closure.

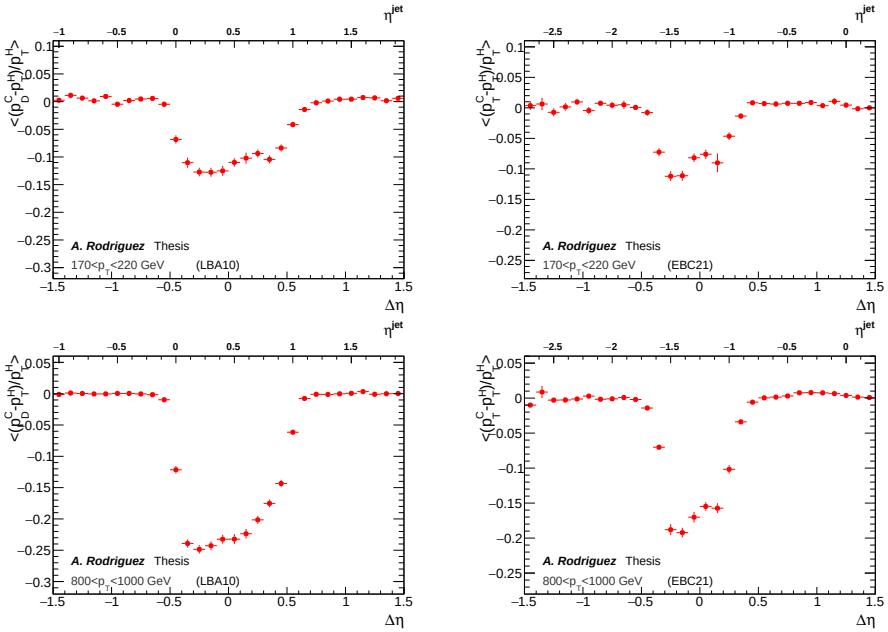

FIGURE A.2: Relative energy loss of jets overlapping in ϕ with one of the modules in different p_{T} ranges as a function of the distance to the centre of the module in η. Here p_{T}^{H} is the *healthy* p_{T} of the jet, and p_{T}^{D} is the *damaged* jet p_{T}, calculated from the ideal and real samples, respectively.

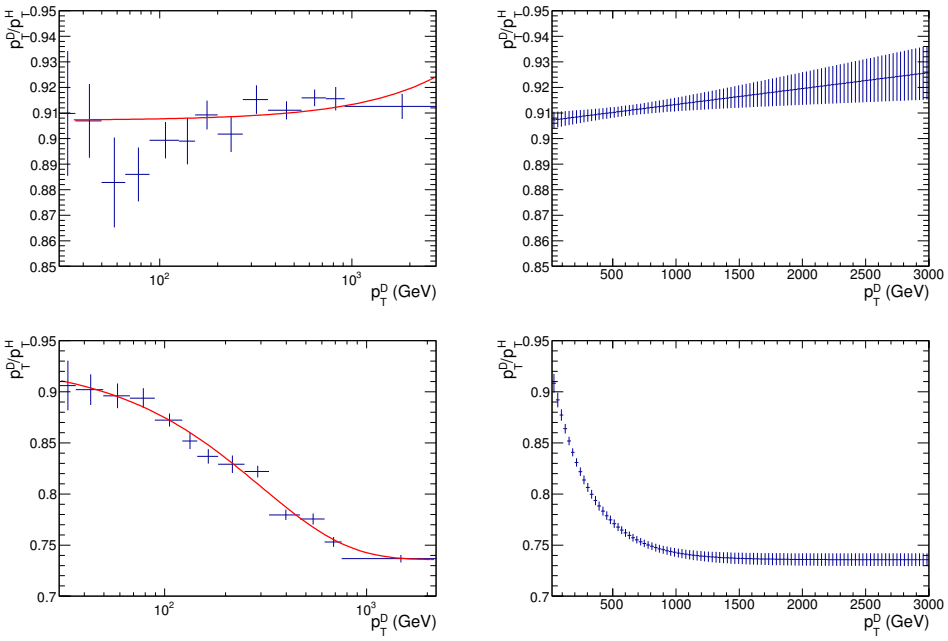

FIGURE A.3: Two examples of the fitting functions used to fit the parameterisation of the correction for jets. On the top, function f_2 is used, for jets within $-0.3 < \Delta\eta < -0.2$ and $0.05 < |\Delta\phi| < 0.1$ of the EBC21 module. On the bottom, function f_1 is used to fit the parameterisation for jets within $\Delta\eta < 0.1$ and $|\Delta\phi| < 0.05$ of the LBA10 module. The plots on the right show the 1σ confidence intervals.

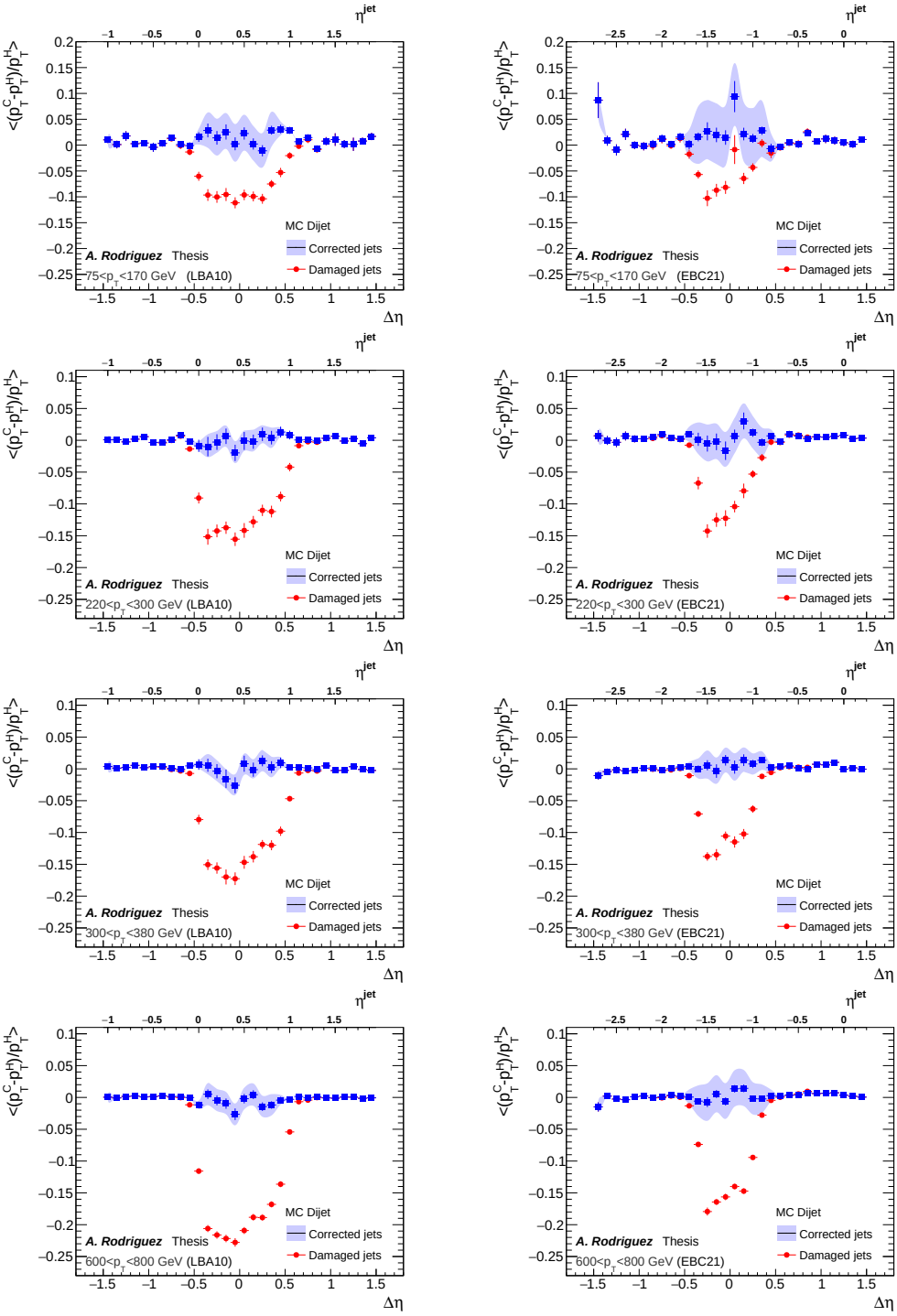

FIGURE A.4: Comparison of corrected (blue) and damaged (red) jet p_{T} to healthy for several ranges of truth p_{T} and jets overlapping in ϕ with the LB (left) and EB (right) modules. The uncertainties on the points show the statistical error, and the shadowed area indicates the assigned systematic uncertainties.

A.4 Validation

A series of studies performed to validate the correction in data and MC samples were carried out, and are detailed in this section.

A.4.1 Jet resolution

Some pulls of the reconstructed and truth-level jet p_{T} are shown in figure A.5 for healthy, damaged, and corrected jets, for jets pointing inside the masked modules. Figure A.6 shows jets pointing outside the modules. In the case where the jets point inside the module, the width of the distribution increases significantly, and the mean is displaced to lower values. When the correction is applied, the mean gets back to its original value, but the width of the distribution is not improved. In the case when the jet points outside the module, the change in the distribution is mild, and the correction is also small. These effects are summarised in figure A.7, where the mean and RMS of these distributions are shown as a function of the jet p_{T}. The average p_{T} is recovered with the correction. Although the RMS is worsened after the correction, especially in the long barrel, the mean follows the ideal behaviour very closely. For instance, the pull RMS for $\sim$ 500 GeV jets increases by 4%, while the mean value is corrected for about 20%. As the correction is computed on average, some overcorrection occurs, particularly for very high-p_{T} jets in the long barrel, but this is covered by the systematic uncertainties described in section A.3. In the case of the edge-affected the changes in RMS and mean are very small, and the correction performs very well. As seen in figure A.8, the mean value is nicely recovered, and the impact on the RMS is negligible.

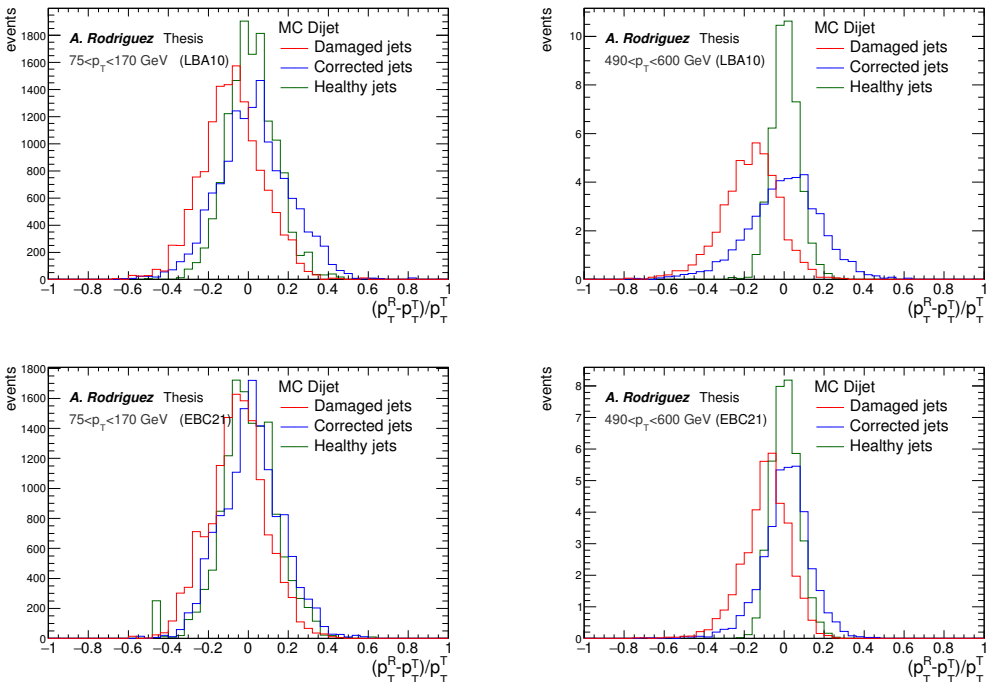

FIGURE A.5: Jet response before and after applying the correction to jets pointing inside the module, compared to the non-damaged jets in the long (top) and extended (bottom) barrels, for several ranges of jet p_{T}.

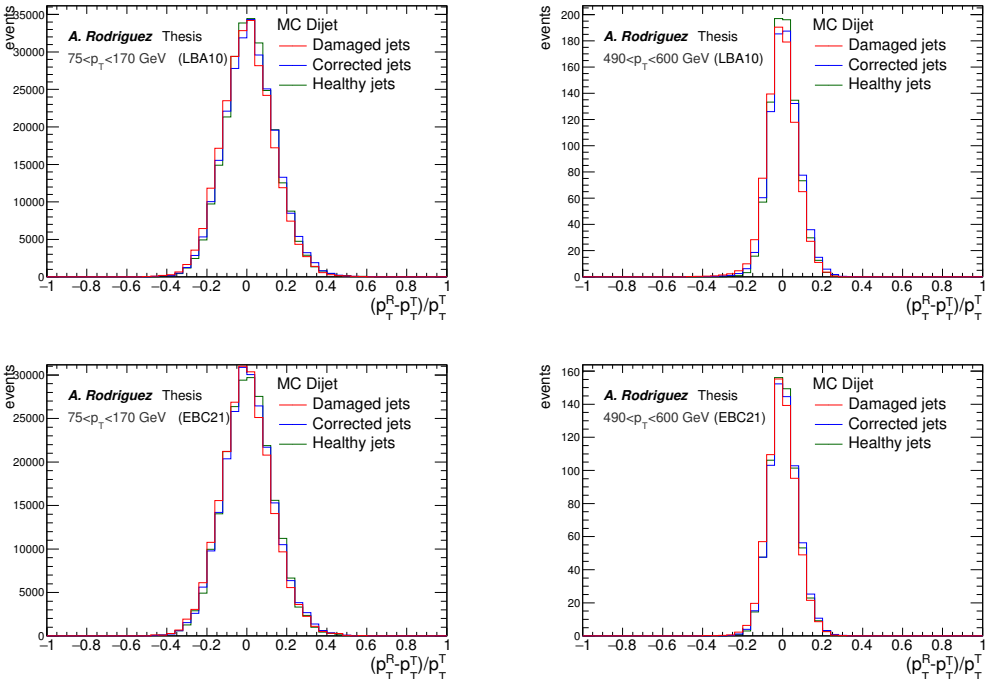

FIGURE A.6: Jet response before and after applying the correction to jets pointing outside the module, compared to the non-damaged jets in the long (top) and extended (bottom) barrels, for several ranges of jet p_{T}.

A.4.2 Dijet balance

A usual way to study the p_{T} resolution without relying on truth jets is to look at dijet (back-to-back) events. If no other activity is present, the p_{T} of the two leading jets should balance each other. The study was performed on the MC samples detailed in section A.1, and applying the selection:

- $p_{\mathrm{T}}^{1,2} > 35$ GeV,
- $\Delta\phi^{1,2} > 2.5$,
- $p_{\mathrm{T}}^{3} < p_{\mathrm{T}}^{\mathrm{avg}}/4$,

where $p_{\mathrm{T}}^{\mathrm{avg}}$ is the average p_{T} of the two leading jets.

One of the two leading jets is considered as the reference, and required to be central ($|\eta^{\mathrm{ref}}| < 0.8$) and not affected by any of the masked calorimeter regions. The other jet (probe) is required to be affected by one of the masked regions included in the simulation. The resolution is shown in figure A.9 in terms of the ratio $\mathcal{R} = p_{\mathrm{T}}^{\mathrm{probe}}/p_{\mathrm{T}}^{\mathrm{ref}}$. It can be seen that core-affected jets lose up to 25% of their p_{T} in the LB, as anticipated, and the corrected jets follow closely the healthy points. The case of jets pointing outside the modules has again a small effect, and it is very well recovered after applying the correction.

A.4.3 Effects on the $E_{\mathrm{T}}^{\mathrm{miss}}$

The effects of the masked modules and the jet correction applied were also studied in terms of the reconstructed missing transverse energy. Since the loss of energy in misreconstructed jets due to the TileCal failures can potentially create big tails in the

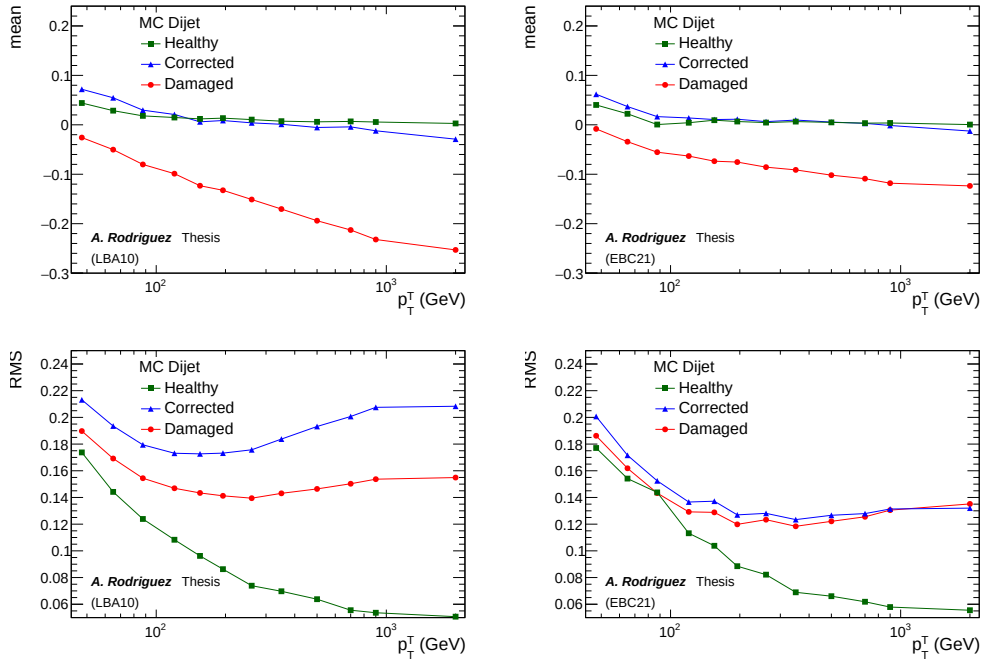

FIGURE A.7: Mean (top) and RMS (bottom) of the response distributions of core-affected jets as a function of the jet p_T for LB (left) and EB (right) modules.

MET distribution. The E_T^{miss} used for the studies is reconstructed as described in chapter 4. The same selection as in the previous section A.4.2 is applied, with one of the two jets affected by the masked regions.

In figure A.10 the E_T^{miss} distribution is shown for dijet events, where the E_T^{miss} is recomputed after having corrected the jets, and compared to the ideal case. For the event topology selected, the E_T^{miss} arises mainly from jet misreconstruction, and therefore is directly affected by the hadronic losses in TileCal. It can be seen in the figure that the tales are indeed larger when one of the jets points to one of the modules, and an analogous but milder effect is observed for jets affected on the edge. The correction improves slightly these tails, but the effect is very small.

A.4.4 γ+jet balance

The ultimate test for the correction was done on real data. In order to do this, γ+jet events were selected. This study is also complementary to the dijet analysis at low jet p_T. Single photon triggers were used, and the event selection includes

- A reconstructed photon with $p_T^\gamma > 27$ GeV and $|\eta| < 1.37$
- At least one reconstructed jet with $p_T > 20$ GeV and $|\eta| < 2.1$
- The photon and the leading jet are separated in ϕ by at least 2.9 ($\Delta\phi > 2.9$)
- The second (if any) jet is soft compared to the leading jet-photon pair $p_T^2 < 0.2 p_T^\gamma$

Similarly to what was done for dijet events, the p_T of the leading jet is compared to that of the photon, and in the ideal γ+jet scenario, the ratio of their p_T would be similar to 1. Figure A.11 shows this quantity as a function of the photon p_T in data and MC for all jets affected by each of the two modules. As seen in the bottom ratio

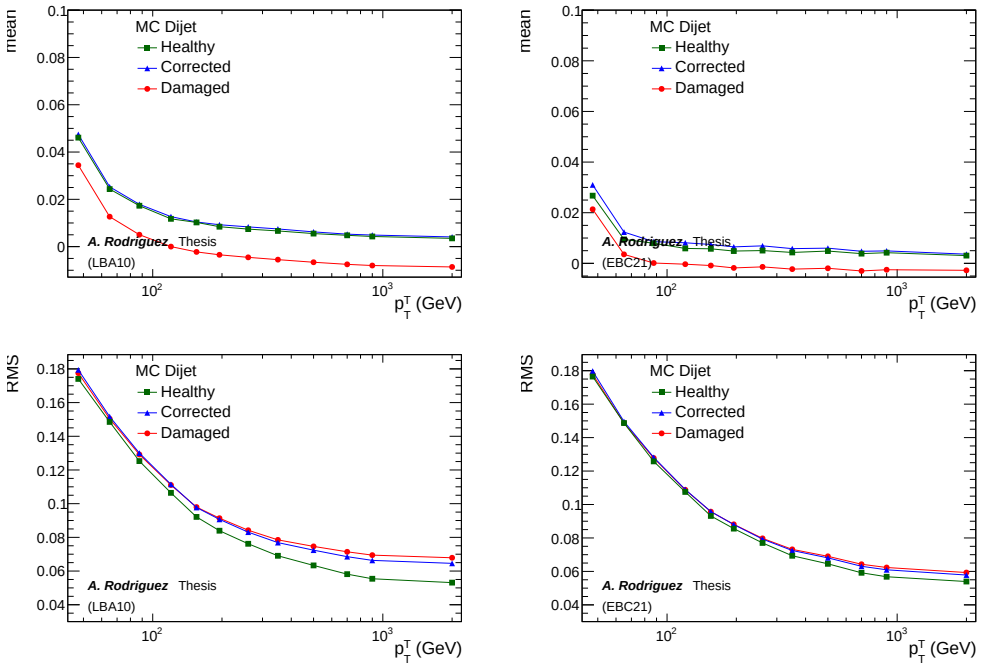

FIGURE A.8: Mean (top) and RMS (bottom) of the response distributions of edge-affected jets as a function of the jet p_T for LB (left) and EB (right) modules.

in the figures, the correction tends to restore the p_T to the expected for a healthy jet. Although in general the correction improves the damaged jets, a small overcorrection is observed in some cases. It is due to the statistical fluctuations of the uncorrected samples, and it is covered by the systematic uncertainties assigned to the correction.

A.4.5 JetTileCorrection Tool

As a result of the studies summarised here, a tool to apply the correction was developed and approved as an official ATLAS tool. It uses the parameterisation described in section A.3 to correct all the damaged reconstructed jets in data and simulation. It is provided with a list of the masked modules in data and/or MC. For each reconstructed jet, the tool determines whether it is affected by any module in the list, and corrects (if needed) with the relevant factor depending on the distance in η and ϕ to the module, and the p_T. The tool returns the jet with the modified reconstructed four-momentum. Additionally, it provides the original p_T of the jet, and whether the jet was not affected, core-affected or edge-affected.

In the case where a jet is affected by two modules, a conservative approach is followed, and the tool applies all relevant corrections in a decreasing order. In the case where the modules are adjacent, the correction is not expected to work with the same efficiency, since for a jet pointing in the middle too much information would be lost in the dead region. Further studies would be needed in this case.

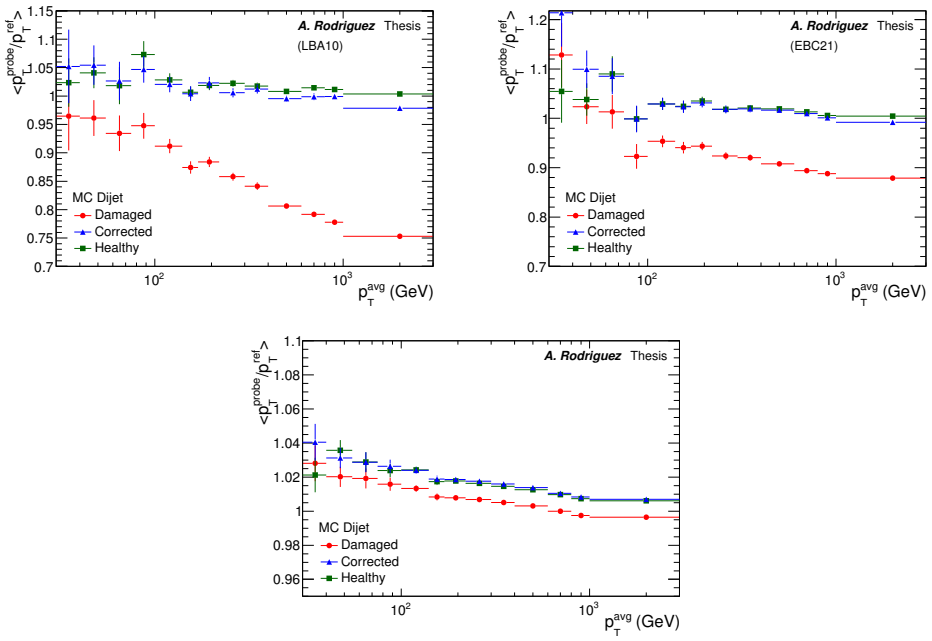

FIGURE A.9: Dijet balance as a function of the average dijet p_{T} for jets pointing at the LB module (top left), at the EB module (top left) and outside of the masked modules (bottom).

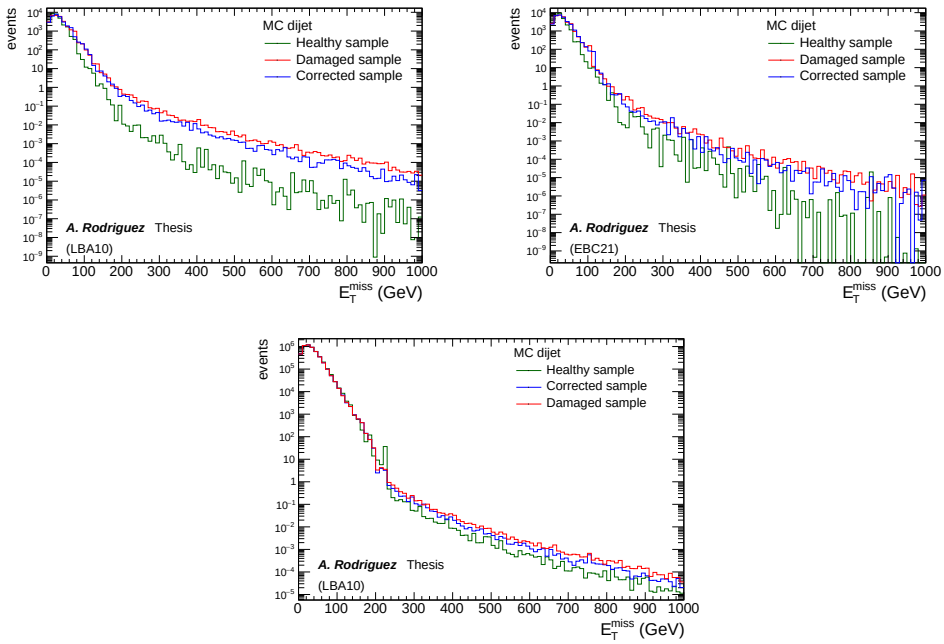

FIGURE A.10: Distribution of $E_{\mathrm{T}}^{\mathrm{miss}}$ in events with dijet selection where one of the jets points to LB (top left), EB (top right), or outside of the modules (bottom).

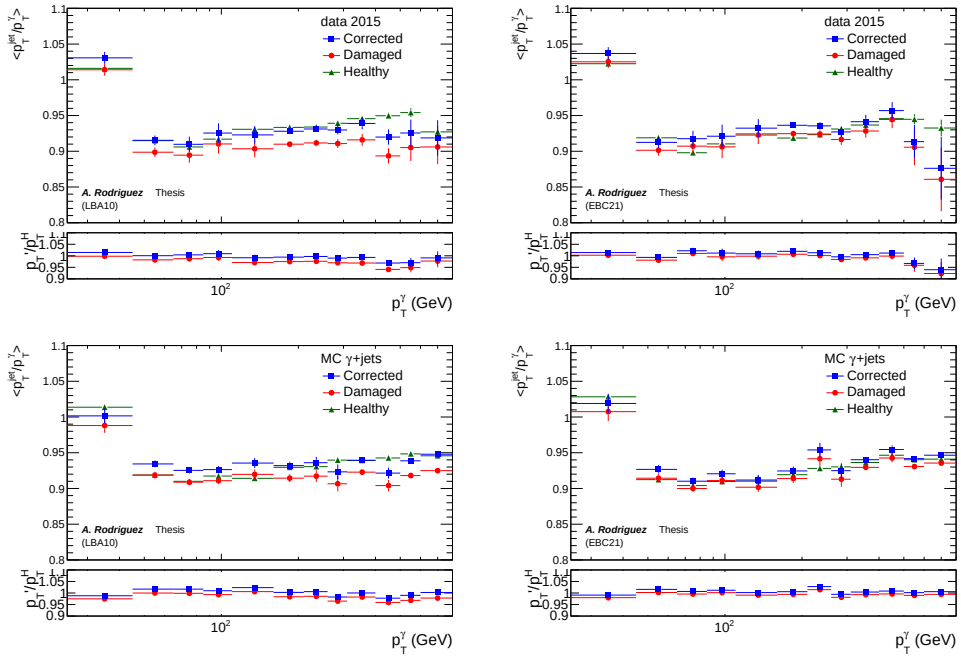

FIGURE A.11: Comparison of γ+jet balance before and after applying the correction. All affected jets included, in data (top) and MC (bottom).

APPENDIX B

Test Beam Studies for the ATLAS Tile Calorimeter Upgrade

The upgrade of the Large Hadron Collider will increase the luminosity from the nominal 10^{34} cm^{-2} s^{-1} to about 5 to 7 times higher. This will provide a unique opportunity to search for new physics and make precise measurements of the SM, but the increase in luminosity will present significant challenges for the experiments, which will have to upgrade their detectors consequently.

In particular, the Tile Calorimeter will update the readout electronics to face larger rates and pile-up. In order to test the performance of the new components, a prototype was equipped with the upgraded readout and exposed to test beams of electrons, muons and hadrons. This chapter details the analysis of the data collected. A summary of the upgrade for TileCal is given in section B.1. Then, the test beam set up is described in section B.2, and the results are given in section B.3. Although my contribution to the analysis was focused on the muon data, electron and hadron results are shown as well for completeness.

B.1 TileCal upgrade

The increase of luminosity of the LHC will result in a corresponding increase of particle fluxes through the ATLAS subdetectors, which will face a higher radiation and will necessitate more efficient trigger and data acquisition systems. Most of the TileCal components will not be replaced, like the tiles, the photomultipliers (PMTs) , the absorbers and the fibres. However, the readout system will experience significant changes [138]. In order to achieve these requirements, the front-end electronics will be replaced with a new system that will provide fully-digital trigger data at 40 MHz (instead of the current 100kHz) with higher granularity and precision. For comparison, the old and new electronics readout systems are shown in figure B.1. In the current trigger system of TileCal, analogue signals are used for the first level trigger, corresponding to towers of 0.1×0.1 in $\Delta\eta \times \Delta\phi$. In the upgraded system, the information of the trigger will be fully digital, which will also require an increase in the system data bandwidth. The new trigger system will have access to the digital information of each calorimeter cell with low electronic noise level and accurate energy calibration.

In the current readout system in ATLAS, up to 48 photomultipliers are readout by a single *super-drawer*, the basic readout unit. In the upgrade, in order to reduce the impact of a potential super-drawer failure, they will be replaced by 4 *mini-drawers* each. This will avoid problems as the masked TileCal modules discussed in the previous appendix A.

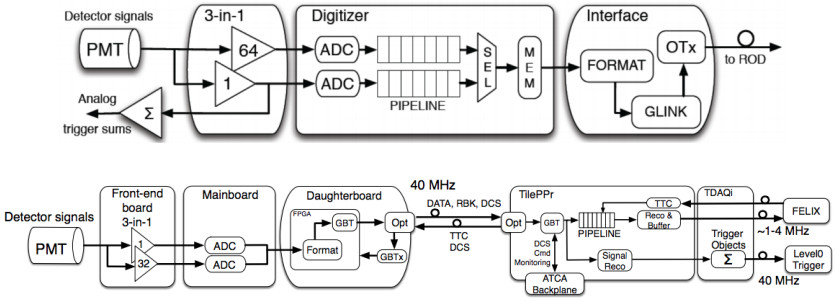

FIGURE B.1: Scheme of the current (top) and upgraded (bottom) TileCal readout systems.

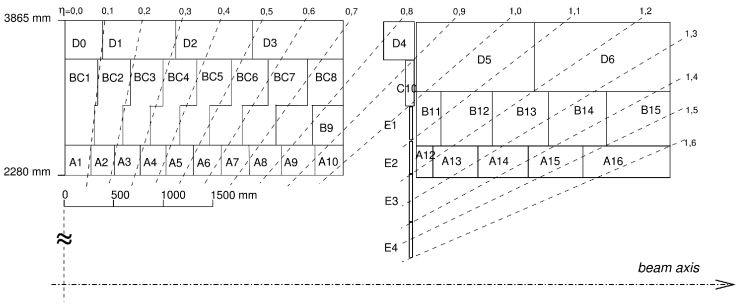

FIGURE B.2: Sketch of the cell structure of a TileCal module.

B.2 Test Beam setup

In order to test the performance of the new readout system, a prototype (also referred to as *demonstrator*) was exposed to test beams of different particles (muons, electrons and hadrons). The data were collected in September 2017 with the setup schemed in figure B.3. Along the beam line, three Cherenkov counters are placed that are used for particle detection, alongside with two trigger scintillators used in coincidence to trigger the data. Finally, two beam chambers measure the position of the beam before it hits the table were the modules for study are placed.

As it was described in section 3.2.2.2, a Tile Calorimeter module is divided in three layers, being the most internal one A, the middle one BC, and the outermost D. Each of them are subdivided into cells, having 10 cells in the A-layer, 9 in the BC-layer and 4 in the D-layer in the long-barrel modules, like the one used for data-collection in the test beam. A scheme of the cells in a module can be seen in figure B.2.

Three modules are placed on the scanning table, one of them being the demonstrator, equipped, as mentioned above, with all the upgrade readout electronics, and calibrated at the electromagnetic scale. The studies presented in the next section were performed using the data collected with this module exposed to several particle beams, as stated above, at different energies and incident angles.

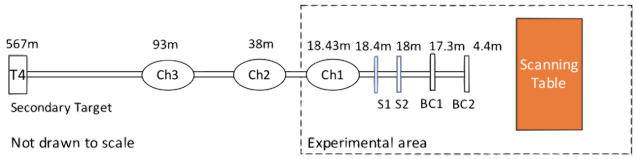

FIGURE B.3: Scheme of the beam- line used for the test beam studies. Three Cherenkov counters(Ch1, Ch2 and Ch3) are used for particle identification; two trigger scintillators (S1 and S2) are used in coincidence for triggering, and two beam chambers (BM1 and BM2) measure the position of the beam. The distances are reported in the figure.

B.3 Test beam results

B.3.1 Results with muons

Muons are expected to lose energy mostly through ionisation as they cross the calorimeter. The high-energy muons used for the studies travel all the way through the demonstrator, and the energy lost in the process is expected to be proportional to the path length.

The data were collected with a muon beam of 165 GeV incident at 90 and 20 degrees. The runs at 20 degrees follow a similar path as those arising from the interaction point in ATLAS, while muons incident at 90 degrees traverse a larger distance inside the module, and are useful to study the energy losses in the calorimeter. The runs at 90 degrees were taken with the beam pointing in the middle of each of the 11 tile-rows of the demonstrator module. Events were selected requiring a total energy reconstructed in the module in the window $700 < E < 15000$ MeV. The lower cut allows to reject fake trigger events. The runs at 20 degrees were taken with the beam pointing at the centre of each of the 10 cells of the A layer, the first one in the projective direction. The event selection includes a cut on the total energy deposited of at least 500 MeV.

The response of the demonstrator to muons was studied in terms of the deposited energy over the path length $\left(\frac{dE}{dl}\right)$ and studies were performed independently for each cell. As it can be seen in figure B.4, the deposited energy follows a Landau distribution.

The muon response for the different cells is calculated as the 97.5% truncated mean of the distributions of $\left(\frac{dE}{dl}\right)$, in such a way that the tales in the positive side of the distribution are not taken into account. The reason is that some of the landau fits show some instabilities due to the function not describing the data in the whole range. The results are shown in terms of the ratio of the response to muons in data over simulation,

$$\mathcal{R} = \frac{\langle dE/dl \rangle_{\text{Data}}}{\langle dE/dl \rangle_{\text{MC}}}. \tag{B.1}$$

In this way, any non-linearity appearing from the truncated mean is avoided.

Figure B.5 shows the results for 90-degree incident muons. The results are shown for all the cells in each layer, and the mean value per layer is also displayed. The maximum offset observed between data and simulation is of about 6%, and the mean value found in the different layers is consistent.

Figure B.6 shows the results for 20-degree incident muons. The points for each layer represent runs in which the beam was pointing to different cells of the A-layer, and they were calculated using one cell in A-layer, two in BC-layer and one or two in D-layer. Layers BC and D were calculated using only runs pointing to cells A1-A8,

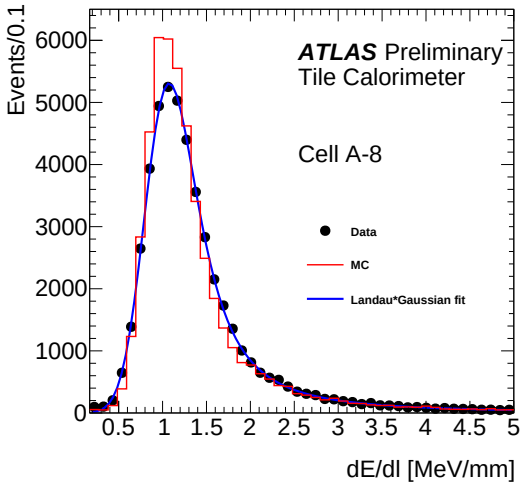

FIGURE B.4: Muon energy deposited over path length in cell A8 for 90-degree incident muons in data (full black points) and simulation (red line). A fit to a Landau function convoluted with a Gaussian is also shown (blue line)

since some energy is lost outside of the module for the rest. The differences between data and MC are larger here, up to 10% in the D-layer. The mean value of $\mathcal{R}$ per layer oscillates between 0.94 and 0.96, lower than in the 90-degree case, but compatible with each other.

B.3.2 Results with electrons

Electron data were collected with beams of 20, 50 and 100 GeV particles incident in cell A4 with an angle of 20 degrees. Electrons are expected to deposit all their energy in the calorimeter, such that $\langle E \rangle / E_{\text{beam}} \sim 1$, where $\langle E \rangle$ is the mean total energy deposited by the electrons.

For the electron analysis, a more sophisticated selection is needed in order to get a clean sample. Two variables related to the shower shape in the calorimeter are used, C_{long} and C_{tot} [139]. The variable C_{long} measures the depth of the shower, and is defined as

$$C_{\text{long}} = \sum_{i=1}^{2} \sum_{j=1}^{3} \frac{E_{ij}}{E_{\text{beam}}}, \tag{B.2}$$

where the sum over i includes the two first layers of the module, and the sum over j represents the three contiguous cells centred in the beam in layer i. The energy E_{ij} is the energy deposited in a certain cell. Hence, C_{long} represents the fraction of energy deposited in the first two layers of the calorimeter. The variable C_{tot} gives a measure of the spread of the shower, and is calculated as

$$C_{\text{tot}} = \frac{1}{\sum_c E_c^\alpha} \sqrt{\frac{1}{N_{\text{cell}}} \sum_c \left(E_c^\alpha - \frac{1}{N_{\text{cell}}} \sum_c E_c^\alpha \right)^2}. \tag{B.3}$$

Here E_c is the energy of cell c and $N_{\text{cell}} = 9$ represents the number of cells considered. The exponent $\alpha = 0.6$ was obtained from simulation optimising the electron separation. These two variables are used in combination to select a clean electron sample. Figure B.7 shows the two variables for a 50 GeV electron sample. Two clusters can

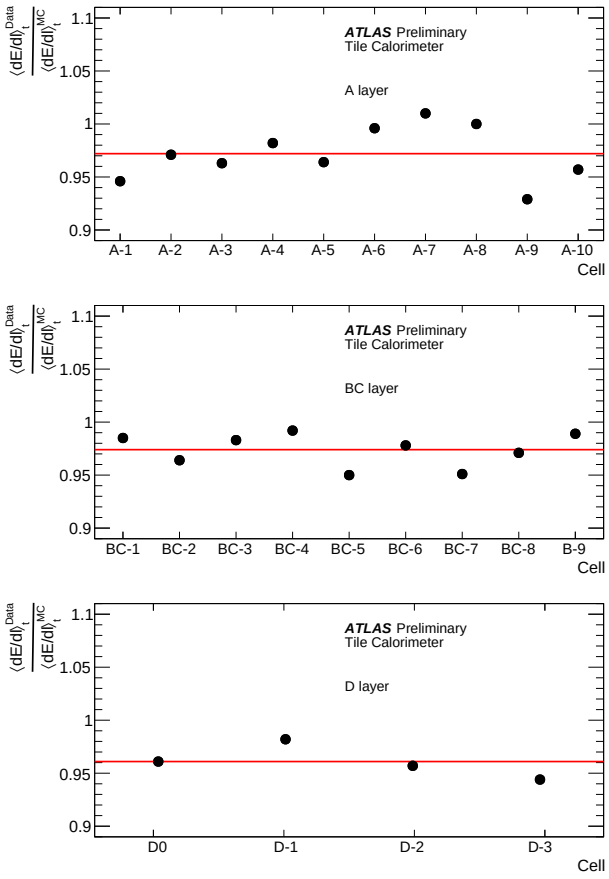

FIGURE B.5: Ratio of the truncated means of the energy distributions per unit of path length deposited in the demonstrator in data over simulation. The results are for 90 degree muons of 165 GeV, and are shown as a function of the cell number in each layer. The horizontal red lines represent the mean value in each layer.

be observed, the denser one on the top right of the figure corresponding to electrons, the other one to hadrons. The requirements applied to C_{long} and C_{tot} depend on the beam energy, being $C_{\text{long}} > 0.88$ and $C_{\text{tot}} > 6.5$ for 100 GeV electrons. For a low energy beam of 20 GeV the selection is $C_{\text{long}} > 0.75$ and $C_{\text{tot}} > 2.1$, and an extra requirement on the signal of the Cherenkov counters to achieve better purity, which has to be larger than 500 analogue-to-digital converter (ADC) counts.

The distribution of the total energy deposited by the electrons with the different energy beams is shown in figure B.8. The data and MC distributions are overlaid. As it can be seen in the figure, the agreement between data and simulation is very good, and the total energy deposited in the module follows a gaussian distribution. This proves the purity of the electron selection, since the simulated sample contains only electrons. The electron response is sensitive to the periodicity of the position of the scintillating tiles in the calorimeter. The energy deposited is therefore a periodic function of the beam position, and the determination of the response is done through a fit to the function

$$E(X) = p_0 \left[1 + p_1 \sin\left(\frac{2\pi X}{p_2} \right) \right], \tag{B.4}$$

where p_1, p_2 and p_3 are parameters of the function. Since p_0 is the mean energy around which the oscillations occur, it is taken as the value of the electron response.

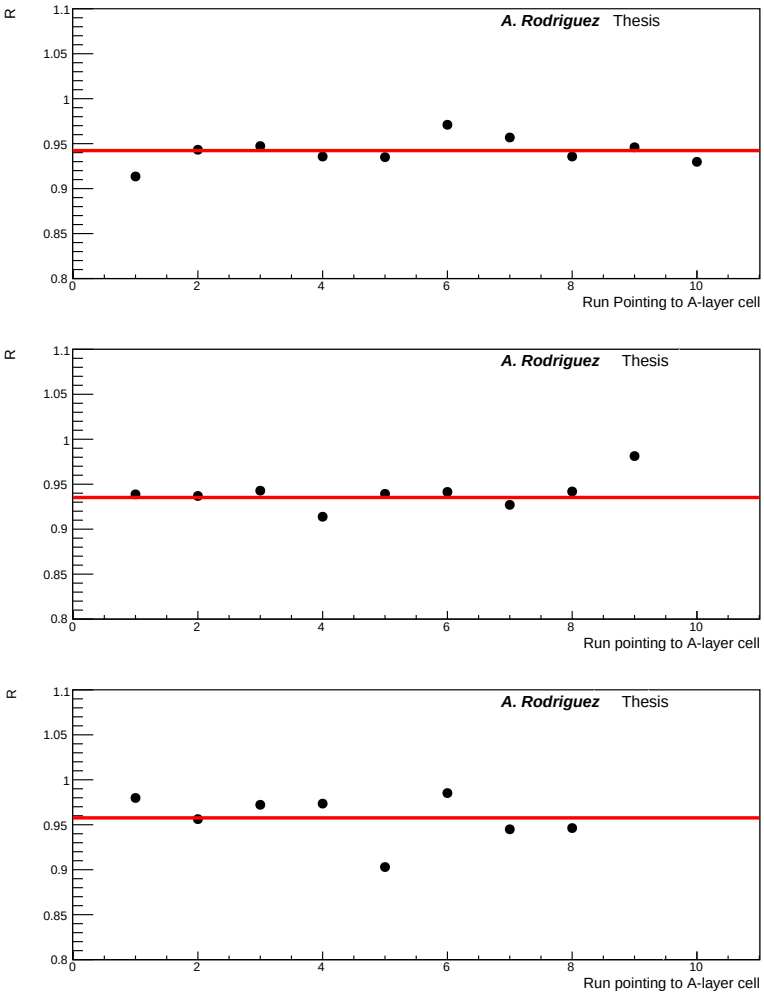

FIGURE B.6: Ratio of the truncated means of the energy distributions per unit of path length deposited in the demonstrator in data over simulation. The results are for 20-degree incident muons of 165 GeV and are displayed as a function of the A-layer cell where the beam points in each case. Only A1-A8 are shown for BC and D-layers. The red horizontal line shows the mean for each layer.

This is shown in figure B.9, where the ratio between the parameter p_0 of the fit (here called E_{fit} and the beam energy is displayed for the different beams. The results show that the computed mean is within 2% of the total energy.

B.3.3 Results with hadrons

The demonstrator was finally exposed to hadron beams of 16, 18, 20 and 30 GeV incident in cell A3 with a projective angle of about 15 degrees. In this case, the particle identification and selection is done using the Cherenkov counters upstream the detector. Figure B.10 shows the signal in the Cherenkov counters 1 and 3 vs the total energy deposited. The type of particles to which each of the clusters corresponds and the cuts applied for selection are shown in the figure. For proton and kaon selection, the signal in Cher1 is required to be lower than 400 ADC, and in Cher3 lower than 420 ADC, while for pions the requirements are inverted. Figure B.11 shows the Cher2 vs Total energy scatter plot after applying one of these selections in Cher1 and Cher3.

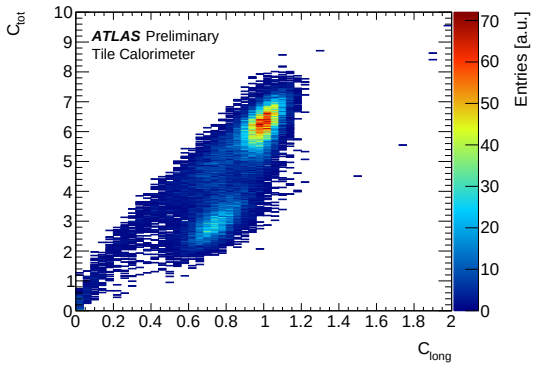

FIGURE B.7: Distribution of C_{long} vs C_{tot} for a 50 GeV electron beam. The larger cluster on the top right corresponds to electrons, while the smaller one is the hadron contamination.

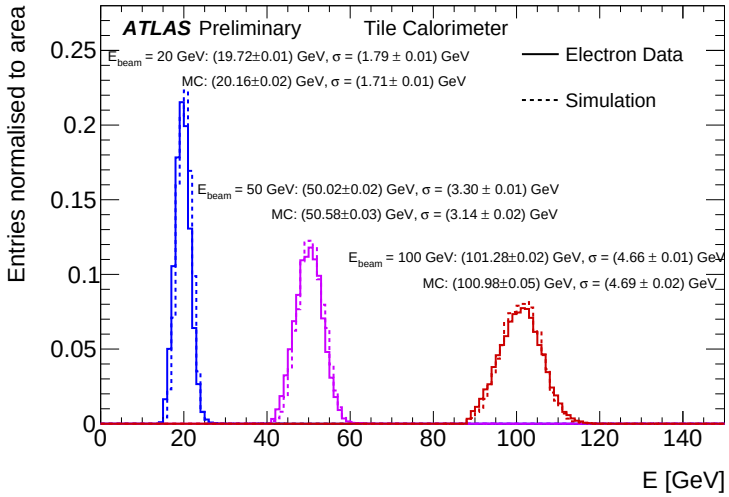

FIGURE B.8: Distribution of total electron deposited energy for different beam energies and an incident beam at 20 degrees on cell A4. The solid line corresponds to data, while the dotted line shows the simulation.

For proton selection, the Ch2 signal is required to be Ch2 $<$ 460 ADC, for pions Ch2$>$ 3900 ADC, and for kaons Ch2$>$ 460 ADC.

The determination of the hadron response in each case is done fitting the total energy distribution to a gaussian, with the range of the fit reduced to 2σ around the peak. As it can be seen in figure B.12, a secondary peak appears in the low energy spectrum due to muons from kaon decay. The reduced range for the fit avoids this peak from being taken into account, giving a better measure of the hadron energy.

The results are shown in figure B.13. The mean and RMS of the gaussian fit are shown for protons, kaons and pions as a function of the beam energy. The ratio of data and simulation is also displayed. Lower response to protons than kaons and pions is observed, as expected from a non-compensating hadronic calorimeter. The agreement with simulation improves with increasing energy, since the contamination from electrons and muons is lower at higher energies.

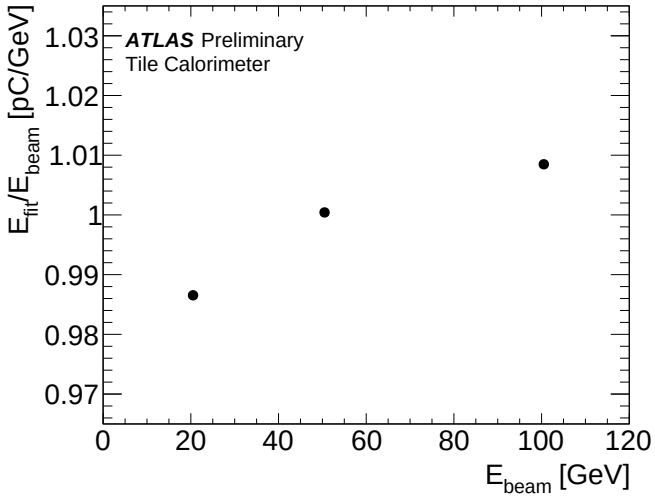

FIGURE B.9: Electron response as a function of the beam energy for 20-degree incident muons on cell A4.

B.4 Conclusions

The Tile Calorimeter readout system will be upgraded for the HL-LHC era. A prototype with the new components was exposed to test beams of muons, electrons and hadrons. Studies performed with 165 GeV muons incident at 20 and 90 degrees confirm the uniformity of the calorimeter response, and the expected linearity of the muon energy deposited with path length is observed. Electron data collected for 20, 50 and 100 GeV beams incident at 20 degrees show good agreement with simulation and the total energy deposited corresponds with the beam energy within 2%. The analysis of the hadron data collected with 16, 18, 20 and 30 GeV beams show good agreement with simulation and the expected good response of the calorimeter to different hadrons.

These results confirm the good performance of the new TileCal electronics, and good agreement between simulation and calibrated data. This guarantees a good calorimeter signal when the new electronics will be installed in the detector.

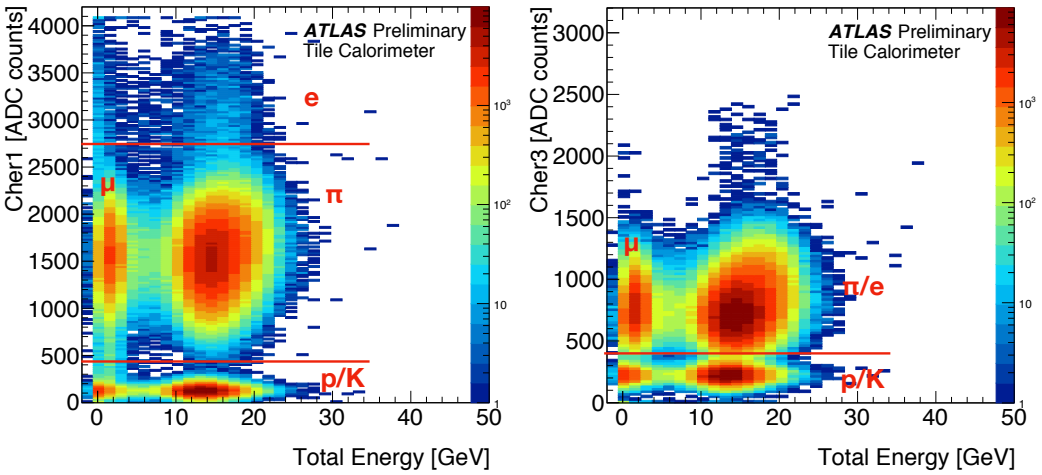

FIGURE B.10: Signal in Ch1 and Ch3 counters vs total energy for hadron beams of 18 GeV. The particle identification of each of the clusters is overlaid in the figures, as well as the requirements applied for particle selection.

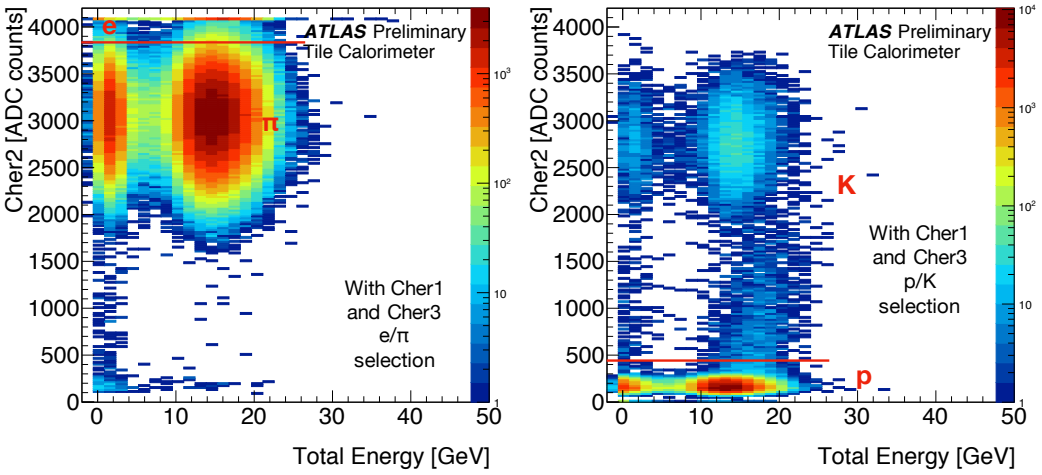

FIGURE B.11: Signal in Ch2 counter vs total energy for hadron beams of 18 GeV after applying electron and pion selection (left) and proton and kaon selection (right) in Ch1 and Ch3. The particle identification and requirements applied for selection are overlaid in the figures.

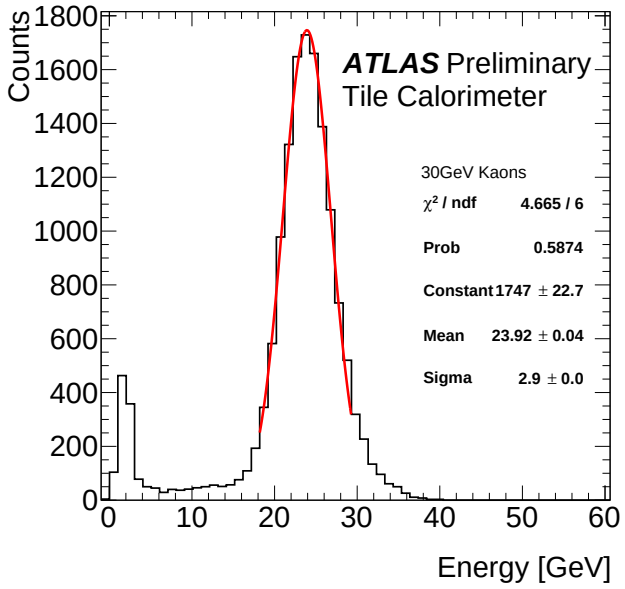

FIGURE B.12: Distribution of total energy for 30 GeV hadron beam with kaon selection applied. The gaussian fit is performed using only the range of 2σ within the peak.

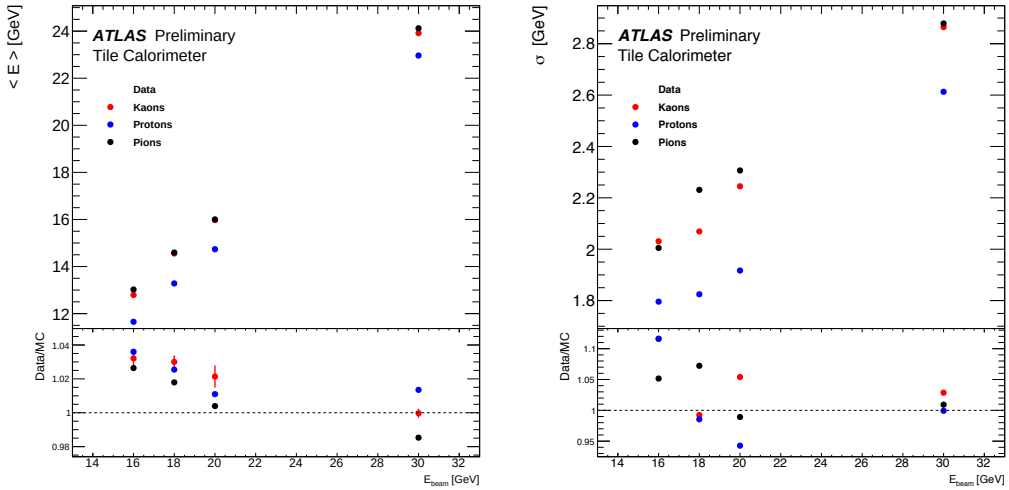

FIGURE B.13: Mean and standard deviation of the gaussian fits to the energy distribution for kaons, protons and pions as a function of the beam energy. Lower plots show data over simulation.

Bibliography

[1] S. Glashow. In: *Nuclear Physics* 22 (1961), pp. 579–588.

[2] Steven Weinberg. "A Model of Leptons". In: *Phys. Rev. Lett.* 19 (21 1967), pp. 1264–1266. DOI: 10.1103/PhysRevLett.19.1264.

[3] Abdus Salam. "Gauge Unification of Fundamental Forces". In: *Rev. Mod. Phys.* 52 (1980). [,306(1980)], pp. 525–538. DOI: 10.1103/RevModPhys.52.525.

[4] Albert Einstein. "The foundation of the General Theory of Relativity". In: *Annalen Der Physik* 49 (1916).

[5] ATLAS Collaboration. "Observation of a new particle in the search for the Standard Model Higgs boson with the ATLAS detector at the LHC". In: *Phys. Lett.* B716 (2012), pp. 1–29. DOI: 10.1016/j.physletb.2012.08.020. arXiv: 1207.7214 [hep-ex].

[6] CMS Collaboration. "Observation of a new boson at a mass of 125 GeV with the CMS experiment at the LHC". In: *Phys. Lett.* B716 (2012), pp. 30–61. DOI: 10.1016/j.physletb.2012.08.021. arXiv: 1207.7235 [hep-ex].

[7] Gerard 't Hooft. "Dimensional regularization and the renormalization group". In: *Nucl. Phys.* B61 (1973), pp. 455–468. DOI: 10.1016/0550-3213(73)90376-3.

[8] C. Patrignani et al. "Review of Particle Physics". In: *Chin. Phys.* C40.10 (2016), p. 100001. DOI: 10.1088/1674-1137/40/10/100001.

[9] Super-Kamiokande Collaboration. "Evidence for oscillation of atmospheric neutrinos". In: *Phys. Rev. Lett.* 81 (1998), pp. 1562–1567. DOI: 10.1103/PhysRevLett.81.1562. arXiv: hep-ex/9807003 [hep-ex].

[10] R. P. Feynman. "Mathematical Formulation of the Quantum Theory of Electromagnetic Interaction". In: *Phys. Rev.* 80 (3 1950), pp. 440–457. DOI: 10.1103/PhysRev.80.440.

[11] J. Schwinger. "Quantum Electrodynamics. I. A Covariant Formulation". In: *Physical Review* 74 (Nov. 1948), pp. 1439–1461. DOI: 10.1103/PhysRev.74.1439.

[12] S. Tomonaga. "On a Relativistically Invariant Formulation of the Quantum Theory of Wave Fields*". In: *Progress of Theoretical Physics* 1.2 (1946), pp. 27–42. DOI: 10.1143/PTP.1.27. eprint: /oup/backfile/content_public/journal/ptp/1/2/10.1143_pt

[13] Michael Peskin and Daniel Schroeder. *An intoduction to Quantum Field Theory*. 1995.

[14] David Griffiths. *Introduction to Elementary Particle Physics*. 2008.

[15] Enrico Fermi. "Tentativo di una teoria dei raggi β". In: *La Ricerca Scientifica* 2 (), pp. 1–20.

[16] F. Englert and R. Brout. "Broken Symmetry and the Mass of Gauge Vector Mesons". In: *Phys. Rev. Lett.* 13 (9 1964), pp. 321–323. DOI: 10.1103/PhysRevLett.13.321.

[17] Peter W. Higgs. "Broken Symmetries and the Masses of Gauge Bosons". In: *Phys. Rev. Lett.* 13 (16 1964), pp. 508–509. DOI: 10.1103/PhysRevLett.13.508.

[18] J. Goldstone. "Field theories with Superconductor solutions". In: *Il Nuovo Cimento (1955-1965)* 19.1 (1961), pp. 154–164. ISSN: 1827-6121. DOI: 10.1007/BF02812722.

[19] Jeffrey Goldstone, Abdus Salam, and Steven Weinberg. "Broken Symmetries". In: *Phys. Rev.* 127 (3 1962), pp. 965–970. DOI: 10.1103/PhysRev.127.965.

[20] H. Fritzsch, M. Gell-Mann, and H. Leutwyler. "Advantages of the color octet gluon picture". In: *Physics Letters B* 47.4 (1973), pp. 365 –368. ISSN: 0370-2693. DOI: https://doi.org/10.1016/0370-2693(73)90625-4.

[21] O. W. Greenberg. "Spin and Unitary-Spin Independence in a Paraquark Model of Baryons and Mesons". In: *Phys. Rev. Lett.* 13 (20 1964), pp. 598–602. DOI: 10.1103/PhysRevLett.13.598.

[22] C. Quigg. *Gauge Theories of the Strong, Weak and Electromagnetic Interactions.*

[23] ATLAS Collaboration. "Determination of the strong coupling constant α_s from transverse energy-energy correlations in multijet events at $\sqrt{s} = 8$ TeV using the ATLAS detector." In: *Eur. Phys. J. C* 77.CERN-EP-2017-093 (2017), 872. 49 p.

[24] John C. Collins, Davison E. Soper, and George F. Sterman. "Factorization of Hard Processes in QCD". In: *Adv. Ser. Direct. High Energy Phys.* 5 (1989), pp. 1–91. DOI: 10.1142/9789814503266_0001. arXiv: hep-ph/0409313 [hep-ph].

[25] G. Altarelli and G. Parisi. "Asymptotic freedom in parton language". In: *Nuclear Physics B* 126.2 (1977), pp. 298 –318. ISSN: 0550-3213. DOI: https://doi.org/10.1016/055

[26] Richard D. Ball et al. "Parton distributions for the LHC Run II". In: *JHEP* 04 (2015), p. 040. DOI: 10.1007/JHEP04(2015)040. arXiv: 1410.8849 [hep-ph].

[27] V. V. Sudakov. "Vertex parts at very high-energies in quantum electrodynamics". In: *Sov. Phys. JETP* 3 (1956). [Zh. Eksp. Teor. Fiz.30,87(1956)], pp. 65–71.

[28] S. Catani et al. "QCD matrix elements + parton showers". In: *JHEP* 11 (2001), p. 063. DOI: 10.1088/1126-6708/2001/11/063. arXiv: hep-ph/0109231 [hep-ph].

[29] Michelangelo L. Mangano et al. "Matching matrix elements and shower evolution for top-quark production in hadronic collisions". In: *JHEP* 01 (2007), p. 013. DOI: 10.1088/1126-6708/2007/01/013. arXiv: hep-ph/0611129 [hep-ph].

[30] Stephen D. Ellis and Davison E. Soper. "Successive combination jet algorithm for hadron collisions". In: *Phys. Rev.* D48 (1993), pp. 3160–3166. DOI: 10.1103/PhysRevD.48.3160. arXiv: hep-ph/9305266 [hep-ph].

[31] Bo Andersson et al. "Parton Fragmentation and String Dynamics". In: *Phys. Rept.* 97 (1983), pp. 31–145. DOI: 10.1016/0370-1573(83)90080-7.

[32] Torbjorn Sjostrand. "Jet Fragmentation of Nearby Partons". In: *Nucl. Phys.* B248 (1984), pp. 469–502. DOI: 10.1016/0550-3213(84)90607-2.

[33] B. R. Webber. "A QCD Model for Jet Fragmentation Including Soft Gluon Interference". In: *Nucl. Phys.* B238 (1984), pp. 492–528. DOI: 10.1016/0550-3213(84)90333-X.

[34] G. Marchesini and B. R. Webber. "Monte Carlo Simulation of General Hard Processes with Coherent QCD Radiation". In: *Nucl. Phys.* B310 (1988), pp. 461–526. DOI: 10.1016/0550-3213(88)90089-2.

[35] ATLAS Collaboration. "Measurement of the underlying event in jet events from 7 TeV proton-proton collisions with the ATLAS detector". In: *Eur. Phys. J.* C74.8 (2014), p. 2965. DOI: 10.1140/epjc/s10052-014-2965-5. arXiv: 1406.0392 [hep-ex].

[36] Torbjorn Sjostrand, Stephen Mrenna, and Peter Z. Skands. "PYTHIA 6.4 Physics and Manual". In: *JHEP* 05 (2006), p. 026. DOI: 10.1088/1126-6708/2006/05/026. arXiv: hep-ph/0603175 [hep-ph].

[37] Torbjorn Sjostrand, Stephen Mrenna, and Peter Z. Skands. "A Brief Introduction to PYTHIA 8.1". In: *Comput. Phys. Commun.* 178 (2008), pp. 852–867. DOI: 10.1016/j.cpc.2008.01.036. arXiv: 0710.3820 [hep-ph].

[38] T. Gleisberg et al. "Event generation with SHERPA 1.1". In: *JHEP* 02 (2009), p. 007. DOI: 10.1088/1126-6708/2009/02/007. arXiv: 0811.4622 [hep-ph].

[39] Stefano Frixione, Paolo Nason, and Carlo Oleari. "Matching NLO QCD computations with Parton Shower simulations: the POWHEG method". In: *JHEP* 11 (2007), p. 070. DOI: 10.1088/1126-6708/2007/11/070. arXiv: 0709.2092 [hep-ph].

[40] Johan Alwall et al. "MadGraph 5 : Going Beyond". In: *JHEP* 06 (2011), p. 128. DOI: 10.1007/JHEP06(2011)128. arXiv: 1106.0522 [hep-ph].

[41] G. Corcella et al. "HERWIG 6: An Event generator for hadron emission reactions with interfering gluons (including supersymmetric processes)". In: *JHEP* 01 (2001), p. 010. DOI: 10.1088/1126-6708/2001/01/010. arXiv: hep-ph/0011363 [hep-ph].

[42] David Gross, David Politzer, and Frank Wilczek. "The 2004 Nobel Prize in Physics - Popular Information". In: *Nobel Media AB 2014* ().

[43] K. G. Begeman, A. H. Broeils, and R. H. Sanders. "Extended rotation curves of spiral galaxies: Dark haloes and modified dynamics". In: *Mon. Not. Roy. Astron. Soc.* 249 (1991), p. 523.

[44] Gianfranco Bertone, Dan Hooper, and Joseph Silk. "Particle dark matter: Evidence, candidates and constraints". In: *Phys. Rept.* 405 (2005), pp. 279–390. DOI: 10.1016/j.physrep.2004.08.031. arXiv: hep-ph/0404175 [hep-ph].

[45] E. Komatsu et al. "Seven-Year Wilkinson Microwave Anisotropy Probe (WMAP) Observations: Cosmological Interpretation". In: (). arXiv: arXiv:1001.4538v3 [astro-ph].

[46] Leszek Roszkowski, Enrico Maria Sessolo, and Sebastian Trojanowski. "WIMP dark matter candidates and searches - current issues and future prospects". In: *Rept. Prog. Phys.* 81.6 (2018), p. 066201. DOI: 10.1088/1361-6633/aab913. arXiv: 1707.06277 [hep-ph].

[47] J.-L. Gervais and B. Sakita. "Field theory interpretation of supergauges in dual models". In: *Nuclear Physics B* 34.2 (1971), pp. 632 –639. ISSN: 0550-3213. DOI: https://doi.org/10.1016/0550-3213(71)90351-8.

[48] Manuel Drees. "An Introduction to supersymmetry". In: *Current topics in physics. Proceedings, Inauguration Conference of the Asia-Pacific Center for Theoretical Physics (APCTP), Seoul, Korea, June 4-10, 1996. Vol. 1, 2.* 1996. arXiv: hep-ph/9611409 [hep-ph].

[49] Daniel Z. Freedman, P. van Nieuwenhuizen, and S. Ferrara. "Progress toward a theory of supergravity". In: *Phys. Rev. D* 13 (12 1976), pp. 3214–3218. DOI: 10.1103/PhysRevD.13.3214.

[50] Makoto Kobayashi and Toshihide Maskawa. "CP Violation in the Renormalizable Theory of Weak Interaction". In: *Prog. Theor. Phys.* 49 (1973), pp. 652–657. DOI: 10.1143/PTP.49.652.

[51] Edward Witten. "Dynamical Breaking of Supersymmetry". In: *Nucl. Phys.* B188 (1981), p. 513. DOI: 10.1016/0550-3213(81)90006-7.

[52] Christoph Borschensky et al. "Squark and gluino production cross sections in pp collisions at $\sqrt{s} = 13$, 14, 33 and 100 TeV". In: *Eur. Phys. J.* C74.12 (2014), p. 3174. DOI: 10.1140/epjc/s10052-014-3174-y. arXiv: 1407.5066 [hep-ph].

[53] W. Beenakker et al. "Stop production at hadron colliders". In: *Nucl. Phys.* B515 (1998), pp. 3–14. DOI: 10.1016/S0550-3213(98)00014-5. arXiv: hep-ph/9710451 [hep-ph].

[54] Wim Beenakker et al. "Supersymmetric top and bottom squark production at hadron colliders". In: *JHEP* 08 (2010), p. 098. DOI: 10.1007/JHEP08(2010)098. arXiv: 1006.4771 [hep-ph].

[55] Lyndon Evans and Philip Bryant. "LHC Machine". In: *Journal of Instrumentation* 3.08 (2008), S08001.

[56] The ALICE Collaboration. "The ALICE experiment at the CERN LHC". In: *Journal of Instrumentation* 3.08 (2008), S08002.

[57] ATLAS Collaboration. "The ATLAS Experiment at the CERN Large Hadron Collider". In: *JINST* 3 (2008), S08003. DOI: 10.1088/1748-0221/3/08/S08003.

[58] CMS Collaboration. "The CMS Experiment at the CERN LHC". In: *JINST* 3 (2008), S08004. DOI: 10.1088/1748-0221/3/08/S08004.

[59] LHCb Collaboration. "The LHCb Detector at the LHC". In: *JINST* 3 (2008), S08005. DOI: 10.1088/1748-0221/3/08/S08005.

[60] Christiane Lefevre. "The CERN accelerator complex. Complexe des accelerateurs du CERN". 2008.

[61] M Capeans et al. *ATLAS Insertable B-Layer Technical Design Report*. Tech. rep. CERN-LHCC-2010-013. ATLAS-TDR-19. 2010.

[62] ATLAS collaboration. "Performance of the ATLAS Track Reconstruction Algorithms in Dense Environments in LHC Run 2". In: *Eur. Phys. J.* C77.10 (2017), p. 673. DOI: 10.1140/epjc/s10052-017-5225-7. arXiv: 1704.07983 [hep-ex].

[63] ATLAS collaboration. "Readiness of the ATLAS Liquid Argon Calorimeter for LHC Collisions. Readiness of the ATLAS Liquid Argon Calorimeter for LHC Collisions". In: *Eur. Phys. J. C* 70.arXiv:0912.2642. CERN-PH-EP-2010-041 (2010), 723–753. 31 p.

[64] ATLAS Collaboration. "Readiness of the ATLAS Tile Calorimeter for LHC collisions". In: *Eur. Phys. J.* C70 (2010), pp. 1193–1236. DOI: 10.1140/epjc/s10052-010-1508-y. arXiv: 1007.5423 [physics.ins-det].

[65] ATLAS collaboration. "Performance of the ATLAS Trigger System in 2015". In: *Eur. Phys. J.* C77.5 (2017), p. 317. DOI: 10.1140/epjc/s10052-017-4852-3. arXiv: 1611.09661 [hep-ex].

[66] ATLAS collaboration. "Luminosity determination in pp collisions at $\sqrt{s} = 8$ TeV using the ATLAS detector at the LHC". In: *Eur. Phys. J.* C76.12 (2016), p. 653. DOI: 10.1140/epjc/s10052-016-4466-1. arXiv: 1608.03953 [hep-ex].

[67] A Barriuso Poy et al. "The detector control system of the ATLAS experiment". In: *JINST* 3 (2008), P05006.

[68] T. Golling et al. "The ATLAS Data Quality Defect Database System". In: *Eur. Phys. J.* C72 (2012), p. 1960. DOI: 10.1140/epjc/s10052-012-1960-y. arXiv: 1110.6119 [physics.ins-det].

[69] A Corso-Radu et al. *Data Quality Monitoring Framework for the ATLAS Experiment at the LHC*. Tech. rep. ATL-DAQ-CONF-2008-006. ATL-COM-DAQ-2007-033. Geneva: CERN, 2007.

[70] T Cornelissen et al. "The new ATLAS track reconstruction (NEWT)". In: *Journal of Physics: Conference Series* 119.3 (2008), p. 032014.

[71] ATLAS collaboration. "Reconstruction of primary vertices at the ATLAS experiment in Run 1 proton-proton collisions at the LHC". In: *Eur. Phys. J.* C77.5 (2017), p. 332. DOI: 10.1140/epjc/s10052-017-4887-5. arXiv: 1611.10235 [physics.ins-det].

[72] ATLAS collaboration. "Electron and photon energy calibration with the ATLAS detector using LHC Run 1 data". In: *Eur. Phys. J.* C74.10 (2014), p. 3071. DOI: 10.1140/epjc/s10052-014-3071-4. arXiv: 1407.5063 [hep-ex].

[73] W Lampl et al. *Calorimeter Clustering Algorithms: Description and Performance*. Tech. rep. ATL-LARG-PUB-2008-002. ATL-COM-LARG-2008-003. Geneva: CERN, 2008.

[74] *Electron identification measurements in ATLAS using $\sqrt{s}$ = 13 TeV data with 50 ns bunch spacing*. Tech. rep. ATL-PHYS-PUB-2015-041. Geneva: CERN, 2015.

[75] ATLAS collaboration. "Muon reconstruction performance of the ATLAS detector in proton-proton collision data at $\sqrt{s}$ =13 TeV". In: *Eur. Phys. J.* C76.5 (2016), p. 292. DOI: 10.1140/epjc/s10052-016-4120-y. arXiv: 1603.05598 [hep-ex].

[76] ATLAS Collaboration. "Measurement of the muon reconstruction performance of the ATLAS detector using 2011 and 2012 LHC proton-proton collision data". In: *Eur. Phys. J.* C74.11 (2014), p. 3130. DOI: 10.1140/epjc/s10052-014-3130-x. arXiv: 1407.3935 [hep-ex].

[77] ATLAS Collaboration. "Muon reconstruction efficiency and momentum resolution of the ATLAS experiment in proton-proton collisions at $\sqrt{s}$ = 7 TeV in 2010". In: *Eur. Phys. J.* C74.9 (2014), p. 3034. DOI: 10.1140/epjc/s10052-014-3034-9. arXiv: 1404.4562 [hep-ex].

[78] ATLAS Collaboration. "Measurement of the muon reconstruction performance of the ATLAS detector using 2011 and 2012 LHC proton-proton collision data". In: *Eur. Phys. J.* C74.11 (2014), p. 3130. DOI: 10.1140/epjc/s10052-014-3130-x. arXiv: 1407.3935 [hep-ex].

[79] Matteo Cacciari, Gavin P. Salam, and Gregory Soyez. "The Anti-k(t) jet clustering algorithm". In: *JHEP* 04 (2008), p. 063. DOI: 10.1088/1126-6708/2008/04/063. arXiv: 0802.1189 [hep-ph].

[80] ATLAS Collaboration. "Topological cell clustering in the ATLAS calorimeters and its performance in LHC Run 1". In: *Eur. Phys. J.* C77 (2017), p. 490. DOI: 10.1140/epjc/s10052-017-5004-5. arXiv: 1603.02934 [hep-ex].

[81] ATLAS Collaboration. "Jet energy scale measurements and their systematic uncertainties in proton-proton collisions at $\sqrt{s}$ = 13 TeV with the ATLAS detector". In: *Phys. Rev.* D96.7 (2017), p. 072002. DOI: 10.1103/PhysRevD.96.072002. arXiv: 1703.09665 [hep-ex].

[82] ATLAS Collaboration. "Jet energy measurement and its systematic uncertainty in proton-proton collisions at $\sqrt{s}$ = 7 TeV with the ATLAS detector". In: *Eur. Phys. J.* C75 (2015), p. 17. DOI: 10.1140/epjc/s10052-014-3190-y. arXiv: 1406.0076 [hep-ex].

[83] Matteo Cacciari and Gavin P. Salam. "Pileup subtraction using jet areas". In: *Phys. Lett.* B659 (2008), pp. 119–126. DOI: 10.1016/j.physletb.2007.09.077. arXiv: 0707.1378 [hep-ph].

[84] S Catani et al. "Longitudinally-invariant $k_\perp$-clustering algorithms for hadron-hadron collisions". In: *Nucl. Phys. B* 406.CERN-TH-6775-93. LU-TP-93-2 (1993), 187–224. 38 p.

[85] D Lopez Mateos, E W Hughes, and A Schwartzman. *A Simple p_T- and η-Dependent Monte Carlo-Based Jet Calibration*. Tech. rep. ATL-PHYS-INT-2009-077. Geneva: CERN, 2009.

[86] ATLAS Colaboration. "Jet energy measurement with the ATLAS detector in proton-proton collisions at $\sqrt{s} = 7$ TeV". In: *Eur. Phys. J.* C73.3 (2013), p. 2304. DOI: 10.1140/epjc/s10052-013-2304-2. arXiv: 1112.6426 [hep-ex].

[87] ATLAS Colaboration. "Performance of b-Jet Identification in the ATLAS Experiment". In: *JINST* 11.04 (2016), P04008. DOI: 10.1088/1748-0221/11/04/P04008. arXiv: 1512.01094 [hep-ex].

[88] *Optimisation of the ATLAS b-tagging performance for the 2016 LHC Run*. Tech. rep. ATL-PHYS-PUB-2016-012. Geneva: CERN, 2016.

[89] ATLAS Collaboration. "Performance of missing transverse momentum reconstruction with the ATLAS detector using proton-proton collisions at $\sqrt{s} = 13$ TeV". In: (2018). arXiv: 1802.08168 [hep-ex].

[90] *Performance of missing transverse momentum reconstruction for the ATLAS detector in the first proton-proton collisions at at $\sqrt{s}$= 13 TeV*. Tech. rep. ATL-PHYS-PUB-2015-027. Geneva: CERN, 2015.

[91] ATLAS Collaboration. "Performance of algorithms that reconstruct missing transverse momentum in $\sqrt{s} = 8$ TeV proton-proton collisions in the ATLAS detector". In: *Eur. Phys. J.* C77.4 (2017), p. 241. DOI: 10.1140/epjc/s10052-017-4780-2. arXiv: 1609.09324 [hep-ex].

[92] Luca Lista. *Statistical Methods for Data Analysis in Particle Physics*. 2016.

[93] Alexander L. Read. "Presentation of search results: The CL(s) technique". In: *J. Phys.* G28 (2002). [,11(2002)], pp. 2693–2704. DOI: 10.1088/0954-3899/28/10/313.

[94] Glen Cowan. "Statistics for Searches at the LHC". In: *Proceedings, 69th Scottish Universities Summer School in Physics : LHC Phenomenology (SUSSP69): St.Andrews, Scotland, August 19-September 1, 2012*. 2013, pp. 321–355. DOI: 10.1007/978-3-319-05362-2_9. arXiv: 1307.2487 [hep-ex].

[95] Glen Cowan et al. "Asymptotic formulae for likelihood-based tests of new physics". In: *Eur. Phys. J.* C71 (2011). [Erratum: Eur. Phys. J.C73,2501(2013)], p. 1554. DOI: 10.1140/epjc/s10052-011-1554-0,10.1140/epjc/s10052-013-2501-z. arXiv: 1007.1727 [physics.data-an].

[96] M. Baak et al. "HistFitter software framework for statistical data analysis". In: *Eur. Phys. J.* C75 (2015), p. 153. DOI: 10.1140/epjc/s10052-015-3327-7. arXiv: 1410.1280 [hep-ex].

[97] ATLAS Collaboration. "Search for direct pair production of the top squark in all-hadronic final states in proton-proton collisions at $\sqrt{s} = 8$ TeV with the ATLAS detector". In: *JHEP* 09 (2014), p. 015. DOI: 10.1007/JHEP09(2014)015. arXiv: 1406.1122 [hep-ex].

[98] ATLAS Collaboration. "ATLAS Run 1 searches for direct pair production of third-generation squarks at the Large Hadron Collider". In: *Eur. Phys. J.* C75.10 (2015). [Erratum: Eur. Phys. J.C76,no.3,153(2016)], p. 510. DOI: 10.1140/epjc/s10052-015-3726-9,10.1140/epjc/s10052-016-3935-x. arXiv: 1506.08616 [hep-ex].

[99] ATLAS Collaboration. "Search for new phenomena in final states with an energetic jet and large missing transverse momentum in pp collisions at $\sqrt{s} = 13$ TeV using the ATLAS detector". In: *Phys. Rev.* D94.3 (2016), p. 032005. DOI: 10.1103/PhysRevD.94.032005. arXiv: 1604.07773 [hep-ex].

[100] ATLAS Collaboration. "Search for top-squark pair production in final states with one lepton, jets, and missing transverse momentum using 36 fb^{-1} of $\sqrt{s} = 13$ TeV pp collision data with the ATLAS detector". In: (2017). arXiv: 1711.11520 [hep-ex].

[101] ATLAS Collaboration. "Search for direct top squark pair production in final states with two leptons in $\sqrt{s} = 13$ TeV pp collisions with the ATLAS detector". In: *Eur. Phys. J.* C77.12 (2017), p. 898. DOI: 10.1140/epjc/s10052-017-5445-x. arXiv: 1708.03247 [hep-ex].

[102] CMS Collaboration. "Search for direct production of supersymmetric partners of the top quark in the all-jets final state in proton-proton collisions at $\sqrt{s} = 13$ TeV". In: *JHEP* 10 (2017), p. 005. DOI: 10.1007/JHEP10(2017)005. arXiv: 1707.03316 [hep-ex].

[103] CMS Collaboration. "Search for top squark pair production in pp collisions at $\sqrt{s} = 13$ TeV using single lepton events". In: *JHEP* 10 (2017), p. 019. DOI: 10.1007/JHEP10(2017)019. arXiv: 1706.04402 [hep-ex].

[104] CMS Collaboration. "Search for top squarks and dark matter particles in opposite-charge dilepton final states at $\sqrt{s} = 13$ TeV". In: *Phys. Rev.* D97.3 (2018), p. 032009. DOI: 10.1103/PhysRevD.97.032009. arXiv: 1711.00752 [hep-ex].

[105] CMS Collaboration. "Search for supersymmetry in proton-proton collisions at 13 TeV using identified top quarks". In: *Phys. Rev.* D97.1 (2018), p. 012007. DOI: 10.1103/PhysRevD.97.012007. arXiv: 1710.11188 [hep-ex].

[106] CMS Collaboration. "Search for new phenomena with the M_{T2} variable in the all-hadronic final state produced in proton-proton collisions at $\sqrt{s} = 13$ TeV". In: *Eur. Phys. J.* C77.10 (2017), p. 710. DOI: 10.1140/epjc/s10052-017-5267-x. arXiv: 1705.04650 [hep-ex].

[107] Johan Alwall, Philip Schuster, and Natalia Toro. "Simplified Models for a First Characterization of New Physics at the LHC". In: *Phys. Rev.* D79 (2009), p. 075020. DOI: 10.1103/PhysRevD.79.075020. arXiv: 0810.3921 [hep-ph].

[108] W. Beenakker et al. "Squark and Gluino Hadroproduction". In: *Int. J. Mod. Phys.* A26 (2011), pp. 2637–2664. DOI: 10.1142/S0217751X11053560. arXiv: 1105.1110 [hep-ph].

[109] Christoph Borschensky et al. "Squark and gluino production cross sections in pp collisions at $\sqrt{s} = 13$, 14, 33 and 100 TeV". In: *Eur. Phys. J.* C74.12 (2014), p. 3174. DOI: 10.1140/epjc/s10052-014-3174-y. arXiv: 1407.5066 [hep-ph].

[110] S. Agostinelli et al. "GEANT4: A Simulation toolkit". In: *Nucl. Instrum. Meth.* A506 (2003), pp. 250–303. DOI: 10.1016/S0168-9002(03)01368-8.

[111] A. D. Martin et al. "Parton distributions for the LHC". In: *Eur. Phys. J.* C63 (2009), pp. 189–285. DOI: 10.1140/epjc/s10052-009-1072-5. arXiv: 0901.0002 [hep-ph].

[112] ATLAS Collaboration. "The ATLAS Simulation Infrastructure". In: *Eur. Phys. J.* C70 (2010), pp. 823–874. DOI: 10.1140/epjc/s10052-010-1429-9. arXiv: 1005.4568 [physics.ins-det].

[113] Richard D. Ball et al. "Parton distributions with LHC data". In: *Nucl. Phys.* B867 (2013), pp. 244–289. DOI: 10.1016/j.nuclphysb.2012.10.003. arXiv: 1207.1303 [hep-ph].

[114] Simone Alioli et al. "A general framework for implementing NLO calculations in shower Monte Carlo programs: the POWHEG BOX". In: *JHEP* 06 (2010), p. 043. DOI: 10.1007/JHEP06(2010)043. arXiv: 1002.2581 [hep-ph].

[115] Hung-Liang Lai et al. "New parton distributions for collider physics". In: *Phys. Rev.* D82 (2010), p. 074024. DOI: 10.1103/PhysRevD.82.074024. arXiv: 1007.2241 [hep-ph].

[116] Peter Z. Skands. "The Perugia Tunes". In: *Proceedings, 1st International Workshop on Multiple Partonic Interactions at the LHC (MPI08): Perugia, Italy, October 27-31, 2008*. 2009, pp. 284–297. arXiv: 0905.3418 [hep-ph].

[117] *Simulation of top quark production for the ATLAS experiment at sqrt(s) = 13 TeV*. Tech. rep. ATL-PHYS-PUB-2016-004. Geneva: CERN, 2016.

[118] J. Alwall et al. "The automated computation of tree-level and next-to-leading order differential cross sections, and their matching to parton shower simulations". In: *JHEP* 07 (2014), p. 079. DOI: 10.1007/JHEP07(2014)079. arXiv: 1405.0301 [hep-ph].

[119] *Multi-Boson Simulation for 13 TeV ATLAS Analyses*. Tech. rep. ATL-PHYS-PUB-2016-002. Geneva: CERN, 2016.

[120] D. J. Lange. "The EvtGen particle decay simulation package". In: *Nucl. Instrum. Meth.* A462 (2001), pp. 152–155. DOI: 10.1016/S0168-9002(01)00089-4.

[121] Leif Lonnblad and Stefan Prestel. "Merging Multi-leg NLO Matrix Elements with Parton Showers". In: *JHEP* 03 (2013), p. 166. DOI: 10.1007/JHEP03(2013)166. arXiv: 1211.7278 [hep-ph].

[122] *Tagging and suppression of pileup jets with the ATLAS detector*. Tech. rep. ATLAS-CONF-2014-018. Geneva: CERN, 2014.

[123] Alan Barr, Christopher Lester, and P. Stephens. "m(T2): The Truth behind the glamour". In: *J. Phys.* G29 (2003), pp. 2343–2363. DOI: 10.1088/0954-3899/29/10/304. arXiv: hep-ph/0304226 [hep-ph].

[124] C. G. Lester and D. J. Summers. "Measuring masses of semiinvisibly decaying particles pair produced at hadron colliders". In: *Phys. Lett.* B463 (1999), pp. 99–103. DOI: 10.1016/S0370-2693(99)00945-4. arXiv: hep-ph/9906349 [hep-ph].

[125] Steve Baker and Robert D. Cousins. "Clarification of the Use of Chi Square and Likelihood Functions in Fits to Histograms". In: *Nucl. Instrum. Meth.* 221 (1984), pp. 437–442. DOI: 10.1016/0167-5087(84)90016-4.

[126] Paul Jackson, Christopher Rogan, and Marco Santoni. "Sparticles in motion: Analyzing compressed SUSY scenarios with a new method of event reconstruction". In: *Phys. Rev. D* 95 (3 2017), p. 035031. DOI: 10.1103/PhysRevD.95.035031.

[127] Haipeng An and Lian-Tao Wang. "Opening up the compressed region of top squark searches at 13 TeV LHC". In: *Phys. Rev. Lett.* 115 (2015), p. 181602. DOI: 10.1103/PhysRevLett.115.181602. arXiv: 1506.00653 [hep-ph].

[128] Sebastian Macaluso et al. "Revealing Compressed Stops Using High-Momentum Recoils". In: *JHEP* 03 (2016), p. 151. DOI: 10.1007/JHEP03(2016)151. arXiv: 1506.07885 [hep-ph].

[129] ATLAS Collaboration. "Search for squarks and gluinos with the ATLAS detector in final states with jets and missing transverse momentum using 4.7 fb^{-1} of $\sqrt{s} = 7$ TeV proton-proton collision data". In: *Phys. Rev.* D87.1 (2013), p. 012008. DOI: 10.1103/PhysRevD.87.012008. arXiv: 1208.0949 [hep-ex].

[130] Daniele Alves. "Simplified Models for LHC New Physics Searches". In: *J. Phys.* G39 (2012). Ed. by Nima Arkani-Hamed et al., p. 105005. DOI: 10.1088/0954-3899/39/10/105005. arXiv: 1105.2838 [hep-ph].

[131] Michele Papucci, Joshua T. Ruderman, and Andreas Weiler. "Natural SUSY Endures". In: *JHEP* 09 (2012), p. 035. DOI: 10.1007/JHEP09(2012)035. arXiv: 1110.6926 [hep-ph].

[132] Ian J. R. Aitchison. "Supersymmetry and the MSSM: An Elementary introduction". In: (2005). arXiv: hep-ph/0505105 [hep-ph].

[133] ATLAS Collaboration. "Search for top squarks in final states with one isolated lepton, jets, and missing transverse momentum in $\sqrt{s} = 13$ TeV pp collisions with the ATLAS detector". In: *Phys. Rev.* D94.5 (2016), p. 052009. DOI: 10.1103/PhysRevD.94.052009. arXiv: 1606.03903 [hep-ex].

[134] ATLAS Collaboration. "Search for squarks and gluinos in events with isolated leptons, jets and missing transverse momentum at $\sqrt{s} = 8$ TeV with the ATLAS detector". In: *JHEP* 04 (2015), p. 116. DOI: 10.1007/JHEP04(2015)116. arXiv: 1501.03555 [hep-ex].

[135] ATLAS Collaboration. "Summary of the ATLAS experiment's sensitivity to supersymmetry after LHC Run 1 interpreted in the phenomenological MSSM". In: *JHEP* 10 (2015), p. 134. DOI: 10.1007/JHEP10(2015)134. arXiv: 1508.06608 [hep-ex].

[136] *Prospects for benchmark Supersymmetry searches at the high luminosity LHC with the ATLAS Detector*. Tech. rep. ATL-PHYS-PUB-2013-011. Geneva: CERN, 2013.

[137] Andrea Rodriguez Perez et al. *Jet p_{T} reconstruction in the presence of TileCal masked regions*. Tech. rep. ATL-PHYS-INT-2016-031. Geneva: CERN, 2016.

[138] ATLAS Collaboration. *ATLAS Tile Calorimeter Phase-II Upgrade Technical Design Report*. Tech. rep. ATL-COM-TILECAL-2017-047. Geneva: CERN, 2017.

[139] ATLAS Collaboration. "Testbeam studies of production modules of the ATLAS Tile Calorimeter". In: *Nuclear Instruments and Methods in Physics Research Section A: Accelerators, Spectrometers, Detectors and Associated Equipment* 606.3 (2009), pp. 362 –394. ISSN: 0168-9002. DOI: https://doi.org/10.1016/j.nima.2009.04.009.

Acknowledgements

The work presented in this thesis is the result of four years of effort that would not have been the same without the contribution, in an academic or personal way, of many people.

First of all, I would like to thank my supervisor, Mario. He was always very supportive, and his guidance during all these years was attentive and patient. His corrections to this thesis made it what it is, and I will never be thankful enough for everything I achieved under his supervision.

During my first years at IFAE, Martin Tripiana guided my baby steps in ATLAS, and I would never have learned so much and so fastly without him, he deserves a very special thank you. The IFAE office at CERN was also shared with many talented postdocs. Thanks a lot to Arely, Remi and Rachel, for the interesting discussions and the great help.

My first work in the ATLAS Collaboration was related to the Tile Calorimeter activities. For this time, I have to deeply thank Ilya Korolkov, Sanya Solodkov, David Miller and Irene Vichou, among many others in the TileCal group. The jet and MET group also helped a lot during this period for the approval of the JetTileCorrection, and I would like to thank them for that.

All the time I worked within the Stop 0-lepton group in the analysis, I relied on the help of many people, especially Walter Hopkins, Vasiliki Kouskoura and George Redlinger. They were always responsive and willing to help with every kind of issue, and for that I have to thank them. Thanks also to Fabrizio Miano for sharing cutflow frustration and other amusements.

During all my time at CERN I had the chance to share the office with great people that made the experience much more enjoyable. Thanks for this to Cora, and very big thanks to Silvia and Jose, for their support in the office and for their very special friendship, and thanks to Marc and Irina, who made me learn more than they realized. On the other side of CERN, but also working at IFAE, thanks to Chiara, my very first friend in Geneva.

Outside of working hours, my period in Geneva was a wonderful experience thanks to many people, and I can not possibly mention them all, but big thanks and lots of love to Roger, Ceci, Nacho, Barbosa, Emma, Claudia, Aleksandra, Aleks, Sabrina, Javi, Damián, Arthur and many others. Of course, infinite thanks to my flatmates, Carlito, Alex and Joanna, living with you was an amazing experience; and the later comers Oskar and Vebjorn.

Even in the distance, the support from older friends was very important, my physicists in Bilbao, Barcelona and around the world, Victor, Mar, Adrián, Ari, Laura, Lander, Santi, Albin, Adri, I wouldn't be here without you.

To my parents and my sisters, who were a huge support in the difficult moments and were always proud and trusted me. Gracias a vosotros estoy hoy aquí. Gracias por confiar en mí, y por entenderme en los largos periodos de ausencia.

Finally, thank you Fabio. Thanks for all the time you were here, and for when you were not. Thanks for the fun in Brighton, and the time in Geneva. Thanks for Portugal, and Tuscany. Grazie per essere sempre là per me.